Steuerungs- und Regelungstechnik

Bernhard Rolle

Model Predictive Energy Management for Induction Motor Drives and All-Wheel-Drive Battery Electric Vehicles

Band 57

**Berichte aus dem
Institut für Systemdynamik
Universität Stuttgart**

Model Predictive Energy Management for Induction Motor Drives and All-Wheel-Drive Battery Electric Vehicles

A Flatness Based Approach

Von der Fakultät Konstruktions-, Produktions- und Fahrzeugtechnik
der Universität Stuttgart
zur Erlangung der Würde eines Doktor-Ingenieurs (Dr.-Ing.) genehmigte
Abhandlung

Vorgelegt von

Bernhard Friedrich Karl Rolle
geboren in Johannesburg Südafrika

Hauptberichter:	Prof. Dr.-Ing. Dr. h.c. Oliver Sawodny
Mitberichter:	Prof. Dr.-Ing. Knut Graichen
Tag der mündlichen Prüfung:	21. Dezember 2020

Institut für Systemdynamik der Universität Stuttgart

2020

Berichte aus dem
Institut für Systemdynamik
Universität Stuttgart

Band 57

Bernhard Rolle

Model Predictive Energy Management for Induction Motor Drives and All-Wheel-Drive Battery Electric Vehicles

A Flatness Based Approach

D 93 (Diss. Universität Stuttgart)

Shaker Verlag
Düren 2021

Bibliographic information published by the Deutsche Nationalbibliothek
The Deutsche Nationalbibliothek lists this publication in the Deutsche Nationalbibliografie; detailed bibliographic data are available in the Internet at http://dnb.d-nb.de.

Zugl.: Stuttgart, Univ., Diss., 2020

Printed in Germany.

ISBN 978-3-8440-7897-8
ISSN 1863-9046

Shaker Verlag GmbH • Am Langen Graben 15a • 52353 Düren
Phone: 0049/2421/99011-0 • Telefax: 0049/2421/99011-9
Internet: www.shaker.de • e-mail: info@shaker.de

Vorwort

Die vorliegende Arbeit entstand während meiner Tätigkeit als wissenschaftlicher Mitarbeiter am Institut für Systemdynamik der Universität Stuttgart in Zusammenarbeit mit der Daimler AG.

Ich bedanke mich bei allen, die mich in dieser spannenden und überaus herausfordernden Zeit begleitet und unterstützt haben. In einem lebhaften und familiären Umfeld konnte ich von inspirierenden Menschen lernen, die alle in vielfältiger Art und Weise zum erfolgreichen Abschluss der Promotion beigetragen haben.

Mein besonderer Dank gilt Herrn Prof. Oliver Sawodny für die ausgezeichnete Betreuung und das entgegengebrachte Vertrauen. Herrn Prof. Knut Graichen danke ich für den anregenden und freundlichen Austausch sowie die schnelle Übernahme des Mitberichts. Außerdem danke ich Herrn Prof. Hans-Christian Reuss für die angenehme und beruhigende Atmosphäre, die im Vorsitz der Prüfungskommission ausgestrahlt wurde. Ebenfalls bedanke ich mich bei Herrn Prof. Michael Zeitz und Herrn Dr. Eckhard Arnold für ihr ermutigendes Interesse und die hilfreichen, fachlichen Diskussionen.

Im Weiteren bedanke ich mich herzlich bei allen Kolleginnen und -kollegen der Abteilung RD/EIC für die hilfsbereite Atmosphäre und die gute Zusammenarbeit. Speziell gilt mein Dank Herrn Ulrich Springer und Herrn Tobias Wolf für ihre umfangreiche Unterstützung und die vielen Möglichkeiten, die mir in einem exzellenten Projektrahmen geboten wurden.

Ich bin überaus dankbar am Institut, nicht nur tolle Kolleginnen und -kollegen, sondern auch gute Freunde gefunden zu haben. Euch danke ich für euren Rat und die vielen unvergesslichen Momente. Ein großes Dankeschön an das Sekretariat und die Werkstatt für ihr offenes Ohr und die bedingungslose Hilfsbereitschaft. Auch den Studierenden, denen ich in der Vorlesungsbetreuung und der Betreuung der Abschlussarbeiten begegnet bin, danke ich für die gewonnenen Ideen und Erfahrungen.

Mein ausdrücklicher Dank gilt meiner Familie für ihren beständigen Rückhalt. Besonders danke ich meiner Frau für ihre Geduld, ihr Verständnis und die hartnäckige Ermutigung mal abzuschalten und zu entspannen.

Stuttgart, Januar 2021 Bernhard Rolle

Abstract

Since emission and fuel economy standards have risen significantly, car manufacturers find themselves forced to invest in new battery and related technologies. Research on methods and technologies that improve the efficiency of both the battery and the electric powertrain, pose the greatest challenges of this technological transition. Therefore, software solutions for energy management and motion control as well as economic driving strategies are becoming more and more the focus of future developments. Software solutions allowing for potential economic savings are particularly appealing, since these do not require any structural or mechanical design changes.

With the main objective of increasing economic savings, this present work investigates analytical models of the electric powertrain for a battery electric vehicle with two drive modules on the front and rear axle. The modeling approach focuses on loss processes associated with the energy conversion of the voltage source inverters and induction motors. Due to a wide spectrum of involved time constants in the range of seconds to a few milliseconds, efficiency analyses of electric vehicles rarely follow model-based approaches and instead rely on characteristic loss maps, which neglect dynamic effects and physical limitations, for example, those resulting from the limited battery voltage. This widespread sespectrum comes from both the longitudinal dynamics of the vehicle and the voltage and current harmonics that result from high frequency switchings of the inverters' semi-conductors. New dynamical models are thus proposed that can be efficiently integrated into vehicle simulations and also be implemented online on embedded systems, such as the motor control unit of the investigated vehicle. In doing so, an average value model of the voltage source inverter is derived, based on a double Fourier integral analysis of the semi-conductor switching signals. Furthermore, a widely used model of the induction motor, applied for motor analysis and control design, is reformulated into an equivalent differential flat system based on the definition of a new flat output. Both component models are integrated into a vehicle simulation of a Mercedes Benz EQC prototype and are thoroughly validated through extensive simulative studies and experimental test series.

With the help of the newly introduced models and with the assistance of modern vehicle sensor systems, control strategies of the electric powertrain are investigated that aim for the most energy efficient operation. In a first step, decentralized optimal control approaches are proposed that improve the efficiency of the electric drive module, not

only during stationary operation, but also during transient torque con-ditions. This improvement is achieved by an appropriate field oriented control method. In a second step, optimization-based torque allocation strategies are investigated and evaluated experimentally. Finally, a centralized predictive control approach is presented that exploits all operational degrees of freedom, which are the variable torque allocation, the front and rear axle magnetic flux, and the adjustment of the vehicle speed according to topographical and traffic dependent conditions. Significant economic savings are demonstrated for the decentralized control methods as well as for the centralized control approach.

The high level of accuracy and performance that is achieved by the proposed model-based framework and predictive operational strategies are only made possible by exploiting the positive structural properties of the newly introduced differential flat system representation of the induction motor.

Kurzfassung

Durch die fortschreitende Verschärfung der gesetzlichen Anforderungen sehen sich Automobilhersteller gezwungen, in die zunehmende Verwendung von Batteriesystemen zu investieren. Die größte Herausforderung dieses technologischen Wandels stellen Verbesserungen im Bereich der Batterietechnologie mit dem Fokus einer effizienteren Energieumwandlung dar. In Anbetracht der Tatsache, dass in naher Zukunft keine disruptive neue Batterietechnologie erwartet wird, rücken softwaretechnische Lösungen im Energie- und Vortriebsmanagement und sogenannte Eco-Driving Assistenzsysteme immer weiter in den Vordergrund der Forschung und Entwicklung. Entsprechende Technologien sind von großem Interesse, da sie keine baulichen Änderungen erfordern.

Die vorliegende Arbeit beschäftigt sich mit der analytischen Modellbildung des elektrischen Antriebsstrangs eines batterieelektrischen Fahrzeugs mit zwei Antriebseinheiten auf der Vorder- und Hinterachse mit dem Ziel einer effizienteren Energiewandlung. Im Vordergrund der Modellierung stehen die Verlustprozesse der Wechselrichter und Asynchronmaschinen. Aufgrund des hohen Spektrums der dominanten Zeitkonstanten im Bereich von wenigen Millisekunden bis hin zu einigen Sekunden, hervorgerufen durch die Trägheit der Fahrzeuglängsdynamik sowie der Strom- und Spannungsoberwellen des Wechselrichters, finden dynamische Modelle der elektrischen Komponenten in Effizienzanalysen elektrischer Fahrzeuge selten Anwendung. So werden Verlustkennfelder gegenüber modellbasierten Ansätzen weitgehend bevorzugt. Stationäre Kennfelder sind jedoch nicht in der Lage, dynamische Verlusteffekte und Randbedingungen, die z.B. aus dem Abfall der Batteriespannung bei hohen Leistungsanforderungen resultieren, abzubilden. Diese Arbeit stellt neue dynamische Modellansätze vor, die nicht nur eine effiziente Integration in einer Gesamtfahrzeugsimulation ermöglichen, sondern aufgrund Ihrer Echtzeitfähigkeit auch auf der Motorsteuerung des betrachteten Versuchsfahrzeugs implementiert werden können. Die Modellierung des Wechselrichters erfolgt dabei im Frequenzbereich durch die Betrachtung einer zweidimensionalen Fourier-Entwicklung der Halbleiter-Schaltsignale. Ein in der feldorientierten Regelung häufig genutztes Modell der Asynchronmaschine wird durch die Definition eines neuen flachen Ausgangs in eine äquivalente differenzielle Form transformiert. Beide Teilmodelle werden in ein Fahrzeugmodell eines Versuchsträgers, der auf einem Mercedes Benz EQC basiert, integriert und durch umfangreiche Simulationen und Messungen validiert.

Die Betriebsstrategie des elektrischen Antriebsstrangs wird auf Basis der neu vorgestellten Modelle unter Berücksichtigung zusätzlicher Fahrzeugsensorik hinsichtlich der Energieeffizienz optimiert. Zunächst wird eine dezentrale Optimalsteuerung betrachtet, welche die Effizienz der Asynchronmaschine durch eine variable Feldstärke im stationären Betrieb wie auch bei dynamischen Momentenanforderungen steigert. Anschließend wird eine Optimalsteuerung für die Verteilung des Antriebsmoments implementiert und experimentell bewertet. Abschließend wird eine zentrale modellprädiktive Regelung untersucht, die alle verfügbaren Freiheitsgrade nutzt: die variable Momentenverteilung, die Feldstärke beider Antriebseinheiten und die Anpassung der Geschwindigkeit an die topographischen und verkehrsbedingten Gegebenheiten. Sowohl für das dezentrale als auch für das zentrale Reglungskonzept kann eine deutliche Verbesserung der Effizienz nachgewiesen werden.

Der wesentliche Beitrag dieser Arbeit ist die neue flache Darstellung der Asynchronmaschine, ohne die das modellprädiktive Regelungskonzept in dem vorgestellten Detaillierungsgrad nur mit sehr hohem rechentechnischem Aufwand umsetzbar wäre.

Contents

1 Introduction

By 2017, the world's total energy supply had more than doubled compared to 1971 [99]. Since 1971, oil has been the predominant energy source amounting to one third of the total primary energy supply. While the share of the total final consumption has hardly changed for most sectors, the consumption from the transport sector is continually growing. As transportation still heavily relies on fossil fuels, it is responsible for nearly one quarter of the world's *Greenhouse Gas Emissions* (GHGEs) [63, 100], where passenger transport accounts for three quarters of this amount [62, 98]. Due to shorter development periods and lifetimes of passenger cars and light duty vehicles compared to aircrafts, trains, and ships, high expectations are placed on new vehicle technologies [212]. However, after a steady decline of the average emissions from new passenger cars between 2010 and 2016, the fleet-average *Carbon Dioxide* (CO_2) emissions increased in the two consecutive years [225]. Reasons for this upward trend are the strong demand for high-powered vehicles and *Sport Utility Vehicles* (SUVs) as well as a growing share of newly registered petrol cars in response to the Volkswagen emissions scandal [201]. Furthermore, the increasing demand for transport highly contributes to air pollution with harmful concentrations of nitrogen dioxide and particulate matter, especially in urban and highly populated areas [36]. These environmental pressures and the resulting climate change raise more and more public concerns, which motivate stricter regulatory actions.

Consequently, global CO_2 emission and fuel economy standards have become significantly more progressive in order to create incentives for the car industry to invest in new technologies, mitigate global warming, and improve environmental health [35]. The historical development of fleet emissions performance and current standards for passenger cars are presented in Figure 1.1. The European emissions regulations, with a fleet average target of 95 gCO_2/km by 2021, is the most stringent in the world. A violation of the manufacturer's specific limit incurs a fine of 95 EUR per year for every excess gram of CO_2 multiplied by the number of newly registered vehicles (cf. Article 8 [168]). Only a few manufacturers are on track and will be able to reach their 2021 targets [62], which is why Europe's thirteen top manufacturers are facing serious penalties with more than 14.5 bn EUR in fines [164]. Due to technological advancements of battery technologies and the drastic decrease of battery costs over the last decade [100], car manufacturers have announced a diversified portfolio of *Electric Vehicles* (EVs) in order to comply with the emission reduction targets. In the European Union about sixty models were available at the end of 2018 whereas 333

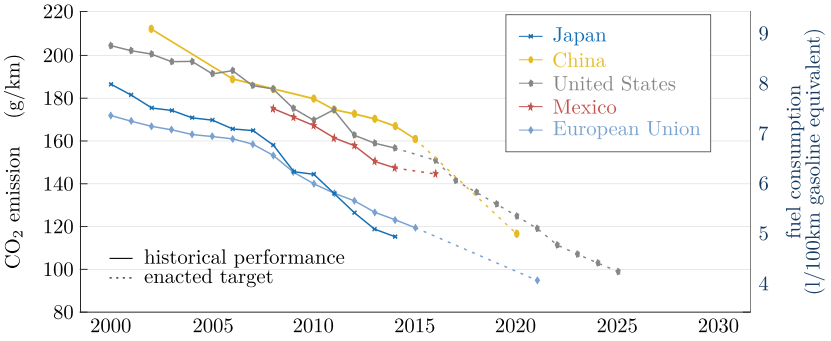

Figure 1.1: Fleet CO_2 emissions performance and current standards (normalized to the New European Driving Cycle; cf. Figure 2 [35]).

models are expected in 2025 [38, 225]. While the numbers of available *Plug-In Hybrid EVs* (PHEVs) and *Fuel Cell EVs* (FCEVs) seems to flatten, the growth of *Battery EVs* (BEVs) continue to follow a strong linear upward trend. To accelerate the rate of electrification, markets are increasingly adopting zero-emission vehicle mandate programs [37] and are gradually transforming from direct to more indirect forms of subsidies, including an increased support for the charging infrastructure.

As BEV sales are expanding at a fast pace and a mass-market adoption for battery production in Europe is triggered [225], EVs and in particular BEVs present the key future component of a sustainable mobility in the upcoming decade. The main advantages of BEVs include:

- a considerably better efficiency than conventional *Internal Combustion Engine* (ICE) vehicles, which offers a high potential for GHGEs reductions,
- zero tailpipe emissions, well suited to address air pollution issues in urban areas,
- dependencies on oil imports are reduced since electricity can be produced with a variety of resources and fuels, and is often generated domestically,
- decarbonisation of electricity supply benefits both, battery manufacturing facilities and charging, which amplifies advantages of EVs relative to other powertrains.

However, to unleash the full potential of BEVs, it is crucial to discuss disadvantages and to understand the environmental impact associated with all stages of their life cycle [61, 104]. A comparison of life-cycle GHGEs of an average mid size car for different powertrains is shown in Figure 1.2. Being the component with the most

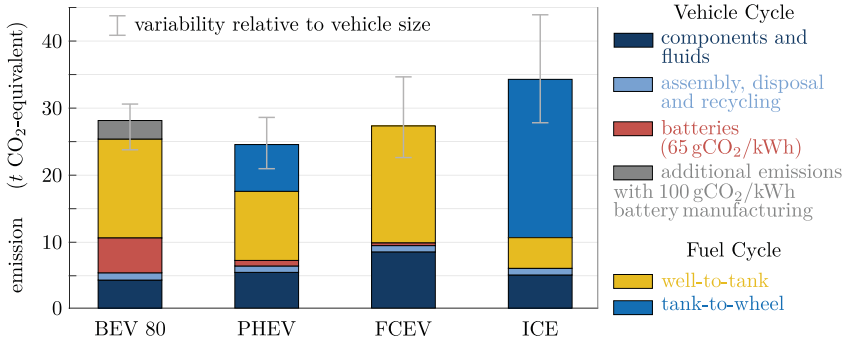

Figure 1.2: Life-cycle GHGEs over ten year lifetime of an average mid-size car by powertrain: battery electric vehicle with an 80 kWh battery (BEV 80), plug-in hybrid electric vehicle (PHEV), fuel cell electric vehicle (FCEV), internal combustion engine (ICE); cf. [100, 104]).

energy-intensive manufacturing process, the battery can be responsible for up to a third of the vehicle's life-cycle emissions. Apart from GHGEs, the battery has a high impact on raw materials. Furthermore, due to the limited battery capacity, the limited range is still one of the main barriers for customers to buy BEVs. Therefore manufacturers aim to increase the energy density of batteries. However, by adding more cells to the battery pack, the environmental impact due to the additional weight, raw material extraction, and processing increases as well. Nevertheless, based on the average electricity mix in Europe, it can be concluded that the high efficiency of BEV powertrains can reduce the well-to-wheel emissions during the fuel cycle and therefore has the potential to decrease GHGEs when compared to ICE vehicles [61]. The extent of which depends on various factors including amongst others the progress of the electricity generation mix, the vehicle's lifetime mileage, size, and weight as well as the driving location and style. In particular, an increase in weight leads to a disproportional increase of the GHGEs during the tank-to-wheel life cycle. If the weight of a BEV cannot be reduced, this deficit has to be compensated for by improving the overall efficiency of the electric powertrain.
The enhancement of battery performances, such as cost, density, and cycle life, are the decisive factors for the success of electric mobility. Future potential battery technologies, however, are not yet beyond the laboratory stage leaving the Li-ion battery to likely dominate the BEV market over the next decade [100]. Therefore, it is fundamentally important to investigate methods that improve the BEV energy efficiency, considering both present and near future means.

1.1 Battery Electric Vehicles

The battery is not the only BEV system that needs to be redesigned and improved in order to meet the growing demands and concerns of the future electrification of mobility. The electric powertrain also offers great potential for optimizing the energy conversion of the stored electrochemical energy into traction, braking, and thermal energy. When focusing on motion control, energy conversion is provided by two main components: power electronics and the electric motor. The most commonly used motors of current BEVs are the *Induction Motor* (IM) and the *Permanent Magnet Synchronous Motor* (PMSM) [252]. Advantages and disadvantages of different motors used in vehicle applications are discussed in numerous studies including [65, 169, 247]. As was concluded in [10, 156], no definite statement can be made on which motor type generally has the highest energy efficiency. Therefore, the selection of the motor type must be based on a well-defined operational range and the associated power ratings. These in turn are determined by various dynamic drive and load cycles and are mainly influenced by the vehicle size and weight. Besides the choice of motor type, several general powertrain configurations exist [8, 64] that may be classified according to

- the number of powered axles $\in$ {single axle, all-wheel-drive},
- the number of motors $\in \{1, 2, 3, 4\}$,
- the alignment of multiple motors $\in$ {longitudinal, lateral},
- the type of transmission $\in$ {single-speed, multiple-speed},
- the usage of a clutch to disengage the motor.

Transmissions are adopted for EVs in order to operate at higher rotor speeds than ICEs and to enable an increased power density. A single-speed transmission is often preferred to multi-speed systems due to the low design complexity and the high efficiency of PMSMs over a wide speed range [54]. Clutches are required, for example, in the case of a PMSM to avoid high idling losses and sudden jamming during faulty operation.

The vehicle investigated in this study is a *Mercedes-Benz EQC* prototype. In 2019 the *EQC* was the first battery electric *Mercedes-Benz* vehicle launched under the *EQ* brand. The electric powertrain of the EQC features a 400 V battery with a nominal energy storage of 85 kWh. Two centered 150 kW IMs, each with different characteristics, are installed in longitudinal alignment on the front and rear axle. Each motor is equipped with a single-speed transmission and a power inverter with *Insulated-Gate Bipolar Transistor* (IGBT) modules, which have a maximum rating of 650 V/800 A. The transmission, the electric motor, and the power electronics are all integrated into one compact *Electric Drive Module* (EDM) to optimize the package, weight and cost.

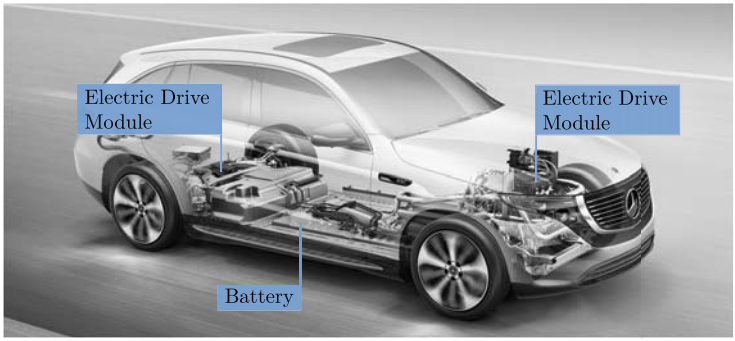

Figure 1.3: Electric Powertrain of the Mercedes-Benz EQC [41].

Apart from the EDM, the battery also supplies a 12 V electrical system via a DC/DC converter. Low voltage systems, which for example include the control units, the head unit, and the high voltage thermal management system, are considered as auxiliaries. In order to keep the system temperature of the battery and both EDMs in their nominal ranges, all three components are provided with water and convection based cooling systems. Furthermore, to attain a high power density, the motor rotor shafts are flooded with cooling water for heat discharge. *Positive Temperature Coefficient* (PTC) heaters are used in cold weather conditions mainly for cabin heating and to maintain the nominal battery temperature.

1.2 Operational Strategies

The research to date has not been able to establish a convincing analytical framework that supports the conceptional design of *All-Wheel-Drive* (AWD) BEVs. One of the main reasons is that the possibilities and limitations of operational strategies for electric powertrains are insufficiently considered in explorative studies and during design decisions. Operational strategies refer to supervisory controls, component controls, and software solutions for energy management, thermal management, and motion control. All three strategies together determine how the associated components should operate and interact in order to satisfy the control or motion task in the safest, the most convenient, and efficient way. Software and control approaches with potential economic savings are particularly appealing, since these do not require any structural or mechanical changes.

A typical application for energy management is the battery management system which, for example, observes the battery's state of charge [40]. Based on all state observations of the battery, measures are taken to guarantee a safe and optimal operation, e. g. in terms of cycle life [188]. Energy management is thus also associated with control functions that regulate and coordinate the power flow of all involved energy sources. Thermal management encompasses all control tasks in association with heating, air conditioning, and cooling [200]. Finally, motion control determines an optimal driving strategy while considering dynamic, driveability, and economic aspects. Subsequently this strategy is implemented by applying and coordinating the corresponding control actions for all available actuators. Motion contro strategies are sometimes also referred to as energy management strategies. This work focuses on *energy management* strategies of EDMs as well as on *driving strategies* for motion control of AWD BEVs. The guiding research questions are:

- How can energy management strategies improve the efficiency of BEVs in real world driving conditions and how do they differ from strategies developed for *Hybrid EVs* (HEVs) and conventional ICE vehicles?
- What are the main factors that influence the electromechanical energy conversion and how can meaningful representations of these be derived in a model-based framework that supports the design of energy management strategies and powertrain concepts in a computationally efficient manner?

1.3 State-of-The-Art Review

The following synopsis of literature is restricted to EV motion control strategies that are capable of improving the energy efficiency of the electric powertrain. Since special emphasis is placed on the experimental evaluation of such strategies, modeling approaches of EDMs are reviewed with the intention to derive an accurate system representation of the investigated BEV.

1.3.1 Economic Driving

An important step along the energy conversion path of any vehicle is the wheel-to-distance conversion of the mechanical energy, stored in the form of momentum, into kinetic energy of the speed profile and the potential energy dictated by the road topography [206]. This conversion is accompanied with a substantial amount of energy losses and is mainly influenced by weight, aerodynamic drag, and rolling friction as well as the driving style and traffic conditions. Contrary to improvements anticipated for the tank-to-wheel path, the optimal wheel-to-distance conversion aims at a maximum utilization of the available energy at the wheels, independent of the powertrain type. Corresponding methods can be applied to all kinds of vehicles including trains [32],

buses [244], and FCEV [3]. However, generally, the two problems addressing the tank-to-wheel and wheel-to-distance efficiency are not decoupled so that the energy management of the powertrain has a strong influence on the optimal driving strategy. This is demonstrated by the similarities in the cases of a pulse-and-glide strategy for a gasoline engine [80, 130] and the state of charge strategy for a PHEV [87, 88].

Much of the literature on energy efficiency focuses particularly on *Economic Driving* (ED) strategies that predominantly act on the vehicle's speed and acceleration. An overview on modeling approaches and solution methods for ED is presented in [205, 206]. Based on the original findings of [207], the authors propose a classification of ED strategies as systems that offer advice: before departure, e. g. by proposing the most energy efficient route [149, 150], during the trip supported by advanced driver-assistance systems, and after arrival through encouraging summaries and statistics. In this context, advanced driver-assistance systems can be further classified as systems that provide

- feedback advice based on the historic and current performance, for example by means of an ED indicator [49],
- feedforward advice based on upcoming events, for example using a haptic accelerator pedal [144],
- and means for adaptive or predictive cruise control [129, 230].

The former two systems are often based on heuristic rules that are inspired by the best practice of an energy-efficient driver, who is also referred to as hypermiler. Recent methods for adaptive and predictive cruise control, on the other hand, are designed in a more general framework, in which ED is regarded as an optimal control problem [15]. The discipline of optimal control looks at the optimization of a dynamic process that is described by a system of *Ordinary Differential Equation*s (ODEs) or differential algebraic equations. To this end an objective function is defined, which in the case of ED is equivalent to the energy consumption over a pre-defined time or distance horizon. Typically, the consumption is expressed in terms of l/100km in the case of an ICE vehicle and kWh/100km in the case of a BEV. The aim of the optimization is to minimize an objective, where the arguments for minimization are control inputs that are applied to the vehicle. The control inputs for most powertrains can be chosen to be the traction and braking force or equivalent representations of these. Additional controls and degrees of freedom for HEVs and PHEVs, for example, are the selected gear [86] and the torque split ratio between the engine and the electric motor [110]. The optimized control policies and resulting vehicle states have to comply with the state dynamics, which might be influenced and constrained by traffic conditions [5, 145], and at the same time are limited by input and state constraints that are imposed by the technological boundaries of the powertrain.

Frequently adopted solution methods of optimal control problems in automotive applications are based on the indirect method of *Pontryagin's Maximum Principle* (PMP) as well as *Dynamic Programming* (DP) [70, 206]. PMP methods transform the optimal control problem into a multi-point boundary value problem via the necessary conditions of optimality. For special cases, including the ED problems in [80, 108, 163, 205], an analytical solution can be derived for the control inputs of the powertrain. These examples assume that the driving scenario over the optimization horizon is known. The indirect method of PMP yields highly accurate solutions for these scenarios and is well suited for theoretical analyses of the problem structure, from which rule-based strategies can be derived [93, 170, 243]. A considerable disadvantage of indirect methods is the laborious derivation of the necessary conditions of optimality. These conditions must be determined for every problem instance and driving scenario and may require several different special cases depending on the state and input constraints. Likely for such reasons, DP is the most common method, primarily employed for HEVs and PHEVs [134, 174, 177, 232]. DP methods are based on Bellman's Principle of optimality [13]. In a discrete form, in which both the control inputs and system states are discretized, they have the great advantage of finding a global solution for the discretized system regardless of the chosen model complexity, yet, they suffer from the *curse of dimensionality*. This means that a slight increase in the problem's dimension, for example, by using a more sophisticated model of the powertrain with multiple states or by considering more degrees of freedom, induces an unacceptable growth in the required computational time. A method that does not require any prior knowledge of the driving cycle and that is computationally less demanding, yet can combine the merits of both DP and PMP, is known in the HEV literature as the *equivalent consumption minimization strategy* [162, 165, 208]. This method presents a systematic approach for an optimized coordination of both power sources via the electric motor and the combustion engine, using the definition of an equivalent fuel consumption. A more extensive overview and thorough review on optimized ED and energy management strategies for HEVs and PHEVs is found in [17, 88].

Despite the extensive literature on ED, only a few studies validate the proposed driving and energy management strategies using experiments with real world driving conditions. In [85], an online-capable discrete DP method is implemented for an ICE truck, which on highways achieves a fuel saving of 6 % at the cost of a 2 % longer travel time. An example using ICE passenger cars, is presented in [185], where the fuel consumption is improved by 10 % while the average speed is maintained. Savings of up to 3 % compared to a heuristic approach are demonstrated on a chassis dynamometer for optimized energy management of a HEV truck [234]. However, the traveling time is not examined. Focusing on BEVs, a discrete DP method is implemented for a *Tesla Roadster*, which reduced the energy consumption by more than 6 % without any notable impact on the traveling time [185]. A number of experiments are conducted

in urban areas by [70, 71, 189] using a battery electric *Smart ForTwo*. The authors achieve an efficiency improvement of 6 % with a 1 % increase of traveling time. This is done by optimizing the speed trajectory as well as an adaptive cruise control that follows the traffic-dictated speed.

1.3.2 Optimal Torque Distribution

While there is a large body of literature on ED and energy management for HEVs and PHEVs, very few studies investigate optimal control strategies that are particularly suited for BEVs. The coordination of the engine and the electric motor of hybrid vehicles, as well as the degrees of freedom that are presented by the multi-speed transmission and the possibility to regenerate energy during braking, are the factors that make the ED control problem challenging. This high number of degrees of freedom represent a promising opportunity to improve the overall efficiency. A BEV on the other hand, only has a single power source, typically adopts a single-speed transmission, and, therefore, offers less savings potential from a control perspective. However, AWD concepts allow for a variable distribution of the traction and braking torque between front and rear axle. Since both axles are involved in the energy conversion process there is an increased regenerative braking potential. Furthermore, with only three components in the EDM energy conversion chain (power inverter, motor, transmission), the efficiency can be improved by a favorable shift of the motor's operating points. In an extensive simulative study [8], it is demonstrated that an AWD BEV with two motors and longitudinal torque distribution can be the most energy efficient concept for a sport utility BEV. For this powertrain configuration, an optimization-based torque distribution strategy is proposed, which aims for the minimum power demand in every operating point using the front and rear axle torque as the arguments for minimization. To this end, power losses are represented through speed and torque dependent efficiency maps. Optimized design explorations for two motor concepts with integrated power distribution are presented in [45, 95]. Both methods approximate power losses along the design process using quadratic functions, however, [45] derives these based on more sophisticated component models. Following the model-based approach, the authors show that an optimal power distribution between differently sized motors can improve the overall efficiency by 0.7 %, compared to a single driven axle using one motor. However, as other studies indicate, the full potential is not yet fully exploited.

With this in mind, research has turned towards energy-efficient operations using torque distribution and control allocation methods over the past decade. A comprehensive overview of corresponding strategies is presented in the state-of-the art review in [209]. Contributions are arranged in chronological order and categorized according to the powertrain configuration, the considered loss processes, the modeling assumptions

of the vehicle dynamics, and validation means, i.e simulation and experiments. The vast majority of investigations focus on configurations with four motors and, thus, in addition to the flow of energy, are mainly concerned with aspects related to driving dynamics including longitudinal and lateral tire slip [171] and direct yaw moment control [123, 172, 173]. In [53], the authors look at a case study featuring a BEV *Range Rover Evoque*, in which all four EDMs have the same characteristics. For this specific powertrain configuration, it is shown that the lateral torque distribution is optimal when both front and rear axle motors are operated in either traction or regeneration. Furthermore, in the case of small torque demands, drive via a single axle is optimal, whereas an even longitudinal distribution is the most energy efficient solution for high torque demands. If only a single-axle is energized, the front motors are selected due to safety aspects and the tendency to oversteer. Based on these findings, an optimal switching point between these two modes of operation is derived as a function of the vehicle speed. Adopting this switching characteristic, energy savings of up to 3 % compared to a single powered axle are demonstrated in experiments of the *Artimes Road* driving cycle with a constant 8 % uphill slope.

As a result of implementing an ED strategy, which exhibits only moderate acceleration values, lateral driving dynamics and losses due to tire slip can be neglected. Nevertheless, in an optimized torque distribution problem formulation, a road curvature can enforce limitations due to the non-negligible centrifugal acceleration [185]. A notable example of an optimization based distribution strategy for a two-PMSM concept with dog clutches that solely considers the tank-to-wheel conversion is analyzed in [115]. The clutches are used to disengage the motors in order to reduce idling losses. Instead of using the front and rear axle torque as optimization arguments, the control is reduced to a single input of the distribution factor, also referred to as torque split. The optimization problem is solved offline for every possible torque and speed combination and the solution is represented as a distribution factor map. Moreover, an optimal control problem is introduced, which considers a simple dynamic model of the clutches and penalizes a frequent engaging and disengaging of these. This problem is solved by a DP method and requires a minimum prediction horizon of three seconds. A simulative study indicates an energy saving potential of 6.5 %.

1.3.3 Electric Drive Modeling and Control

All of the mentioned torque distribution strategies evaluate losses of the powertrain components using polynomial approximations or efficiency maps and neglect dynamic effects and physical constraints of the BEV powertrain. A model-based approach, which acts on all physical domains along the energy conversion chain aims for a better understanding of how loss processes influence the overall efficiency in dynamic driving scenarios. Following this approach, it is essential also to consider the control strategies

of the powertrain components, since these may have a substantial impact on the overall performance. In particular, it is worthwhile analyzing the electromechanical energy conversion of the motor, which can be influenced according to the amount of energy that is stored in the magnetic field which couples the electrical powertrain and the mechanical drivetrain.

Modeling approaches that simulate both the transient and steady state behavior of a variable-speed electric motors essentially differ in whether they assume sinusoidally or non-sinusoidally distributed windings and whether they account for detailed magnetic properties and design features (for example hysteresis losses or dynamic air-gap variations) or consider linear magnetic circuits and simplified symmetric designs (such as a uniform air gap). While simplified assumptions are valid approximations in most cases and establish the foundation of models for control design [159, 183, 203] and consequently for this study, they lead to less accurate approximations of voltage and current wave forms required, for example, during design processes or machine diagnostics. Technological advances and the exponential progress in computational power have motivated the development of electromagnetic *Finite Element Analysis* (FEA) methods used, for example, in the software package Motor-CAD [153]. However, FEA has the disadvantage of long calculation times. A computationally less intense approach for motor analysis, which accounts for arbitrary windings and unbalanced operation conditions, is known as *Winding Function Theory* (WFT). WFT was established by [224] and modified in [160] and [22]. A detailed description of the WFT concept and an exemplary derivation of a multiple coupled circuit model is presented in [138]. A third possibility for motor analysis is the *Magnetic Equivalent Circuit* (MEC) approach. This has a reduced modeling complexity compared to FEA and an enhanced accuracy compared to the WFT approach [139, 217]. Instead of deriving circuit models with equivalent electrical parameters, as done in the WFT aproach, the MEC concept is based on magnetic circuit models, which allow for a more accurate and straightforward consideration of local saturation, leakage, and iron losses. An extensive overview and comparison of different modeling approaches is found in [248]. All of these modeling approaches have the disadvantage of long computation times due to extremely demanding time constants of the current dynamics compared to the longitudinal dynamics of the vehicle.

Equivalent circuit models of electric motors which are derived from the WFT, compute the angular rotor speed and the electromagnetic torque based on the motors' phase voltage inputs. However, range and efficiency analyses of electric vehicles are based on load cycles that are described by speed and torque profiles. Thus, motor controls have to be considered in the modeling process in order to establish the causality between the inputs of the electrical motor and the load cycle of a driving scenario. The most common control algorithms for IMs and PMSMs are *Field Oriented Control* (FOC), sometimes also referred to as vector control, and *Direct Torque Control* (DTC). The

concept of FOC, originally pioneered by [18, 82], is at present a well established control method widely used in industrial applications thanks to practical implementations and advancements introduced by [73, 105, 124, 125] and many others. An extensive list of publications has been reported on the topic of FOC including the textbooks [126, 183, 203]. In this work, the concept of FOC will be discussed in more detail which is why the main aspects and differences of DTC are now briefly described.
One of the first contributions on DTC was published by [48]. Both schemes FOC and DTC compute the control actions, i. e. switching instances of the inverter's semiconductors, based on the error of the measured or estimated torque and flux (rotor flux for FOC and stator flux for DTC). However, DTC does not require any means for current control, coordinate transformations, or any type of *Pulse Width Modulation* (PWM) [92]. Instead, it schedules the switching instances with the support of hysteresis comparators and optimal switching tables [76, 154]. For this reason, the classical DTC is readily implemented on an embedded system and does not put any high demands on the control hardware. The lack of direct current control [28], however, makes FOC more attractive for BEV applications. By analyzing the similarities of both control approaches, [229] proposed a method using current hysteresis comparators to combine the merits of both FOC and DTC.

Regardless of the chosen motor control, the magnetic flux can be controlled independently of the torque or speed. This additional degree of freedom is exploited in a *Loss Minimizing Technique* (LMT) to find an optimal balance between different loss processes that act on the electric and magnetic domain of the motor [11]. IMs especially benefit from a LMT as demonstrated in the comperative study of IMs and PMSMs in BEV applications [25]. Corresponding strategies for PMSMs are commonly referred to as *Maximum Torque Per Ampere* (MTPA) [181, 222]. Nonlinear model predictive control schemes for PMSMs are presented in [58, 59]. Though modern power electronic devices are generally assumed to achieve high efficiencies, these values are only reached in a very specific torque and speed region. If BEVs are operated in a partial load area far below the maximum power rating, the efficiency is significantly reduced. To guarantee an energy-efficient operation over the entire torque and speed range, search-based LMTs try to converge to a minimum power loss by means of a dedicated feedback loop [79, 228], wheres model-based LMTs strive for analytical expressions of the optimal flux level [131, 148]. A nonlinear model predictive control scheme and optimal setpoint computation for IMs is proposed in [60].

As will be shown in this work, IM analyses and control designs of LMTs can gain advantages from a system theoretic perspective that is based on the concept of differential flatness. The theory of differential flatness is built on concepts of differential geometry and has been successfully established in the field of nonlinear system analyses and control design [67, 128]. In [33], it was demonstrated that the IM is linearizable by a dynamic state feedback which is essentially equivalent to a proof of differential

flatness [66]. Based on these findings, it was originally shown by [140, 141] and confirmed by [47] that the angle of the rotor flux orientation and rotor angle form a flat output. All electrical and magnetic states of the motor can be represented as analytical functions of the flat output and its successive time derivatives. These functions are referred to as state- and input-parametrization. One disadvantage of the variable choice in [140, 141] is the dependency of the derived state- and input-parametrization on the load torque, which is assumed to be known. However, due to complex friction effects of the drivetrain and tires as well as unpredictable road conditions, the load torque and its time derivatives are prone to high uncertainties. Furthermore, when it comes to the problem of range and efficiency analyses, the rotor flux orientation angle is not an intuitive choice as it is neither directly connected to the FOC task of the IM nor to the motion control task of the vehicle.

1.4 Goals and Contributions of this Dissertation

In this study a model-based framework is developed that accurately represents the energy flow of the electrical powertrian of an AWD BEV in a variety of stationary and dynamic operating conditions. Contrary to characteristic loss maps that are typically used in analyses of energy management strategies for electric powertrains, the introduced framework adopts equivalent circuit models of the IM and *Voltage Source Inverter* (VSI). These are defined only by a few electrical parameters, of which VSI parameters are easily obtained form the manufacturers data-sheets. Furthermore, identification procedures of IM model parameters have reached a maturity level with considerably lower costs and time-expenditure than empirically determined loss or efficiency maps. These require extensive measurements over a wide torque and speed range, which have to be repeated at different temperatures and battery voltage levels. A further advantage of the model-based approach is a straight forward consideration of the temperature and battery voltage dependencies. For example, temperature dependent variations of losses can be considered by adjusting the resistive parameters of the IM and VSI. The voltage dependency of the motors maximum torque rating is inherently represented by the voltage equations of the IM. Furthermore, since meaningful IM circuit parameters are obtained through FEA, analyses of operational strategies can be performed in an early development phase of a BEV.
In order to raise the acceptance of the proposed model-based framework within the automotive field, it is important to evaluate its accuracy and highlight its limitations. The component models of the electric powertrain are thus validated by using the case study of a *Mercedes-Benz EQC* prototype. In the scope of this study modeling and analysis processes of the EQC powertrain concept are considered. Nevertheless, due to the modular structure of the component models, the framework can be readily generalized to incorporate other concepts with PMSMs, multi-speed gears, and clutches.

Despite the many advantages of a model based approach, previous studies, including the reviewed studies on ED and torque distribution, have struggled to implement sophisticated models of electric powertrain components mainly due to the associated time scales. While the vehicle's longitudinal dynamics are governed by time constants in the range of seconds, current transients of the motor occur in a few milliseconds and are therefore several orders of magnitude faster than the frequencies that appear in a typical driving cycle. In [196, 197], it is demonstrated how these voltage and current harmonics can have an impact on the performance and design of an electric powertrain. The main difficulty that arises with these wide spread time scales is the computational burden associated with the numerical solution of the underlying ODEs. A unique characteristic and one of the most significant contributions of this study is the representation of IM system dynamics as a new differential flat system that overcomes the previously discussed disadvantages of existing approaches. By exploiting the positive structural properties and, in particular, the canonical form of this equivalent system, the IM model is reformulated as a set of equivalent linear differential equations. In other words, the canonical form can be interpreted as a chain of integrators in which system dynamics are described by straightforward differentiation of the flat output. Consequently, if the flat output trajectory is known, all states and inputs are also known by algebraic relations of the *state-* and *input-parametrization*. The central benefit of this equivalent representation is that IM dynamics in its canonical form can be considered as "less dynamic" compared to the IM current dynamics and is therefore better suited for simulation and optimal control design. Based on this flat system representation and a newly derived average value model of the VSI, it is possbile to compute BEV losses online, using the vehicle's *Motor Control Unit* (MCU). Moreover, as noted in [176], an inversion-based approach such as the flat system enables a computationally efficient solution for optimal control.

For these reasons the differential flat model framework is well suited for the investigation and systematic design of ED strategies. Based on this framework, energy management strategies are formulated as optimal control problems and analyzed on the component level of the IM and a centralized BEV system level. The degrees of freedom used to improve the powertrain's efficiency are

- the magnetic flux of the electric motor,
- the longitudinal torque distribution,
- and the vehicle's acceleration and speed.

Contrary to DP and PMP methods that are widely adopted in automotive applications, this work introduces a direct multiple shooting method to solve the optimal control problems in a *Nonlinear Model Predictive Control* (NMPC) fashion [50, 51]. Direct methods, including collocation methods [195, 227], single shooting methods, and multiple shooting methods [19, 112], are based on a discretization of the infinite-dimensional optimal control problem into a finite-dimensional nonlinear optimization.

Numerical solution methods for nonlinear optimization have been considerably improved in terms of reliablity and computational speed due to algorithmic developments, for example, of *Sequential Quadratic Programming* (SQP) and *Interior Point* (IP) methods [158].

Following this approach the central role of the magnetic field is thoroughly investigated in the context of ED and energy management strategies for BEVs. The findings gained from the analytical perspective of the differential flat system representation allows for a more profound understanding of how energy conversion is influenced and improved by motion control strategies. Only through this representation it is possible to derive optimal control formulations on a component and vehicle system level that accounts for all BEV specific boundary conditions and operational degrees of freedom and can still be solved in a reasonable amount of time with sufficient accuracy.

1.5 Thesis Overview

This work is laid out in three main chapters. The general structure is illustrated in Figure 1.4. Chapter 2 lays the foundation of the model-based framework and introduces the component models for the BEV powertrain. Emphasis is placed on the components with the fastest dynamics, which are the IM and the VSI. Together both components can be responsible for approximately $18\,\% - 40\,\%$ of associated powertrain losses. The remaining losses are attributed to the drivetrain, the auxiliaries and, with a comparatively small proportion, to internal battery losses. Models of these components are presented, which represent the essential physical interactions along the electromechanical energy conversion chain. Eventually all component models are integrated in a system model of the investigated experimental vehicle and validated by an extensive series of experimental tests.

The BEV system model expresses the relation of how a voltage input influences the vehicle's motion. However, if the driver steps on or releases the accelerator or break pedal, the electrical powertrain acts as a torque transducer where the wheel torque almost instantaneously follows the commanded torque. This causality is established based on appropriate controls of the electric drive. The impact of IM controls on the vehicle's energy management and particularly the influence of the magnetic field as the central link of the electrical powertrain and mechanical drivetrain are discussed in Chapter 3. With the key objective of an optimized energy management, a loss minimizing FOC strategy is presented in an algorithmic form that can be easily integrated on embedded systems and MCUs. Based on a new definition of a flat output and the resulting equivalent system representation, structural insights of IM dynamics are provided from which both FOC or DTC schemes may benefit. Furthermore, extensions of these conventional control methods are investigated that

exploit the properties of the inverse IM model, which is given by the differential flat state- and input-parametrization. Based on the developed algorithm and the inverse model, advanced optimal control strategies are proposed to further improve the component's efficiency and dynamic performance.

Finally in Chapter 4, electric drive controls are integrated into a differential flat model of the BEV powertrain. Within a field study, model-based range analyses are conducted in order to assess the validity of the model, improve the understanding of loss processes in real world driving conditions and to identify economic saving potentials. Built on these findings, an optimized torque allocation strategy is presented in an algorithmic form. Though the control algorithm solely exploits the torque distribution, it accounts for the physical limitations that are imposed by the FOC of the IM. A sequence of experimental tests demonstrate that a re-distribution of traction and braking energy can achieve considerable energy savings compared to a single axle operation. Finally, all degrees of freedom presented by a variable flux level, torque distribution, and driving style are controlled in a centralized NMPC ED strategy, which in a simulative study indicates significant energy saving potentials. A conclusive summary and outlook are provided in Chapter 5.

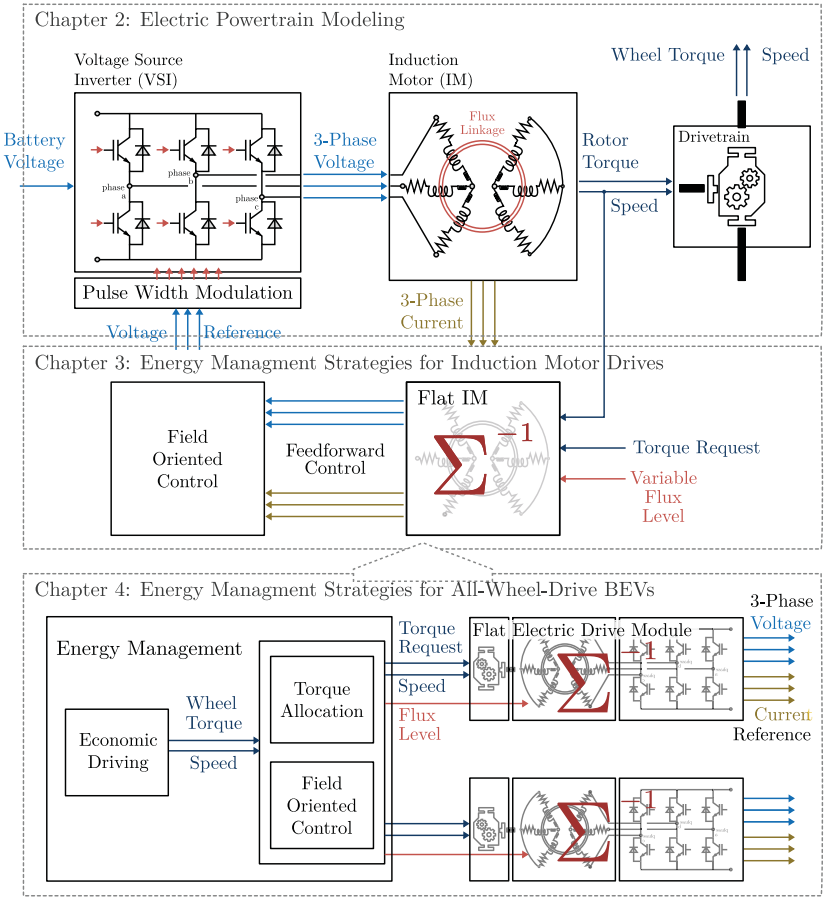

Figure 1.4: Model predictive energy management for induction motor drives and all-wheel-drive battery electric vehicles.

2 Electric Powertrain Modeling

This chapter introduces the modeling assumptions for the components of the investigated BEV powertrain shown in Figure 2.1. Most of the attention is placed on the electrical domain and in particular on the IM and VSI. The central aim of the modeling approach is to accurately simulate the electrical states and related loss processes in order to provide realistic and conclusive evaluations of the powertrain's efficiency and the electric range.

Following the direction of energy conversion for motion control, Section 2.1 starts with modeling the power electronic circuit of the VSI. The bidirectional power transfer between the battery and the IM requires the supply of a balanced three-phase voltage set. The power flow is controlled by a designated PWM strategy, which schedules the switching instances of the individual semi-conductor switches of the half-bridge three-phase inverter. Corresponding power electronics circuit analyses are either conducted in the time- or frequency-domain [21] and, usually, both are required to fully understand the system behavior. Simulations in the time-domain often rely on behavioral based models [29], which, for example, are used in the circuit-oriented software package PLECS [4, 179]. The major difficulty of time-domain analyses is the discrete nature of semi-conductor switching. It is therefore necessary to know exactly when the switching has occurred and how the circuit topology has changed. By combining both discrete switching and continuous circuit components, a VSI classifies as a hybrid system [142]. While avoiding the complexity of a time-domain simulation that comes with switching frequencies of a magnitude in the order of 10 kHz, Section 2.1 derives analytical expressions for VSI losses in the frequency-domain based on a novel waveform model and a double Fourier integral analysis.

Section 2.2 continues with the electromechanical energy conversion of the IM. The derivation of the well known dq equivalent cirquit model of a squirrel-cage IM [119, 120] establishes expressions for torque in terms of the electrical machine variables, i. e. the *Alternating Current* (AC) voltages and currents. A short overview of the reference frame and the turns ratio transformation is presented, as these are at the core of motor analyses. To enable an accurate representation of motor losses the dq-model is extended by a basic loss model for frequency dependent magnet hysteresis losses and eddy currents. While the VSI model is fully parameterized based on information that is typically provided in technical data sheets, resistive and inductive parameters of the IM circuit model have to be identified from FEA or test procedures. A review

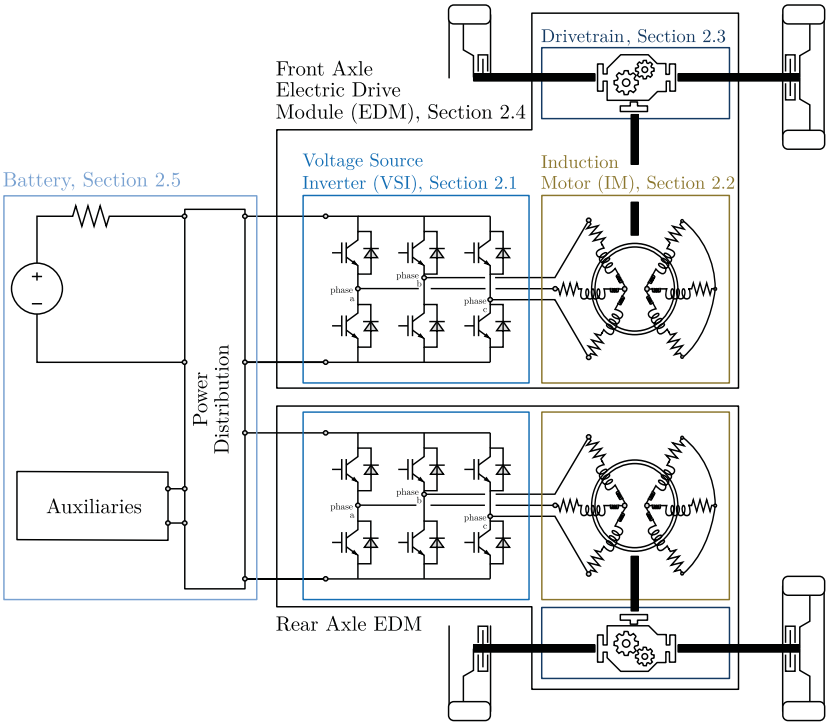

Figure 2.1: Electric powertrain of an all-wheel-drive battery electric vehicle.

of parameter estimation methods for online and offline identification is presented for a simple adaptation in vehicle applications. Offline methods require special test procedures and measurement equipment, whereas online methods have the potential to run on the MCU of the BEV during normal operation. An overview on identification methods with numerous references to related publications is found in [223]. In addition to these standard methods, a novel in-vehicle identification procedure is introduced that does not require any additional test equipment and only relies on information that is available on the vehicle's communication bus system.

The vehicle's motion in response to the wheel torque is described by a longitudinal dynamics model. The causality between the wheel torque and the electromechanical torque of the IM is outlined in Section 2.3. With the main focus on the electrical

powertrain, only the main influencing loss processes of the drivetrain are considered. These primarily attribute to the mechanical brake and the amount of energy that can be regenerated via the IM and also to friction losses of the transmission gear. Both are approximated through empirical models.

Arriving at the central model of this study, all three component models discussed so far are joined to a mathematical description of the EDM system in Section 2.4. Interactions of internal system states as well as the voltage input and wheel torque output relation are illustrated in a comprehensive block diagram. The influence of the battery supply voltage, which has not yet been considered, is discussed in Section 2.5. Finally, the accuracy of the EDM and battery model are evaluated in an experimental validation in Section 2.6. A conclusive model summary is provided in Section 2.7.

2.1 Voltage Source Inverter

A VSI is composed of three half-bridge, single-phase inverters, for which, each single half-bridge is assumed to connect two ideal transistors and inverse conduction diodes as shown in Figure 2.2 [21, 56]. The most common switching device in almost all commercially available BEV drives is the IGBT [186]. However, recent advances in the field of silicon carbide unipolar technologies are expected to improve the performance and efficiency of next-generation power semi-conductors [101]. Exemplary voltage characteristics u_{Tr} and u_{D}, as well as switching energies $E_{\mathrm{on,off}}$ and E_{rec} of a transistor and diode are shown in Figure 2.2 as a function of the conduction current. These characteristics are usually provided in accompanying data-sheets.

2.1.1 Pulse Width Modulation

The power flow to an electric drive is determined by the amplitude and frequency of its phase voltage. Both are controlled by means of a PWM method that schedules the switching instants of each individual switch so that the fundamental volt-second average of the output voltage matches the fundamental of a reference waveform. Various PWM methods show significant differences in terms of the attainable voltage range and harmonic distortion [83, 92]. An intuitive way to explain PWM methods and VSI loss dependencies, is the triangular intersection method and waveform model depicted in Figure 2.3 [84, 202]. A PWM method can be viewed as a low level control that is governed by the supervisory control of the electric drive through the command of a sinusoidal voltage request

$$u_{\mathrm{as,n}} = M_{\mathrm{i}} \cos\left(\omega_0 t\right) \,, \tag{2.1}$$

where

$$M_{\mathrm{i}} = \min\left\{ \frac{\pi}{2 a_{\mathrm{pwm}}} \frac{\hat{u}}{u_{\mathrm{dc}}} \,, 1 \right\} \,, \tag{2.2}$$

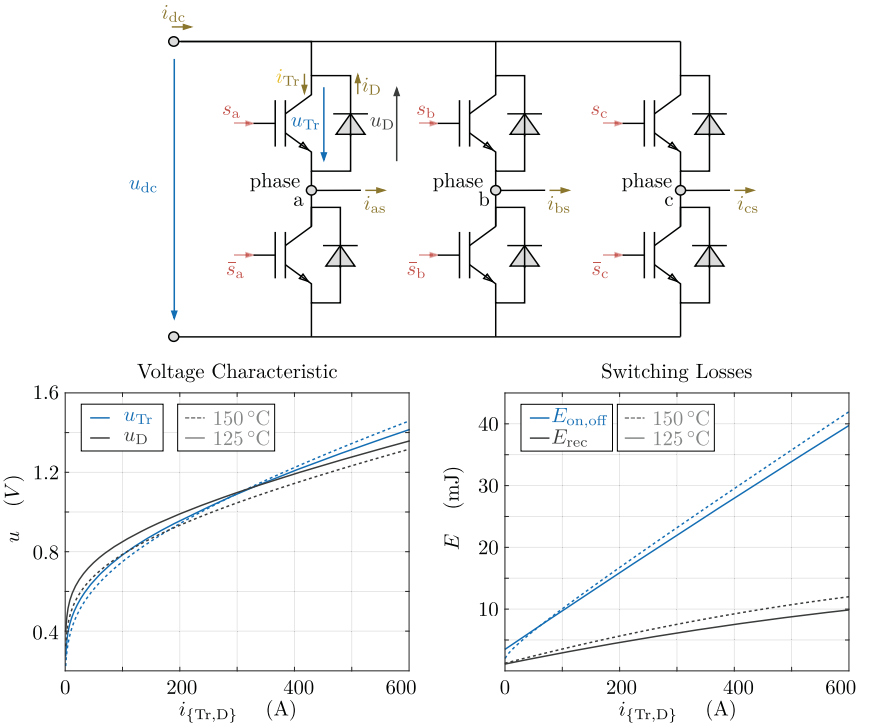

Figure 2.2: Voltage source inverter circuit model and IGBT characteristics.

is the modulation index. The modulation index is a function of the desired phase voltage peak value $\hat{u}$, the terminal voltage u_{dc} and the maximum attainable voltage range of the PWM method denoted by a_{pwm}, which takes on values of $\pi/4$ for sinusoidal PWM and reaches its maximum of one during a six-step modulation. The reference wave (2.1) is modulated by the injection of a so called zero-sequence system. As discussed in [84] and listed in the Appendix A.2, all carrier-based PWM methods can be distinguished by a specific zero-sequence signal u_{zss}. Due to the digital implementation process of PWM, the resulting reference signal is sampled and held constant, which introduces a phase delay. This process is referred to as regular sampling. Finally, the sampled waveform is compared against a high frequency triangular carrier wave to obtain the balanced set of switching or gating signals of the upper switch

$$s_a, s_b, s_c \in \{0, 1\} \ . \tag{2.3}$$

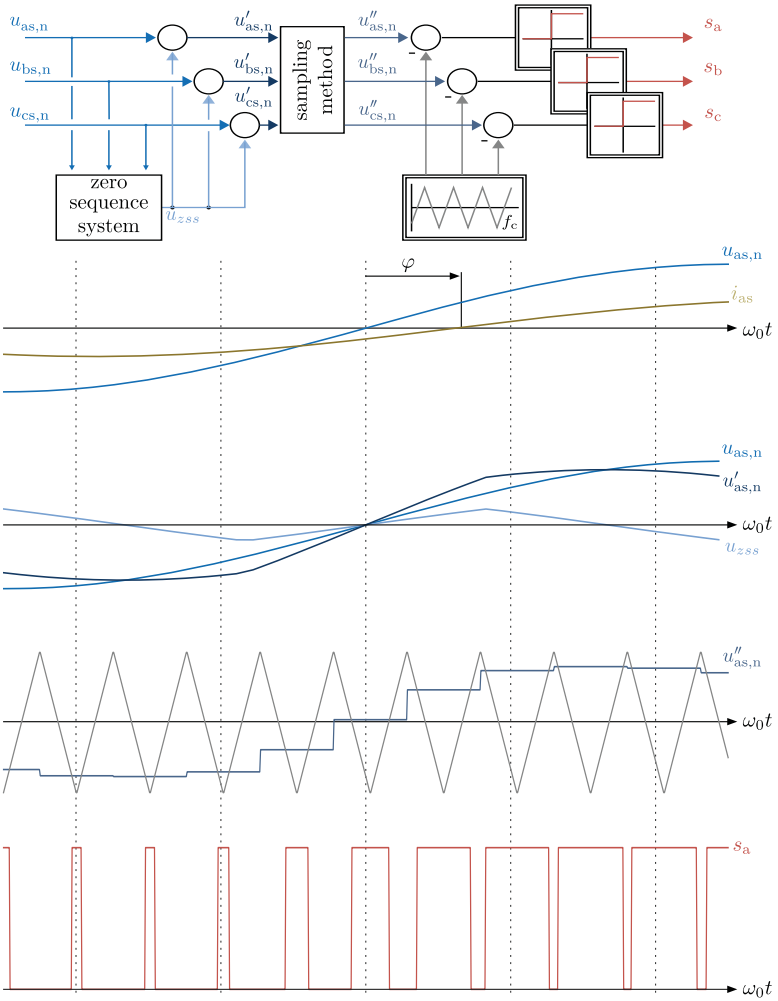

Figure 2.3: Pulse width modulation triangle intersection method and waveform model for regular sampled space vector PWM.

Zero represents a blocking-state and one represents an on-state in which the particular phase-leg potential is connected to the positive *Direct Current* (DC) rail. To prevent a short circuit, the lower switch is controlled by the complement $\bar{s}_{\{a,b,c\}} = 1 - s_{\{a,b,c\}}$.

2.1.2 Conduction & Switching Losses

The two predominant loss processes in semi-conductor devices are attributed to switching and on-state losses of the transistors and diodes [116, 117]. As will be shown shortly, both are functions of the switched load current, the power factor angle φ, and the PWM method [116]. Since an electric drive essentially acts as an inductive load, it is assumed that the resulting phase current

$$i_{\mathrm{as}} = \hat{i} \cos\left(\omega_0 t + \varphi\right) , \tag{2.4}$$

is sinusoidal and shifts in phase by the power factor angle φ. During the positive half-period of (2.4), the upper transistor is energized only if the switch is in an on-state. Whereas, during the negative half-period, the upper diode is energized if the switch is in an on-state. Consequently, the transistor and diode current for the upper switch are

$$i_{\mathrm{Tr,u}} = \begin{cases} i_{\mathrm{as}}\, s_{\mathrm{a}} , & i_{\mathrm{as}} \geq 0 \\ 0 , & i_{\mathrm{as}} < 0 \end{cases} , \quad i_{\mathrm{D,u}} = \begin{cases} 0 , & i_{\mathrm{as}} \geq 0 \\ i_{\mathrm{as}}\, s_{\mathrm{a}} , & i_{\mathrm{as}} < 0 \end{cases} . \tag{2.5}$$

The current values for the lower switch, $i_{\mathrm{Tr,l}}$ and $i_{\mathrm{D,l}}$, are derived accordingly using the complement of the switching signal. Considering the markedly different voltage characteristics and switching energies of transistor and diode, it follows that VSI losses can be expressed as a function of the switching signal, the switching frequency f_{c}, the power factor angle φ, and the *Root Mean Square* (RMS) transistor and diode currents according to

$$\begin{aligned} P_{\mathrm{l,vsi}} = \frac{3}{2} \Big(& u_{\mathrm{Tr}}\left(i_{\mathrm{Tr,u}}\right) i_{\mathrm{Tr,u}} + u_{\mathrm{Tr}}\left(i_{\mathrm{Tr,l}}\right) i_{\mathrm{Tr,l}} + u_{\mathrm{D}}\left(i_{\mathrm{D,u}}\right) i_{\mathrm{D,u}} + u_{\mathrm{D}}\left(i_{\mathrm{D,l}}\right) i_{\mathrm{D,l}} + \\ & \left[E_{\mathrm{on,off}}\left(i_{\mathrm{Tr,u}}\right) + E_{\mathrm{on,off}}\left(i_{\mathrm{Tr,l}}\right) + E_{\mathrm{rec}}\left(i_{\mathrm{D,u}}\right) + E_{\mathrm{rec}}\left(i_{\mathrm{D,l}}\right)\right] f_{\mathrm{c}} \Big) . \end{aligned} \tag{2.6}$$

The effect of the PWM method contribute to the discrete nature of the switching signals (2.3) which result in unwanted harmonic components and resulting harmonic distortions of the switched load current $i_{\mathrm{as}} s_{\mathrm{a}}$. These harmonic distortions can be quantified and analyzed by means of the *Harmonic Distortion Function* (HDF) and the *Switching Loss Function* (SLF) [116, 117]. The HDF quantifies the harmonic distortion, which results from sub-harmonic stimulation, i. e. the voltage and current waveform quality, and therefore is a measure of harmonic copper loss. The SLF is used to compare switching losses of various PWM methods. Both characteristics HDF and SLF are well suited to compare different PWM strategies and are typically used to evaluate the harmonic performance.

2.1.3 Double Fourier Analysis

An analytic framework to analyze the harmonic performance of a particular PWM implementation in a more general context was presented in [191]. Also, based on the findings of [143] and [91], it is shown how the switched current is computed in the frequency domain by means of a double Fourier integral analysis. Following this analysis process, a switching signal is assumed to be a double variable controlled waveform $s_\mathrm{a}(\mathrm{x},\mathrm{y})$ in which time variation is determined by two independent time variables, the modulation carrier wave x and the low frequency reference wave y

$$\mathrm{x} = 2\pi f_\mathrm{c} t, \quad \mathrm{y} = \omega_0 t\,. \tag{2.7}$$

In the following step, this switching signal is expressed in a double Fourier series expansion

$$s_\mathrm{a}(\mathrm{x},\mathrm{y}) = \underbrace{\frac{A_{00}}{2}}_{\text{dc offset}} + \underbrace{\sum_{\mathrm{n}=1}^{\infty}\left(A_{0\mathrm{n}}\cos(\mathrm{ny}) + B_{0\mathrm{n}}\sin(\mathrm{ny})\right)}_{\text{baseband harmonics}} + \underbrace{\sum_{\mathrm{m}=1}^{\infty}\left(A_{\mathrm{m}0}\cos(\mathrm{mx}) + B_{\mathrm{m}0}\sin(\mathrm{mx})\right)}_{\text{carrier harmonics}} + \underbrace{\sum_{\mathrm{m}=1}^{\infty}\sum_{\mathrm{n}=-\infty}^{\infty}\left(A_{\mathrm{mn}}\cos(\mathrm{mx}+\mathrm{ny}) + B_{\mathrm{mn}}\sin(\mathrm{mx}+\mathrm{ny})\right)}_{\text{sideband harmonics}} \tag{2.8a}$$

with Fourier coefficients being defined as

$$C_\mathrm{mn} = \frac{A_\mathrm{mn} - \mathrm{j}B_\mathrm{mn}}{2} = \frac{1}{(2\pi)^2}\int_{-\pi}^{\pi}\int_{\mathrm{x_{lb}}}^{\mathrm{x_{ub}}} s_\mathrm{a}(\mathrm{x},\mathrm{y})\,\mathrm{e}^{-\mathrm{j}(\mathrm{mx}+\mathrm{ny})}\,\mathrm{d}\,\mathrm{x}\,\mathrm{d}\,\mathrm{y}\,,\ \mathrm{m},\mathrm{n}\in\mathbb{Z}\,. \tag{2.8b}$$

The lower and upper limits, $\mathrm{x_{lb}}$ and $\mathrm{x_{ub}}$, of the inner integral in (2.8b) are defined as a function of the PWM method and the modulation index. As shown in Figure 2.4, these are constructed by means of a so-called unit cell. A unit cell defines constant regions in the (x,y) plane, whose boundaries constitute a PWM specific contour. This PWM contour is defined by the projection of the intersections between the carrier wave and reference voltage $u_\mathrm{as,n}$ onto the (x,y) plane, as illustrated at the top left of Figure 2.4 for a single carrier cycle and fundamental period. The switching signal is obtained from these contours by a periodic continuation of the unit cell in x and y directions. Both time variables are connected via the carrier ratio

$$\mathrm{p} = \frac{2\pi f_\mathrm{c}}{\omega_0} = \frac{\mathrm{x}}{\mathrm{y}}\,, \tag{2.9}$$

which defines a straight line in the enclosed space of unit cells. The switching signal results from the projection of this line onto the PWM specific contours of each unit cell, as seen at the top right of Figure 2.4.

Analytical solutions of the Fourier coefficients for switching signals of typical regular sampled PWM methods exist and are discussed in great detail by Holmes and Lipo in

[91] and [90]. A symmetrical, regular sampled *Space Vector PWM* (SVPWM) is the most commonly used PWM method. The Fourier coefficients of an even switching signal s_a for this SVPWM are given by $B_\mathrm{mn} = 0\ \forall \mathrm{m}, \mathrm{n}$ and

$$A_{00} = 1\,,\ A_{01} = \frac{M_\mathrm{i}}{2}\,, \tag{2.10a}$$

$$\begin{aligned} A_\mathrm{mn} =& \frac{4}{s_\mathrm{mn}\pi^2}\left(\frac{\pi}{6}\sin\left([s_\mathrm{mn}+\mathrm{n}]\frac{\pi}{2}\right)\left[\mathrm{J_n}\left(\sqrt{3}s_\mathrm{mi}\right)+2\cos\left(\mathrm{n}\frac{\pi}{6}\right)\mathrm{J_n}\left(s_\mathrm{mi}\right)\right]+\right. \\ & \frac{\varsigma(0)}{\mathrm{n}}\left[\mathrm{J_0}\left(\sqrt{3}s_\mathrm{mi}\right)-\mathrm{J_0}\left(s_\mathrm{mi}\right)\right]\Big|_{\mathrm{n}\neq 0}+ \\ & \sum_{\substack{\mathrm{k}=1\\ \mathrm{k}\neq -\mathrm{n}}}^{\infty}\left(\frac{\varsigma(\mathrm{k})}{\mathrm{n}+\mathrm{k}}\left[\mathrm{J_k}\left(\sqrt{3}s_\mathrm{mi}\right)+2\cos\left([2\mathrm{n}+3\mathrm{k}]\frac{\pi}{6}\right)\mathrm{J_k}\left(s_\mathrm{mi}\right)\right]\right)+ \\ & \left.\sum_{\substack{\mathrm{k}=1\\ \mathrm{k}\neq \mathrm{n}}}^{\infty}\left(\frac{\varsigma(-\mathrm{k})}{\mathrm{n}-\mathrm{k}}\left[\mathrm{J_k}\left(\sqrt{3}s_\mathrm{mi}\right)+2\cos\left([2\mathrm{n}-3\mathrm{k}]\frac{\pi}{6}\right)\mathrm{J_k}\left(s_\mathrm{mi}\right)\right]\right)\right), \end{aligned} \tag{2.10b}$$

where $\varsigma : \mathbb{N} \to \mathbb{R}$ is

$$\varsigma(\mathrm{v}) = \sin\left([s_\mathrm{mn}+|\mathrm{v}|]\frac{\pi}{2}\right)\cos\left([\mathrm{n}+\mathrm{v}]\frac{\pi}{2}\right)\sin\left([\mathrm{n}+\mathrm{v}]\frac{\pi}{6}\right)\,, \tag{2.10c}$$

$\mathrm{J_k}$ are Bessel functions of the first kind and order k, and where

$$s_\mathrm{mn} = \mathrm{m}+\frac{\mathrm{n}}{\mathrm{p}},\ s_\mathrm{mi} = s_\mathrm{mn}\frac{\sqrt{3}}{4}\pi M_\mathrm{i}\,. \tag{2.10d}$$

The Fourier coefficients of (2.10) for a modulation index of $M_\mathrm{i} = 0.9$ and a carrier ratio of $\mathrm{p} = 60$, at a vehicle speed close to 50 km/h, are shown in Figure 2.4. They are divided into baseband harmonic components $A_{0\mathrm{n}}|_{n>0}$, carrier harmonic components $A_{\mathrm{m}0}|_{m>0}$ and sideband harmonic components $A_\mathrm{mn}|_{m>0,n\in(-\infty,\infty)}$, which are located in the vicinity of the carrier frequencies. Indicated in blue, are overlapping components that are determined, for example, by the sum of baseband and sideband components. From Figure 2.4, it is observed that baseband amplitudes drop rapidly for higher harmonic components. The same applies for sideband components with an increasing distance from the carrier harmonics. Since the IM acts as an inductive load, the influence of harmonic components decreases at high frequencies. Therefore, it is sufficient to only consider the first few baseband components of the switching signal for loss computations. However at higher vehicle speeds and accordingly decreasing carrier ratio, the sideband harmonic components near the first carrier frequency move into the direction of lower frequencies, which leads to more overlapping components in the baseband. This effect results in a higher harmonic distortion of the phase current that eventually leads to an increase of VSI losses.

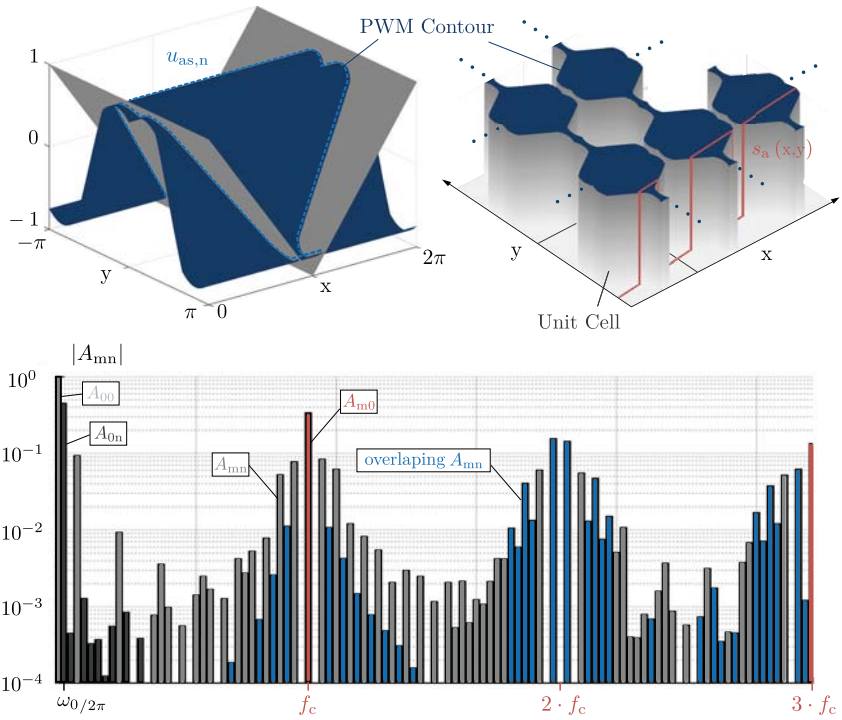

Figure 2.4: Double Fourier integral analysis and harmonic spectrum of SVPWM.

2.1.4 Average Value Model

To derive an analytical expression for conduction and switching losses (2.6), it is necessary to obtain an expression of the switched current $i_{as}s_a$. Following a similar approach as in [143], such an expression is derived within the frequency domain based on the convolution

$$i_{as}s_a \circ\!\!-\!\!\bullet\, I_{as}(\omega) * S_a(\omega) \,, \tag{2.11}$$

with

$$i_{as} \circ\!\!-\!\!\bullet\, I_{as}(\omega) = \frac{\hat{i}}{2}\Big(\delta(\omega-\omega_0)+\delta(\omega+\omega_0)\Big)\, e^{j\varphi\omega/\omega_0} \,, \tag{2.12}$$

where S_a characterizes the harmonic spectrum of the switching signal, (2.10) defines an example of this, and δ is the Dirac delta function, which is the identity element of the convolution operator. Equation (2.11) is equal to

$$I_\mathrm{as}\left(\omega\right) * S_\mathrm{a}\left(\omega\right) = \frac{\hat{i}}{2}\left(S_\mathrm{a}\left(\omega-\omega_0\right)\mathrm{e}^{\mathrm{j}\varphi} + S_\mathrm{a}\left(\omega+\omega_0\right)\mathrm{e}^{-\mathrm{j}\varphi}\right), \tag{2.13}$$

and simply represents the sum of two shifted PWM spectra. After some elaborate reformulations using trigonometric identities, (2.13) can be transformed back to the time domain yielding

$$\begin{aligned} i_\mathrm{as}s_\mathrm{a} = \frac{\hat{i}}{2}\Bigg(& A_{01}\cos\left(\varphi\right) + \sum_{\mathrm{n}=1}^{\infty}\left[A_{0\mathrm{n}\text{-}1}\cos\left(\mathrm{n}\omega_0 t+\varphi\right) - A_{0\mathrm{n}+1}\cos\left(\mathrm{n}\omega_0 t-\varphi\right)\right] + \\ & \sum_{\mathrm{m}=1}^{\infty}\sum_{\mathrm{n}=-\infty}^{\infty}\left[A_{0\mathrm{n}\text{-}1}\cos\left(\left[\mathrm{mp}+\mathrm{n}\right]\omega_0 t+\varphi\right) - A_{0\mathrm{n}+1}\cos\left(\left[\mathrm{mp}+\mathrm{n}\right]\omega_0 t-\varphi\right)\right]\Bigg). \end{aligned} \tag{2.14}$$

Similar expressions are derived in the same way for the square value of the switched current and the switched current of the lower switch by exploiting the fact that for the binary signal

$$s_\mathrm{a}^2 = s_\mathrm{a}\,, \qquad \bar{s}_\mathrm{a} = 1 - s_\mathrm{a}\,. \tag{2.15}$$

Given a closed form solution of the switched current, expressions for transistor and diode current (2.5) and eventually for (2.6) are readily derived. Considering the use in powertrain simulations, however, it is undesirable to compute the higher order components of the switched load current as this consumes essential computational power. A reasonable trade-off between computational efficiency and model accuracy is achieved by means of an average value model. Transistor and diode current (2.5) are thus averaged over one fundamental cycle by employing the time integral over the positive half period of $i_\mathrm{Tr,u}$ and the time integral over the negative half period of $i_\mathrm{D,u}$:

$$\bar{i}_\mathrm{Tr,u} = \frac{1}{2\pi}\int_{-\frac{\pi}{2}-\varphi}^{\frac{\pi}{2}-\varphi} i_\mathrm{as}s_\mathrm{a}\,\mathrm{d}\,\mathrm{y}\,, \qquad \bar{i}_\mathrm{D,u} = \frac{1}{2\pi}\int_{\frac{\pi}{2}-\varphi}^{\frac{3\pi}{2}-\varphi} i_\mathrm{as}s_\mathrm{a}\,\mathrm{d}\,\mathrm{y}\,, \tag{2.16}$$

which eventually leads to

$$\bar{i}_\mathrm{Tr,u} = \hat{i} - \bar{i}_\mathrm{D,l} = \frac{\hat{i}}{4}A_{01}\cos\left(\varphi\right) + I_\mathrm{h,1}\left(\varphi\right), \tag{2.17a}$$

$$\bar{i}_\mathrm{D,u} = \hat{i} - \bar{i}_\mathrm{Tr,l} = \frac{\hat{i}}{4}A_{01}\cos\left(\varphi\right) + I_\mathrm{h,1}\left(\varphi+\pi\right), \tag{2.17b}$$

$$\bar{i}^2_\mathrm{Tr,u} = \hat{i}^2 - \bar{i}^2_\mathrm{D,l} = \frac{\hat{i}^2}{8}\left(A_{00} + \frac{A_{02}}{2}\cos\left(\varphi\right)\right) + I_\mathrm{h}^2\left(\varphi\right), \tag{2.17c}$$

$$\bar{i}^2_\mathrm{D,u} = \hat{i}^2 - \bar{i}^2_\mathrm{Tr,l} = \frac{\hat{i}^2}{8}\left(A_{00} + \frac{A_{02}}{2}\cos\left(\varphi\right)\right) + I_\mathrm{h}^2\left(\varphi+\pi\right). \tag{2.17d}$$

For the sake of brevity, the harmonic current term $I_{\mathrm{h,k}}$ of order k at an arbitrary phase angle β is defined as

$$I_{\mathrm{h,k}}(\beta) = \frac{\hat{i}}{2\pi}\left(\sum_{\mathrm{n=k}}^{\infty}\chi(\mathrm{n})\left[A_{\mathrm{0n\text{-}k}}\cos(\mathrm{n}\beta-\varphi)+A_{\mathrm{0n+k}}\cos(\mathrm{n}\beta+\varphi)\right]+\right. \tag{2.17e}$$
$$\sum_{\mathrm{m=1}}^{\infty}\sum_{\mathrm{n=-\infty}}^{\infty}\chi(\mathrm{mp+n})\left[A_{\mathrm{mn\text{-}k}}\cos([\mathrm{mp+n}]\beta-\varphi)\ +\right.$$
$$\left.\left.A_{\mathrm{mn+k}}\cos([\mathrm{mp+n}]\beta+\varphi)\right]\right),$$

the square value I_{h}^2 at β is defined as

$$I_{\mathrm{h}}^2(\beta) = \frac{\hat{i}}{4}I_{\mathrm{h,2}}+\frac{\hat{i}^2}{4\pi}\left(\frac{A_{01}}{2}\cos(\beta-\varphi)+\frac{A_{03}}{2}\cos(\beta+\varphi)\ +\right. \tag{2.17f}$$
$$\sum_{\mathrm{n=1}}^{\infty}\chi(\mathrm{n})\ A_{\mathrm{0n}}\cos(\mathrm{n}\beta)\ +$$
$$\left.\sum_{\mathrm{m=1}}^{\infty}\sum_{\mathrm{n=-\infty}}^{\infty}\chi(\mathrm{mp+n})\ A_{\mathrm{mn}}\cos([\mathrm{mp+n}]\beta)\right),$$

and $\chi:\mathbb{N}\to\mathbb{Q}$ at index v is defined as

$$\chi(\mathrm{v}) = \frac{2}{\mathrm{v}}\sin\left(\mathrm{v}\frac{\pi}{2}\right). \tag{2.17g}$$

Over a wide speed range, a sufficient approximation of the VSI power loss (2.6) is obtained, using the average value models (2.17) with a finite number of baseband harmonic components $A_{0\mathrm{n}}$ assuming that $A_{\mathrm{mn}}|_{m>0}=0$. If the voltage characteristics and switching energies of the power semi-conductor device, shown in Figure 2.2, are approximated by linear functions

$$u_{\mathrm{Tr}} = R_{\mathrm{Tr}}\,i_{\mathrm{Tr}}+U_{\mathrm{Tr}}\,, \tag{2.18}$$
$$u_{\mathrm{D}} = R_{\mathrm{D}}\,i_{\mathrm{Tr}}+U_{\mathrm{D}}\,, \tag{2.19}$$
$$E_{\mathrm{on,off}} = E'_{\mathrm{on,off}}\,i_{\mathrm{Tr}}\,, \tag{2.20}$$
$$E_{\mathrm{rec}} = E'_{\mathrm{rec}}\,i_{\mathrm{D}}\,, \tag{2.21}$$

equation (2.6) is further simplified to

$$P_{\mathrm{l,vsi}} = \frac{3}{2}\left([R_{\mathrm{Tr}}+R_{\mathrm{D}}]\,\hat{i}^2+[R_{\mathrm{Tr}}-R_{\mathrm{D}}]\,\frac{\hat{i}^2}{4\pi}\,h_{\mathrm{pwm}}\ +\right. \tag{2.22a}$$
$$\left[U_{\mathrm{Tr}}+f_{\mathrm{c}}E'_{\mathrm{on,off}}\right]\left(1+\frac{2}{\pi}\right)\hat{i}\ +$$
$$\left.[U_{\mathrm{D}}+f_{\mathrm{c}}E'_{\mathrm{rec}}]\left(1-\frac{2}{\pi}\right)\hat{i}\right),$$

where the influence of the PWM method is modeled by means of the harmonic factor

$$
\begin{aligned}
h_{\mathrm{pwm}} = \Bigg(& A_{01} + \left(A_{03} - \frac{2}{3} A_{01} \right) \cos\left(2\varphi\right) + \frac{2}{5} A_{03} \cos\left(4\varphi\right) \; + \\
& \sum_{\mathrm{n}=1}^{\infty} \chi\left(\mathrm{n}\right) \; \left[\cos\left(\mathrm{n}\varphi\right) - \cos\left(\mathrm{n}\varphi + \mathrm{n}\pi\right) \right] A_{0\mathrm{n}} \; + \\
& \sum_{\mathrm{n}=5}^{\infty} \chi\left(\mathrm{n}+2\right) \; \left[\cos\left(\left[\mathrm{n}+2\right]\varphi\right) - \cos\left(\left[\mathrm{n}+2\right]\left(\varphi+\pi\right)\right) \right] A_{0\mathrm{n}} \; + \\
& \sum_{\mathrm{n}=5}^{\infty} \chi\left(\mathrm{n}-2\right) \; \left[\cos\left(\left[\mathrm{n}-2\right]\varphi\right) - \cos\left(\left[\mathrm{n}-2\right]\left(\varphi+\pi\right)\right) \right] A_{0\mathrm{n}}, \Bigg) .
\end{aligned}
\tag{2.22b}
$$

The defining parameters are the conduction resistance R_{Tr}, forward voltage drop U_{Tr}, and variation rate of the turn-on and turn-off switching energy $E'_{\mathrm{on,off}}$ associated with the transistor as well as the conduction resistance R_{D}, forward voltage drop U_{D}, and variation rate of the reverse recovery energy associated with the diode. All parameters are derived from the IGBT characteristics depicted in Figure 2.2. These are typically provided in the technical specification of the VSI. Equation (2.22) is a function of the constant switching frequency f_{c} and the fundamental electric frequency ω_0, the phase current peak value $\hat{i}$, the power factor angle φ, and the baseband harmonic Fourier coefficients that characterize the PWM method. These in turn are functions of the switching frequency, the fundamental frequency, and the modulation index, which itself is a function of the phase voltage (2.1) and terminal voltage. Except for the terminal voltage, all of these variables are directly linked to the operating points of an electric motor and are computed with the help of the state space model presented in the following Section 2.2. The main advantage of the proposed modeling approach is the explicit computation of the average transistor and diode current (2.17) which enables a straight forward integration in thermal models to account for the strong junction-temperature dependency of transistor and diode parameters.

2.2 Induction Motor

BEVs require sophisticated motor designs that aim for a perfect sinusiodal winding distribution. With the intention of implementing optimal control algorithms, simulation speed is of the utmost importance, which is why the simplified assumptions of a uniform air gap, a linear magnetic circuit, and concentrated sinusoidally distributed winding functions are considered to be reasonable for the intended use. All higher harmonics of the stator winding distribution are thus neglected, so that only the fundamental component is considered. As a consequence, it is assumed that a sinosoidal *Magneto-Motive-Force* (MMF) wave is produced in space. The most commonly known modeling approach, based on such simplified assumptions, is the dq-model of a squirrel-cage IM [119], which uses equivalent electrical circuit parameters and is derived from

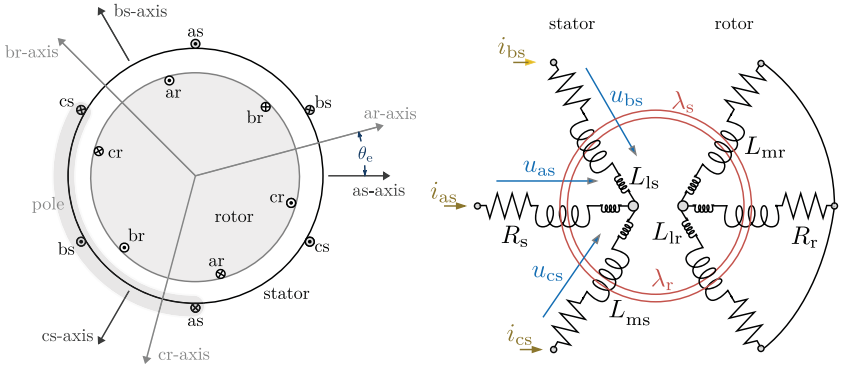

Figure 2.5: Model of a symmetrical 3-phase 2-pole induction motor.

the 3-phase 2-pole model shown in Figure 2.5 [120, 203]. Windings of this motor are modeled as coils with identical resistances $R_{\{s,r\}}$, leakage self-inductances $L_{l\{s,r\}}$, and self-inductances $L_{m\{s,r\}}$ for either stator (subscript s) or rotor (subscript r). According to Faraday's law and Kirchhoff's voltage law, the line-to-neutral voltages are

$$\begin{bmatrix} \boldsymbol{u}_{\mathrm{abc,s}} \\ \boldsymbol{0} \end{bmatrix} = \begin{bmatrix} \boldsymbol{R}_{\mathrm{s}} & \boldsymbol{0} \\ \boldsymbol{0} & \boldsymbol{R}_{\mathrm{r}} \end{bmatrix} \begin{bmatrix} \boldsymbol{i}_{\mathrm{abc,s}} \\ \boldsymbol{i}_{\mathrm{abc,r}} \end{bmatrix} + \frac{\mathrm{d}}{\mathrm{dt}} \begin{bmatrix} \boldsymbol{\lambda}_{\mathrm{abc,s}} \\ \boldsymbol{\lambda}_{\mathrm{abc,r}} \end{bmatrix} , \tag{2.23}$$

where $\boldsymbol{R}_{\{s,r\}} = \mathrm{diag}\left(R_{\{s,r\}}, R_{\{s,r\}}, R_{\{s,r\}}\right) \in \mathbb{R}^{3\times3}$ is a block diagonal matrix containing the respective stator or rotor resistances. Within the magnetically coupled circuit, the flux $\boldsymbol{\lambda}_{abc,\{s,r\}} = \left(\lambda_{a\{s,r\}}\, \lambda_{b\{s,r\}}\, \lambda_{c\{s,r\}}\right) \in \mathbb{R}^3$ linking stator and rotor coils is derived from Ampère's circuit law

$$\begin{bmatrix} \boldsymbol{\lambda}_{\mathrm{abc,s}} \\ \boldsymbol{\lambda}_{\mathrm{abc,r}} \end{bmatrix} = \begin{bmatrix} \boldsymbol{L}_{\mathrm{s}} & \boldsymbol{L}_{\mathrm{sr}} \\ \boldsymbol{L}_{\mathrm{sr}}^{T} & \boldsymbol{L}_{\mathrm{r}} \end{bmatrix} \begin{bmatrix} \boldsymbol{i}_{\mathrm{abc,s}} \\ \boldsymbol{i}_{\mathrm{abc,r}} \end{bmatrix} , \tag{2.24a}$$

where the symmetric self inductance matrix is

$$\boldsymbol{L}_{\{\mathrm{s,r}\}} = \boldsymbol{L}_{\{\mathrm{s,r}\}}^{T} = \begin{bmatrix} L_{l\{s,r\}} + L_{m\{s,r\}} & -0.5L_{m\{s,r\}} & -0.5L_{m\{s,r\}} \\ \cdot & L_{l\{s,r\}} + L_{m\{s,r\}} & -0.5L_{m\{s,r\}} \\ \cdot & \cdot & L_{l\{s,r\}} + L_{m\{s,r\}} \end{bmatrix} , \tag{2.24b}$$

and the rotor position dependent mutual inductance matrix is

$$\boldsymbol{L}_{\mathrm{sr}}\left(\theta_{\mathrm{m}}\right) = \begin{bmatrix} L_{\mathrm{sr}}\cos\left(\theta_{\mathrm{m}}\right) & L_{\mathrm{sr}}\cos\left(\theta_{\mathrm{m}} + \frac{2\pi}{3}\right) & L_{\mathrm{sr}}\cos\left(\theta_{\mathrm{m}} - \frac{2\pi}{3}\right) \\ L_{\mathrm{sr}}\cos\left(\theta_{\mathrm{m}} - \frac{2\pi}{3}\right) & L_{\mathrm{sr}}\cos\left(\theta_{\mathrm{m}}\right) & L_{\mathrm{sr}}\cos\left(\theta_{\mathrm{m}} + \frac{2\pi}{3}\right) \\ L_{\mathrm{sr}}\cos\left(\theta_{\mathrm{m}} + \frac{2\pi}{3}\right) & L_{\mathrm{sr}}\cos\left(\theta_{\mathrm{m}} - \frac{2\pi}{3}\right) & L_{\mathrm{sr}}\cos\left(\theta_{\mathrm{m}}\right) \end{bmatrix} , \tag{2.24c}$$

with L_{sr} being the mutual inductance between stator and rotor (cf. [120] page 81-83). The rotor position is determined by the rotor angle θ_{m}. Due to the assumption of a sinusoidal MMF wave, three-phase sets of voltages, currents, and flux linkages in stationary operation are assumed to be in balanced conditions with equal amplitudes and mutual 120° phase displacement. For example, the line-to-neutral voltages $\boldsymbol{u}_{\mathrm{abc,s}} = (u_{\mathrm{as}}\, u_{\mathrm{bs}}\, u_{\mathrm{cs}})^T \in \mathbb{R}^3$ and stator phase currents $\boldsymbol{i}_{\mathrm{abc,s}} = (i_{\mathrm{as}}\, i_{\mathrm{bs}}\, i_{\mathrm{cs}})^T \in \mathbb{R}^3$ are given by

$$\boldsymbol{u}_{\mathrm{abc,s}} = \begin{bmatrix} \hat{u}\cos(\omega_0 t) \\ \hat{u}\cos\left(\omega_0 t - \frac{2\pi}{3}\right) \\ \hat{u}\cos\left(\omega_0 t + \frac{2\pi}{3}\right) \end{bmatrix}, \quad \boldsymbol{i}_{\mathrm{abc,s}} = \begin{bmatrix} \hat{i}\cos(\omega_0 t + \varphi) \\ \hat{i}\cos\left(\omega_0 t - \frac{2\pi}{3} + \varphi\right) \\ \hat{i}\cos\left(\omega_0 t + \frac{2\pi}{3} + \varphi\right) \end{bmatrix}, \tag{2.25}$$

where ω_0 is the fundamental electrical angular frequency, φ is the power factor angle, and $\hat{u}$, $\hat{i}$ are the peak values of the phase voltage and phase current.

The functional principle of an IM with additional poles hardly differs in its essentials from the 3-phase 2-pole model. Within one electrical period of the fundamental frequency, the MMF wave only passes through the sector that is spanned by a single pole pair. Multiple poles may thus be interpreted as a scaling factor and can be generalized as a 2-pole model by using the definition of the electrical rotor angle and electric rotor angular frequency

$$\theta_{\mathrm{e}} = Z_{\mathrm{p}}\theta_{\mathrm{m}}\,, \quad \omega_{\mathrm{e}} = \dot{\theta}_{\mathrm{e}} = Z_{\mathrm{p}}\omega_{\mathrm{m}}\,, \tag{2.26}$$

instead of the rotor angle and rotor frequency $\omega_{\mathrm{m}} = \dot{\theta}_{\mathrm{m}}$. The scaling factor is determined by the number of pole pairs Z_{p}.

2.2.1 Reference Frame Transformation

In the modeling process of the dq equivalent circuit model, flux linkage and voltage equations (2.23) and (2.24) are considerably simplified by a change of variables that is based on what is known as the reference frame theory [120, 204]. Transformations based on the work of Park [167] and Clarke [34] are both special cases of this general theory. As shown in Figure 2.6, the basic idea of this transformation is to represent electric and magnetic variables in a rotating reference frame. The resulting complex-valued space vector $\underline{x} \in \mathbb{C}$ is obtained by employing the transformation for stator variables

$$\begin{aligned} \underline{x}_{\mathrm{s}} &= \frac{2}{3}\left(x_{\mathrm{as}} + x_{\mathrm{bs}}\,\mathrm{e}^{\mathrm{j}2\pi/3} + x_{\mathrm{cs}}\,\mathrm{e}^{-\mathrm{j}2\pi/3}\right)\mathrm{e}^{-\mathrm{j}\alpha} \\ &= x_{\mathrm{ds}} + \mathrm{j}x_{\mathrm{qs}}\,, \end{aligned} \tag{2.27a}$$

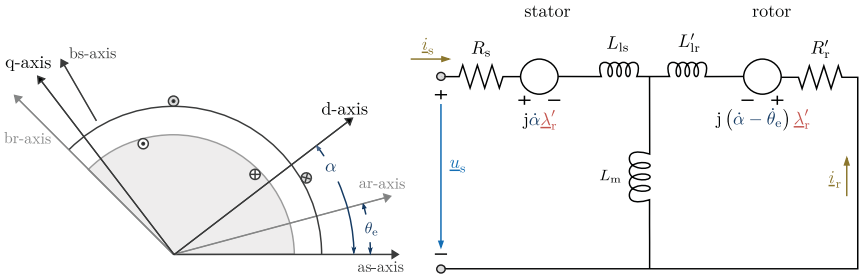

Figure 2.6: T-form equivalent circuit model of an induction motor represented in a rotating dq-reference frame.

and rotor variables

$$\begin{aligned} \underline{x}_\mathrm{r} &= \frac{2}{3}\left(x_\mathrm{ar} + x_\mathrm{br}\,\mathrm{e}^{\mathrm{j}2\pi/3} + x_\mathrm{cr}\,\mathrm{e}^{-\mathrm{j}2\pi/3}\right)\mathrm{e}^{-\mathrm{j}(\alpha-\theta_\mathrm{e})} \\ &= x_\mathrm{dr} + \mathrm{j}x_\mathrm{qr}\,, \end{aligned} \tag{2.27b}$$

where the leading factor 2/3 is chosen in such a way that the magnitude of the space vector $|\underline{x}|$ is equal to the peak value $\hat{x}$ of the respective voltage, current, or flux linkage. The orientation of the reference frame real axis is denoted by α. A space vector may be thought of as a variable that determines the instantaneous magnitude and angular position of the peak value of a sinusoidally distributed wave. The wave itself results from the sinusoidally distributed windings. As done in [120], it is also possible to represent (2.27) as a real-valued dq0 vector. However, the general formulation of a complex-valued space vector, introduced by [118], provides a means of expressing the dq-model in a more compact form. For the inverse transformation as well as the dq0 formulation of (2.27) the reader is referred to the Appendix A.1.

A further simplification of the voltage and flux equations is achieved by relating all rotor variables to the stator coils according to the appropriate ratio of turns $N_{\{s,r\}}$ of stator and rotor coils

$$\underline{\lambda}'_\mathrm{r} = \frac{N_\mathrm{s}}{N_\mathrm{r}}\underline{\lambda}_\mathrm{r}\,, \qquad \underline{u}'_\mathrm{r} = \frac{N_\mathrm{s}}{N_\mathrm{r}}\underline{u}_\mathrm{r}\,, \qquad \underline{i}'_\mathrm{r} = \frac{N_\mathrm{r}}{N_\mathrm{s}}\underline{i}_\mathrm{r}\,, \tag{2.28a}$$

and by using the following definition

$$R'_\mathrm{r} = \left(\frac{N_\mathrm{s}}{N_\mathrm{r}}\right)^2 R_\mathrm{r}\,, \qquad L'_\mathrm{lr} = \left(\frac{N_\mathrm{s}}{N_\mathrm{r}}\right)^2 L_\mathrm{lr}\,. \tag{2.28b}$$

This transformation is known as turns ratio transformation [159]. For the sake of simplicity, the prime notation used in (2.28) is dropped in the further course of this work. If not stated otherwise, rotor variables are always referred to the stator coils. Altogether, this yields the dq equivalent circuit model shown in Figure 2.6:

$$\begin{bmatrix} \underline{u}_\mathrm{s} \\ 0 \end{bmatrix} = \begin{bmatrix} R_\mathrm{s} & 0 \\ 0 & R_\mathrm{r} \end{bmatrix} \begin{bmatrix} \underline{i}_\mathrm{s} \\ \underline{i}_\mathrm{r} \end{bmatrix} + \begin{bmatrix} \mathrm{j}\dot{\alpha} + \frac{\mathrm{d}}{\mathrm{dt}} & 0 \\ 0 & \mathrm{j}\left(\dot{\alpha} - \omega_\mathrm{e}\right) + \frac{\mathrm{d}}{\mathrm{dt}} \end{bmatrix} \begin{bmatrix} \underline{\lambda}_\mathrm{s} \\ \underline{\lambda}_\mathrm{r} \end{bmatrix} , \tag{2.29a}$$

$$\begin{bmatrix} \underline{\lambda}_\mathrm{s} \\ \underline{\lambda}_\mathrm{r} \end{bmatrix} = \begin{bmatrix} L_\mathrm{ls} + L_\mathrm{m} & L_\mathrm{m} \\ L_\mathrm{m} & L_\mathrm{lr} + L_\mathrm{m} \end{bmatrix} \begin{bmatrix} \underline{i}_\mathrm{s} \\ \underline{i}_\mathrm{r} \end{bmatrix} , \tag{2.29b}$$

which has the major advantage that the undesirable variation in the mutual impedance matrix (2.24c) with respect to the rotor position is eliminated in (2.29b). The mutual inductance L_m in (2.29b) is a result of the reference frame transformation and is equal to three halves of the stator self-inductance L_ms.

2.2.2 State Space Model

In the literature there are various representations of the dq-model (2.29) depending on the choice of the reference frame and the system states. Throughout this work the dq-reference frame is used, in which the real or direct axis synchronously rotates with the rotor flux linkage $\underline{\lambda}_\mathrm{r}$. As a result of this field orientation, the complex component of the flux linkage is equal to zero at all times $\underline{\lambda}_\mathrm{r} = \lambda_\mathrm{r} + \mathrm{j}0$. The direct axis thereby moves across the stator at a frequency of

$$\dot{\alpha} = \frac{L_\mathrm{m}}{\tau_\mathrm{r}} \frac{i_\mathrm{qs}}{\lambda_\mathrm{r}} + Z_\mathrm{p}\omega_\mathrm{m} \,, \tag{2.30}$$

and across the rotor with slip frequency

$$\omega_\mathrm{sl} = \dot{\alpha} - \omega_\mathrm{e} = s_\mathrm{sl}\,\dot{\alpha} \,, \tag{2.31}$$

where s_sl denotes the slip factor and τ_r is the rotor time constant defined in (2.34). During steady state operation, the reference frame frequency $\dot{\alpha}$ is equal to the synchronous frequency ω_0. Other commonly used reference frames are summarized in the Appendix A.1.

By choosing the phase current $\underline{i}_\mathrm{s}$ and rotor flux linkage $\underline{\lambda}_\mathrm{r}$ as independent system states and the stator phase voltage $\underline{u}_\mathrm{s}$ as input, voltage and flux equations of the dq equivalent circuit (2.29) are reformulated as a nonlinear, time varying, input-affine state space model:

$$\begin{bmatrix} \dot{i}_\mathrm{ds} \\ \dot{i}_\mathrm{qs} \\ \dot{\lambda}_\mathrm{r} \end{bmatrix} = \begin{bmatrix} -\frac{i_\mathrm{ds}}{\tau_\mathrm{c}} + \omega_\mathrm{e} i_\mathrm{qs} + \frac{L_\mathrm{m}}{\tau_\mathrm{r}} \left(\frac{i_\mathrm{qs}^2}{\lambda_\mathrm{r}} + \frac{\lambda_\mathrm{r}}{\sigma L_\mathrm{r} L_\mathrm{s}} \right) \\ -\frac{i_\mathrm{qs}}{\tau_\mathrm{c}} - \omega_\mathrm{e} i_\mathrm{ds} - \frac{L_\mathrm{m}}{\tau_\mathrm{r}} \left(\frac{i_\mathrm{qs} i_\mathrm{ds}}{\lambda_\mathrm{r}} + \omega_\mathrm{e}\tau_\mathrm{r} \frac{\lambda_\mathrm{r}}{\sigma L_\mathrm{r} L_\mathrm{s}} \right) \\ -\frac{\lambda_\mathrm{r}}{\tau_\mathrm{r}} + \frac{L_\mathrm{m}}{\tau_\mathrm{r}} i_\mathrm{ds} \end{bmatrix} + \begin{bmatrix} \frac{1}{\sigma L_\mathrm{s}} & 0 \\ 0 & \frac{1}{\sigma L_\mathrm{s}} \\ 0 & 0 \end{bmatrix} \begin{bmatrix} u_\mathrm{ds} \\ u_\mathrm{qs} \end{bmatrix} , \tag{2.32}$$

where the time dependence is due to the electric rotor speed $\omega_\mathrm{e} = \dot{\theta}_\mathrm{e}$. The mutual inductance L_m, stator resistance R_s, rotor resistance R_r, and the stator and rotor inductances

$$L_\mathrm{s} = L_\mathrm{ls} + L_\mathrm{m}\,, \qquad L_\mathrm{r} = L_\mathrm{lr} + L_\mathrm{m}\,, \tag{2.33}$$

constitute the defining parameter set and determine the rotor and current time constant

$$\tau_\mathrm{r} = \frac{L_\mathrm{r}}{R_r}\,, \quad \tau_\mathrm{c} = \frac{\sigma L_\mathrm{r} L_\mathrm{s}}{L_\mathrm{r} R_\mathrm{s} + (1-\sigma) L_\mathrm{s} R_\mathrm{r}}\,, \tag{2.34}$$

as well as the leakage coefficient

$$\sigma = 1 - \frac{L_\mathrm{m}^2}{L_\mathrm{r} L_\mathrm{s}}\,. \tag{2.35}$$

Space vectors of the stator flux linkage and the rotor phase current are retrieved from the system states of (2.32) using the following transformation

$$\begin{bmatrix} \underline{\lambda}_\mathrm{s} \\ \underline{i}_\mathrm{r} \end{bmatrix} = \begin{bmatrix} \sigma L_\mathrm{s} & \frac{L_\mathrm{m}}{L_\mathrm{r}} \\ -\frac{L_\mathrm{m}}{L_\mathrm{r}} & \frac{1}{L_\mathrm{r}} \end{bmatrix} \begin{bmatrix} \underline{i}_\mathrm{s} \\ \underline{\lambda}_\mathrm{r} \end{bmatrix}. \tag{2.36}$$

Equation (2.36) does not depend on the reference frame and can be used to derive other dynamic system representations of the dq-model.

Physically measurable quantities, which are often used in performance analyses, are the peak values defined in (2.25), i. e.

$$\hat{i} = \sqrt{i_\mathrm{ds}^2 + i_\mathrm{qs}^2}\,, \tag{2.37}$$

$$\hat{u} = \sqrt{u_\mathrm{ds}^2 + u_\mathrm{qs}^2}\,, \tag{2.38}$$

and the power factor angle

$$\varphi = \operatorname{atan}\left(\frac{i_\mathrm{qs}}{i_\mathrm{ds}}\right) - \operatorname{atan}\left(\frac{u_\mathrm{qs}}{u_\mathrm{ds}}\right)\,. \tag{2.39}$$

The electromagnetic rotor torque T_e, which is coupled to the electric system via the magnetic field, is given by

$$T_\mathrm{e} = \frac{3}{2} Z_\mathrm{p} \frac{L_\mathrm{m}}{L_\mathrm{r}} \lambda_\mathrm{r} i_\mathrm{qs}\,. \tag{2.40}$$

Equation (2.40) is derived by considering the change of energy stored in the coupling field or corresponding change of the associated co-energy [120]. Together, with the resulting rotor speed ω_m, the rotor torque defines the operating point and determines the mechanical power flow from or to the drivetrain

$$P_\mathrm{m} = T_\mathrm{e}\,\omega_\mathrm{m}\,. \tag{2.41}$$

The required electrical power through-put in every operating point

$$P_{\mathrm{e,im}} = \frac{3}{2}\hat{\imath}\hat{u}\cos(\varphi) = \frac{3}{2}\left(i_{\mathrm{ds}}u_{\mathrm{ds}} + i_{\mathrm{qs}}u_{\mathrm{qs}}\right) , \tag{2.42}$$

must obey the law of conservation of energy and, therefore, compensates for the power loss of stator and rotor resistances and leakage inductances

$$P_{\mathrm{l,im}} = P_{\mathrm{e,im}} - P_{\mathrm{m}} . \tag{2.43}$$

With the convention adopted in this work, the energy supplied by the electric source is considered positive whereas the energy supplied by the drivetrain is negative. Therefore, both electric and mechanical power are negative when energy is supplied to the electrical source and positive when energy is supplied to the drivetrain. This means that $P_{\mathrm{e,im}}$ and P_{m} are positive during acceleration and coasting and negative during regenerative braking.

2.2.3 Core Losses & Saturation

For an accurate computation of the electrical power output in vehicle applications, it is recommended to also consider frequency dependent losses, which attribute to magnetic hysteresis losses and eddy currents occurring in the ferromagnetic material of all magnetic fields [113, 218]. Both are generally referred to as core losses $P_{\mathrm{l,core}}$. Additional frequency dependent losses are introduced by the skin effect in rotor bars [20, 136].

Following the simplified loss-model approach presented in [131], it is assumed that stator and rotor core losses are both proportional to the square of the magnetizing flux level. Furthermore, hysteresis losses are proportional to the effective electric angular frequency, whereas eddy current losses are proportional to the square value of the effective electric angular frequency. In the case of the stator system, this frequency is equal to ω_0 and in the case of the rotor system it is equal to the slip frequency (2.31). Due to small slip frequencies, the overall core loss predominantly depends on the core loss in the stator, which is approximated by

$$P_{\mathrm{l,core}} = \frac{3}{2}\frac{\left(\omega_{\mathrm{e}}L_{\mathrm{m}}\right)^2}{R_{\mathrm{fe}}}i_{\mathrm{ds}}^2 . \tag{2.44}$$

The constant parameter R_{fe} is the empirically determined core loss resistance [127]. In line with the simplified approach [131], the model structure of (2.29) and (2.32) remains unchanged and does not require an equivalent iron loss branch placed in parallel to the magnetizing branch of the equivalent circuit as presented in [127] and illustrated in Figure 2.7. The simplification is justified by the fact that the magnetizing current is much larger than the current loss of the parallel iron loss branch. In the further course of this study, core losses will always be associated with the motor so

that $P_{\mathrm{l,im}}$ refers to all modeled loss processes of the IM including $P_{\mathrm{l,core}}$.

All of the above mentioned states and values are affected by magnetic saturation. Saturation generates additional harmonic components in the air gap flux [31] and leads to cross-coupling effects [236, 237] of the flux linkags, which are not predicted by the linear model of (2.29b). In [147], the WFT is used to derive a dynamic model of an AC motor which, in an experimental setup, has proven to predict saturation effects accurately. For optimized energy management of BEVs, however, it is undesirable to operate the IM in its saturation region due to the high stator current and the associated disproportionately high power loss. The magnetic circuit is thus assumed to be linear.

2.2.4 Steady State Equations

Analytical expressions that are regularly considered during system analyses of the upcoming chapters, are based on the steady state model of (2.32), where

$$\left(\dot{i}_{\mathrm{ds}}\, \dot{i}_{\mathrm{qs}}\, \dot{\lambda}_{\mathrm{r}}\right)^T = \mathbf{0}\,.$$

These are derived in detail in Section 3.3 with the help of the equivalent flat system representation. However, for a better overview the steady state equations (superscript st) are presented below. These are functions of the rotor speed ω_{m}, electromagnetic torque T_{e}, and the rotor flux λ_{r}

$$i_{\mathrm{ds}}^{\mathrm{st}} = \frac{\lambda_{\mathrm{r}}}{L_{\mathrm{m}}}\,, \tag{2.45a}$$

$$i_{\mathrm{qs}}^{\mathrm{st}} = \frac{2}{3}\frac{L_{\mathrm{r}}}{L_{\mathrm{m}}}\frac{T_{\mathrm{e}}}{Z_{\mathrm{p}}\lambda_{\mathrm{r}}}\,, \tag{2.45b}$$

$$u_{\mathrm{ds}}^{\mathrm{st}} = \frac{1}{L_{\mathrm{m}}}\left(R_{\mathrm{s}}\lambda_{\mathrm{r}} - \sigma L_{\mathrm{s}}L_{\mathrm{r}}\left(\frac{4}{9}R_{\mathrm{r}}\frac{T_{\mathrm{e}}}{Z_{\mathrm{p}}\lambda_{\mathrm{r}}^2} + \frac{2}{3}Z_{\mathrm{p}}\omega_{\mathrm{m}}\right)\frac{T_{\mathrm{e}}}{Z_{\mathrm{p}}\lambda_{\mathrm{r}}}\right), \tag{2.45c}$$

$$u_{\mathrm{qs}}^{\mathrm{st}} = \frac{1}{L_{\mathrm{m}}}\left(L_{\mathrm{s}}Z_{\mathrm{p}}\omega_{\mathrm{m}}\lambda_{\mathrm{r}} + \frac{2}{3}\left(L_{\mathrm{s}}R_{\mathrm{r}} + L_{\mathrm{r}}R_{\mathrm{s}}\right)\frac{T_{\mathrm{e}}}{Z_{\mathrm{p}}\lambda_{\mathrm{r}}}\right). \tag{2.45d}$$

The steady state power loss of the IM including core losses is

$$P_{\mathrm{l,im}}^{\mathrm{st}} = \frac{3}{2}\left(\frac{R_{\mathrm{s}}}{L_{\mathrm{m}}^2} + \frac{\left(Z_{\mathrm{p}}\omega_{\mathrm{m}}\right)^2}{R_{\mathrm{fe}}}\right)\lambda_{\mathrm{r}}^2 + \frac{2}{3}\left(R_{\mathrm{r}} + \frac{L_{\mathrm{r}}^2}{L_{\mathrm{m}}^2}R_{\mathrm{s}}\right)\frac{T_{\mathrm{e}}^2}{Z_{\mathrm{p}}^2\lambda_{\mathrm{r}}^2}\,. \tag{2.45e}$$

The stationary stator current and voltage peak values are given by

$$\hat{i}^{\mathrm{st}} = \frac{1}{L_{\mathrm{m}}}\sqrt{\lambda_{\mathrm{r}}^2 + \frac{4}{9}L_{\mathrm{r}}^2\frac{T_{\mathrm{e}}^2}{Z_{\mathrm{p}}^2\lambda_{\mathrm{r}}^2}}\,, \tag{2.45f}$$

$$\hat{u}^{\mathrm{st}} = \frac{2}{3}\frac{\sigma L_{\mathrm{s}}L_{\mathrm{r}}}{L_{\mathrm{m}}}\sqrt{\begin{array}{l}\left(\frac{4}{9}R_{\mathrm{r}}^2\frac{T_{\mathrm{e}}^2}{Z_{\mathrm{p}}^2\lambda_{\mathrm{r}}^4} + \frac{4}{3}R_{\mathrm{r}}\frac{T_{\mathrm{e}}\omega_{\mathrm{m}}}{\lambda_{\mathrm{r}}^2} + \frac{(L_{\mathrm{s}}R_{\mathrm{r}})^2 + 2R_{\mathrm{r}}R_{\mathrm{s}}L_{\mathrm{m}}^2 + (L_{\mathrm{r}}R_{\mathrm{s}})^2}{(\sigma L_{\mathrm{s}}L_{\mathrm{r}})^2} + (Z_{\mathrm{p}}\omega_{\mathrm{m}})^2\right)\frac{T_{\mathrm{e}}^2}{Z_{\mathrm{p}}^2\lambda_{\mathrm{r}}^2} + \\ 3\frac{\left(L_{\mathrm{s}}^2R_{\mathrm{r}} + L_{\mathrm{m}}^2R_{\mathrm{s}}\right)}{(\sigma L_{\mathrm{s}}L_{\mathrm{r}})^2}T_{\mathrm{e}}\omega_{\mathrm{m}} + \frac{9}{4}\frac{\left(R_{\mathrm{s}}^2 + (L_{\mathrm{s}}Z_{\mathrm{p}}\omega_{\mathrm{m}})^2\right)}{(\sigma L_{\mathrm{s}}L_{\mathrm{r}})^2}\lambda_{\mathrm{r}}^2\end{array}}\,. \tag{2.45g}$$

2.2.5 Offline Identification

A standardized offline identification method is the IEEE test procedures for poly-phase IMs and generators [97]. The standard prescribes the measurement of the per phase stator resistance R_{s} by means of a DC [96]. For a symmetrical three-phase motor, the stator resistance is equal to one-half of the terminal-to-terminal resistance. If the resistance is known at a specific temperature ϑ_0, it can be adjusted to any other temperature ϑ_{s} by

$$R_{\mathrm{s}} = R_{\mathrm{s}}|_{\vartheta_0}\left(1 + \alpha_{\mathrm{R}}\left(\vartheta_{\mathrm{s}} - \vartheta_0\right)\right), \tag{2.46}$$

where α_{R} is the temperature coefficient of the corresponding conduction material (100 % IACS conductivity copper $\alpha_{\mathrm{R}} = 4.264 \times 10^{-3}\,1/\mathrm{K}$; aluminum $\alpha_{\mathrm{R}} = 4.444 \times 10^{-3}\,1/\mathrm{K}$). Relation (2.46) also applies to the rotor resistance R_{r}.

Given the stator resistance, the T-form equivalent circuit parameters are derived from voltage and current measurements recorded during two separate test procedures, known as the locked rotor test and the no-load test. Different methods exist to determine the input impedance of the motor based on these tests. The discussion below follows the method presented in [203]. The input impedance Z_{IM} is defined as

$$Z_{\mathrm{IM}} = \frac{\underline{u}_{\mathrm{s}}^0}{\underline{i}_{\mathrm{s}}^0} = \frac{u_{\alpha\mathrm{s}} + \mathrm{j}u_{\beta\mathrm{s}}}{i_{\alpha\mathrm{s}} + \mathrm{j}i_{\beta\mathrm{s}}}\,, \tag{2.47}$$

where $u_{\alpha\mathrm{s}}, u_{\beta\mathrm{s}}$ and $i_{\alpha\mathrm{s}}, i_{\beta\mathrm{s}}$ are the measured voltage and current values represented in the stationary reference frame (indicated using the superscript 0). In the case of a squirrel-cage motor, the rotor is a symmetrical bar winding, which means that the input impedance dependency on rotor position is negligible.

The locked rotor test is conducted by applying a balanced set of ac-voltages with a relatively low amplitude and a synchronous frequency of ω_0 to the IM while the rotor

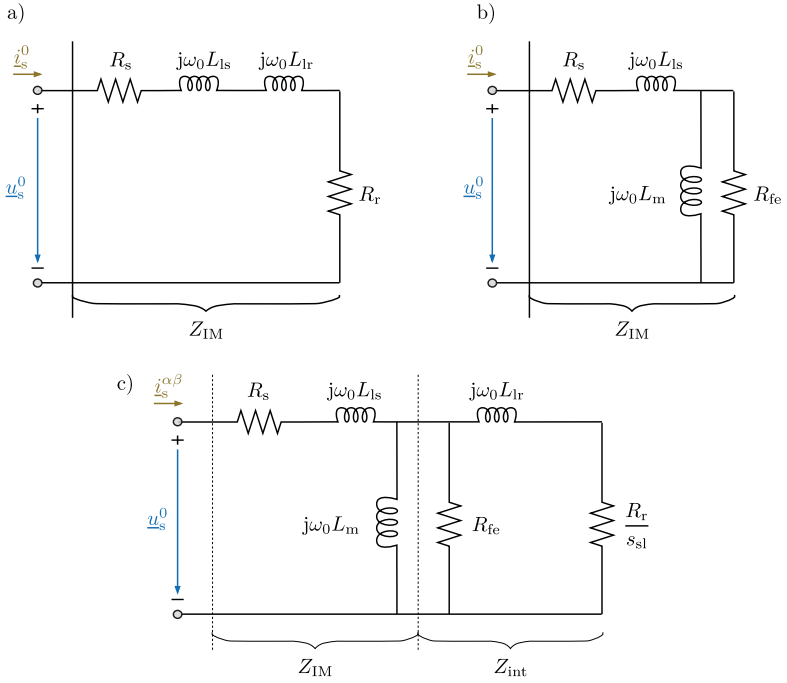

Figure 2.7: Simplified equivalent circuit model of the induction motor during the locked rotor test a) and the no-load test b); T-form equivalent circuit model in the stationary reference frame c).

is locked in position. For these test conditions, almost the entire electrical input power compensates for the conduction losses and, therefore, is highly sensitive to the stator and rotor resistance. Due to the low voltage and correspondingly low flux level, iron losses are negligible. Based on the slip frequency of $\omega_\mathrm{sl} = \omega_0$ and a relatively high reactance of the main magnetizing path, the equivalent circuit is assumed to be of the form shown in Figure 2.7 a). Under this assumption, the initial estimation of the rotor resistance is determined by the real part of the input impedance

$$R_\mathrm{r} = \Re\{Z_\mathrm{IM}\} - R_\mathrm{s}\,. \tag{2.48}$$

Correspondingly, the sum of the leakage inductance is derived from the imaginary

part of the input impedance

$$L_{\mathrm{ls}} + L_{\mathrm{lr}} = \frac{\Im\left\{Z_{\mathrm{IM}}\right\}}{\omega_0} \,. \tag{2.49}$$

If no design details are available, the ratio of $L_{\mathrm{ls}}/L_{\mathrm{lr}}$ is assumed to be equal to one. Other factors may apply for different motor design types (cf. section 5.10.3.2 [97]).

The no-load test makes use of a balanced set of ac-voltages while operating at a negligible rotor torque and a steady state rotor speed. In this no-load configuration the input power is predominantly divided into conduction and iron losses as well as friction losses of the rotor. Since at no load the slip frequency is close to zero, the equivalent circuit is assumed to be of the form shown in Figure 2.7 b). It is noted, that due to the low slip frequency the pole pair number is determined by the closest integer to $Z_{\mathrm{p}} \approx \omega_0/\omega_{\mathrm{m}}$. After (2.47) is computed based on the current and voltage measurements, the value of the iron core resistance can be obtained with

$$R_{\mathrm{fe}} = \frac{\left(\Re\left\{Z_{\mathrm{IM}}\right\} - R_{\mathrm{s}}\right)^2 + \left(\Im\left\{Z_{\mathrm{IM}}\right\} - \omega_0 L_{\mathrm{ls}}\right)^2}{\Re\left\{Z_{\mathrm{IM}}\right\} - R_{\mathrm{s}}} \,, \tag{2.50}$$

and the mutual inductance is determined as

$$L_{\mathrm{m}} = \frac{\left(\Re\left\{Z_{\mathrm{IM}}\right\} - R_{\mathrm{s}}\right)^2 + \left(\Im\left\{Z_{\mathrm{IM}}\right\} - \omega_0 L_{\mathrm{ls}}\right)^2}{\omega_0 \left(\Im\left\{Z_{\mathrm{IM}}\right\} - \omega_0 L_{\mathrm{ls}}\right)} \,. \tag{2.51}$$

The estimation of the rotor resistance and leakage inductance can be improved using the identified values for $R_{\mathrm{s}}, R_{\mathrm{fe}}, L_{\mathrm{ls}}, L_{\mathrm{m}}$ and the full T-form equivalent circuit model depicted in Figure 2.7 c). Evaluating (2.47) once again for the current and voltage measurements of the locked-rotor test, an intermediate impedance is defined according to

$$\begin{aligned} Z_{\mathrm{int}} =& R_{\mathrm{fe}} \frac{\left(R_{\mathrm{fe}} - \left(\Re\left\{Z_{\mathrm{IM}}\right\} - R_{\mathrm{s}}\right)\right)\left(\Re\left\{Z_{\mathrm{IM}}\right\} - R_{\mathrm{s}}\right) - \left(\Im\left\{Z_{\mathrm{IM}}\right\} - \omega_0 L_{\mathrm{ls}}\right)^2}{\left(R_{\mathrm{fe}} - \left(\Re\left\{Z_{\mathrm{IM}}\right\} - R_{\mathrm{s}}\right)\right)^2 + \left(\Im\left\{Z_{\mathrm{IM}}\right\} - \omega_0 L_{\mathrm{ls}}\right)^2} + \\ & \mathrm{j} R_{\mathrm{fe}}^2 \frac{\Im\left\{Z_{\mathrm{IM}}\right\} - \omega_0 L_{\mathrm{ls}}}{\left(R_{\mathrm{fe}} - \left(\Re\left\{Z_{\mathrm{IM}}\right\} - R_{\mathrm{s}}\right)\right)^2 + \left(\Im\left\{Z_{\mathrm{IM}}\right\} - \omega_0 L_{\mathrm{ls}}\right)^2} \,. \end{aligned} \tag{2.52}$$

Finally, the update of the rotor resistance and leakage inductance yields

$$R_{\mathrm{r}} = \frac{\left(\omega_0 - \omega_{\mathrm{m}}\right) \omega_0 \, \Re\left\{Z_{\mathrm{int}}\right\} L_{\mathrm{m}}^2}{\Re\left\{Z_{\mathrm{int}}\right\}^2 + \left(\omega_0 L_{\mathrm{m}} - \Im\left\{Z_{\mathrm{int}}\right\}\right)^2} \,, \tag{2.53}$$

$$L_{\mathrm{lr}} = \frac{\omega_0 \, \left(\omega_0 L_{\mathrm{m}} - \Im\left\{Z_{\mathrm{int}}\right\}\right) L_{\mathrm{m}}^2}{\Re\left\{Z_{\mathrm{int}}\right\}^2 + \left(\omega_0 L_{\mathrm{m}} - \Im\left\{Z_{\mathrm{int}}\right\}\right)^2} - L_{\mathrm{m}} \,. \tag{2.54}$$

Various other identification methods exist, that impose special conditions during the test procedure. For example, [210] identifies parameters from transient tests

while presupposing conditions on the rotor slip, whereas [30] performs locked rotor tests in which only one phase is energized. More recently, [121] introduced a genetic algorithm for an adapted IM model, that accounts for saturation and skin effects. The maturity level of offline identification methods is particularly evident when looking at self-commissioning procedures, in which the motor controller automatically determines all model parameters [106, 194].

2.2.6 Online Identification

The accuracy of the IM model improves if parameter variations are tracked online, especially because the stator and rotor resistance are temperature dependent (2.46). However, the number of parameters that can be identified online is restricted. Their selection depends on the model structure and structural identifiability of the involved parameter [14]. The two major groups of online identification methods are observer-based techniques and methods that are based on a *Model Reference Adaptive System* (MRAS) [223]. The principle idea of a MRAS is to construct an error signal from a modeled reference and its corresponding measurement. This error signal can be used in a feedback loop to correct the parameter estimate so that the reference signal more closely resembles the observed behavior. Ideally, a signal is chosen that is sensitive to the parameter. A recent example of a MRAS, used in the context of a BEV, is presented in [245]. This method identifies the rotor resistance and mutual inductance. The most prominent technique, however, is the *Extended Kalman Filter* (EKF) [7, 249]. The EKF, along with other online identification methods, are tested on a small experimental setup with a 1.5 kW motor in [9]. The identifiablity of the analyzed methods is evaluated by consulting the Fisher information. This information arises as a measure of the expected error in a modeled output. A lower bound of the parameter variance for a given test procedure can be derived from the Fischer information via the Cramer-Rao inequality [72].

2.2.7 In-Vehicle Identification

The previously discussed methods all require measurements of the rotor speed, the stator phase voltages, and stator phase currents at high sampling frequencies. However, it is often the case in practice that the access to internal control functions and measurements are restricted. Vehicle state on the internal communication bus that are readily accessible are

- the RMS value of the stator phase current $i_{\mathrm{rms}} = \hat{i}/\sqrt{2}$,
- the electric power throughput of the IM $P_{\mathrm{e,im}}$,
- an accurate estimation of the rotor torque T_{e},

- and the rotor speed ω_m

at sampling frequencies of 1 kHz. This selection of measurement data at relatively low sampling frequencies strongly limits the chance of identifying the IM parameters. It is therefore necessary to make further assumptions on the model structure and to reduce the number of parameters to be identified.

The first assumption is that the IM is operated in steady state. An experimental study presented in [193], demonstrates that this assumption is sufficient to accurately reproduce the observed phase current and power loss for a dynamic driving cycle. A more detailed discussion of the steady state assumption follows in Section 2.6.2. Furthermore, the pole pair number Z_p and stator resistance R_s are assumed to be known. The pole pair number is typically provided in the technical specification of the motor. As per [97], the stator resistance is easily measured at the terminals of the motor. Consequently the steady state current and power loss model (2.45) are fully defined by the parameter set

$$\left\{ \frac{L_\mathrm{r}}{L_\mathrm{m}^2} , \tau_\mathrm{r} , \frac{L_\mathrm{r}}{R_\mathrm{fe}} \right\} . \tag{2.55}$$

The second assumption is made on the rotor flux. The fundamental problem of an online identification method is the unknown rotor flux λ_r. In the case of an EKF, the rotor flux is estimated along with the rotor time constant. As soon as an accurate estimation of the rotor flux is available, the identification of the rotor time constant and mutual inductance becomes straight forward. With this motive in mind, it is assumed that IM controls in BEV applications make use of loss-minimizing control strategies or are able to determine the rotor flux empirically to guarantee the maximum possible IM efficiency. In both cases, this a priori knowledge of the operating strategy can be used to derive an estimation of the rotor flux. For the considered experimental vehicle this assumption is verified in Section 3.2. As will be shown there, the rotor flux that minimizes conduction, leakage and core losses (LMT), is expressed as a function of the rotor speed and torque

$$\lambda_\mathrm{r}^\mathrm{lmt} = \left(\frac{4}{9} \frac{R_\mathrm{r} L_\mathrm{m}^2 + R_\mathrm{s} L_\mathrm{r}^2}{R_\mathrm{s} + \dfrac{\left(L_\mathrm{m} Z_\mathrm{p} \omega_\mathrm{m}\right)^2}{R_\mathrm{fe}}} \frac{T_\mathrm{e}^2}{Z_\mathrm{p}^2} \right)^{0.25} . \tag{2.56}$$

Equation (2.56) is valid as long as the IM is not operated in magnetic saturation or at the maximum attainable phase voltage. This assumption is realistic at moderate power and torque demands. Therefore, in a partial load area, (2.56) can be used in

(2.45) to obtain

$$P_{\mathrm{e,im}} = \frac{2}{L_{\mathrm{m}}} \sqrt{\left(R_{\mathrm{s}} + \frac{L_{\mathrm{m}}^2 \omega_{\mathrm{e}}^2}{R_{\mathrm{fe}}} \right) \left(R_{\mathrm{r}} L_{\mathrm{m}}^2 + R_{\mathrm{s}} L_{\mathrm{r}}^2 \right) \frac{T_{\mathrm{e}}^2}{Z_{\mathrm{p}}^2}} + \omega_{\mathrm{m}} T_{\mathrm{e}} \,, \tag{2.57}$$

$$\hat{i}^2 = \frac{2}{3 L_{\mathrm{m}}^2} \left(\sqrt{\frac{R_{\mathrm{r}} L_{\mathrm{m}}^2 + R_{\mathrm{s}} L_{\mathrm{r}}^2}{R_{\mathrm{s}} + L_{\mathrm{m}}^2 \omega_{\mathrm{e}}^2 / R_{\mathrm{fe}}}} + L_{\mathrm{r}}^2 \sqrt{\frac{R_{\mathrm{s}} + L_{\mathrm{m}}^2 \omega_{\mathrm{e}}^2 / R_{\mathrm{fe}}}{R_{\mathrm{r}} L_{\mathrm{m}}^2 + R_{\mathrm{s}} L_{\mathrm{r}}^2}} \right) \sqrt{\frac{T_{\mathrm{e}}^2}{Z_{\mathrm{p}}^2}} \,. \tag{2.58}$$

Both expressions, (2.57) and (2.58), define different parameterized mappings for the same model output

$$y = \left(P_{\mathrm{e,im}} - \omega_{\mathrm{m}} T_{\mathrm{e}} \right) \hat{i}^2 \,, \tag{2.59}$$

which are given by

$$y = \frac{L_{\mathrm{r}}}{L_{\mathrm{m}}^2} \left(\frac{2}{6} \frac{\left(P_{\mathrm{e,im}} - \omega_{\mathrm{m}} T_{\mathrm{e}} \right)^2}{\dfrac{1}{\tau_{\mathrm{r}}} + R_{\mathrm{s}} \dfrac{L_{\mathrm{r}}}{L_{\mathrm{m}}^2}} + \frac{4}{3} \left(\frac{1}{\tau_{\mathrm{r}}} + R_{\mathrm{s}} \frac{L_{\mathrm{r}}}{L_{\mathrm{m}}^2} \right) \frac{T_{\mathrm{e}}^2}{Z_{\mathrm{p}}^2} \right) \tag{2.60}$$

and

$$y = \frac{4}{3} \frac{L_{\mathrm{r}}}{L_{\mathrm{m}}^2} \left(\frac{1}{\tau_{\mathrm{r}}} + 2 \frac{L_{\mathrm{r}}}{L_{\mathrm{m}}^2} R_{\mathrm{s}} + \frac{L_{\mathrm{r}}}{R_{\mathrm{fe}}} Z_{\mathrm{p}}^2 \omega_{\mathrm{m}}^2 \right) \frac{T_{\mathrm{e}}^2}{Z_{\mathrm{p}}^2} \,. \tag{2.61}$$

It is noted that the above mappings only depend on the parameter set defined in (2.55). Another possible control strategy is to choose the flux level in a way that minimizes the phase current instead of the IM losses. Following such an MTPA strategy, it is shown in Section 3.2 that the rotor flux is equal to

$$\lambda_{\mathrm{r}}^{\mathrm{mtpa}} = \left(\frac{4}{9} L_{\mathrm{r}}^2 \frac{T_{\mathrm{e}}^2}{Z_{\mathrm{p}}^2} \right)^{0.25} \,. \tag{2.62}$$

However, at a speed of

$$\omega_{\mathrm{m},0} = \frac{\sqrt{R_{\mathrm{r}} R_{\mathrm{fe}}}}{Z_{\mathrm{p}} L_{\mathrm{r}}} \,, \tag{2.63}$$

where the strategies (2.56) and (2.62) are identical, a third mapping of the phase current square value is given by

$$\hat{i}^2 \big|_{\omega_{\mathrm{m},0}} = \frac{4}{3} \frac{L_{\mathrm{r}}}{L_{\mathrm{m}}^2} \sqrt{\frac{T_{\mathrm{e}}^2}{Z_{\mathrm{p}}^2}} \,. \tag{2.64}$$

Based on these mappings, an identification procedure is proposed in [193], which determines the parameter set (2.55) in three steps. Following this approach the torque

and speed operating range of the IM is divided into a region defined by (2.63) with the neighborhood of $\omega_{\mathrm{m},0}$ as well as a partial load area, in which it is guaranteed that the IM is not magnetically saturated or operated at the maximum phase voltage. Though, the boundary of the partial load area and the speed $\omega_{\mathrm{m},0}$ are not known beforehand, a first iteration of the identification procedure results in a sufficiently close estimation of (2.55) by choosing a conservative selection of low torque operating points and a speed that is close to the base speed of the IM. The base speed is defined by the point at which the product of the rated torque and speed is equal to the nominal power. This initial guess can be used in a second iteration to identify the partial load area more precisely and to restrict the actual speed range of $\omega_{\mathrm{m},0}$.

For the first step of the identification procedure, data of the RMS phase current and rotor torque are collected for operating points in the vicinity of $\omega_{\mathrm{m},0}$. The parameter $L_{\mathrm{r}}/L_{\mathrm{m}}^2$ is then derived from a linear regression using (2.64). For the second and third step, data of the current, rotor torque, rotor speed and electric power are recorded in the partial load area. Preferably, information over a wide speed range is included. The second step identifies the combination of parameters $1/\tau_{\mathrm{r}} + L_{\mathrm{r}}/L_{\mathrm{m}}^2 R_{\mathrm{s}}$ as a single parameter by the least square error of (2.60). A huge advantage of this combined parameter, is that the mapping (2.60) does not depend on any other model parameter except for the previously identified value of $L_{\mathrm{r}}/L_{\mathrm{m}}^2$, which only linearly scales the relation. The rotor time constant τ_{r} is then derived using the estimate of $L_{\mathrm{r}}/L_{\mathrm{m}}^2$ and the known stator resistance. Finally, the remaining parameter $L_{\mathrm{r}}/R_{\mathrm{fe}}$ is obtained from (2.61).

After completion of these three identification steps, it is possible to obtain an estimate of the magnetic parameters by adopting an initial guess of the leakage coefficient σ so that

$$L_{\mathrm{r}} = L_{\mathrm{s}} = \frac{1}{1-\sigma}\frac{L_{\mathrm{m}}^2}{L_{\mathrm{r}}}\,, \qquad L_{\mathrm{m}} = \sqrt{\frac{1}{1-\sigma}}\frac{L_{\mathrm{m}}^2}{L_{\mathrm{r}}}\,. \tag{2.65}$$

In an iterative process, the guess of the leakage coefficient is improved by evaluating the conformity of the modeled phase current and IM power loss similar to a MRAS based approach.

2.3 Drivetrain

Within this work the operating points $(\omega_{\mathrm{m}}, T_{\mathrm{e}})$ of an IM drive are defined by the vehicle's longitudinal dynamics. Since the focus is placed on energy management of electric drives, the longitudinal dynamics are not expressed in terms of the vehicle speed v and force, but rather in terms of the wheel angular speed

$$\omega_{\mathrm{whl}} = v/r_{\mathrm{whl}}\,, \tag{2.66a}$$

and the wheel torque T_{whl}

$$\left(r_{\mathrm{whl}}^2 m + J\right)\, \dot{\omega}_{\mathrm{whl}} = T_{\mathrm{whl}} + T_{\mathrm{brk}} - r_{\mathrm{whl}} F_{\mathrm{res}}\,, \tag{2.66b}$$

where r_{whl} is the effective wheel radius, $T_{\mathrm{brk}} \in \mathbb{R}_-$ is the nonpositive brake torque applied via the friction brake, and $F_{\mathrm{res}} \in \mathbb{R}_+$ is the sum of the aerodynamic resistance, rolling friction force, and the force induced by gravity

$$F_{\mathrm{res}} = \frac{1}{2} A_{\mathrm{d}} c_{\mathrm{d}} \rho (\omega_{\mathrm{whl}}\, r_{\mathrm{whl}} - v_{\mathrm{h}})^2 + mg(c_{\mathrm{r}} \cos(\gamma) + \sin(\gamma))\,. \tag{2.66c}$$

Depending on the wheel and brake torque, the vehicle can operate in three different modes

- traction $\mathcal{T} = \{T_{\mathrm{whl}}, T_{\mathrm{brk}} \in \mathbb{R} \times \mathbb{R}_- \,|\, T_{\mathrm{whl}} > 0 \,\wedge\, T_{\mathrm{brk}} = 0\}$,
- coasting $\mathcal{C} = \{T_{\mathrm{whl}}, T_{\mathrm{brk}} \in \mathbb{R} \times \mathbb{R}_- \,|\, T_{\mathrm{whl}} = 0 \,\wedge\, T_{\mathrm{brk}} = 0\}$,
- braking $\mathcal{B} = \{T_{\mathrm{whl}}, T_{\mathrm{brk}} \in \mathbb{R} \times \mathbb{R}_- \,|\, T_{\mathrm{whl}} + T_{\mathrm{brk}} < 0\}$.

Vehicle parameters are the vehicle mass m, the inertia of all rotating components J, the projected vehicle frontal area A_{d}, the drag coefficient c_{d}, and the rolling resistance coefficient c_{r}. These may vary, for example, due to an additional payload or changing road and weather conditions. Other environmental factors of influence are the density of the ambient air ρ, the headwind v_{h}, the acceleration due to gravity g, and the road grade γ. The former two are in general unknown and therefore introduce uncertainties. The road grade for a specified route can be obtained from road preview data provided by navigational services.

As observed in [151], the vehicle dynamics present the greatest source of uncertainty and require special attention. Detailed sensitivity analyses of parameter uncertainties and their influence on the energy consumption are conducted in [149]. Derived from these findings, estimation methods are proposed which are suitable to reduce the error dependencies of the rolling resistance coefficient. This has been identified as the most critical parameter. In this study, the vehicle mass, the effective wheel radius, the inertia of all rotating components, and the projected vehicle frontal area of the longitudinal dynamics model (2.66b) are given by the vehicle manufacturer. Also given is the aerodynamic drag coefficient, which is determined in dedicated wind tunnel tests. The remaining rolling friction coefficient is identified from torque and speed measurements. This is done by a linear regression based on (2.66b) and (2.69), in which the acceleration is computed with a differentiating filter and the road grade is obtained from *Global Positioning System* (GPS) and navigational data [149].

2.3.1 Regenerative Braking

The regenerative braking potential of a BEV has a huge influence on the electric energy consumption [78]. Depending on the design and the control of the braking

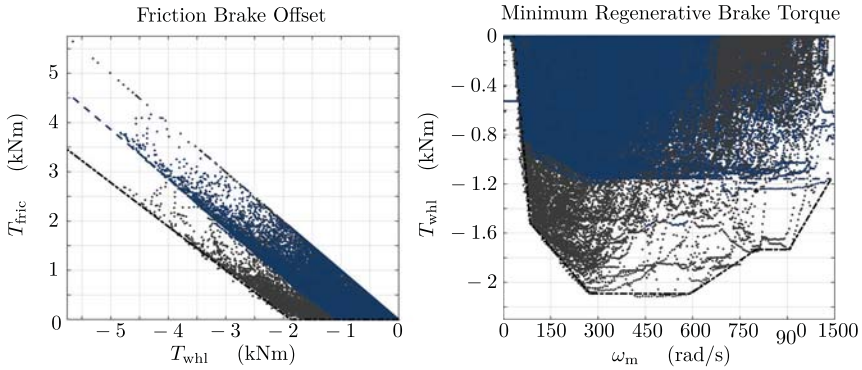

Figure 2.8: Regenerative braking characteristics.

system, only a limited amount of kinetic and potential energy can be regenerated to charge the battery, while the remaining energy is dissipated via the mechanical friction brake. The influence of the friction brake is approximated by the following definition of an electric wheel torque

$$\begin{aligned} T_{\mathrm{e,whl}} &= T_{\mathrm{whl}} + T_{\mathrm{brk}}\,, \\ &= \begin{cases} T_{\mathrm{whl}}\,, & T_{\mathrm{whl}} \geq 0 \\ \max\left\{T_{\mathrm{whl}} + T_{\mathrm{fric}}\left(T_{\mathrm{whl}}\right), T_{\mathrm{whl,lb}}\left(\omega_{\mathrm{whl}}\right)\right\}\,, & T_{\mathrm{whl}} < 0 \end{cases} . \end{aligned} \tag{2.67}$$

The causality between the requested wheel torque and the electric wheel torque is governed by characteristics and control functions that are defined by control strategies of the MCU. The minimum regenerative brake torque $T_{\mathrm{whl,lb}}$ is bound from below to account for drivability requirements [133] or system requirements and is computed within the MCU as a function of the wheel speed. If the battery is fully charged for example, the minimum regenerative brake torque is restricted to $T_{\mathrm{whl,lb}} = 0$ so that solely the friction brake is applied. Design and control specific influences of the braking system are modeled by a friction brake offset T_{fric}, which is a function of the applied wheel torque. These characteristics may change, depending on the driving mode or the current driving situation.

Both the friction brake offset T_{fric} and minimum regenerative brake torque $T_{\mathrm{whl,lb}}$ are identified from EDM torque, brake torque, and speed measurements recorded during a field study. For every driving mode, the lower bound of the electric wheel torque is represented as a piece-wise affine, speed dependent function. Two examples are illustrated as dotted lines in the right graph of Figure 2.8. Similarly, as shown in the left graph, the friction brake offset is fitted to a piece-wise affine function of the wheel torque.

2.3.2 Friction Losses

To see how the electromagnetic rotor torque T_e is connected to the electric wheel torque $T_\mathrm{e,whl}$, several friction processes of the drivetrain have to be considered. Components that considerably contribute to friction losses are transmission gears, torque couplers, power split devices, and rotor internal cooling systems. Furthermore, due to the high amount of rotor losses, the rotor shaft is an integral element of the cooling system and thus flooded with a cooling fluid. Consequently, the cooling system and the lubrication of the gear affect these friction processes. All of these effects are beyond the scope of this work, which is why drivetrain losses are modeled as the parasitic friction torque

$$T_\mathrm{dt} = p_{0dt} + p_{1dt}\,\frac{\omega_\mathrm{whl}}{\omega_\mathrm{nom}} + \mathrm{f}_\mathrm{1dt}\left(\omega_\mathrm{whl}\right)\,\frac{T_\mathrm{e,whl}}{T_\mathrm{nom}} + \mathrm{f}_\mathrm{2dt}\left(\omega_\mathrm{whl}\right)\,\left(\frac{T_\mathrm{e,whl}}{T_\mathrm{nom}}\right)^2 , \tag{2.68a}$$

where $\omega_\mathrm{nom} \in \mathbb{R}_+$ denotes the nominal wheel speed, $T_\mathrm{nom} \in \mathbb{R}_+$ is the nominal wheel torque, and $p_{\{0,1\}dt} \in \mathbb{R}^+$ are constant parameters. The nominal values can be chosen to be the maximum attainable speed and torque. The polynomial speed dependent functions f_1dt and f_2dt both are define by

$$\mathrm{f}_{\{1,2\}\mathrm{dt}}\left(\omega_\mathrm{whl}, T_\mathrm{e,whl}\right) = \begin{cases} p_{0dt,\mathcal{T}} + p_{1dt,\mathcal{T}}\,\dfrac{\omega_\mathrm{whl}}{\omega_\mathrm{nom}} + p_{2dt,\mathcal{T}}\,\left(\dfrac{\omega_\mathrm{whl}}{\omega_\mathrm{nom}}\right)^2, & T_\mathrm{e,whl} \geq 0 \\ p_{0dt,\mathcal{B}} + p_{1dt,\mathcal{B}}\,\dfrac{\omega_\mathrm{whl}}{\omega_\mathrm{nom}} + p_{2dt,\mathcal{B}}\,\left(\dfrac{\omega_\mathrm{whl}}{\omega_\mathrm{nom}}\right)^2, & T_\mathrm{e,whl} < 0 \end{cases} , \tag{2.68b}$$

with the constant parameters $p_{\{0,1,2\}dt,\{\mathcal{B},\mathcal{T}\}} \in \mathbb{R}$. Changing characteristics in propulsion and regeneration are accounted for in the two cases of (2.68b). Note that the first affine speed dependent term in (2.68a) is obtained by a simple linear friction model. Finally, the connection between electric wheel torque, wheel speed, and the operating point $(\omega_\mathrm{m}, T_\mathrm{e})$ of an electric drive is given by

$$\omega_\mathrm{m} = \omega_\mathrm{whl}\,\iota_\mathrm{dt} , \qquad T_\mathrm{e} = \frac{T_\mathrm{whl} + T_\mathrm{dt}}{\iota_\mathrm{dt}} , \tag{2.69a}$$

where ι_dt denotes the fixed gear ratio. A huge advantage of the proposed modeling approach is the possibility to use (2.68) and (2.69a) in both directions of the transmission yielding

$$T_\mathrm{whl} = \frac{-f_\mathrm{1dt}\left(\omega_\mathrm{whl}\right) - T_\mathrm{nom} + \sqrt{\left(f_\mathrm{1dt}\left(\omega_\mathrm{whl}\right) + T_\mathrm{nom}\right)^2 - 4 f_\mathrm{2dt}\left(\omega_\mathrm{whl}\right)\left(p_{0dt} + p_{1dt}\,\dfrac{\omega_\mathrm{whl}}{\omega_\mathrm{nom}} - T_\mathrm{e}\iota_\mathrm{dt}\right)}}{2\dfrac{f_\mathrm{2dt}\left(\omega_\mathrm{whl}\right)}{T_\mathrm{nom}}} . \tag{2.69b}$$

The quasi stationary model of the drivetrain's friction torque (2.68) is identified with the help of a test stand on which each axle is connected to an electric drive. Since the wheel torque is directly controlled by the test stand, the friction torque can be

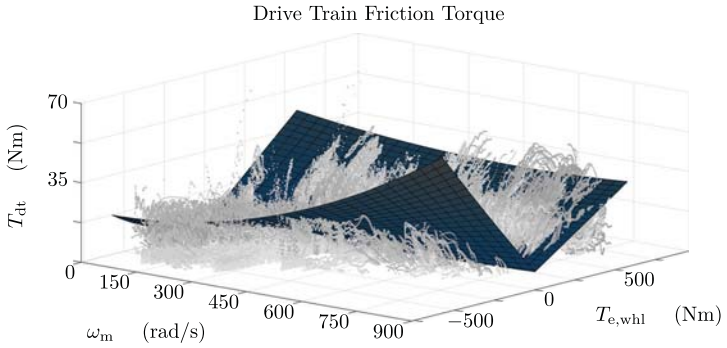

Figure 2.9: Identified quasi stationary model of the drivetrain friction torque.

approximated by the difference between the estimated EDM rotor torque and the controlled wheel torque. This difference is shown in Figure 2.9 as a function of the EDM rotor speed and torque, where a selection of measurements is recorded during a dynamic driving cycle. The graph only shows operating points for low acceleration values and situations in which the friction brake is inactive. The identified, least-square fit of the model (2.68) is displayed as a surface. Despite the clear errors that are expected for complex friction processes, a more detailed comparison in Section 2.6.1, shows that the average friction torque is well represented by (2.69).

2.4 Electric Drive Module

So far, a dynamic component model of the IM has been derived in Section 2.2, an average value model of the VSI is presented in Section 2.1 and a quasi-stationary model of the transmission, as part of the drivetrain, is modeled in Section 2.3. These three components form an EDM.

2.4.1 Block Diagram

A graphical representation of the EDM, which summarizes the results of the previous chapter, is depicted in Figure 2.10. The block diagram illustrates the interactions of internal system states and highlights the input/output relations of all subsystems. Starting with the voltage reference $u_{\mathrm{a}}^*, u_{\mathrm{b}}^*, u_{\mathrm{c}}^*$ on the left of Figure 2.10, Clarke's transformation (see Appendix A.1) is applied to obtain the equivalent space vector

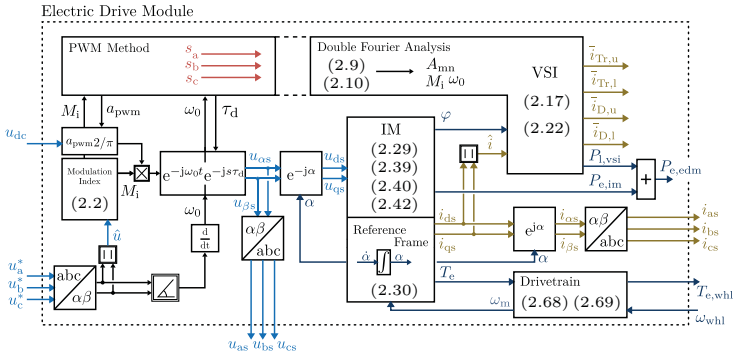

Figure 2.10: Electric drive module block diagram.

representation in the stationary reference frame with coordinates $u^*_{\alpha s}$ and $u^*_{\beta s}$. This space vector moves across the stator with a commanded fundamental frequency ω_0 and magnitude $\hat{u}^*$. The magnitude of the applied voltage $u_{\alpha s}, u_{\beta s}$ is saturated depending on the maximum attainable voltage range of the PWM method according to $M_i \in [0, 1]$. Furthermore, the commanded reference is delayed by τ_d due to the digital implementation process of regular sampling. This time shift is formulated with help of the time delay property of the Laplace transformation, where $s \in \mathbb{C}$ denotes the Laplace variable. In the following step, the states of the electric drive are computed based on the IM state-space model within its reference frame. Both the transformation to the reference frame of the motor $e^{-j\alpha}$ and inverse transformation back to the stationary reference frame $e^{j\alpha}$ require the knowledge of the reference frame orientation α. Separated into the individual components, the transformation $e^{\pm j\alpha}$ between frame A and B is given by

$$\Re\left\{\underline{x}^{\mathrm{A}}\right\} = \cos(\alpha)\,\Re\left\{\underline{x}^{\mathrm{B}}\right\} \mp \sin(\alpha)\,\Im\left\{\underline{x}^{\mathrm{B}}\right\}\,, \tag{2.70a}$$

$$\Im\left\{\underline{x}^{\mathrm{A}}\right\} = \cos(\alpha)\,\Im\left\{\underline{x}^{\mathrm{B}}\right\} \pm \sin(\alpha)\,\Re\left\{\underline{x}^{\mathrm{B}}\right\}\,. \tag{2.70b}$$

Downstream of the motor model, the resulting power factor angle φ and stator phase current magnitude $\hat{i}$ are used to compute VSI losses as well as the average transistor and diode currents. Finally the generated rotor torque T_e is applied to the drivetrain via the quasi stationary model of the gear. Measurable states are the rotor speed ω_m, the terminal voltage u_{dc}, the phase voltages u_{as}, u_{bs}, u_{cs}, and the phase currents i_{as}, i_{bs}, i_{cs}. Based on these measurements, state estimation techniques are employed to obtain the RMS phase current i_{rms}, the electromagnetic rotor torque T_e, the electric power input $P_{e,edm}$, and the IM power throughput $P_{e,im}$ which are all available on the

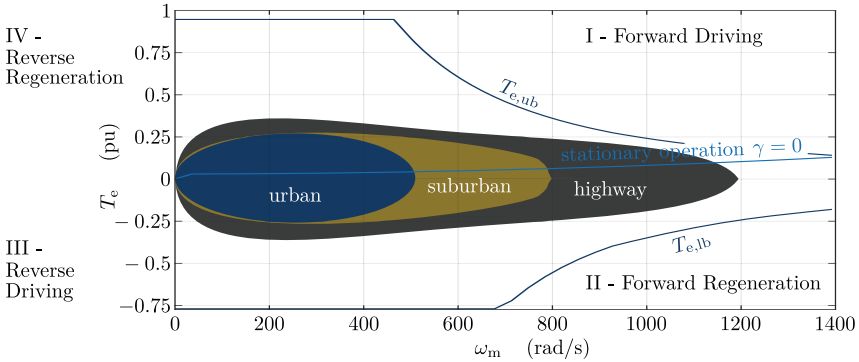

Figure 2.11: Qualitative representation of typically occurring operating points of various driving cycles, based on [156].

internal vehicle communication bus system.

2.4.2 Operating Region

The operating region of the EDM, defined by

$$\mathcal{O}_{\text{edm}} = \{\omega_{\text{m}}, T_{\text{e}} \in \mathbb{R}_{+} \times \mathbb{R} | \, T_{\text{e,lb}}\left(\omega_{\text{m}}, u_{\text{dc}}, \hat{i}_{\text{ub}}\right) \leq T_{\text{e}} \leq T_{\text{e,ub}}\left(\omega_{\text{m}}, u_{\text{dc}}, \hat{i}_{\text{ub}}\right)\} \, , \tag{2.71}$$

is shown in Figure 2.11. Without loss of generality, it is assumed that the BEV is only operated in forward motion. The maximum torque rating for driving is denoted by $T_{\text{e,ub}}$, whereas the minimum rating for regenerative braking is $T_{\text{e,lb}}$. Both are functions of the rotor angular speed ω_{m} and the terminal voltage u_{dc}. Furthermore, both may be limited by a bound on the magnitude of the phase current $\hat{i}_{\text{ub}}$. The electromagnetic torque for steady state operation at constant speed and zero road grade γ is displayed for reference proposes. Furthermore, typically occurring operating regions of various driving cycles are illustrated as shaded areas. These are calssified as urban, suburban and highway cycles according to [156].

2.5 Battery

Lithium-ion batteries have become the preferred choice for BEVs. Compared to nickel metal hybrid (NiMH) or nickel cadmium (NiCd) batteries, the most distinctive

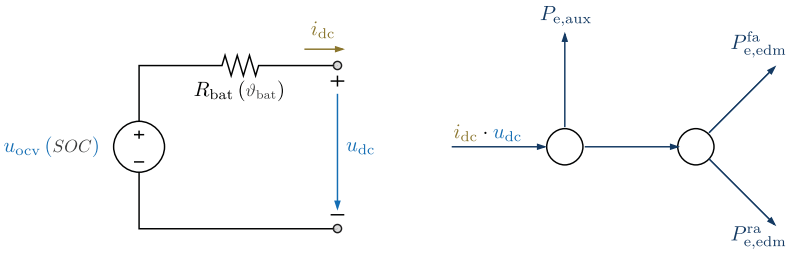

Figure 2.12: Equivalent circuit model of a lithium-based battery and BEV power distribution.

advantages are: energy density, high voltage, low self-discharge rate, long cycle life, and high charging and discharging rate capability [40, 199]. Research on new types of cell chemistries, for example, based on lithium-sulphur [69] as well as on advanced battery management systems [81], seem to offer the most promising potential to improve the range, or, reduce concerns on the limited range of BEVs.

2.5.1 Circuit Model

A basic physical model of a battery which resembles the observed changes of the terminal voltage, current, and state of charge, can be derived by means of an equivalent impedance model of a battery cell [187]. Different equivalent circuit models for automotive applications have been proposed for various cell chemistries [24, 69]. The simplest of these is the model of a lithium-based battery depicted in Figure 2.12. It is composed of an ideal open-circuit voltage source in series with an internal resistance R_{bat}. The open-circuit voltage u_{ocv} represents the equilibrium potential of the entire battery and is given as a function of the *State of Charge* (SOC). The internal resistance R_{bat} accounts for the ohmic resistances in the electrolyte, the electrodes, the interconnection of cells, and the battery terminals as well as the charge-transfer resistance and diffusion resistance of internal electrochemical processes. These processes and resistances show a strong dependency on the battery temperature ϑ_{bat}.

As discussed in Section 2.1 and expressed by (2.2), the attainable voltage range of an electric drive is determined by the PWM method and its terminal voltage. These variables constitute the key factor that influences the maximum power rating of the drive module and thus defines the torque boundaries for motion control. The causality between the terminal voltage and the overall electric power demand P_{bat} is derived

from Kirchhoff's voltage law

$$u_{\mathrm{dc}} - u_{\mathrm{ocv}} - R_{\mathrm{bat}} i_{\mathrm{dc}} = 0\,, \tag{2.72}$$

and is given by

$$u_{\mathrm{dc}} = \frac{u_{\mathrm{ocv}} + \sqrt{u_{\mathrm{ocv}}^2 - 4R_{\mathrm{bat}} P_{\mathrm{bat}}}}{2}\,. \tag{2.73}$$

As the depletion of the battery energy progresses, the open-circuit voltage decreases continuously. This phenomenon is modeled by means of current counting. Given the terminal voltage and overall power demand, the DC battery current is

$$i_{\mathrm{dc}} = \frac{P_{\mathrm{bat}}}{u_{\mathrm{dc}}} \tag{2.74}$$

which is used to derive an expression of the state of charge based on the *Initial Value Problem* (IVP)

$$\frac{\mathrm{d}\,SOC}{\mathrm{dt}} = -\frac{i_{\mathrm{dc}}}{Q_{\mathrm{nom}}} \cdot 100\,\%\,, \tag{2.75}$$

where Q_{nom} denotes the nominal battery capacity. For a short time horizon of a few seconds, the SOC and system temperature, and therefore, the open-circuit voltage and internal resistance, are assumed to be constant.

The battery is subject to extensive investigations throughout the development of an BEV. These investigations include measurements of cell impedances over a wide range of frequencies, that are essential for the battery management system. Consequently, detailed battery models and characteristics are available from which the simplified circuit model of Figure 2.12 is easily derived. For further information on identification methods concerning battery systems, the reader is referred to the series of publications by [180].

2.5.2 Electric Power Distribution

The overall electric power demand is defined by

$$P_{\mathrm{EV}} = \underbrace{\sum_{\forall \mathrm{a} \in \{\mathrm{fa,ra}\}} P_{\mathrm{e,edm}}^{\mathrm{a}} + P_{\mathrm{e,aux}}}_{P_{\mathrm{bat}}} + R_{\mathrm{bat}} i_{\mathrm{dc}}^2\,, \tag{2.76a}$$

The first term in (2.76a) is equal to the overall power throughput of all electric drive modules, the second term summarizes the power demand of auxiliaries $P_{\mathrm{e,aux}} \in \mathbb{R}_+$ and minor loss processes, and the last term approximates internal battery losses. Each drive module's power throughput is equal to its mechanical traction or regenerative braking

power $P_\mathrm{m} \in \mathbb{R}$ plus all losses resulting from electromechanical energy conversion $P_{\mathrm{l},\{\mathrm{im,vsi}\}} \in \mathbb{R}_+$

$$P_\mathrm{e,edm} = P_\mathrm{m} + \sum P_{\mathrm{l},\{\mathrm{im,vsi}\}} \,. \tag{2.76b}$$

For example, the overall loss of an IM drive module encompasses (2.43), (2.44), and (2.22) and is thus given by

$$P_\mathrm{l,edm} = P_\mathrm{l,im} + P_\mathrm{l,vsi} \,. \tag{2.76c}$$

Note that drivetrain losses are not included in this formulation as they are accounted for by the drivetrain friction torque (2.68) and that $P_\mathrm{l,im}$ is the short notation of the sum of (2.43) and (2.44). This allows to examine the electrical powertrain and the drivetrain independently of each other. Therefore, any drivetrain model can be included in the vehicle simulation.

Due to the voltage dependency of the modulation index (2.2) and corresponding dependency of $P_\mathrm{l,vsi}$, the terminal voltage (2.73) is only given implicitly. If this implicit nonlinear equation is not solved by an iterative numerical method, for example, Newton's method [158], the terminal voltage can be approximated in two steps. In the first step, $P_\mathrm{l,vsi}$ is approximated with the help of an average efficiency η_vsi. In case of an IM drive module, this approximation is defined by

$$\hat{P}_\mathrm{l,vsi} = \frac{1-\eta_\mathrm{vsi}}{\eta_\mathrm{vsi}} \left(P_\mathrm{m} + P_\mathrm{l,im}\right) \,. \tag{2.76d}$$

Subsequently this estimation is used to compute (2.76a) as well as the terminal voltage (2.73), which in the second step is used in (2.22) to improve the estimation of $\hat{P}_\mathrm{l,vsi}$.

Eventually, the auxiliary power $P_\mathrm{e,aux}$ is modeled in the same way as done in [151]. Following this approach, $P_\mathrm{e,aux}$ is assumed to be constant and represented as an average power demand that solely depends on the ambient temperature. This assumption is valid as long as the system temperatures of the battery, the cabin, and all drive modules do not considerably differ from their respective nominal temperatures. A violation of this assumption may cause an additional power demand required for thermal conditioning [135]. However, in the scope of this study, it is assumed that the vehicle is in a preconditioned state. The average auxiliary power is then computed by the time average

$$P_\mathrm{e,aux}\left(\vartheta_\mathrm{amb}\right) = \frac{\int_{t_0}^{t_\mathrm{f}} u_\mathrm{dc,aux}\, i_\mathrm{dc,aux}\,\mathrm{d}t}{t_\mathrm{f}-t_0} \,, \tag{2.77}$$

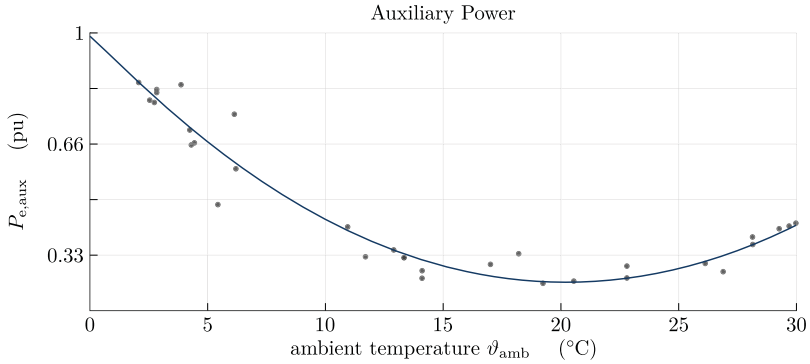

Figure 2.13: Identified auxiliary power demand.

where $u_{\mathrm{dc,aux}}$ and $i_{\mathrm{dc,aux}}$ are the terminal voltage and current measured at the central power distribution unit, which supplies all auxiliary subsystems. The characteristic of (2.77) is shown in Figure 2.13 as a function of the ambient temperature ϑ_{amb}. If the assumption of a preconditioned vehicle is violated, the approximation (2.77) can be generalized by considering an additional amount of energy for thermal conditioning. This amount varies depending on the duration of the trip and the thermal capacities of the individual subsystems. The energy required for thermal conditioning of the cabin, for example, is derived in [149].

2.6 Experimental Validation

Despite the numerous advantages of a model-based approach, empirically determined characteristics benefit from a higher level of confidence and in practice are often considered to represent the true system behavior. However, they are only valid for steady state operations and are limited by the operating conditions of the identifying test procedure. Neither empirically determined characteristics nor the proposed models are universally applicable as various assumptions and simplifications are made. Therefore, it is important to validate the model for its intended use.

To validate the EDM and battery model, a test series was conducted in a controlled environment on a *Powertrain Integration Center* (PIC) test stand. On this test stand, each wheel is connected to a high-power and high-precision electric drive to simulate realistic driving resistances and road conditions. The ambient temperature is kept constant at 20 °C. Before each test cycle, the vehicle is preconditioned so

that all system components reach their nominal operating temperature. Consequently uncertainties due to environmental factors or road conditions are mostly eliminated. Three cycles are driven for three different initial states of the battery charge level and consequently for a varying DC voltage level. These nine scenarios are repeated for five different operational strategies:

- pure *Front Wheel Drive* (FWD),
- pure *Rear Wheel Drive* (RWD),
- AWD with equal torque split,
- AWD with variable torque split and a loss map based allocation scheme,
- AWD with variable torque split and a model-based allocation scheme.

In total, 45 test cycles were completed covering a distance of more than 2.300 km. Test cycles are selected that represent real world driving conditions. These are recorded via the on-board navigation system of the experimental vehicle, which provides information on the GPS position and the vehicle speed. This information is used to match measurements with map related information obtained from HERE Technologies using a *Representational State Transfer* (REST) application programming interface. In doing so, information including heights and slope values are provided for road segments between 2 m and 200 m of length. Along with other attributes, the information is used in [151] to analyze individual driving style characteristics for the purpose of energy consumption forecasts. HERE introduces a classification metric depending on the traffic volume, speed, and connectivity of the road, however, in the context of this study, these road classes may be classified as freeways (class 1), federal highways (class 2), and priority and main roads (class 3). Road classes four and five can be considered as lower priority urban roads. The first mixed cycle of the test series is chosen to represent a mixture of the different road classes and is essentially characterized by a measured average speed of 60 km/h. The second urban cycle only passes through urban areas with a high percentage of main roads and lower priority roads at an average speed below 30 km/h. A third generic cycle is defined, which is a comprehensive sweep of acceleration and braking scenarios between different set vehicle speeds. This cycle is chosen due to the high coverage of the EDMs operational torque and speed range.

For all three cycles, the driving mode with the highest regenerative braking potential is selected so that the friction brake is hardly applied. Signals on the vehicle *Controller Area Network* (CAN) bus and internal control signals of the MCU are recorded at sampling frequencies of 100 Hz and 1 kHz. Available signals are the front and rear axle EDM terminal voltages and currents, the IM RMS phase currents and rotor angular speeds, as well as estimations of the rotor torque and VSI power loss. The electrical input power of the EDM is derived from the terminal measurements. Further information on the experimental series, including the speed, acceleration and road

grade profiles, are presented in Appendix A.4.

The individual component models are validated by comparing simulated results to CAN measurements as well as losses that are computed by means of characteristic loss maps. These loss maps are derived from electrical terminal measurements at various speed ω_m and torque T_e values. Consequently these maps characterize IM and VSI losses. Three loss maps are provided by the motor manufacturer for different DC link voltage levels. Two test cycles conducted for the mixed route and pure FWD/RWD are used for model identification and are, therefore, excluded from the validation data set comprised by the remaining 43 cycles. The characteristic of the drivetrain friction torque is identified as discussed in Section 2.3.2, the parameters of the VSI are obtained from the manufacturer's data-sheet, and the IM parameters are estimated according to the proposed in-vehicle identification method presented in Section 2.2.7. Solely the validation results of the front axle EDM are presented. Similar positive results are obtained for the rear axle.

2.6.1 Electric Drive Module Components

EDM losses, including conduction losses, core losses, and VSI losses, are computed on the basis of the measured angular speed ω_m and rotor torque T_e. The IM phase voltage is controlled so that load profile $(\omega_\mathrm{m}, T_\mathrm{e})$ is ideally tracked. The control algorithm is described in Section 3. Consequently, the IM and VSI are validated independently of the drivetrain friction torque, which is evaluated in a second step using the measured speed ω_m and the wheel torque T_whl. In order to assess the model accuracy for the wide range of operating points, the EDM input power $P_\mathrm{e,edm} = u_\mathrm{dc} i_\mathrm{dc} \in [P_\mathrm{edm,lb}, P_\mathrm{edm,ub}]$ is divided into M equidistant intervals

$$P_{\mathrm{e,edm}}{}^{[\mathrm{i}]} = P_\mathrm{edm,lb} + (\mathrm{i}-1)\,\Delta P_\mathrm{e,edm}\,, \qquad \forall \mathrm{i} \in 1(1)\mathrm{M}\,, \tag{2.78a}$$

$$P_\mathrm{edm,ub} = P_\mathrm{edm,lb} + \mathrm{M}\,\Delta P_\mathrm{e,edm}\,. \tag{2.78b}$$

As a measure for the accuracy of the model, the absolute error

$$e_{\left\{P_\mathrm{e,edm}, P_\mathrm{l,vsi}, i_\mathrm{rms}, T_\mathrm{e}\right\}} = \left\{P_\mathrm{e,edm}, P_\mathrm{l,vsi}, \hat{i}, T_\mathrm{e}\right\}\Big|_\mathrm{mdl} - \left\{P_\mathrm{e,edm}, P_\mathrm{l,vsi}, \hat{i}, T_\mathrm{e}\right\}\Big|_\mathrm{mea} \tag{2.79}$$

and the relative error

$$\epsilon_{\left\{P_\mathrm{e,edm}, P_\mathrm{l,vsi}, i_\mathrm{rms}, T_\mathrm{e}\right\}} = \frac{e_{\left\{P_\mathrm{e,edm}, P_\mathrm{l,vsi}, \hat{i}, T_\mathrm{e}\right\}}\Big|_{mdl}}{\left\{P_\mathrm{e,edm}, P_\mathrm{l,vsi}, \hat{i}, T_\mathrm{e}\right\}\Big|_\mathrm{mea}} \tag{2.80}$$

are computed for the electrical input power $P_\mathrm{e,edm}$, the VSI power loss $P_\mathrm{l,vsi}$, the stator phase current RMS value i_rms, and the rotor torque T_e. The notation $x|_{mdl}$ indicates

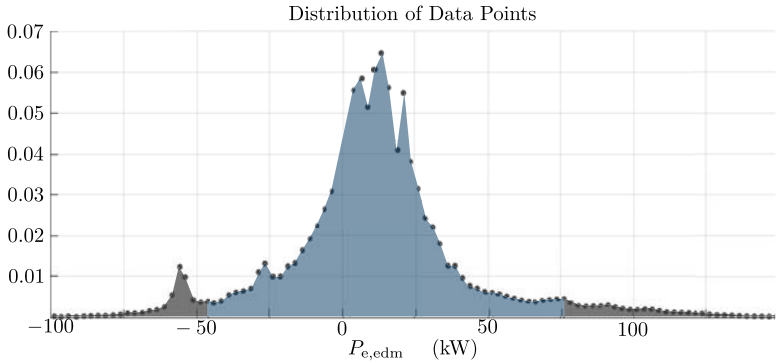

Figure 2.14: Distribution of the 8.9 million data points recorded for the electric drive module input power during the PIC test series.

that the state x is computed by the model, whereas $x|_{mea}$ denotes a measurement. Subsequently, the mean value and the 5 % and 95 % percentile are computed for all data points of the 43 test cycles within every interval $\left[{P_{\mathrm{e,edm}}}^{[\mathrm{i}]}, {P_{\mathrm{e,edm}}}^{[\mathrm{i+1}]}\right]$. The distribution of the 8.9 million data points, recorded during the test series for the EDM under consideration, is shown in Figure 2.14. All of these points only represent driving or braking conditions. Data points during stand still are not considered.

The results obtained for this analysis are presented in Figure 2.15. The top graph shows the absolute and relative error of the electrical power throughput computed by the power loss map and the EDM model. The average error is shown as a line and the 90 % confidence interval, defined by the 5 % and 95 % percentile, is indicated as a surface. For the majority of operating points within $P_{\mathrm{e,edm}} \in [-65\,\mathrm{kW}, 80\,\mathrm{kW}]$, the average relative error of the modeled input power is below $|\epsilon_{P_{\mathrm{e,edm}}}| < 8\,\%$ where in 90 % of the samples $\epsilon_{P_{\mathrm{e,edm}}} \in [-19, 21]\,\%$. The model clearly outperforms the loss map, which in this operating range has an average error of $|\epsilon_{P_{\mathrm{e,edm}}}| < 12\,\%$ and a 90 % confidence level of $\epsilon_{P_{\mathrm{e,edm}}} \in [-58, 55]\,\%$. In absolute terms, the average error of the model is below $|e_{P_{\mathrm{e,edm}}}| < 3.5\,\mathrm{kW}$ compared to the loss map with $|e_{P_{\mathrm{e,edm}}}| < 6.5\,\mathrm{kW}$.

Outside the region of $P_{\mathrm{e,edm}} \in [-65\,\mathrm{kW}, 85\,\mathrm{kW}]$, the accuracy of the modeled EDM power is high for regenerative braking, whereas it develops a trend of underestimating the observed losses for higher power demands in very dynamic driving situations. The accuracy of the EDM can be improved by taking saturation of the IM into account and by considering the thermal dependency of the resistive parameters, if, instead of economic driving, the focus is placed on dynamic driving performance.

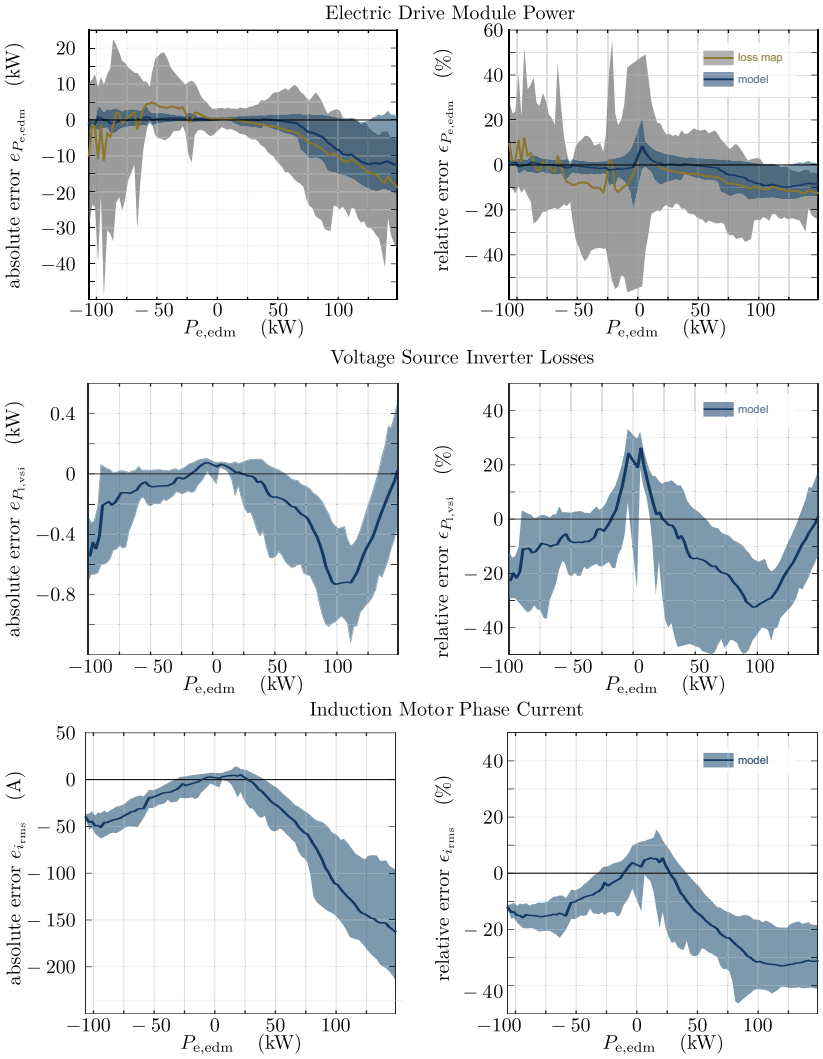

Figure 2.15: Comparison of modeled and measured induction motor and voltage source inverter states.

The effect of assuming a linear magnetic IM circuit becomes clear when looking at the bottom graph of Figure 2.15 showing the absolute and relative error of the RMS phase current. While being in an acceptable range for the intended use, the error of the IM phase current is comparably high in contrast to the EDM input power. As expected, the model underestimates the magnitude of the phase current at high power demands due to the assumption of a constant inductance. A closer inspection of (2.64) or (2.58) and their parameter sensitivity indicates that the current estimate can be improved by a nonlinear magnetic model and in particular by a current dependent mutual inductance, which linearly scales the stator phase current. A nonlinear magnetic model with current dependent mutual inductance is presented in [242]. It is noteworthy that similar results are obtained when comparing the relative error of the phase current in the bottom right graph of Figure 2.15 with the characteristic of the nonlinear mutual inductance of Fig.3 in [242].

A phase current mismatch directly affects the accuracy of the VSI model. The absolute and relative error of the VSI loss derived from an internal control signal of the MCU is shown in the second graph of Figure 2.15. Comparing the relative error of the phase current and VSI loss, both develop a similar tendency of underestimating the observed behavior. At low power demands, an overestimation of the current leads to increased switching losses. With a rising power demand and, therefore, an increasing current, an underestimation of the current mainly results in a reduced conduction loss. Above 100 kW, a different PWM method is applied, that has significantly lower switching losses. However, since high power demands are not the major concern in this study, the model only considers a space vector PWM. Consequently, the error of the VSI loss decreases although the phase current continues to be underestimated. Nevertheless, in the case of braking and low power demands for driving, where the current error is relative low, the mean relative error of the VSI model is below $|\epsilon_{P_{\mathrm{l,vsi}}}| < 10\,\%$. Overall the accuracy level with a mean absolute error that lies between $e_{P_{\mathrm{l,vsi}}} \in [-750\,\mathrm{W}, 75\,\mathrm{W}]$ and is most of the time below $e_{P_{\mathrm{l,vsi}}} \leq |200\,\mathrm{W}|$, is adequate for the intended use.

So far, the IM and VSI model are evaluated separately from the drivetrain. Thus, the question is raised how accurately the inputs to these models are computed by the quasi stationary model of the drivetrain friction torque. Figure 2.16 displays the absolute and relative error of the modeled IM rotor torque. As expected, friction processes generally are complex and, therefore, lead to high variations with a confidence level of $\epsilon_{T_\mathrm{e}} \in [-45, 40]\,\%$. However, within the region of $P_{\mathrm{e,edm}} \in [-65\,\mathrm{kW}, 80\,\mathrm{kW}]$ the mean relative error is below $|\epsilon_{T_\mathrm{e}}| < 10\,\%$ with a mean absolute error of $|e_{T_\mathrm{e}}| < 5\,\mathrm{Nm}$. At high regenerative power demands, which are mainly influenced by the friction brake offset and the minimum brake torque, the error increases and the error becomes more or less inconsistent. One possible justification is the low number of data points in this operating region. Another explanation is the intervention of additional safety functions. When considering the simple form of the model, however, the results are

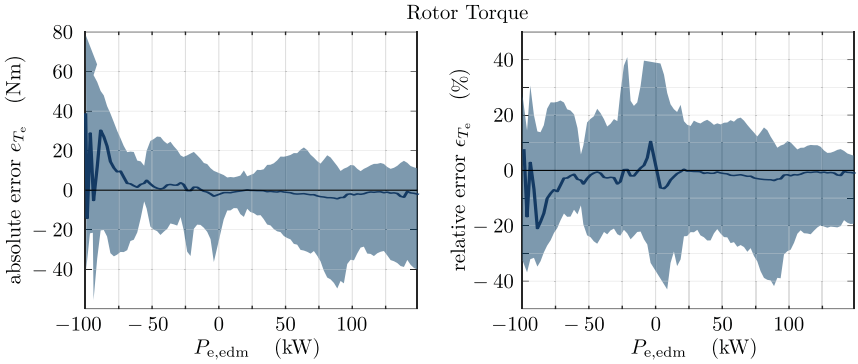

Figure 2.16: Comparison of modeled and estimated induction motor rotor torque.

reasonable.

2.6.2 Comparison of Steady State and Transient Operation

For the identification of the IM model parameter, it assumed in Section 2.2.7 that the steady state equations of Section 2.2.4 are sufficient to describe a dynamic driving scenario. In order to justify this assumption, Figure 2.17 compares EDM measurements with simulation results of a steady state and dynamic model for an acceleration scenario, in which the electromagnetic rotor torque T_e is increased to almost 100 Nm within 550 ms. In this time frame, the increase of the rotor speed is negligible so that $\omega_m \approx 0$. The steady state model computes all IM states according to the assumptions in Section 2.2.7. Comparing the EDM electrical input power and the IM RMS phase current, both models show a high resemblance between the measurement and the simulation. When starting the acceleration the dynamical model demonstrates a better estimation compared to the steady state model. However, at higher torque values, as soon as the rotor torque approaches its desired value, both models become indistinguishable. To evaluate this observation for a wider operational range, the steady state electric input power and phase current are computed for all test cycles of the PIC test series and, together with the simulation of the dynamical model, are compared to CAN measurements in a similar analysis as conducted in the previous section. Figure 2.18 presents the absolute error (2.79) and relative error (2.80) of the simulation results. It is again demonstrated that both models approximate the actual system behavior equally well. This confirms the conclusion in Section 2.2.7, which is based on the findings of [193].

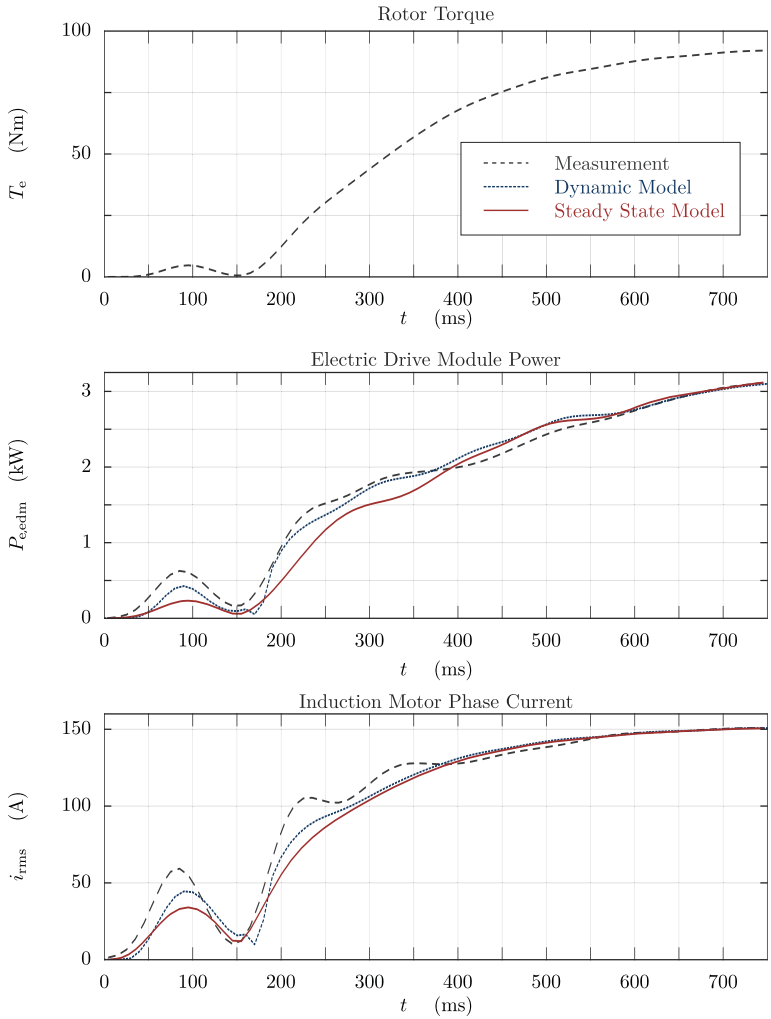

Figure 2.17: Comparison of steady state and dynamic modeling assumptions for a acceleration scenario from standstill ($\omega_m \approx 0$) .

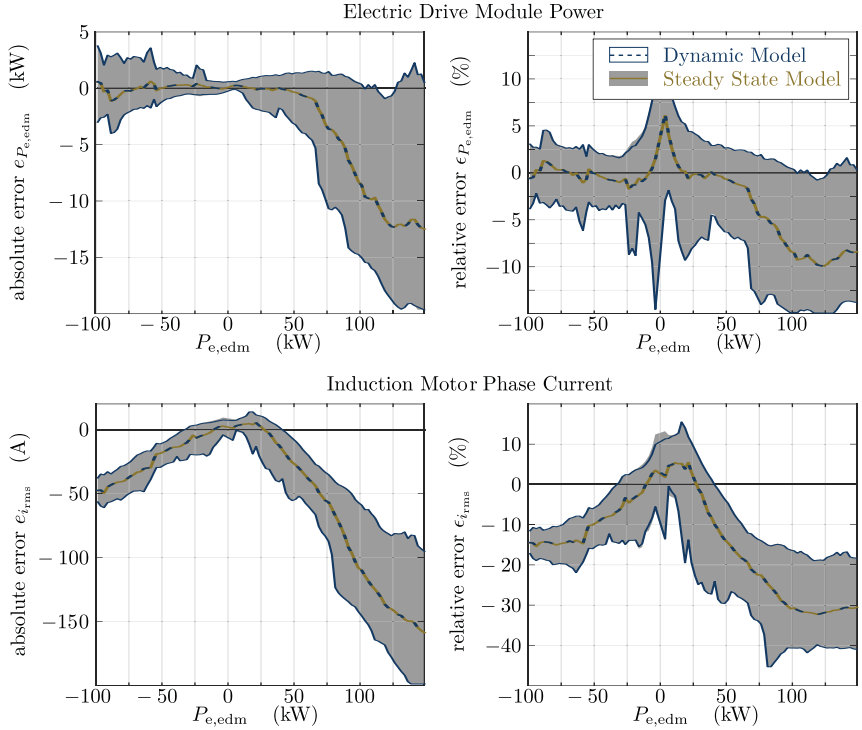

Figure 2.18: Comparison of steady state and dynamic modeling assumptions for all cycles of the PIC test series.

2.6.3 Battery Voltage

The EDM operation is mainly influenced by the battery voltage and the resulting EDM DC terminal voltage. An inaccurate estimation of the power demand and especially an error of the estimated auxiliary power may cause an ever-increasing deviation of the modeled and observed behavior. Particularly for long driving cycles it is undesirable to propagate an error over time. Due to this error propagation, the terminal voltage is evaluated by comparing the measured and modeled state for the most critical cycle of the test series, which is the longest driving cycle of acceleration and braking scenarios with the lowest initial battery voltage and pure FWD. For this purpose, the modeled EDM power and the estimated average auxiliary power is used as input to the battery model. Figure 2.19 displays the profile and resulting absolute

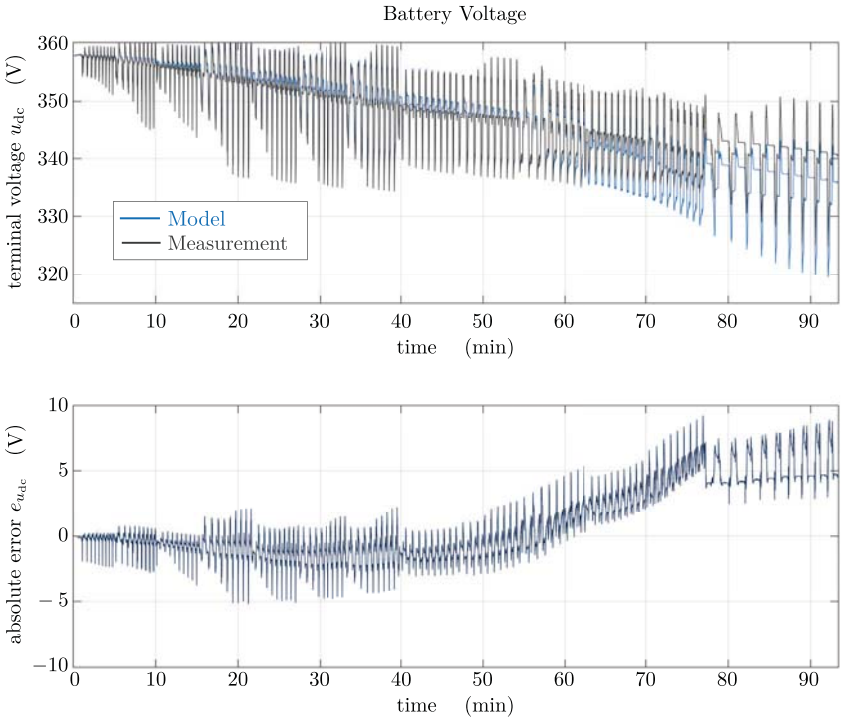

Figure 2.19: Comparison of modeled and measured EDM terminal voltage.

error of the EDM terminal voltage $e_{u_{dc}} = u_{dc}|_{mod} - u_{dc}|_{mea}$. In the upper graph it is seen that the voltage level decreases as the battery is discharged. The oscillation result from the accelerations and subsequent deceleration between different vehicle speeds (see Figure A.5). Within the first 20 min, the actual auxiliary power demand is slightly underestimated. Consequently, the battery discharge is reduced and the modeled voltage level is above the observed value. During acceleration and braking at the peaks of the EDM power throughput, the model predicts a more severe voltage drop. This is mainly due to the simplified assumption of the battery circuit model, which does not contain any capacitive elements. Nevertheless, for up to 55 min, the overall behavior is well represented with an absolute error below $|e_{u_{dc}}| < 5\,\mathrm{V}$. After 55 min, the vehicle is supposed to rapidly accelerate up to a speed of 130 km/h with a single motor. This drives the EDM to its maximum torque rating. Since the EDM power is underestimated for these high power demands, the battery is discharged less,

which, in turn, results in a modeled terminal voltage that is above the measurement. Even though the model deviates from the actual behavior during the remaining 40 min, the absolute error is below $|e_{u_{\mathrm{dc}}}| < 10\,\mathrm{V}$, which is sufficient for the intended use. Not least because the error propagation can be inhibited by a continuous update of the actual voltage level.

2.7 Model Summary

This chapter lays the foundation for a model-based design of energy management strategies. A new average value model of the VSI is introduced that computes the per fundamental average of IGBT conduction and switching losses. This model is derived from frequency analyses and is based on analytical expressions of the switched load current. A particular benefit of the VSI model is the straight-forward consideration of thermal effects, which can be accounted for by temperature dependent resistive parameters. Furthermore, since VSI losses are computed as a function of IM states, a first step is made towards an inversion-based system representation in which electrical system states are computed based on a motion profile. The second step is made by the quasi stationary model of the drivetrain, which either computes the parasitic friction torque as a function of the wheel torque or is based on the input of the electromagnetic rotor torque. Therefore, this model can act in both directions of the transmission. In doing so, main influences of the friction brake and the regenerative braking strategy are considered. As interfaces of the VSI and drivetrain model are defined in terms of motor variables, the electromechanical energy conversion of the EDM is governed by the electric and magnetic model equations of the IM. From a control perspective, the standard dq-model of the IM is the most effective system representation in terms of accuracy and computational efficiency. The electrical potential at which this conversion takes place is described by an equivalent circuit model of the battery.

The experimental validation provides strong evidence that the model-based approach allows for a more accurate estimation of the EDM electrical input power than empirically determined loss maps. Compared to polynomial representations of loss maps, which are derived from empirical considerations and only approximate the system behavior in a limited operational range, the proposed model structure is particularly well suited to represent losses in vehicle simulations. Moreover, the EDM model can provide additional information on the electrical states, which are otherwise only made available by empirical methods at an unreasonable expense. The significant improvement, not only of the average error, but also of the confidence level, is remarkable in that the VSI and IM parameters are easily obtained from data-sheets and identified from a single driving cycle by using standard vehicle CAN bus measurements. It is expected that even better results can be obtained if dedicated offline

and online estimation methods for IM parameters and nonlinear magnetic models are employed. Due to the consistency of the stationary and dynamic model, it can be concluded that a precise knowledge of fast electrical dynamics is not required during a dynamic driving cycle to resemble the observed behavior of the EDM input power, the VSI power loss, and the IM phase current. Consequently, based on the steady state equations of the IM, the average value model of the VSI, and the quasi stationary model of the drivetrain, powertrain losses and information on the electrical states can be computed as functions of torque, speed and the magnetic flux. While torque and speed are typical control variables for motion control, the rotor flux constitutes a degree of freedom that can be exploited to improve the powertrain's efficiency.

3 Energy Management Strategies for Induction Motor Drives

The EDM model that is presented in the previous chapter establishes the relation between the variables of the electrical powertrain and the mechanical drivetrain. It computes the wheel torque and speed based on a phase voltage input. However, in range or efficiency analyses of ED strategies it is preferable to compute the electrical variables as a function of the mechanical input. This requires the consideration of IM controls. The chosen control strategy has a substantial impact on the overall performance of the BEV. This influence is readily explained by a different viewpoint on the electromechanical energy conversion that is derived from a more energetic and control theoretic perspective. This particular view is the subject of this chapter and emphasis is put on the magnetic field, which couples the mechanical drivetrain and the electrical powertrain.

The EDM may be interpreted as a port-Hamiltonian system as shown in Figure 3.1, which allows for modeling the energy flow between systems of different physical domains using a systematic and insightful framework [233]. Following this modeling approach, subsystems are represented as energy-storing elements $\mathcal{S}$ and energy-dissipating elements $\mathcal{R}$. These elements are coupled via a port-based network and interact through power-conserving elements, which are formalized by the geometric notation of a Dirac structure $\mathcal{D}$. The Dirac structure links different subsystems via pairs of equally dimensioned vectors of flow and effort. Their product is equal to power. In the case of the EDM and the kinetic rotational subdomain of the drivetrain, the flow is equal to the torque T_e, the effort is equal to the angular velocity ω_m, and the energy is stored in form of the angular momentum. Energy is dissipated via the pair of the drivetrain friction torque and the angular speed $(\omega_\mathrm{m}, T_\mathrm{dt})$. For the magnetic coupling field of a single phase, the flow is given by the phase voltage $u_{\{\mathrm{a,b,c}\}\mathrm{s}}$ and the effort is defined by the phase current $i_{\{\mathrm{a,b,c}\}\mathrm{s}}$. Furthermore, the energy is stored in form of the flux linkage and dissipated due to leakage and core losses in the ferromagnetic material. Finally, in the case of the electric subdomain of the powertrain, the flow is equal to the DC current i_dc, the effort is equal to the DC voltage u_dc, and the state that determines the energy storage is the charge of the battery. Within the electrical subdomain, heat loss occurs due to the resistance of the current-carrying conductors.

State-of-the-art control methods of IM allow to change the rotor flux level independent-

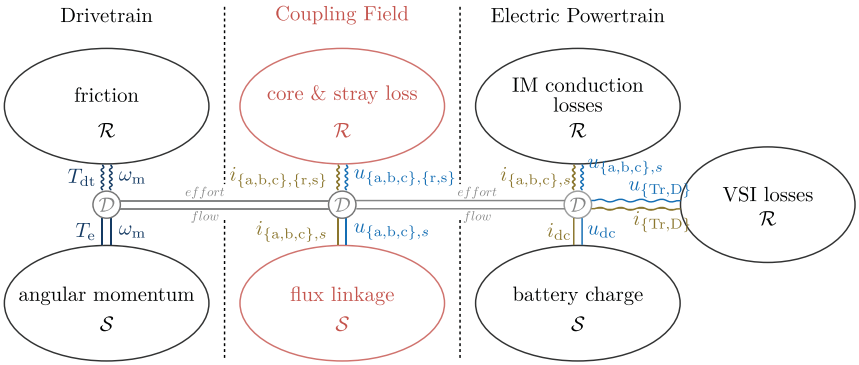

Figure 3.1: Energy balance within the port-Hamiltonian representation of an electric drive module.

ly of the electromagnetic torque. This degree of freedom can be exploited to balance between core and leakage losses, IM conduction losses, and VSI losses during steady state and transient operation. For example, during a braking event, a high flux level results in an effort and flow pair with a high phase voltage and low phase current. Therefore, conduction losses of the IM and VSI are low, while core losses of the coupling field are relatively high. A low flux level, on the other hand, leads to a power pair with a high current and low voltage. Even though conduction losses increase due to the comparable high phase current, a lower flux level may result in a higher amount of charge and therefore in an improved motion control strategy for regenerative braking.

The first part of this chapter provides a basic overview on EDM feedback loops of sensing, computation, and actuation and highlights the operational boundaries of the IM. Section 3.2 introduces an energy management strategy, which improve the overall efficiency of the IM by appropriate control of the rotor flux level. Section 3.3 introduces the new flat output of the IM and discusses the advantages over the previously known approaches [47, 140, 141]. Exploiting the positive properties of the differential flat system structure the conventional FOC is extended by a *Two Degree of Freedom* (2DOF) control. Building on this control approach, Section 3.4 proposes an optimal control method, which is used as reference governor for the 2DOF control. Finally, in Section 3.5, the different control approaches are compared in a simulative study. A summary of the main findings is provided in Section 3.6.

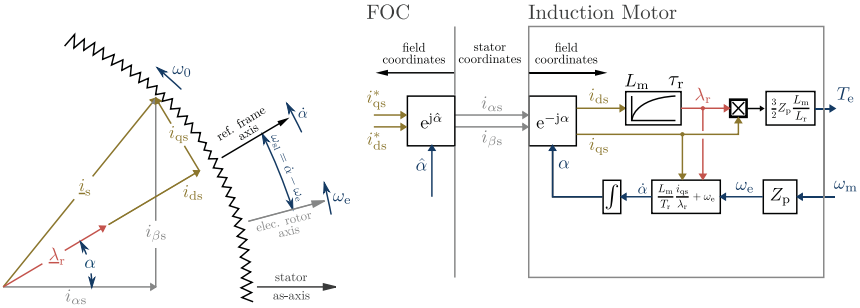

Figure 3.2: The concept of field orientation.

3.1 Field Oriented Control

FOC is best described by assuming temporarily that the stator currents are impressed by an inner feedback loop, which computes the voltage reference in such a way that the desired current reference is ideally met. Since phase voltages become a concern for current control, it is possible to omit them from the dq-model equations (2.32) leaving nothing but the ODE of the rotor flux linkage. From this perspective the dynamic structure of the IM is simplified as shown in Figure 3.2. The space vector diagram on the left and block diagram on the right, show how the rotor flux $\underline{\lambda}_\mathrm{r}$ is controlled by the parallel or direct component i_ds of the stator space vector $\underline{i}_\mathrm{s} = \hat{i}\,\mathrm{e}^{\mathrm{j}\beta_\mathrm{i}}$. The causality between i_ds and the rotor flux λ_r is described by a first order system which is governed by the rotor time constant τ_r. Subsequently, the product of the quadrature component i_qs and the rotor flux determines the electro-magnetic torque T_e.

FOC is aiming for a control structure similar to that of a DC drive, in which T_e is directly controlled by the quadrature component i_qs, independent of i_ds. In a squirrel-cage IM, however, a current in the rotor bars can only be induced by a time varying field as represented by the space vector $\underline{\lambda}_\mathrm{r}$ which moves across the rotor with slip frequency ω_sl. Consequently, the flux and torque generating components of $\underline{i}_\mathrm{s} = i_\mathrm{ds} + \mathrm{j}i_\mathrm{qs}$ are indirectly controlled by means of an appropriate slip frequency of the alternating stator current which, from the perspective of the stationary reference frame, is determined by the space vector components $i_{\alpha\mathrm{s}}$ and $i_{\beta\mathrm{s}}$. This requires a dynamic decoupling as indicated on the right of Figure 3.2. Decoupling is achieved by an inverse transformation of the current reference in the field coordinates $i_\mathrm{ds}, i_\mathrm{qs}$ to stationary coordinates $i_{\alpha\mathrm{s}}, i_{\beta\mathrm{s}}$, which presumes that the estimation of the field orientation $\hat{\alpha}$

is accurate. Consequently, the field coordinates can be chosen independently. This considerably simplifies the design of torque and rotor flux control.

3.1.1 Flux Estimation

For the practical implementation of FOC it is important that the estimated field orientation must be in close agreement with the actual position of the fundamental flux wave. The problem of flux estimation is the acquisition of the rotor flux magnitude $\hat{\lambda}_\mathrm{r}$ and orientation $\hat{\alpha}$. Generally these methods can be classified into direct methods and indirect methods.

The direct method attempts to observe the rotor flux, either by flux density measurements in the air gap, for example by placing suitably spaced Hall-sensors on the stator teeth, or by using speed and terminal voltage as well as current measurements. As it is highly complex to fit a mechanically fragile device to an electric drive, flux observers based on speed and terminal measurements have become more attractive. A presentation on linear observer based methods for flux estimation is found in [238]. A sliding-mode observer is presented in [182]. Nonlinear rotor flux observers with and without feedback corrections and their accuracy attributes w.r.t. parameter uncertainties are discussed in great detail in [102].

The indirect methods, without feedback corrections, use the slip relation to compute the flux position relatively to the rotor by summing up the sensed rotor position signal with the approximated slip position signal. One simple example is based on the stator current model in the rotor fixed reference frame (cf. $I_1\beta_\mathrm{L}$-Model [203]). From this perspective, the reference frame moves across the stator with an electric rotor angular frequency of ω_e. Accordingly, the relative movement of the rotor flux space vector directly determines the slip frequency. In this reference frame, denoted by the superscript $(.)^{\omega_\mathrm{e}}$, the rotor flux equation is derived from (2.29) and (2.36) yielding

$$\dot{\underline{\lambda}}_\mathrm{r}^{\omega_\mathrm{e}} = -\frac{1}{\tau_\mathrm{r}}\underline{\lambda}_\mathrm{r}^{\omega_\mathrm{e}} + \frac{M}{\tau_\mathrm{r}}\underline{i}_\mathrm{s}^{\omega_\mathrm{e}} \,. \tag{3.1}$$

The indirect method according to (3.1) is illustrated in the block diagram of Figure 3.3. From this diagram and (3.1), it becomes apparent that the indirect method based on the current model is sensitive to parameter uncertainties of the rotor time constant and the mutual inductance.

De Doncker and Novotny present a unified approach of decoupling networks for direct and indirect FOC, in which the orientation of the reference frame is linked to an

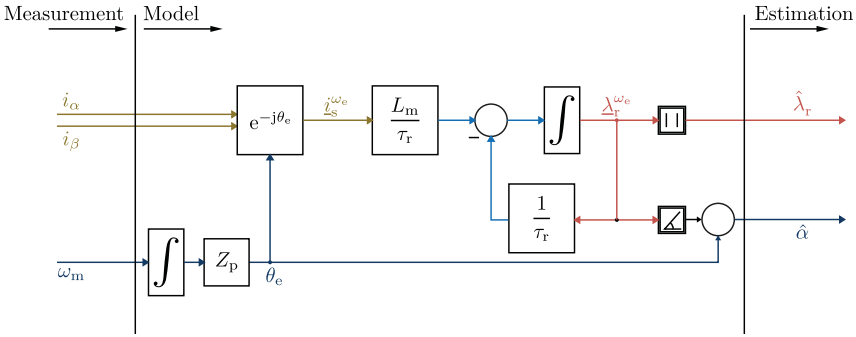

Figure 3.3: Flux estimation based on the stator current model.

arbitrary flux vector [44]. A major disadvantage of FOC in the indirect form, is its sensitivity to parameter uncertainties which are discussed in more detail in [43] and [102]. Still, both direct and indirect methods use model parameters to derive flux estimates and are thus prone to parameter sensitivities. This has motivated a variety of research activities in the field of online parameter estimation, which is discussed in Section 2.2.6.

3.1.2 Current Control

The inner current control loop is depicted in Figure 3.4. In the case of an ideally impressed stator current, it is obvious that the response behavior of the inner feedback loop to set-point changes is of particular importance. Having this objective in mind, recent research activities have focused on predictive control strategies which are based on the method of deadbeat control [132, 215]. Deadbeat predictive control is designed in the domain of sampled or discrete-control systems [1, 103]. It can therefore achieve an extremely fast response behavior, though specific actions must be taken to address delays, disturbances and high sensitivities to modeling errors and noise [146].

A conventional control design concerning the frequency domain allows for a rather simple method of load disturbance and noise attenuation at the cost of an inferior response behavior. For this purpose, plant dynamics are modeled by (2.29) which leads to

$$\underline{u}_\mathrm{s} = \sigma L_\mathrm{s} \left(\frac{1}{\tau_\mathrm{c}} \underline{i}_\mathrm{s} + \frac{\mathrm{d}\,\underline{i}_\mathrm{s}}{\mathrm{dt}} + \underbrace{\mathrm{j}\dot{\alpha}\underline{i}_\mathrm{s}}_{\text{coupling}} \right) - \underbrace{\frac{L_\mathrm{m}}{L_\mathrm{r}} \left(\frac{1}{\tau_\mathrm{r}} - \mathrm{j}\omega_\mathrm{e} \right) \underline{\lambda}_\mathrm{r}}_{\text{back EMF}} . \tag{3.2}$$

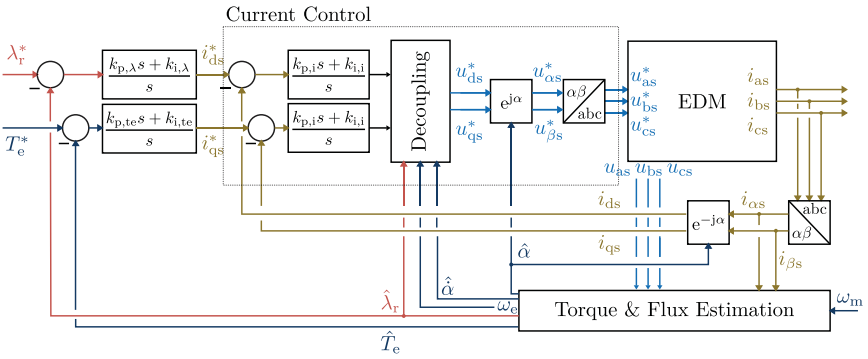

Figure 3.4: Field oriented control.

Identifying the back EMF as disturbance, the transfer function of the control plant is defined as

$$G_{\mathrm{iu}}(s) = \frac{\underline{i}_{\mathrm{s}}(s)}{\underline{u}_{\mathrm{s}}(s)} = \frac{\tau_{\mathrm{c}}}{\sigma L_{\mathrm{s}}} \frac{1}{1 + \tau_{\mathrm{c}} s + \mathrm{j}\dot{\alpha}\tau_{\mathrm{c}}} . \tag{3.3}$$

In case of the investigated EDM, the time constant τ_{c} defined in (2.34) ranges in the order of a few msec. To compensate for the coupling term and the back EMF, it is convenient to introduce a new input $\underline{v}$ along with the nonlinear static state feedback

$$\underline{u}_{\mathrm{s}} = \underline{v} + \underbrace{\mathrm{j}\sigma L_{\mathrm{s}} \dot{\alpha} \underline{i}_{\mathrm{s}}}_{\text{decoupling}} - \underbrace{\frac{L_{\mathrm{m}}}{L_{\mathrm{r}}} \left(\frac{1}{\tau_{\mathrm{r}}} - \mathrm{j}\omega_{\mathrm{e}} \right) \underline{\lambda}_{\mathrm{r}}}_{\text{back EMF compensation}} . \tag{3.4}$$

Assuming a perfect decoupling with an exact knowledge of the involved parameter as well as a good approximation of the rotor flux and the reference fame speed $\dot{\alpha}$, current dynamics (2.32) are simplified by the static state feedback to a decoupled first order system with

$$\frac{\mathrm{d}\,\underline{i}_{\mathrm{s}}}{\mathrm{dt}} = -\frac{1}{\tau_{\mathrm{c}}} \underline{i}_{\mathrm{s}} + \frac{1}{\sigma L_{\mathrm{s}}} \underline{v} . \tag{3.5}$$

The error dynamics of $\underline{e}_{\mathrm{i}} = \underline{i}_{\mathrm{s}}^{*} - \underline{i}_{\mathrm{s}}$ with respect to the reference signals or set-points, are thus readily stabilized by using simple PI controllers

$$C(s) = \frac{\underline{v}(s)}{\underline{e}_{\mathrm{i}}(s)} = \frac{k_{\mathrm{p,i}} s + k_{\mathrm{i,i}}}{s} , \tag{3.6}$$

where the proportional and integral gains for the direct and quadrature component are tuned based on standard methods of linear control theory [6, 68]. Standard

tuning methods, specifically developed for motor drives, are the *Modulus Optimum* and *Symmetrical Optimum* [6, 203].

Several technical aspects strongly limit the response behavior of the static state feedback (3.4) and PI controller. One important aspect is the time delay of the VSI. Since for regular sampled PWM, the calculated voltage reference can only have an effect on the next sampling period, the voltage reference will be shifted in phase and eventually cause unwanted coupling effects. Apart from this plant delay τ_d, a computational delay τ_cd of the digital control loop on an interrupt-driven digital system has to be considered. The plant and computational delays can add up to two sampling periods which range in the order of a view hundred μsec. Following the approach in [203], the transfer from the voltage reference to the actual phase voltage is modeled as a zero-order hold element in series with a dead time

$$G_{\mathrm{uu}^*}(s) = \frac{\underline{u}_\mathrm{s}(s)}{\underline{u}_\mathrm{s}^*(s)} = \underbrace{\frac{1-\mathrm{e}^{-s\tau_\mathrm{cd}}}{\tau_\mathrm{cd}s}}_{\text{computational delay}} \underbrace{\mathrm{e}^{-s\tau_\mathrm{d}}}_{\text{plant delay}} \underbrace{\mathrm{e}^{-\mathrm{j}\dot{\alpha}\tau_\mathrm{d}}}_{\text{coupling}} = G'_{\mathrm{uu}^*}(s)\,\mathrm{e}^{-\mathrm{j}\dot{\alpha}\tau_\mathrm{d}} \,. \tag{3.7}$$

Since time delays belong to the class of partial differential equations they cannot be described by a finite state vector as is the case for ODEs. However they may be approximated by

$$\mathrm{e}^{-s\tau_\mathrm{d}} \approx \frac{1}{\left(1+\frac{\tau_\mathrm{d}}{\mathrm{n}}s\right)^\mathrm{n}} \,, \tag{3.8}$$

for a finite $\mathrm{n} \in \mathbb{Z}$, e. g. $n = 4$. A more accurate approximation is based on the *Padé-Approximation* [68]. The resulting transfer function with decoupling state feedback is

$$G_\mathrm{iv}(s) = \frac{\underline{i}_\mathrm{s}(s)}{\underline{\mathrm{v}}(s)} = \frac{\tau_\mathrm{c}}{\sigma L_\mathrm{s}} \frac{G_{\mathrm{uu}^*}}{1+\tau_\mathrm{c}s+\mathrm{j}\dot{\alpha}\tau_\mathrm{c}-\mathrm{j}\dot{\alpha}\tau_\mathrm{c}G_{\mathrm{uu}^*}} \,. \tag{3.9}$$

Figure 3.5 depicts the block diagram of the closed control loop of (3.9) under the action of static state feedback (3.4) and shows how dynamics are separated into a direct and quadrature component. Transfer function P denotes the plant dynamics of (3.5) and C the control law of (3.6). In the block diagram, it is indicated how coupling effects enter through plant and computational delays and correspondingly it becomes evident, that an attenuation of the approximated disturbances

$$d_\mathrm{d} = \frac{\sigma L_\mathrm{s}\dot{\alpha}\left(\sin\left(\dot{\alpha}\tau_\mathrm{d}\right)i_\mathrm{ds}+\cos\left(\dot{\alpha}\tau_\mathrm{d}\right)i_\mathrm{qs}\right)+\sin\left(\dot{\alpha}\tau_\mathrm{d}\right)u_\mathrm{qs}}{G'_{\mathrm{uu}^*}} \,, \tag{3.10}$$

$$d_\mathrm{q} = \frac{\sigma L_\mathrm{s}\dot{\alpha}\left(\sin\left(\dot{\alpha}\tau_\mathrm{d}\right)i_\mathrm{qs}-\cos\left(\dot{\alpha}\tau_\mathrm{d}\right)i_\mathrm{ds}\right)-\sin\left(\dot{\alpha}\tau_\mathrm{d}\right)u_\mathrm{ds}}{G'_{\mathrm{uu}^*}} \,, \tag{3.11}$$

are particularly relevant for the design process.

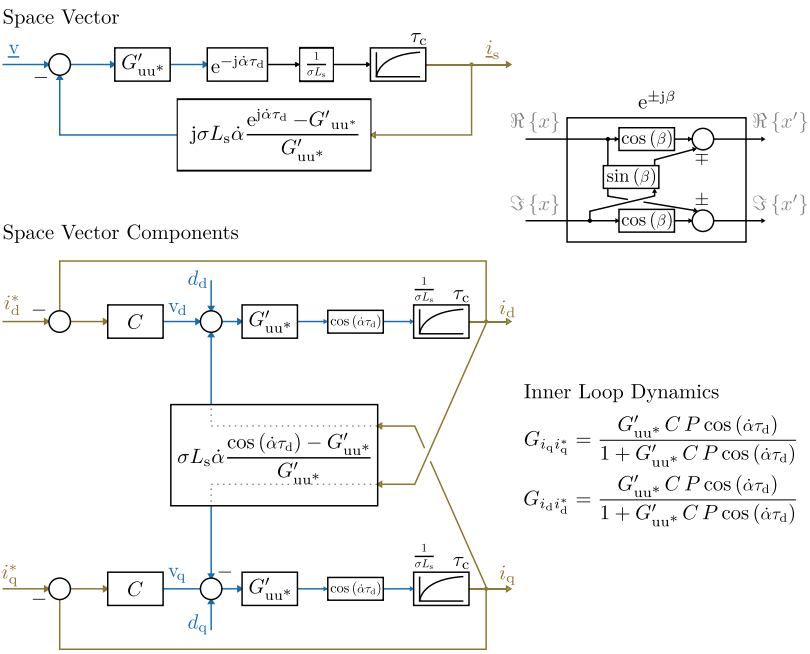

Figure 3.5: Field oriented control: current dynamics.

Another limiting aspect is the maximum voltage $u_{\mathrm{ub}} = a_{\mathrm{pwm}} 2/\pi u_{\mathrm{dc}}$, which can be attained by the PWM method. In case of a dynamic torque demand, the current controller will calculate an excessive phase voltage amplitude due to high current references. To avoid possible oscillations and windup effects, it is important to consider that $\hat{u} \leq u_{\mathrm{ub}}$. A classical anti-windup strategy, however, ignores the geometric relations of space vectors. Therefore an approach is anticipated, which respects the demands for decoupling and back EMF compensation as per (3.4) while considering the geometric possibilities. A dynamic response behavior can be further supported if it is possible to prioritize either field or torque generation and therefore recognize priorities of the individual components u_{ds} and u_{qs}. This leads to three splitting strategies

- u_{qs} has priority over u_{ds}: $u^*_{d,\mathrm{sat}} = \mathrm{sign}\,(u^*_{\mathrm{ds}}) \sqrt{u^2_{\mathrm{ub}} - u^{*\,2}_{\mathrm{qs}}}$,
- u_{ds} has priority over u_{qs}: $u^*_{q,\mathrm{sat}} = \mathrm{sign}\,(u^*_{\mathrm{qs}}) \sqrt{u^2_{\mathrm{ub}} - u^{*\,2}_{\mathrm{ds}}}$,

- phase correct limitation: $u^*_{d,\mathrm{sat}} = u^*_{\mathrm{ds}} \frac{u_{\mathrm{ub}}}{\sqrt{{u^*_{\mathrm{ds}}}^2 + {u^*_{\mathrm{qs}}}^2}}$, $u^*_{q,\mathrm{sat}} = u^*_{\mathrm{qs}} \frac{u_{\mathrm{ub}}}{\sqrt{{u^*_{\mathrm{ds}}}^2 + {u^*_{\mathrm{qs}}}^2}}$.

However, concerning the static state feedback (3.4) it is not always obvious which component should be prioritized. Possible splitting strategies are presented in [183], where for example the priority decision is characterized depending on whether the drive is in driving or regenerating mode. Which strategy is best suited is often unclear.

3.1.3 Torque and Flux Control

Based on the results shown in Figure 3.5, the current dynamics of the inner current control loop for either the d-axis or the q-axis is

$$G_{\mathrm{ii}^*}(s) = \frac{i_{.\mathrm{s}}(s)}{i^*_{.\mathrm{s}}(s)} = \frac{G'_{\mathrm{uu}^*}\left(k_{\mathrm{p,i}} s + k_{\mathrm{i,i}}\right) \tau_{\mathrm{c}} \cos\left(\dot{\alpha}\tau_{\mathrm{d}}\right)}{\sigma L_{\mathrm{s}} s \left(\tau_{\mathrm{c}} s + 1\right) + G'_{\mathrm{uu}^*}\left(k_{\mathrm{p,i}} s + k_{\mathrm{i,i}}\right) \tau_{\mathrm{c}} \cos\left(\dot{\alpha}\tau_{\mathrm{d}}\right)} \,. \tag{3.12}$$

Using (2.40), the plant model of the torque control loop is approximated by

$$G_{T_e \mathrm{i}^*}(s) = \frac{3}{2} Z_{\mathrm{p}} \frac{L_{\mathrm{m}}}{L_{\mathrm{r}}} \lambda_{\mathrm{r}} G_{\mathrm{ii}^*} \,, \tag{3.13}$$

where it is assumed that the rotor flux is nearly constant. It is clear, that the stationary gain of (3.13) decreases with a decreasing flux level. Finally, the open loop transfer function $G_{\lambda \mathrm{i}^*}$ for rotor flux control is obtained by a series connection of (3.12) with a first order system that is defined by (2.32)

$$G_{\lambda \mathrm{i}^*}(s) = \frac{\lambda_{\mathrm{r}}(s)}{i^*_{\mathrm{ds}}(s)} = \frac{L_{\mathrm{m}}}{\tau_{\mathrm{r}} s + 1} G_{\mathrm{ii}^*} \,. \tag{3.14}$$

The error dynamics of $e_\lambda = \lambda^*_{\mathrm{r}} - \hat{\lambda}_{\mathrm{r}}$ and $e_{\mathrm{te}} = T^*_{\mathrm{e}} - T_{\mathrm{e}}$ are stabilized via PI-controllers. These yield the closed loop dynamics of the IM

$$G_{\lambda\lambda *}(s) = \frac{\lambda_{\mathrm{r}}(s)}{\lambda^*_{\mathrm{r}}(s)} = \frac{\left(k_{\mathrm{p},\lambda} s + k_{\mathrm{i},\lambda}\right) L_{\mathrm{m}} G_{\mathrm{ii}^*}}{\left(\tau_{\mathrm{r}} s + 1\right) s + \left(k_{\mathrm{p},\lambda} s + k_{\mathrm{i},\lambda}\right) L_{\mathrm{m}} G_{\mathrm{ii}^*}} \,, \tag{3.15}$$

$$G_{T_e T_e *}(s) = \frac{T_{\mathrm{e}}(s)}{T^*_{\mathrm{e}}(s)} = \frac{\left(k_{\mathrm{p,te}} s + k_{\mathrm{i,te}}\right) 3 Z_{\mathrm{p}} L_{\mathrm{m}} \lambda_{\mathrm{r}} G_{\mathrm{ii}^*}}{2 L_{\mathrm{r}} s + \left(k_{\mathrm{p,te}} s + k_{\mathrm{i,te}}\right) 3 Z_{\mathrm{p}} \lambda_{\mathrm{r}} L_{\mathrm{m}} G_{\mathrm{ii}^*}} \,, \tag{3.16}$$

which describe the response behavior of the process outputs to the reference signals. The respective proportional and integral gains are $k_{\mathrm{p},\lambda}, k_{\mathrm{p,te}}$ and $k_{\mathrm{i},\lambda}, k_{\mathrm{i,te}}$. To reduce the control effort, it is advisable to feed forward the steady state values of the direct and quadrature current given by

$$i^{\mathrm{st}}_{\mathrm{ds}} = \frac{\lambda_{\mathrm{r}}}{L_{\mathrm{m}}} \,, \tag{3.17}$$

$$i^{\mathrm{st}}_{\mathrm{qs}} = \frac{2}{3} \frac{L_{\mathrm{r}}}{L_{\mathrm{m}}} \frac{T_{\mathrm{e}}}{Z_{\mathrm{p}} \lambda_{\mathrm{r}}} \,. \tag{3.18}$$

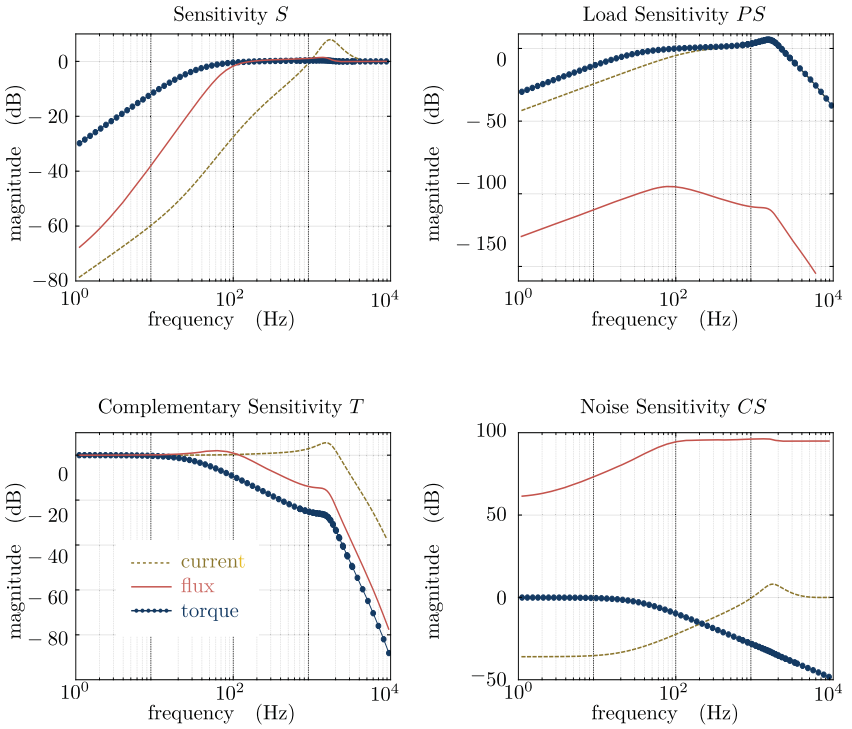

Figure 3.6: Closed loop electric drive module current, flux and torque dynamics.

The dynamic performance of the EDM is characterized by the sensitivity function S, the load sensitivity function PS, the complementary sensitivity function T, and the noise sensitivity function CS, for the closed loop of current (3.12), flux (3.15), and torque (3.16) control. These are shown in Figure 3.6 for an exemplary control design. The sensitive function S, on the upper left, captures the response behavior of the output to process noise, which enters at the output of the system, e. g. measurement noise. On the upper right the load sensitivity PS characterizes the response of the output to load disturbances, for example (3.10). The magnitude of the complementary sensitivity T, in the lower left corner, describes both the response of the output to the reference, and the response of the input to a load disturbance. The magnitude of the noise sensitivity CS shows how the process input reacts to the reference or to the process noise. The inner current control loop is designed for the maximum possible bandwidth, while the outer torque loop is designed for a bandwidth, which is slower

than the inner loop by a factor of 20. The flux control is designed according to the symmetrical optimum [6, 203]. A more detailed analysis of the control performance in the time domain follows in Section 3.3.

3.2 Efficiency Optimized FOC

In FOC the flux in the air-gap is conventionally maintained at a high level which is in general limited by two main factors. Firstly, below the base speed, near 300 rad/s, in the region of

$$\mathcal{X}_{\mathrm{sat}} = \{\lambda_{\mathrm{r}}, T_{\mathrm{e}}, \omega_{\mathrm{m}} \in \mathbb{R}_+ \times \mathcal{O}_{\mathrm{edm}} |\, \lambda_{\mathrm{r}} = \lambda_{\mathrm{ub}}\} \,, \tag{3.19a}$$

(see Figure 3.7), the flux is bounded from above by λ_{ub} due to saturation of the iron core. Secondly, above base speed in the region of

$$\mathcal{X}_{\mathrm{volt}} = \left\{\lambda_{\mathrm{r}}, T_{\mathrm{e}}, \omega_{\mathrm{m}} \in \mathbb{R}_+ \times \mathcal{O}_{\mathrm{edm}} |\, \hat{u} = a_{\mathrm{pwm}} \frac{2}{\pi} u_{\mathrm{dc}}\right\} \,, \tag{3.19b}$$

the flux is limited by the DC-link voltage and the corresponding maximum phase voltage of the chosen PWM method. Technical requirements, for example on the winding insulation, may demand a compliance with an upper current limit $\hat{i}_{\mathrm{ub}}$ within

$$\mathcal{X}_{\mathrm{cur}} = \left\{\lambda_{\mathrm{r}}, T_{\mathrm{e}}, \omega_{\mathrm{m}} \in \mathbb{R}_+ \times \mathcal{O}_{\mathrm{edm}} |\, \hat{i} = \hat{i}_{\mathrm{ub}}\right\} \,. \tag{3.19c}$$

In the case of regenerative braking, the current limit becomes relevant, if the battery is almost fully charged.
Storing a high amount of energy in the coupling field improves the dynamic performance and damping properties of the IM which is roughly explained by the fact that a sudden torque demand only involves a slight adjustment in the quadrature current component i_{qs}. However, in partial-load areas

$$\mathcal{X}_{\mathrm{pl}} = \left\{\lambda_{\mathrm{r}}, T_{\mathrm{e}}, \omega_{\mathrm{m}} \in \mathbb{R}_+ \times \mathcal{O}_{\mathrm{edm}} |\, \lambda_{\mathrm{lb}} \leq \lambda_{\mathrm{r}} < \lambda_{\mathrm{ub}} \wedge \hat{u} < a_{\mathrm{pwm}} \tfrac{2}{\pi} u_{\mathrm{dc}} \wedge \hat{i} < \hat{i}_{\mathrm{ub}}\right\} \,, \tag{3.19d}$$

the prerequisite of a high flux level, leads to a poor EDM efficiency as iron losses are not ideally balanced against conduction losses of the motor and converter. To achieve maximum efficiency, the flux level at part load is substantially reduced. However, reducing the flux level results in an increased delay when a transient torque command requires more increase. Therefore, a minimum flux λ_{lb} is maintained during idling.

An optimized flux reduction based on the relation between two independent motor variables can be expressed. One is used to balance the power loss while the other maintains the mechanical output power at the desired operating point $(\omega_{\mathrm{m}}, T_{\mathrm{e}})$. Early investigations have chosen the stator voltage and slip [113] to derive analytical formulations for the problem of loss minimization, while others used the stator

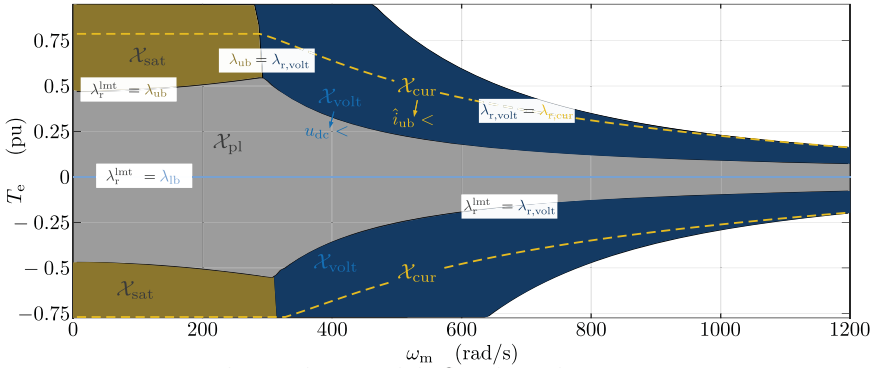

Figure 3.7: Electric drive module flux dependent operating regions.

currents instead of voltages [107] or the magnetizing air-gap flux instead of the slip frequency [111]. More recently attention has focused on accurate representations of loss processes as well as on the consideration of technical limitations for example due to the maximum voltage (3.19b) [242]. The following analysis uses the rotor flux $\lambda_r \in \mathbb{R}_+$ and electromagnetic torque $T_e \in \mathbb{R}$ as independent motor variables to pose the problem of optimized flux reduction within the feasible set of

$$\mathcal{X}_{IM} = \mathcal{X}_{sat} \cup \mathcal{X}_{volt} \cup \mathcal{X}_{cur} \cup \mathcal{X}_{pl} \,. \tag{3.19e}$$

The natural choice of independent variables with respect to FOC and the operating range $\mathcal{O}_{edm}$ allows for a more intuitive interpretation and straight forward implementation of optimization results. This choice is only made possible by the flat system representation of the IM, which is introduced in the upcoming section.

3.2.1 Loss Minimizing Control

The problem of loss minimization is described by the constrained nonlinear optimization problem

$$P_{l,im}^{st*}(T_e, \omega_m) = \min_{\lambda_r \in \mathcal{X}_{IM}^{st}} P_{l,im}^{st}(\lambda_r, T_e, \omega_m) \,, \tag{3.20}$$

where $\mathcal{X}_{IM}^{st}$ represents the feasible set (3.19e) for steady state operating conditions [158]. Using the square of the current and voltage peak value to define feasible regions of $\mathcal{X}_{IM}$

$$\left(a_{pwm}\frac{2}{\pi}u_{dc}\right)^2 - \hat{u}^2(\lambda_r, T_e, \omega_m) \geq 0 \,, \tag{3.21a}$$

$$\hat{i}_{ub}^2 - \hat{i}^2(\lambda_r, T_e, \omega_m) \geq 0 \,, \tag{3.21b}$$

the Lagrangian function of problem (3.20) is defined as

$$L = \left(\begin{array}{c} P^{\mathrm{st}}_{\mathrm{l,im}}\left(\lambda_{\mathrm{r}}, T_{\mathrm{e}}, \omega_{\mathrm{m}}\right) - \mu_1\left(\lambda_{\mathrm{r}} - \lambda_{\mathrm{lb}}\right) - \mu_2\left(\lambda_{\mathrm{ub}} - \lambda_{\mathrm{r}}\right) - \\ \mu_3\left(a^2_{\mathrm{pwm}}\frac{4}{\pi^2}u^2_{\mathrm{dc}} - \hat{u}^2\left(\lambda_{\mathrm{r}}, T_{\mathrm{e}}, \omega_{\mathrm{m}}\right)\right) - \mu_4\left(\hat{i}^2_{\mathrm{ub}} - \hat{i}^2\left(\lambda_{\mathrm{r}}, T_{\mathrm{e}}, \omega_{\mathrm{m}}\right)\right) \end{array} \right) . \tag{3.22}$$

The scalar quantities $\mu_{\mathrm{i}} \in \mathbb{R}_+$, $\mathrm{i} \in \mathcal{I} = 1(1)4$ are called the Lagrange multipliers.

It is easily verified, that the second order partial derivative of the objective w.r.t the rotor flux is positive definite and that the corresponding derivative of the current constraint is positive definite for $|T_{\mathrm{e}}| > 0$, rendering both convex. In the case of driving operation with $T_{\mathrm{e}} \geq 0$, the same applies for the square value of the phase voltage. For regenerative braking $T_{\mathrm{e}} < 0$, the phase voltage unfortunately is not convex.

Every local minimum $\lambda^*_{\mathrm{r}}, \boldsymbol{\mu}^*$ of (3.20) has to satisfy the first-order necessary conditions or *Karush-Kuhn-Tucker* (KKT) conditions

$$\left.\frac{\partial L}{\partial \lambda_{\mathrm{r}}}\right|_{\lambda^*_{\mathrm{r}}, \boldsymbol{\mu}^*} = 0\,, \tag{3.23a}$$

$$\left.\frac{\partial L}{\partial \mu_{\mathrm{i}}}\right|_{\lambda^*_{\mathrm{r}}} \geq 0\,, \quad \forall \mathrm{i} \in \mathcal{I}\,, \tag{3.23b}$$

$$\mu^*_{\mathrm{i}} \geq 0\,, \quad \forall \mathrm{i} \in \mathcal{I}\,, \tag{3.23c}$$

$$\mu^*_{\mathrm{i}} \left.\frac{\partial L}{\partial \mu_{\mathrm{i}}}\right|_{\lambda^*_{\mathrm{r}}} = 0\,, \quad \forall \mathrm{i} \in \mathcal{I}\,. \tag{3.23d}$$

Since the problem is convex, in the case of driving, each local minimum is also a global solution. In the case of regenerative braking, multiple local solutions may exist. At this stage, it is assumed that *Linear Independent Constraint Qualification* (LICQ) holds at the optimum. This means that the gradients of the active constraint are linearly independent. In this case, only one of the four constraints (3.19e) can be active, since λ^*_{r} is clearly determined by the active constraint. In other words, at the most one Lagrange multiplier is nonzero which leaves four options

- $\lambda^*_{\mathrm{r}} = \lambda^{\mathrm{lmt}}_{\mathrm{r}} \in \mathcal{X}^{\mathrm{st}}_{\mathrm{pl}}$ is the solution of the unconstrained problem ($\mu^*_{\mathrm{i}} = 0$, $\forall \mathrm{i} \in \mathcal{I}$),
- λ^*_{r} is equal to either the lower bound λ_{lb} or upper bound λ_{ub} ($\mu^*_1 \neq 0 \vee \mu^*_2 \neq 0$),
- $\lambda^*_{\mathrm{r}} = \lambda_{\mathrm{r,volt}} \in \mathcal{X}^{\mathrm{st}}_{\mathrm{volt}}$ is limited by the maximum voltage ($\mu^*_3 \neq 0$),
- $\lambda^*_{\mathrm{r}} = \lambda_{\mathrm{r,cur}} \in \mathcal{X}^{\mathrm{st}}_{\mathrm{cur}}$ is limited by the maximum current ($\mu^*_4 \neq 0$).

The solution for the unconstrained problem, derived from (3.23a), is

$$\lambda^{\mathrm{lmt}}_{\mathrm{r}} = \left(\frac{4}{9} \frac{R_{\mathrm{r}} L^2_{\mathrm{m}} + R_{\mathrm{s}} L^2_{\mathrm{r}}}{R_{\mathrm{s}} + \dfrac{\left(L_{\mathrm{m}} Z_{\mathrm{p}} \omega_{\mathrm{m}}\right)^2}{R_{\mathrm{fe}}}} \frac{T^2_{\mathrm{e}}}{Z^2_{\mathrm{p}}} \right)^{0.25} . \tag{3.24}$$

The problem of finding the solution at the maximum attainable voltage $\mathcal{X}^{\mathrm{st}}_{\mathrm{volt}}$ as per (2.45g) and (3.23b) translates to a problem of finding the positive real roots $x \in \mathbb{R}_+$ of the fourth order polynomial

$$0 = \left(\frac{4}{9} R_{\mathrm{r}}^2 \frac{T_{\mathrm{e}}^2}{Z_{\mathrm{p}}^2}\, x^2 + \frac{4}{3} R_{\mathrm{r}} T_{\mathrm{e}} \omega_{\mathrm{m}}\, x + \frac{(L_{\mathrm{s}} R_{\mathrm{r}})^2 + 2 R_{\mathrm{r}} R_{\mathrm{s}} L_{\mathrm{m}}^2 + (L_{\mathrm{r}} R_{\mathrm{s}})^2}{(\sigma L_{\mathrm{s}} L_{\mathrm{r}})^2} + (Z_{\mathrm{p}} \omega_{\mathrm{m}})^2 \right) \frac{T_{\mathrm{e}}^2}{Z_{\mathrm{p}}^2}\, x^2 + 3 \left(\frac{\left(L_{\mathrm{s}}^2 R_{\mathrm{r}} + L_{\mathrm{m}}^2 R_{\mathrm{s}}\right)}{(\sigma L_{\mathrm{s}} L_{\mathrm{r}})^2} T_{\mathrm{e}} \omega_{\mathrm{m}} - 3 \left(\frac{L_{\mathrm{m}} a_{\mathrm{pwm}}}{\sigma L_{\mathrm{s}} L_{\mathrm{r}} \pi} \right)^2 u_{\mathrm{dc}}^2 \right) x + \frac{9}{4} \frac{R_{\mathrm{s}}^2 + (L_{\mathrm{s}} Z_{\mathrm{p}} \omega_{\mathrm{m}})^2}{(\sigma L_{\mathrm{s}} L_{\mathrm{r}})^2}\,, \tag{3.25a}$$

which leads to

$$\lambda_{\mathrm{r,volt}} = 1/\sqrt{x}\,. \tag{3.25b}$$

An efficient iterative approach to the solution of (3.25), is a damped Newton's method with the initial guess of (3.24).

For understanding the influence of the current limit in the region of $\mathcal{X}^{\mathrm{st}}_{\mathrm{cur}}$, see the second graph of Figure 3.8. The phase current peak value monotonously increases into the direction of an increasing power output $P_{\mathrm{m}} = T_{\mathrm{e}} \omega_{\mathrm{m}}$. A strict limit on $\hat{i}_{\mathrm{ub}}$ leads to a shift of the line, that is defined by $\mathcal{X}^{\mathrm{st}}_{\mathrm{cur}} \cap \mathcal{X}^{\mathrm{st}}_{\mathrm{IM}}$, into the direction of a reduced power output. This line determines the maximum torque rating $T_{\mathrm{e,ub}}$ generally given by

$$\lambda_{\mathrm{r,cur}}, T_{\mathrm{e,ub}} = \underset{\lambda_{\mathrm{r}}, T_{\mathrm{e}} \in \mathcal{X}^{\mathrm{st}}_{\mathrm{IM}}}{\operatorname{argmax}} \; T_{\mathrm{e}}\,, \tag{3.26a}$$

for driving operations. In the case of regenerative braking, the minimum rating $T_{\mathrm{e,lb}}$ is defined by

$$\lambda_{\mathrm{r,cur}}, T_{\mathrm{e,lb}} = \underset{\lambda_{\mathrm{r}}, T_{\mathrm{e}} \in \mathcal{X}^{\mathrm{st}}_{\mathrm{IM}}}{\operatorname{argmin}} \; T_{\mathrm{e}}\,. \tag{3.26b}$$

If no current limit is set, $T_{\mathrm{e,ub}}$ and $T_{\mathrm{e,lb}}$ are solely defined by the feasible region of $\mathcal{X}^{\mathrm{st}}_{\mathrm{volt}}$. With an initialization of (3.24) and an arbitrary initial guess for T_{e}, problem (3.26) is readily solved with an appropriate numerical optimization method, for example the *Interior Point Optimizer* (IPOPT) [239].

The boundaries of the solution regions, on which the LICQ is violated, are shown in Figure 3.7. They are defined by the roots $T_{\mathrm{e}} \in \mathbb{R}$ of

$$\begin{aligned} \lambda_{\mathrm{r}}^{\mathrm{lmt}} = \lambda_{\mathrm{lb}}, \quad \lambda_{\mathrm{r}}^{\mathrm{lmt}} = \lambda_{\mathrm{ub}}, \quad \lambda_{\mathrm{r}}^{\mathrm{lmt}} = \lambda_{\mathrm{r,volt}} \\ \lambda_{\mathrm{r,volt}} = \lambda_{\mathrm{ub}}, \quad \lambda_{\mathrm{r,volt}} = \lambda_{\mathrm{r,cur}}\,, \end{aligned} \tag{3.27}$$

and are expressed as a function of speed ω_{m}. The indicated vectors in Figure 3.7 show how these boundaries are shifted for a decreasing current limit $\hat{i}_{\mathrm{ub}}$ and a reduced DC-link voltage u_{dc}.

Algorithm 1 : Efficiency Optimized Flux Strategy

Require: IM parameter, voltage range a_{pwm}, lower and upper flux bound $\lambda_{\mathrm{lb}}, \lambda_{\mathrm{ub}}$.

1: **procedure** $\lambda_{\mathrm{r}}^{*}(u_{\mathrm{dc}}, \hat{i}_{\mathrm{ub}}, \omega_{\mathrm{m}}, T_{\mathrm{e}})$
2: $\quad \lambda_{\mathrm{r}} \leftarrow \lambda_{\mathrm{r}}^{\mathrm{lmt}}$ ▷ compute unconstrained solution (3.24).
3: $\quad \lambda_{\mathrm{r}} \leftarrow \max\{\lambda_{\mathrm{lb}}, \min\{\lambda_{\mathrm{r}}, \lambda_{\mathrm{ub}}\}\}$ ▷ limit flux to upper or lower bound.
4: $\quad \hat{u}_{\mathrm{ub}} \leftarrow a_{\mathrm{pwm}} \frac{2}{\pi} u_{\mathrm{dc}}$ ▷ max. attainable voltage range.
5: $\quad \hat{u} \leftarrow \hat{u}^{\mathrm{st}}(\omega_{\mathrm{m}}, T_{\mathrm{e}}, \lambda_{\mathrm{r}})$ ▷ compute phase voltage at operating point (2.45g).
6: $\quad$ **if** $\hat{u} > \hat{u}_{\mathrm{ub}}$ **then** ▷ check if phase voltage exceeds the max. voltage.
7: $\quad\quad \lambda_{\mathrm{r}} \leftarrow \lambda_{\mathrm{r,volt}}$ ▷ solve (3.25).
8: $\quad\quad \hat{u} \leftarrow \hat{u}^{\mathrm{st}}(\omega_{\mathrm{m}}, T_{\mathrm{e}}, \lambda_{\mathrm{r}})$ ▷ update phase voltage at new iterate (2.45g).
9: $\quad$ **end if**
10: $\quad \hat{i} \leftarrow \hat{i}^{\mathrm{st}}(T_{\mathrm{e}}, \lambda_{\mathrm{r}})$ ▷ compute phase current at operating point (2.45f).
11: $\quad$ **if** $\hat{i} > \hat{i}_{\mathrm{ub}}$ or $\hat{u} > \hat{u}_{\mathrm{ub}}$ **then** ▷ check current and voltage limits.
12: $\quad\quad \lambda_{\mathrm{r}}, T_{\mathrm{e}} \in [T_{\mathrm{e,lb}}, T_{\mathrm{e,ub}}] \leftarrow$ (3.26) ▷ solve (3.26) to limit torque.
13: $\quad$ **end if**
14: $\quad$ **return:** $\lambda_{\mathrm{r}}, T_{\mathrm{e}}, \quad (T_{\mathrm{e,lb}}, T_{\mathrm{e,ub}})$

It can be shown that within the operating region of $\mathcal{X}_{\mathrm{volt}}^{\mathrm{st}}$, the flux constrained by the maximum voltage is smaller than the unconstrained flux $\lambda_{\mathrm{r,volt}} < \lambda_{\mathrm{r}}^{\mathrm{lmt}}$, whereas in the region of $\mathcal{X}_{\mathrm{pl}}^{\mathrm{st}}$ the converse is true $\lambda_{\mathrm{r,volt}} > \lambda_{\mathrm{r}}^{\mathrm{lmt}}$. An optimal flux reduction strategy is thus formulated as

$$\lambda_{\mathrm{r}}^{*} = \max\left\{\lambda_{\mathrm{lb}}, \min\left\{\lambda_{\mathrm{r,volt}}, \lambda_{\mathrm{r}}^{\mathrm{lmt}}, \lambda_{\mathrm{ub}}\right\}\right\}. \tag{3.28}$$

Summarizing the above results, a practical flux strategy is implemented in Algorithm 1. Apart from computing the optimal flux level, this procedure also bounds the torque by the minimum or maximum torque rating $T_{\mathrm{e,lb}}, T_{\mathrm{e,ub}}$. If required, these bounds can be computed independently of the if condition in line 11 and provided as return values. The electrical and magnetic states computed for this LMT are depicted in Figure 3.8. From top to bottom, the graphs show the rotor flux magnitude, the phase current peak value, the phase voltage peak value and the EDM power loss for regenerative braking and driving operation. Torque and power loss values are indicated in the *per unit system* (pu). Within the partial load area (3.19d), the flux is gradually increased with rising torque magnitude, whereas the flux is slightly reduced if the speed increases.

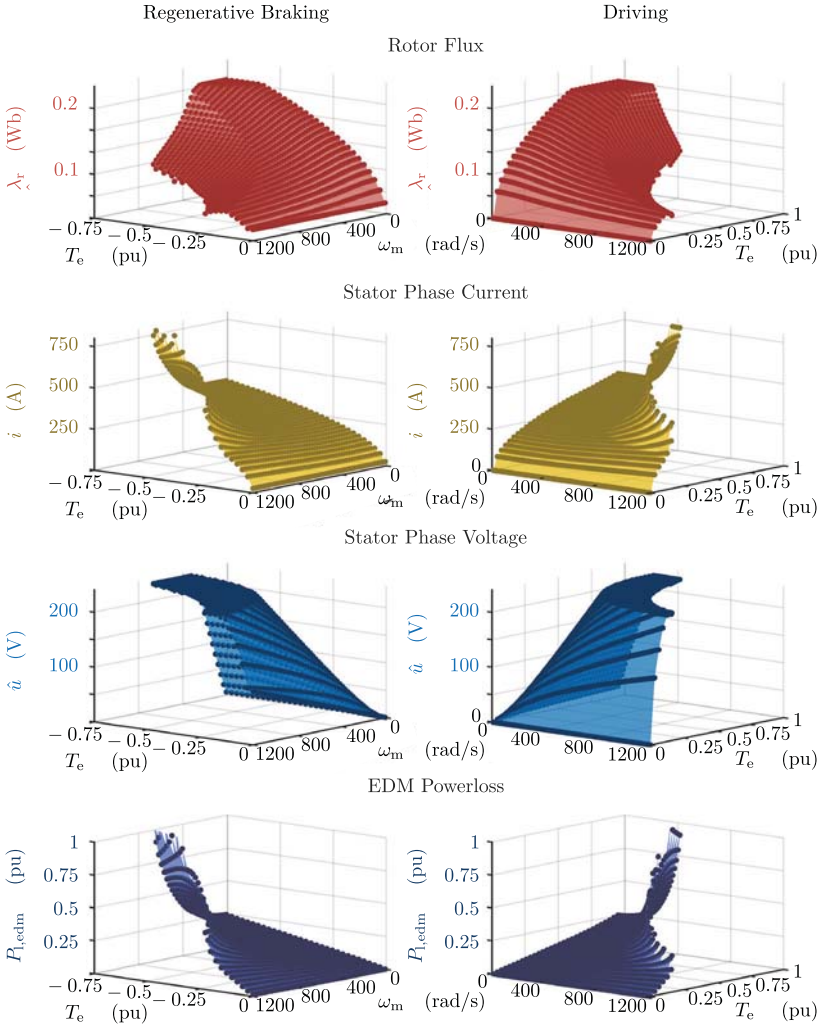

Figure 3.8: Current, voltage and power loss characteristics for the loss minimizing field strategy.

3.2.2 Maximum Torque Per Ampere/Volt

Various alternative strategies for flux reduction have been proposed in the literature. The most common strategy is known as MTPA. Instead of minimizing the power loss, the objective of MTPA is to minimize the phase current according to

$$\hat{i}^{\mathrm{st}*}\left(T_{\mathrm{e}},\omega_{\mathrm{m}}\right)=\min_{\lambda_{\mathrm{r}}\in\mathcal{X}_{\mathrm{IM}}^{\mathrm{st}}}\hat{i}^{\mathrm{st}}\left(\lambda_{\mathrm{r}},T_{\mathrm{e}},\omega_{\mathrm{m}}\right)\,. \tag{3.29}$$

Following the same line of argumentation as for the previously discussed LMT, the solution of problem (3.29) is

$$\lambda_{\mathrm{r}}^{*}=\max\left\{\lambda_{\mathrm{lb}}\,,\min\left\{\lambda_{\mathrm{r,volt}}\,,\lambda_{\mathrm{r}}^{\mathrm{mtpa}}\,,\lambda_{\mathrm{ub}}\right\}\right\}\,, \tag{3.30}$$

where the unconstrained solution is

$$\lambda_{\mathrm{r}}^{\mathrm{mtpa}}=\left(\frac{4}{9}L_{\mathrm{r}}^{2}\frac{T_{\mathrm{e}}^{2}}{Z_{\mathrm{p}}^{2}}\right)^{0.25}\,. \tag{3.31}$$

Algorithm 1 is modified to follow an MTPA strategy by simply replacing the unconstrained solution for the LMT in the second line with (3.31).

The relative difference

$$\epsilon_{\{\lambda,i,u,P_l\}}\frac{\left\{\lambda_{\mathrm{r}},\hat{i},\hat{u},P_{\mathrm{l,edm}}\right\}\big|_{\{\mathrm{MTPA,MTPV}\}}}{\left\{\lambda_{\mathrm{r}},\hat{i},\hat{u},P_{\mathrm{l,edm}}\right\}\big|_{\mathrm{LMT}}} \tag{3.32}$$

between MTPA and the LMT for the rotor flux, stator current, stator voltage and EDM power loss is displayed in the left column of Figure 3.9. While not being symmetric, the relative difference for the driving operation is similar to the shown results. Looking at (3.31), a distinguishing characteristic of the unconstrained MTPA strategy is that the rotor flux is not speed dependent. At the rotor speed of

$$\omega_{\mathrm{m}}=\frac{1}{Z_{\mathrm{p}}}\frac{\sqrt{R_{\mathrm{r}}R_{\mathrm{fe}}}}{L_{\mathrm{r}}}\,. \tag{3.33}$$

both strategies are identical. Below (3.33), in the partial load area, the rotor flux magnitude of MTPA is reduced by up to 13 % compared to the LMT. Above (3.33), the rotor flux almost linearly increases well over 40 % of the loss minimizing solution. Comparing the stator phase voltage, the results are very similar, contrary to the phase current where the proportion is well under 90 % for the maximum speed and under 98 % at standstill. Overall, the power loss is higher for MTPA in comparison to the LMT, except in the case of a view operating points. Since VSI losses are not considered in the derivation of the optimal flux level, these points near zero torque show a reduced loss mainly due to the lower current magnitude and the resulting

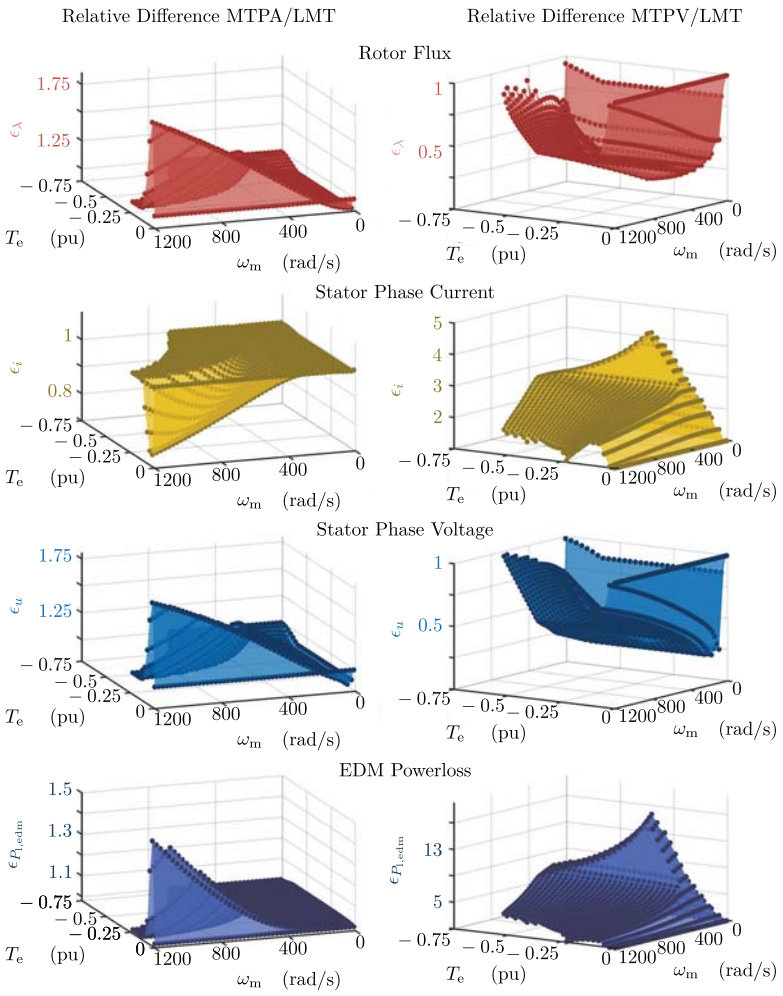

Figure 3.9: Relative difference of maximum torque per ampere (MTPA) and maximum torque per volt (MTPV) compared to the loss minimizing technique (LMT) for regenerative braking.

drop in switching losses. Based on the average value model presented in Section 2.1, VSI losses are easily incorporated into the LMT problem formulation. However, the differences of the obtained flux level are marginal for the considered application and are for this reason not further discussed.

In the case of regenerative braking, it makes sense to consider a different objective in order to improve the overall efficiency. Instead of minimizing the EDM power loss, it is desirable to increase the DC-link current, which in effect leads to a higher charge rate of the battery. One possibility to increase the charge rate is to follow a strategy which can be described as *Maximum Torque Per Volt* (MTPV). Since the minimum voltage will cause a high phase current, provided that the output power is kept constant, this strategy can be seen as the counterpart to MTPA. In this sense, the problem is redefined as

$$\min_{\lambda_\mathrm{r} \in \mathcal{X}_\mathrm{IM}^\mathrm{st}} \hat{u}^\mathrm{st}\left(\lambda_\mathrm{r}, T_\mathrm{e}, \omega_\mathrm{m}\right) . \tag{3.34}$$

Due to the complex form of (2.45g), there is no closed form of the unconstrained solution, but it is implicitly given by a higher order polynomial function. Nevertheless, the problem is solved using IPOPT which converges for an arbitrary choice of an initial guess. Despite the markedly higher power loss of MTPV, it is observed in Figure 3.9, that the phase current is well above the magnitude obtained for the other strategies. Since the phase current is rectified via the VSI and impressed to the battery, this eventually leads to a higher charge rate. However, the main problem of MTPV, as presented in Figure 3.9, is the resulting low flux level and the consequential poor transient performance. Even though this consideration is only theoretical in nature, it shows that a reduction beyond (3.28) and (3.30) can improve the charge rate. Moreover, a MTPV like strategy might be interesting for thermal conditioning through a systematic increase of the overall EDM loss, which for low speeds could be up to ten times higher and for high speeds still double in comparison to an LMT.

3.2.3 Validation of BEV Control Strategies

Even if the access to internal control functions is restricted, the field strategy can be validated by consulting characteristic loss maps of the IM. Given the model parameter, the expression of the stationary power loss (2.45e) is used to derive the rotor flux in a least square manner. For every operating point considered in the characteristic loss map, the rotor flux is computed by solving

$$\lambda_\mathrm{r}\left(\omega_\mathrm{m}, T_\mathrm{e}\right) = \underset{\lambda_\mathrm{r}>0}{\operatorname{argmin}} \left(P_{\mathrm{l,im}}\big|_\mathrm{map} - P_{\mathrm{l,im}}\big|_\mathrm{mdl} \right)^2 . \tag{3.35}$$

The first term, $P_{\mathrm{l,im}}|_\mathrm{map}$, denotes the empirically determined IM loss and the second term, $P_{\mathrm{l,im}}|_\mathrm{mdl}$, is computed by the analytical expression defined in (2.45e). Figure 3.10

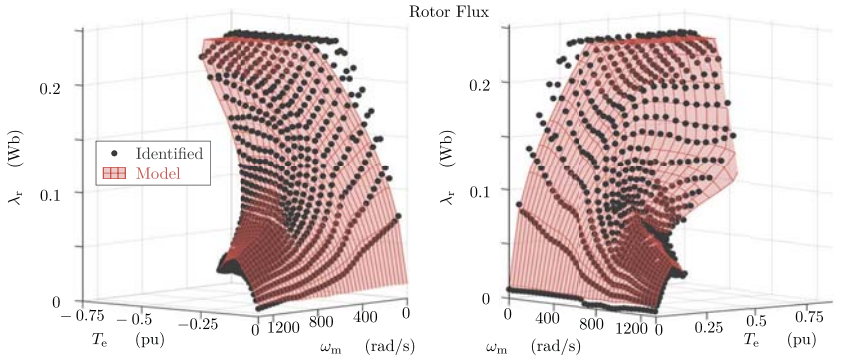

Figure 3.10: Comparison of the modeled rotor flux and the flux level identified from the induction motor loss map.

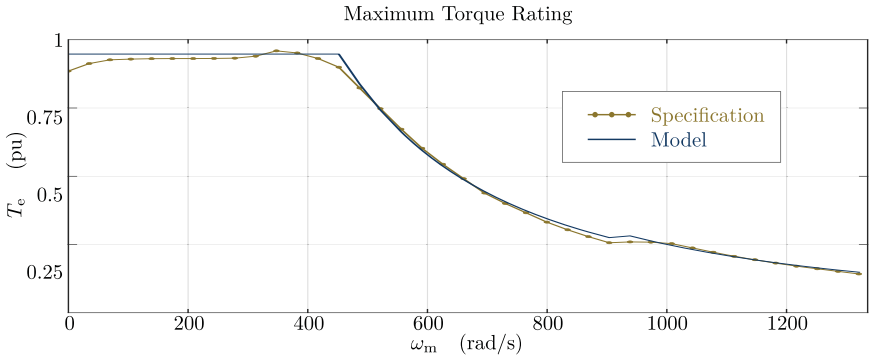

Figure 3.11: Comparison of modeled and specified maximum torque rating.

compares the results of (3.35) with the modeled flux of Algorithm 1. The resemblance confirms the assumption that the EDM employs a flux strategy similar to a LMT. Moreover, EDM loss maps, which are important performance quantifiers of energy management strategies, can be represented by the IM model up to almost any accuracy over the entire operational range, if the flux level is computed by means of a characteristic map derived from (3.35).

The most important performance quantifier of an EDM is the torque rating. Therefore,

it is essential that Algorithm 1 can accurately represent the maximum attainable torque. Figure 3.11 compares the specified rating of the motor manufacturer with the modeled results. At 900 rad/s, a different PWM method is used with a higher voltage range, which, in turn, leads to an increased torque capability. From Figure 3.11 it is concluded that the voltage dependency as well as the overall characteristics are well represented by the model-based approach. In practice, the minimum and maximum torque ratings are represented by characteristic curves $T_{\mathrm{e,whl,ub}}, T_{\mathrm{e,whl,lb}}$ as a function of the vehicle speed. These have to be identified for different voltage levels. Interpolating between these characteristics is only partially accurate. The model-based approach is thus more generally applicable.

3.3 Flatness Based Control

This section introduces a new flat output for an IM that presents a more intuitive choice for vehicle applications compared to existing definitions [140, 141]. The proposition of the flat output is

- the rotor flux magnitude λ_{r},
- the electromagnetic torque T_{e},
- and the rotor speed ω_{m},

which is a natural choice in the context of FOC and BEV motion control. It has to be noted that the rotor flux magnitude and electromagnetic torque have been previously mentioned as flat outputs in [216]. However, no evidence other than the already mentioned references [47, 140, 141] is provided nor is it clear how the load torque, which is used in the definition of the state- and input-parametrization is determined. Defining the flat output as

$$\boldsymbol{z} = (\lambda_{\mathrm{r}}\ T_{\mathrm{e}}\ \omega_{\mathrm{m}}) \tag{3.36}$$

for an augmented system, these issues are avoided.

As originally presented in [192] and discussed in Section 2.2, the nonlinear state space model (2.32) is of the general form

$$\dot{\boldsymbol{x}} = f\,(t, \boldsymbol{x}) + g_{\mathrm{d}}(\boldsymbol{x})u_{\mathrm{ds}} + g_{\mathrm{q}}(\boldsymbol{x})u_{\mathrm{qs}} \tag{3.37}$$

where the state vector $\boldsymbol{x} \in X \subset \mathbb{R}^3$ on manifold X is equal to $\boldsymbol{x} = (i_{\mathrm{ds}}\, i_{\mathrm{qs}}\, \lambda_{\mathrm{r}})$ and where the vector fields $f, g_{\mathrm{d}}, g_{\mathrm{q}}$ are obviously defined according to (2.32). The time variance of (3.37) is due to the rotor speed ω_{m} which is governed by the vehicle longitudinal dynamics and in general is also influenced by the drivetrain dynamics. Many properties of time-invariant systems do not extend to time varying systems, which is why these are often augmented by an additional differential equation for the

evolution of time $\dot{t} = 1$ so that well established analysis methods of time-invariant nonlinear input affine systems can be applied. The central idea of the proof however, is to augment (2.32) via a general representation of speed dynamics

$$\underbrace{\begin{bmatrix}\dot{\tilde{\boldsymbol{x}}}\\ \dot{\omega}_\mathrm{m}\end{bmatrix}}_{=\dot{\tilde{\boldsymbol{x}}}} = \underbrace{\begin{bmatrix}f\left(\tilde{\boldsymbol{x}}\right)\\ f_\omega\left(\tilde{\boldsymbol{x}}\right)\end{bmatrix}}_{=\tilde{f}(\tilde{\boldsymbol{x}})} + \underbrace{\begin{bmatrix}g_\mathrm{d}\left(\tilde{\boldsymbol{x}}\right)\\ 0\end{bmatrix}}_{=\tilde{g}_\mathrm{d}(\tilde{\boldsymbol{x}})} u_\mathrm{ds} + \underbrace{\begin{bmatrix}g_\mathrm{q}\left(\tilde{\boldsymbol{x}}\right)\\ 0\end{bmatrix}}_{=\tilde{g}_\mathrm{q}(\tilde{\boldsymbol{x}})} u_\mathrm{qs} + g_\omega(\tilde{\boldsymbol{x}}) u_\omega \,, \tag{3.38}$$

by introducing a new external input or disturbance $u_\omega \in \mathbb{R}$ and influencing vector fields f_ω and g_ω. Consequently, it is assumed that the rotor speed is governed by a nonlinear input affine system. In its simplest form, this system is derived by Euler's second law of motion so that f_ω accounts for the electromagnetic torque and a possible nonlinear friction term and g_ω is equal to the reciprocal of the rotational inertia. In this case as well as in more detailed considerations, u_ω is equal to the load torque. Since the load torque is an arbitrary external disturbance, it is unknown. However for the derivation of the IM's state- and input parametrization, f_ω, g_ω and u_ω do not have to be known explicitly.
The augmented system (3.38) is diferentially flat if and only if there exists a mapping Ψ_z with a rank equal to the number of independent inputs, which maps the states $\tilde{\boldsymbol{x}}$, the inputs $u_\mathrm{ds}, u_\mathrm{qs}, u_\omega$ and a finite number of derivatives of the inputs onto the flat output so that

$$\boldsymbol{z} = \Psi_\mathrm{z}\left(\tilde{\boldsymbol{x}}, u_\mathrm{ds}, \dot{u}_\mathrm{ds}, .., u_\mathrm{ds}^{(\mathrm{r}_1)}, u_\mathrm{qs}, \dot{u}_\mathrm{qs}.., u_\mathrm{qs}^{(\mathrm{r}_2)}, u, \dot{u}_\omega, .., u_\omega^{(\mathrm{r}_3)}\right) . \tag{3.39}$$

The notation $v^{(\mathrm{r})}$ indicates the time derivative of variable $v \in \mathbb{R}$ up to the order $\mathrm{r} \in \mathbb{Z}$. This mapping is given by

$$\Psi_\mathrm{z} = \begin{bmatrix}\lambda_\mathrm{r}\\ T_\mathrm{e}\\ \omega_\mathrm{m}\end{bmatrix} = \begin{bmatrix}\lambda_\mathrm{r}\\ \frac{3}{2} Z_\mathrm{p} \frac{L_\mathrm{m}}{L_\mathrm{r}} \lambda_\mathrm{r} i_\mathrm{qs}\\ \omega_\mathrm{m}\end{bmatrix}, \tag{3.40}$$

which only depends on the system states. Furthermore, there has to be a state-parametrization Ψ_x of rank four and input-parametrization Ψ_u of rank three which define the algebraic relation between the flat output, its time derivatives, the states and the inputs according to

$$\tilde{\boldsymbol{x}} = \Psi_\mathrm{x}\left(\lambda_\mathrm{r}, \dot{\lambda}_\mathrm{r}, .., \lambda_\mathrm{r}^{(\mathrm{r}_1-1)}, T_\mathrm{e}, \dot{T}_\mathrm{e}, .., T_\mathrm{e}^{(\mathrm{r}_2-1)}, \omega_\mathrm{m}, \dot{\omega}_\mathrm{m}, .., \omega_\mathrm{m}^{(\mathrm{r}_3-1)}\right) , \tag{3.41}$$

$$\left(u_\mathrm{ds}\, u_\mathrm{qs}\, u_\omega\right)^T = \Psi_\mathrm{u}\left(\lambda_\mathrm{r}, \dot{\lambda}_\mathrm{r}, .., \lambda_\mathrm{r}^{(\mathrm{r}_1)}, T_\mathrm{e}, \dot{T}_\mathrm{e}, .., T_\mathrm{e}^{(\mathrm{r}_2)}, \omega_\mathrm{m}, \dot{\omega}_\mathrm{m}, .., \omega_\mathrm{m}^{(\mathrm{r}_3)}\right) . \tag{3.42}$$

where the sum of the highest derivative order $\sum_\mathrm{i} \mathrm{r}_\mathrm{i}$ must be greater or equal to the state dimension. These mappings must comply with

$$\frac{\mathrm{d}\,\Psi_\mathrm{x}}{\mathrm{dt}} = \tilde{f}\left(\Psi_\mathrm{x}\right) + \tilde{g}_\mathrm{d}(\Psi_\mathrm{x})\Psi_{\mathrm{u},1} + \tilde{g}_\mathrm{q}(\Psi_\mathrm{x})\Psi_{\mathrm{u},2} + g_\omega(\Psi_\mathrm{x})\Psi_{\mathrm{u},3} \,. \tag{3.43}$$

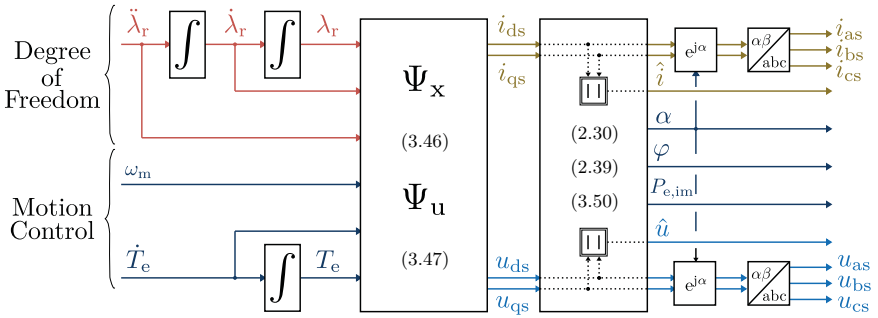

Figure 3.12: Equivalent differential flat system of an induction motor.

Both parametrizations are derived by repetitively applying the Lie derivative on the rows $\mathrm{i} \in \{1, 2, 3\}$ of Ψ_z along the vector field $\tilde{f}$:

$$z_\mathrm{i} = L_{\tilde{f}}^{(0)}\, \Psi_{\mathrm{z,i}} = \Psi_{\mathrm{z,i}}\,(\tilde{\boldsymbol{x}})\ , \tag{3.44a}$$

$$\dot{z}_\mathrm{i} = L_{\tilde{f}} \circ L_{\tilde{f}}^{(0)}\, \Psi_{\mathrm{z,i}} = L_{\tilde{f}}^{(1)}\, \Psi_{\mathrm{z,i}}\,, \tag{3.44b}$$

$$\vdots$$

$$z_\mathrm{i}^{(\mathrm{r_i})} = L_{\tilde{f}}^{(\mathrm{r_i})}\, \Psi_{\mathrm{z,i}} + \sum_{g_{(.)}} L_{g_{(.)}} \circ L_{\tilde{f}}^{(\mathrm{r_i}-1)}\, \Psi_{\mathrm{z,i}}\, u_\mathrm{j} \tag{3.44c}$$

so that the highest order $\mathrm{r_i}$ is determined in such a way that the Lie derivative on $\Psi_{\mathrm{z,i}}$ along the vector fields $g_\mathrm{d}, g_\mathrm{q}, g_\omega$ up to the order $\mathrm{r_i} - 2$ vanish

$$L_{g_\mathrm{j}} \circ L_{\tilde{f}}^{(\mathrm{r_i}-2)}\, \Psi_{\mathrm{z,i}} = 0\,. \tag{3.44d}$$

A particular benefit of the proposed state- and input-parametrization is that IM variables can be decomposed into a stationary part and a transient part as per

$$\Psi_\mathrm{x} = \Psi_\mathrm{x}^\mathrm{st} + \Psi_\mathrm{x}^\mathrm{tr}\,, \tag{3.45a}$$

$$\Psi_\mathrm{u} = \Psi_\mathrm{u}^\mathrm{st} + \Psi_\mathrm{u}^\mathrm{tr}\,. \tag{3.45b}$$

Given the order $r_1 = 2$ and $r_2 = r_3 = 1$, the state-parametrization Ψ_x is defined by

$$i_{ds} = \underbrace{\frac{\lambda_r}{L_m}}_{=i_{ds}^{st}} + \underbrace{\frac{\tau_r}{L_m}\dot{\lambda}_r}_{=i_{ds}^{tr}}, \tag{3.46a}$$

$$i_{qs} = \underbrace{\frac{2}{3}\frac{L_r}{L_m}\frac{T_e}{Z_p\lambda_r}}_{=i_{qs}^{st}} + \underbrace{0}_{=i_{qs}^{tr}}, \tag{3.46b}$$

$$\lambda_r = \lambda_r\,, \quad \omega_m = \omega_m\,. \tag{3.46c}$$

Accordingly, the stationary and transient parts of the input-parametrization Ψ_u are defined by

$$u_{ds} = \underbrace{\frac{1}{L_m}\left(R_s\lambda_r - \sigma L_s L_r\left(\frac{4}{9}R_r\frac{T_e}{Z_p\lambda_r^2} + \frac{2}{3}Z_p\omega_m\right)\frac{T_e}{Z_p\lambda_r}\right)}_{=u_{ds}^{st}} + \tag{3.47a}$$

$$\underbrace{\frac{1}{L_m}\left(\left(\frac{R_s}{R_r}L_r + L_s\right)\dot{\lambda}_r + \sigma L_s\tau_r\ddot{\lambda}_r\right)}_{=u_{ds}^{tr}},$$

$$u_{qs} = \underbrace{\frac{1}{L_m}\left(L_s Z_p\omega_m\lambda_r + \frac{2}{3}\left(L_s R_r + L_r R_s\right)\frac{T_e}{Z_p\lambda_r}\right)}_{=u_{qs}^{st}} + \tag{3.47b}$$

$$\underbrace{\frac{\sigma L_s}{L_m}\left(\frac{2}{3}L_r\frac{\dot{T}_e}{Z_p\lambda_r} + \tau_r Z_p\omega_m\dot{\lambda}_r\right)}_{=u_{qs}^{tr}},$$

and the parametrization of the newly introduced input, which is equal to the unknown load torque is

$$u_\omega = \frac{\dot{\omega}_m - f_\omega\left(\Psi_x\right)}{g_\omega\left(\Psi_x\right)}\,. \tag{3.48}$$

Since (3.46), (3.47) and (3.48) have full rank on

$$Z = \left\{\boldsymbol{z} \in \mathbb{R}^3 \middle|\, \lambda_r \neq 0 \,\wedge\, g_\omega\left(\tilde{x}\right) \neq 0\right\} \tag{3.49}$$

it is proven that (3.36) is a flat output of the augmented system (3.38). The canonical form of the IM is displayed in Figure 3.12.

As the voltage and current coordinates are separable into a stationary and transient part, so are the square values of the stator phase current and phase voltage and the IM power loss

$$P_{\mathrm{l,im}} = P_{\mathrm{l,im}}^{\mathrm{st}} + \underbrace{\frac{3}{2}\left(i_{\mathrm{ds}}^{\mathrm{st}}\, u_{\mathrm{ds}}^{\mathrm{tr}} + i_{\mathrm{ds}}^{\mathrm{tr}} u_{\mathrm{ds}}^{\mathrm{st}} + i_{\mathrm{qs}}^{\mathrm{st}}\, u_{\mathrm{qs}}^{\mathrm{tr}} + \frac{\left(\omega_{\mathrm{e}} \tau_{\mathrm{r}} \dot{\lambda}_{\mathrm{r}}\right)^2}{R_{\mathrm{fe}}} \right)}_{=P_{\mathrm{l,im}}^{\mathrm{tr}}}, \tag{3.50a}$$

$$\hat{i}^2 = \left(\hat{i}^{\mathrm{st}}\right)^2 + \underbrace{\left(2\lambda_{\mathrm{r}} + \tau_{\mathrm{r}} \dot{\lambda}_{\mathrm{r}}\right) \frac{\tau_{\mathrm{r}}}{L_{\mathrm{m}}^2} \dot{\lambda}_{\mathrm{r}}}_{=\left(\hat{i}^{\mathrm{tr}}\right)^2}, \tag{3.50b}$$

$$\hat{u}^2 = \left(\hat{u}^{\mathrm{st}}\right)^2 + \underbrace{2u_{\mathrm{ds}}^{\mathrm{st}}\, u_{\mathrm{ds}}^{\mathrm{tr}} + {u_{\mathrm{ds}}^{\mathrm{tr}}}^2 + 2u_{\mathrm{qs}}^{\mathrm{st}}\, u_{\mathrm{qs}}^{\mathrm{tr}} + {u_{\mathrm{qs}}^{\mathrm{tr}}}^2}_{=(\hat{u}^{\mathrm{tr}})^2}. \tag{3.50c}$$

The stationary components (2.45) are listed before in Section 2.2.4.

One of the most obvious benefits of the equivalent flat system representation is that for a desired electromagnetic torque and speed trajectory, whose design is essential for motion control, IM control is reduced to the problem of planning an appropriate rotor flux trajectory. A good overview on the target of trajectory planning is found in [75]. If a planned trajectory is feasible, which means that all technical limitations discussed in Section 3.2 are considered, the input parametrization can be used to control the IM in a feedforward manner. Feedforward control, however, is only applicable in theory as the nominal control model can never account for all dynamic effects, uncertainties and disturbances.

3.3.1 Two Degree of Freedom Control

For this reason, flatness based control often follows a 2DOF design so that the trajectory generation and feedforward control is complemented by a robust feedback loop which deals with the unknown or neglected plant uncertainties and guarantees that the desired trajectory is tracked [235]. Consequently, control design is differentiated into two problems, the generation of a feasible and possibly optimal trajectory on the one hand and the design of a robust and stable tracking controller on the other. The major advantage of a flatness based approach is the possibility to plan the feedforward trajectory independently of any system state in an open-loop fashion, whereas for feedback design well established methods can be relied upon [42]. A 2DOF structure that builds on FOC is shown in Figure 3.13.

An elegant solution to the problem of online trajectory planning and smoothing, which is particularly suited for integrator chains and motion control, is based on the

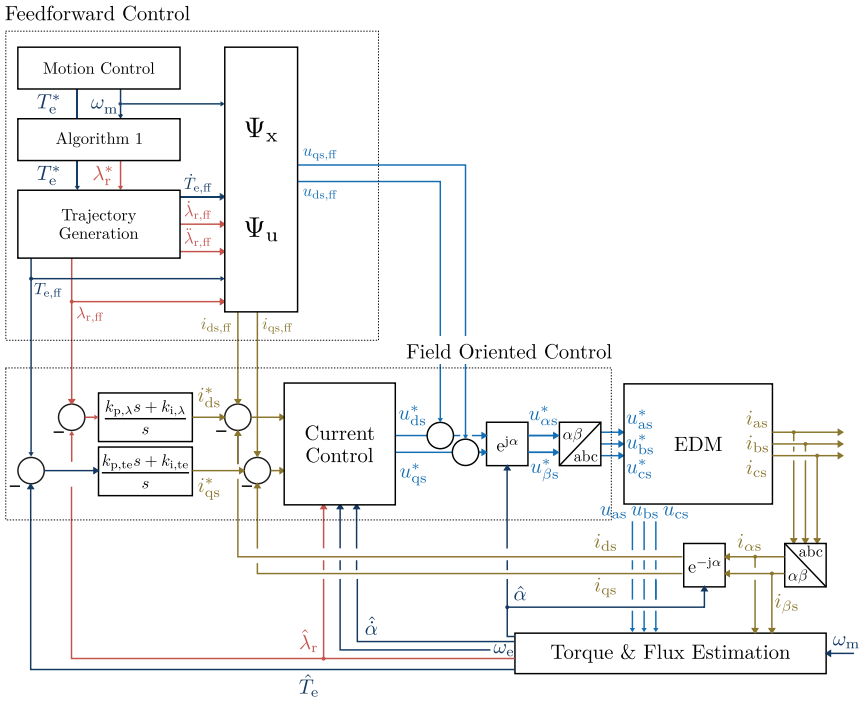

Figure 3.13: Flatness based two degree of freedom control.

implementation of *Finite Impulse Response* (FIR) filters [16]. The proposed method is shown to be equivalent to a function approach with time-optimal, multi-segment, polynomial trajectories and is capable of respecting constraints on the first n derivatives of the trajectory where n denotes the order of the trajectory. Furthermore, it allows to properly shape the frequency spectrum of a motion law. An alternative example of a polynomial approach is presented in [114].

A trajectory $\lambda_\mathrm{r}(t)$ is said to be of the order n, if the first $\mathrm{n}-1$ derivatives are continuous or equivalent, if it is of the class $\mathcal{C}^{\mathrm{n}-1}$. The concept of the trajectory generation is presented in Figure 3.14 and shows that the trajectory $\lambda_\mathrm{r}(t) \in \mathcal{C}^{\mathrm{n}-1}$ is obtained by a step input $\lambda_\mathrm{r}^*(t)$ which is filtered via a series connection of n filter elements, each parameterized by the time constant τ_i, $\mathrm{i} \in 1(1)\mathrm{n}$. In the first stage,

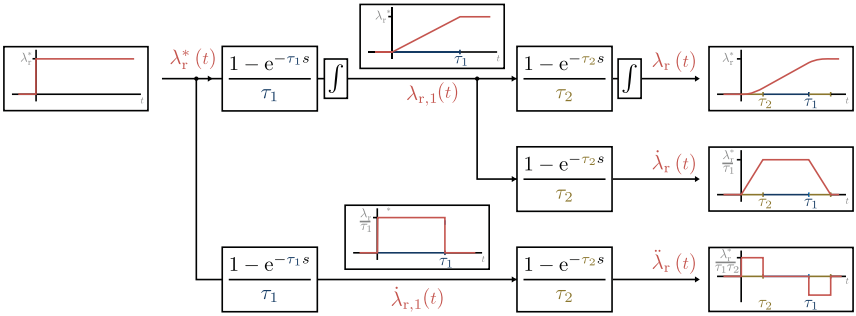

Figure 3.14: Trajectory generation $\lambda_r \in \mathcal{C}^1$ based on a cascade of five filter elements $(1 - e^{-\tau_n s})/\tau_n$ ($n = 2$, s denotes the Laplace variable).

the filters response to a step function of amplitude λ_r^* results in a rectangular profile with a duration of τ_1. The area of this rectangular profile is unitary. Consequently, its integral results in a linear profile from the initial value to the set-point λ_r^* with a change rate given by $\Delta\lambda_{r,1}/\Delta\tau_1$. This directly imposes a desired limit value $\dot{\lambda}_{r,ub}$ on the change rate according to $\tau_1 = |\lambda_r^*|/\dot{\lambda}_{r,ub}$. Propagating the response through the entire series connection, shows that the limit on the second derivative is imposed by $\tau_2 = \dot{\lambda}_{r,ub}/\ddot{\lambda}_{r,ub}$ and that eventually leads to

$$\tau_i = \lambda_{r,ub}^{(i-1)}/\lambda_{r,ub}^{(i)}\,. \tag{3.51}$$

The total time required to reach the endpoint of the trajectory after a set-point change is equal to the sum of the individual time constants $\sum_{\forall i} \tau_i$. If the time constants are chosen in a way that $\tau_i \geq \tau_{i+1} + ... + \tau_n$, the point to point trajectory is time optimal, i. e. it reaches the endpoint in the minimum duration under the consideration of the constraints. Otherwise, the trajectory is still guaranteed to comply with the constraints.

These methods illustrates, how trajectories can be planned for the rotor flux (where $n \geq 2$) in a computationally efficient manner. Furthermore, it is readily applicable for motion control where the dynamics are approximately represented by a second order system. Since the first derivative of the electromagnetic torque is required for the input parametrization of the IM, trajectories for motion control can be planned with $n \geq 1$ filter elements. The main advantage of this method is the possibility to limit the jerk and the acceleration of the vehicle by means of sufficient bounds on T_e and $\dot{T}_e$. Both of these quantities are important measures for driveability considerations [133]. In addition, the prospect of designing the dynamic filters in regard to frequency-domain

specifications of the drivetrain, enables the planning process to include design aspects related to a resonance attenuation of the drivetrain. However, the main disadvantage of this method is that the planning process and the imposed limits on the derivatives are not directly related to state and input constraints of the phase current and voltage, neither are the trajectories evaluated in terms of energy efficiency.

3.4 Optimal Control for Transient Operation

This section presents a more general solution to the problem of an optimal trajectory generation. The objective is to minimize the energy loss for the transition of a starting point $(\omega_\mathrm{m}, T_\mathrm{e})|_{t_0}$ to an endpoint $(\omega_\mathrm{m}, T_\mathrm{e})|_{t_\mathrm{f}}$ while considering flux, voltage and current constraints as well as the dynamic capabilities of the IM. There are relatively few investigations addressing this problem of IM efficiency control during torque transients [60]. A thorough literature survey of this field of research is found in [178]. One of the first detailed studies of this problem is [137], where the authors used a DP approach based on Bellman's principle of optimality. The field received more attention after necessary and sufficient optimality conditions were derived from the calculus of variations for the torque tracking problem without state constraints [27]. Exploiting these analytical results, [214, 215] extended the method and implemented an online predictive control scheme by parameterization of the optimal flux trajectory based on an exponential function. Apart from the DP approach and [60], however, the proposed methods do not allow for an inclusion of the current and voltage constraints. The method, proposed below, addresses this limitation and looks at the general constrained problem

$$\underset{\boldsymbol{u}_\mathrm{fl}}{\text{minimize}} \quad \int_{t_0}^{t_\mathrm{f}} \mathrm{w}_e \, P_{\mathrm{l,im}}\left(\omega_\mathrm{m}, \boldsymbol{x}_\mathrm{fl}, \boldsymbol{u}_\mathrm{fl}\right) + \vartheta\left(\boldsymbol{x}_\mathrm{fl}\right) \mathrm{d}t + \vartheta_f\left(\boldsymbol{x}_\mathrm{fl}|_{t_\mathrm{f}}\right) \tag{3.52a}$$

$$\text{subject to} \quad \dot{\boldsymbol{x}}_\mathrm{fl} = \boldsymbol{A}\boldsymbol{x}_\mathrm{fl} + \boldsymbol{B}\boldsymbol{u}_\mathrm{fl}, \tag{3.52b}$$

$$\boldsymbol{x}_\mathrm{fl}|_{t_0} = \boldsymbol{x}_0, \tag{3.52c}$$

$$a_\mathrm{pwm}\frac{2}{\pi}u_\mathrm{dc} - \hat{u}\left(\omega_\mathrm{m}, \boldsymbol{x}_\mathrm{fl}, \boldsymbol{u}_\mathrm{fl}\right) \geq 0\,, \quad \forall t \in [t_0, t_\mathrm{f}]\,, \tag{3.52d}$$

$$\hat{i}_\mathrm{ub} - \hat{i}\left(\boldsymbol{x}_\mathrm{fl}\right) \geq 0\,, \qquad \forall t \in [t_0, t_\mathrm{f}]\,, \tag{3.52e}$$

$$\boldsymbol{x}_\mathrm{lb} \leq \boldsymbol{x}_\mathrm{fl} \leq \boldsymbol{x}_\mathrm{ub}\,, \qquad \forall t \in [t_0, t_\mathrm{f}]\,, \tag{3.52f}$$

$$\boldsymbol{u}_\mathrm{lb} \leq \boldsymbol{u}_\mathrm{fl} \leq \boldsymbol{u}_\mathrm{ub}\,, \qquad \forall t \in [t_0, t_\mathrm{f}]\,, \tag{3.52g}$$

where $\boldsymbol{x}_{\mathrm{fl}} = (T_{\mathrm{e}}\, \lambda_{\mathrm{r}}\, \dot{\lambda}_{\mathrm{r}}) \in \mathbb{R}^3$ denotes the state of the equivalent flat system and $\boldsymbol{u}_{\mathrm{fl}} = (\dot{T}_{\mathrm{e}}\, \ddot{\lambda}_{\mathrm{r}}) \in \mathbb{R}^2$ is the control variable with

$$\boldsymbol{A} = \begin{bmatrix} 0 & 0 & 0 \\ 0 & 0 & 1 \\ 0 & 0 & 0 \end{bmatrix}, \quad \boldsymbol{B} = \begin{bmatrix} 1 & 0 \\ 0 & 0 \\ 0 & 1 \end{bmatrix}. \tag{3.53}$$

Problem (3.52) belongs to the class of finite horizon optimal control problems with a fixed initial condition (3.52c) [23, 166]. The time integral in (3.52a) is equal to the energy that is dissipated due to IM loss processes plus the distance term ϑ. This term penalizes the deviation of the state trajectory from the desired endpoint $(T_{\mathrm{e}}, \lambda_{\mathrm{r}})|_{t_{\mathrm{f}}}$, where the terminal rotor flux $\lambda_{\mathrm{r}}|_{t_{\mathrm{f}}}$ is determined by the loss minimizing strategy described in Section 3.2. Furthermore, in order to end the transition in a stationary point, a penalty is imposed on the terminal state variable via the distance function ϑ_f. No terminal constraint is used, since the terminal state may not be reached within the consider time horizon. During the transition the rotor speed is assumed to be constant. This may seem counter intuitive at first, though if the time horizon $t \in [t_0, t_{\mathrm{f}}]$ is sufficiently small, the speed is almost constant due to the high inertia of the vehicle. A weighting factor w_e is introduced to balance between the two objectives of energy efficiency and tracking performance, which is the amount of time required to reach the terminal state. Furthermore, constraints are imposed on the system states and inputs as well as on the values of the phase voltage and phase current based on the state- and input-parametrization which were defined in Section 3.3. Altogether, the constraints define the feasible set $\mathcal{X}_{\mathrm{IM}}$ of (3.19), which was discussed in Section 3.2. Restrictions on the torque T_{e} and its time derivative $\dot{T}_{\mathrm{e}}$ arise from technical limitations of the drivetrain and drivability requirements [155].

The main difference of (3.52), compared to a problem formulation that is based on the original state space model (2.32) as conducted in [60], is the shift of nonlinearities from the system dynamics to the constraints. Instead of a nonlinear state space model, the problem is defined by the canonical form of the equivalent flat system (3.52b), which is the integrator chains for the torque and rotor flux as shown in Figure 3.12. Compared to IM current dynamics (3.3) with a time constant that is ten times lower than the rotor flux time constant, the proposed formulation is clearly reduced in complexity. Yet, this simplification is gained at the expense of nonlinear state constraints (3.52d),(3.52e), whereas the use of the original state variables $i_{\mathrm{ds}}, i_{\mathrm{qs}}$ and inputs $u_{\mathrm{ds}}, u_{\mathrm{qs}}$ describes the feasible set $\mathcal{X}_{\mathrm{IM}}$ via quadratic constraints. The positive structural properties of the flatness based problem formulation have previously been discussed in [192], where (3.52) is solved for a fixed terminal state by discrete DP.

3.4.1 Direct Multiple Shooting

The following section extends the findings of [192] and solves (3.52) applying a direct multiple shooting method [19, 50]. Therefore, the infinite dimensional problem (3.52) is relaxed to a finite dimensional problem after introducing a discretization of the control trajectory $\boldsymbol{u}_{\mathrm{fl}} \in \mathbb{R}^{\mathrm{n}_u}$ on N equidistant intervals

$$t_{\mathrm{k}} = t_0 + (\mathrm{k}-1)t_{\mathrm{d}}\,, \qquad \forall \mathrm{k} \in 1(1)\mathrm{N}{+}1\,, \tag{3.54a}$$

$$t_{\mathrm{f}} = t_0 + \mathrm{N}t_{\mathrm{d}}\,, \tag{3.54b}$$

where $\{t_{\mathrm{k}}\}$ defines the shooting grid and $t_{\mathrm{d}} \in \mathbb{R}_+$ denotes the discrete time interval. The control trajectory is further restricted to a piecewise constant function so that on each interval $t \in [t_{\mathrm{k}}, t_{\mathrm{k+1}}]\ \ \forall \mathrm{k} \in 1(1)\mathrm{N}$ the control is parameterized by a constant $\boldsymbol{u}_{\mathrm{fl}}{}^{[\mathrm{k}]} \in \mathbb{R}^{\mathrm{n}_u}$. For simplification an additional control $\boldsymbol{u}_{\mathrm{fl}}{}^{[\mathrm{N+1}]}$ in the final point $t_{\mathrm{f}} + t_{\mathrm{d}}$ of the shooting grid is added and fixed to the value of the previous shooting interval

$$\boldsymbol{u}_{\mathrm{fl}}{}^{[\mathrm{N}]} = \boldsymbol{u}_{\mathrm{fl}}{}^{[\mathrm{N+1}]}\,. \tag{3.55}$$

In addition to the control parametrization, the multiple shooting method also introduces a discretization of the state trajectory $\boldsymbol{x}_{\mathrm{fl}}$ on the shooting grid which is defined by N IVPs

$$\dot{\boldsymbol{x}}_{\mathrm{kfl}} = \boldsymbol{A}\boldsymbol{x}_{\mathrm{kfl}} + \boldsymbol{B}\boldsymbol{u}_{\mathrm{fl}}\,, \qquad t \in [t_{\mathrm{k}}, t_{\mathrm{k+1}}]\ \ \forall \mathrm{k} \in 1(1)\mathrm{N}\,, \tag{3.56a}$$

$$\boldsymbol{x}_{\mathrm{kfl}}\big|_{t_{\mathrm{k}}} = \boldsymbol{x}_{\mathrm{fl}}{}^{[\mathrm{k}]}\,. \tag{3.56b}$$

Continuity of the state trajectory is enforced by matching the final value $\boldsymbol{x}_{\mathrm{kfl}}\big|_{t_{\mathrm{k+1}}}$ obtained by the solution of (3.56) at the end of an interval with the initial point of the succeeding shooting interval

$$\boldsymbol{x}_{\mathrm{kfl}}\big|_{t_{\mathrm{k+1}}} - \boldsymbol{x}_{\mathrm{fl}}{}^{[\mathrm{k+1}]} = 0\,, \qquad \forall \mathrm{k} \in 1(1)\mathrm{N}\,. \tag{3.57}$$

Considering the canonical form of an arbitrary flat output $z \in \mathbb{R}$ with the state vector $\boldsymbol{x}_{\mathrm{z}} = \left(z\ \dot{z}\ \ddot{z} \ldots z^{(\mathrm{r}-1)}\right)^T \in \mathbb{R}^{\mathrm{r}}$ and differential order $\mathrm{r} \in \mathbb{Z}$, the solution of the IVP on the shooting interval starting at t_{k} with constant input $z^{(\mathrm{r})}$ is

$$\boldsymbol{x}_{\mathrm{kz}}\big|_{t_{\mathrm{k+1}}} = \begin{bmatrix} 1 & t_{\mathrm{d}} & \frac{t_{\mathrm{d}}}{2} & & \cdots & & \frac{t_{\mathrm{d}}^{\mathrm{r}-1}}{(\mathrm{r}-1)!} \\ 0 & 1 & t_{\mathrm{d}} & \frac{t_{\mathrm{d}}}{2} & \cdots & & \frac{t_{\mathrm{d}}^{\mathrm{r}-2}}{(\mathrm{r}-2)!} \\ & & \ddots & & & & \\ \vdots & & & \ddots & & & \vdots \\ & & & & \ddots & & \\ & & & & & 1 & t_{\mathrm{d}} \\ 0 & & \cdots & & & 0 & 1 \end{bmatrix} \boldsymbol{x}_{\mathrm{z}}{}^{[\mathrm{k}]} + \begin{bmatrix} \frac{t_{\mathrm{d}}^{\mathrm{r}}}{\mathrm{r}!} \\ \frac{t_{\mathrm{d}}^{\mathrm{r}-1}}{(\mathrm{r}-1)!} \\ \vdots \\ t_{\mathrm{d}} \end{bmatrix} z^{(\mathrm{r})\,[\mathrm{k}]}\,. \tag{3.58}$$

Finally the inequality and box constraints (3.52d)-(3.52g) are relaxed by enforcing them solely on the shooting grid $\{t_\mathrm{k}\}$. This generally enlarges the feasible set and may lead to constraint violations. However, in practice these violations are often negligible, or can be reduced by choosing a finer shooting grid.

Altogether this yields the general form of a large-scale nonlinear optimization problem with a resulting decision vector

$$\boldsymbol{v} = \begin{bmatrix} \boldsymbol{x}_\mathrm{fl}{}^{[1]} & \boldsymbol{u}_\mathrm{fl}{}^{[1]} & \dots & \boldsymbol{x}_\mathrm{fl}{}^{[\mathrm{k}]} & \boldsymbol{u}_\mathrm{fl}{}^{[\mathrm{k}]} & \dots & \boldsymbol{x}_\mathrm{fl}{}^{[\mathrm{N}+1]} & \boldsymbol{u}_\mathrm{fl}{}^{[\mathrm{N}+1]} \end{bmatrix}^T \tag{3.59}$$

of $(\mathrm{N}+1)(\mathrm{n}_x + \mathrm{n}_u)$ unknowns:

$$\begin{aligned}
\underset{\boldsymbol{v}}{\text{minimize}} \quad & \sum_{\mathrm{k}=1}^{\mathrm{N}} P_\mathrm{l}{}^{[\mathrm{k}]} + \vartheta_f\left(\boldsymbol{x}_\mathrm{fl}{}^{[\mathrm{N}+1]}\right) && \text{(3.60a)}\\
\text{subject to} \quad & \boldsymbol{x}_{\mathrm{k}\mathrm{fl}}\big|_{t_{\mathrm{k}+1}} - \boldsymbol{x}_\mathrm{fl}{}^{[\mathrm{k}+1]} = 0\,, \quad \forall \mathrm{k} \in 1(1)\mathrm{N}, && \text{(3.60b)}\\
& \boldsymbol{x}_\mathrm{fl}{}^{[1]} - \boldsymbol{x}_0 = 0, && \text{(3.60c)}\\
& \boldsymbol{u}_\mathrm{fl}{}^{[\mathrm{N}+1]} - \boldsymbol{u}_\mathrm{fl}{}^{[\mathrm{N}]} = 0, && \text{(3.60d)}\\
& c_\mathrm{i}\left(\boldsymbol{x}_\mathrm{fl}{}^{[\mathrm{k}]}, \boldsymbol{u}_\mathrm{fl}{}^{[\mathrm{k}]}\right) \geq 0\,, \qquad \forall \mathrm{k} \in 1(1)\mathrm{N}{+}1\,, \forall \mathrm{i} \in \mathcal{I}, && \text{(3.60e)}\\
& \boldsymbol{x}_\mathrm{lb} \leq \boldsymbol{x}_\mathrm{fl}{}^{[\mathrm{k}]} \leq \boldsymbol{x}_\mathrm{ub}\,, \qquad \forall \mathrm{k} \in 1(1)\mathrm{N}{+}1, && \text{(3.60f)}\\
& \boldsymbol{u}_\mathrm{lb} \leq \boldsymbol{u}_\mathrm{fl}{}^{[\mathrm{k}]} \leq \boldsymbol{u}_\mathrm{ub}\,, \qquad \forall \mathrm{k} \in 1(1)\mathrm{N}{+}1\,, && \text{(3.60g)}
\end{aligned}$$

where

$$P_\mathrm{l}{}^{[\mathrm{k}]} = \mathrm{w}_e P_{\mathrm{l},\mathrm{im}}\left(\omega_\mathrm{m}{}^{[\mathrm{k}]}, \boldsymbol{x}_\mathrm{fl}{}^{[\mathrm{k}]}, \boldsymbol{u}_\mathrm{fl}{}^{[\mathrm{k}]}\right) + \vartheta\left(\boldsymbol{x}_\mathrm{fl}{}^{[\mathrm{k}]}\right). \tag{3.61}$$

It is noted that due to the time discretization, the consideration of a discretized speed profile $\omega_\mathrm{m}{}^{[\mathrm{k}]}$ is straight-forward. The total number of constraints is equal to $(\mathrm{N}+1)\left(3\mathrm{n}_x + 2\mathrm{n}_u + \mathrm{n}_c\right) + \mathrm{n}_u$ where $\mathrm{n}_c \in \mathbb{Z}$ is the cardinality of the index set $\mathcal{I}$ which includes the voltage and current constraints (3.52d) and (3.52e) with $\mathrm{n}_c = 2$. If the weight w_e is chosen to be equal to t_d, the first term in (3.60a) is interpreted as the energy that is dissipated during the transition. The penalty term and terminal cost are defined as

$$\vartheta\left(\boldsymbol{x}_\mathrm{fl}{}^{[\mathrm{k}]}, \boldsymbol{u}_\mathrm{fl}{}^{[\mathrm{k}]}\right) = \sum_{\mathrm{i}=1}^{\mathrm{n}_x} \mathrm{w}_{x,\mathrm{i}}\left(x^*_{\mathrm{fl},\mathrm{i}} - x_{\mathrm{fl},\mathrm{i}}{}^{[\mathrm{k}]}\right)^2\,, \tag{3.62a}$$

$$\vartheta_f\left(\boldsymbol{x}_\mathrm{fl}{}^{[\mathrm{N}+1]}, \boldsymbol{u}_\mathrm{fl}{}^{[\mathrm{N}+1]}\right) = \vartheta\left(\boldsymbol{x}_\mathrm{fl}{}^{[\mathrm{N}+1]}, \boldsymbol{u}_\mathrm{fl}{}^{[\mathrm{N}+1]}\right)\,, \tag{3.62b}$$

where $\boldsymbol{x}^*_\mathrm{fl} \in \mathbb{R}^{\mathrm{n}_x}$ is the desired terminal state. This is a stationary point

$$\boldsymbol{x}^*_\mathrm{fl}\big|_{t_\mathrm{f}} = \begin{bmatrix} T_\mathrm{e}\big|_{t_\mathrm{f}} & \lambda_\mathrm{r}\big|_{t_\mathrm{f}} & 0 \end{bmatrix}^T\,, \tag{3.63a}$$

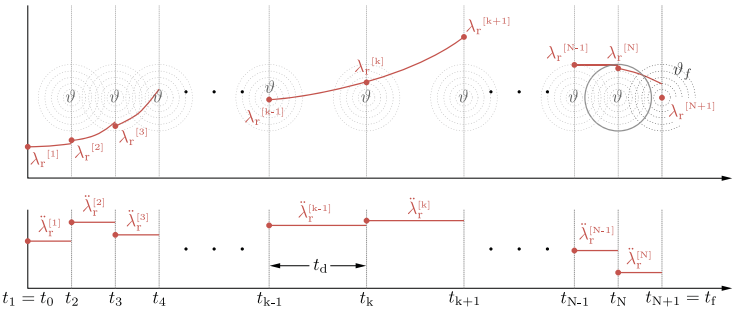

Figure 3.15: Multiple shooting grid for the flux trajectory of class $\mathcal{C}^1$.

for which the flux level $\lambda_r|_{t_f}$ is determined by Algorithm 1 as a function of the reference torque $T_e|_{t_f}$. Since the trajectory is not constrained to end in (3.63), the weights $w_x \in \mathbb{R}^{n_x}$ are introduced in addition to w_e as tuning parameters. This approach may be viewed as a potential field, in which the penalty term and terminal cost (3.62) are interpreted as the sum of attractive potentials which pull the trajectory towards the desired reference while considering the physical limitations of the system. The first term of (3.60a), weighted by w_e, is interpreted as a repulsive potential which tries to reduce the dissipated energy. In doing so, the method emphasizes on computational efficiency, rather than on guaranteeing the attainment of the reference. However, by increasing the artificial forces induced by the potential fields of (3.62), the solution evolves more towards the reference. This can be done by either increasing the magnitude of the reference value or by adjusting the corresponding weight. The principle concept of the multiple shooting method for the flux trajectory with piecewise constant input $\ddot{\lambda}_r$ is illustrated in Figure 3.15.

In order to generate a smooth trajectory for motion control which complies with comfort requirements, it is desirable to impose an additional smoothness constraint on the jerk $\dot{T}_e$ [155]. This is done apart from the limit on its magnitude. The sum-of-norms regularization has gained more and more attention as a solution to this problem [109, 161]. In particular, the l_1 norm is known to force many elements of a decision vector to zero when added to the objective. This characteristic is exploited for example in feature selection and the Lasso regression [221]. As it is also anticipated to reduce the magnitude and occurrence of jerk variations, an l_1 norm regularization term is added to the objective

$$\vartheta_f\left(\boldsymbol{x}_{fl}{}^{[N+1]}, \boldsymbol{u}_{fl}{}^{[N+1]}\right) + \varsigma_{Te} \sum_{k=1}^{N+1} s_p{}^{[k]} + s_n{}^{[k]}, \tag{3.64}$$

where $\varsigma_{\mathrm{Te}} \in \mathbb{R}_+$ is a regularization factor and where ${\mathrm{s}_p}^{[\mathrm{k}]}, {\mathrm{s}_n}^{[\mathrm{k}]} \in \mathbb{R}_+$ are artificial variables which are introduced by the constraints

$$\dot{T}_{\mathrm{e}}^{[\mathrm{k}]} + {\mathrm{s}_p}^{[\mathrm{k}]} - {\mathrm{s}_n}^{[\mathrm{k}]} = 0\,, \quad \forall \mathrm{k} \in 1(1)\mathrm{N}{+}1\,, \tag{3.65a}$$

$${\mathrm{s}_p}^{[\mathrm{k}]} \geq 0\,, \quad \forall \mathrm{k} \in 1(1)\mathrm{N}{+}1\,, \tag{3.65b}$$

$${\mathrm{s}_n}^{[\mathrm{k}]} \geq 0\,, \quad \forall \mathrm{k} \in 1(1)\mathrm{N}{+}1\,. \tag{3.65c}$$

This increases the decision vector by $2(\mathrm{N}+1)$ variables and adds $3(\mathrm{N}+1)$ constraints to the problem, however the computational effort is only slightly increased while the solution is drastically improved in the desired way. Similar as for the jerk, a l_1 norm regularization with regularization factor $\varsigma_\lambda \in \mathbb{R}_+$ is applied for the second time derivative of the rotor flux, which further improves the transition behavior, which is discussed in great detail in Section 3.5.

3.4.2 Optimized Reference Governor

By solving the *Direct Multiple Shooting* (DMS) problem (3.60), a state and input trajectory is obtained, which complies with the physically and operationally imposed limits and which tries to accomplish an energy efficient transition from an initial operating point to a desired endpoint. Both trajectories are used in the 2DOF control structure, shown in Figure 3.13, as feed-forward commands and references. To account for disturbances and model uncertainties a receding horizon or *Model Predictive Control* (MPC) scheme can be employed [51]. Difficulties associated with NMPC arise in terms of closed-loop stability, recursive feasibility, and the necessity to find a solution of the optimal control problem in real-time [52]. Due to the small time constants of IM current dynamics, finding a solution in real-time is not the main intention of the DMS approach. Nevertheless, the DMS problem formulation provides an efficient framework to analyze optimal transitions, from which heuristics or rule based control methods can be derived. Unlike a classical NMPC scheme, the proposed method classifies as a *reference governor* [74]. If the trajectories are forced to end in a stationary point within a sufficiently long time horizon, issues related to stability are taken care of by the primal controller, which is the FOC. Proving the stability and recursive feasibility of the control concept is not in the scope of this work. Nevertheless, positive results are observed in simulative studies.

Following the receding horizon philosophy, only the first fraction of the optimized trajectory with a prediction horizon t_{f} is applied to the system. Subsequently, the DMS problem is recalculated based on the measured or estimated state, which defines the new initial operating point for the next transition with a possible updated reference. The rate at which the state and reference are updated are defined by the time scale $t_{\mathrm{mpc}} < t_{\mathrm{f}}$. In order to run in real-time, the DMS problem has to be solved within this

Table 3.1: Direct multiple shooting parameter of the optimization-based induction motor control strategy.

$t_\mathrm{f} - t_0$	t_d	t_mpc	w_e	w_x	ς_Te	ς_λ
80 ms	1 ms	10 ms	$20 \cdot t_\mathrm{d}$	$(1\,,10\,,1e{-}4)$	$1e{-}3$	$1e{-}3$

time frame.

Problem (3.60) with l_1 regularization is solved on a single thread of an *Intel Core* i7-5600U processor using the modeling language *JuMP* v0.20.0 for mathematical optimization [57] and IPOPT. Table 3.4.2 lists the considered time horizon $t_\mathrm{f} - t_0$, the time discretization t_d, the MPC update rate t_mpc, the problem weights $\mathrm{w}_e, \mathrm{w}_x$, and the l_1 regularization factor ς_Te and ς_λ for an exemplary implementation. A detailed discussion of the numerical solution method for the DMS problem is found in Appendix A.3. The computational effort is evaluated by solving several problem instances for various step changes of the rotor torque. In total more than 5000 step scenarios are solved for an initial value of zero and 10 % of the maximum torque $T_\mathrm{e,max}$ up to a set point of 10 %, 30 %, 50 %, and 100 % of $T_\mathrm{e,max}$. Scenarios are repeated for all step responses at $\omega_\mathrm{m} \in 80(40)1040\,\mathrm{rad/s}$ and a current limit of $\hat{i}_{ub} \in 400(25)1200\,\mathrm{A}$. The voltage limit is defined by a battery voltage of 395 V. On average, the DMS problem of a single MPC step converges within 342 ms. However, depending on the number of constraints that are active within the control horizon of 80 ms, a single MPC step may require several seconds. As expected, this shows that the problem cannot be solved by means of the chosen numerical method and mathematical programming language within a reasonable MPC update rate. For a real-time implementation, alternative strategies are required.

Two illustrative examples of a set-point change between zero and maximum torque at a speed of 200 rad/s and 1000 rad/s are shown in Figure 3.16. A current limit of 900 A is imposed on the trajectory at a lower speed and the trajectory at the higher speed is limited by 500 A. The first two rows present the torque trajectory, the following three rows display the rotor flux trajectory and the bottom two rows show the resulting stator phase current and voltage peak values. Reference values and limits are indicated as red dotted lines. In the first scenario, the optimal torque trajectory follows an exponential profile and reaches the maximum torque $T_\mathrm{e,max}$ value within 20 ms. It rapidly decreases back to zero within 20 ms. The torque trajectory complies with the predefined limits on the jerk. The transition time of the optimal flux trajectory with 30 ms and 17 ms is considerably longer. During the almost linear transition of the rotor flux, the current is at its specified limit. The peak value of the voltage reference follows a non-trivial profile and remains within its boundaries.

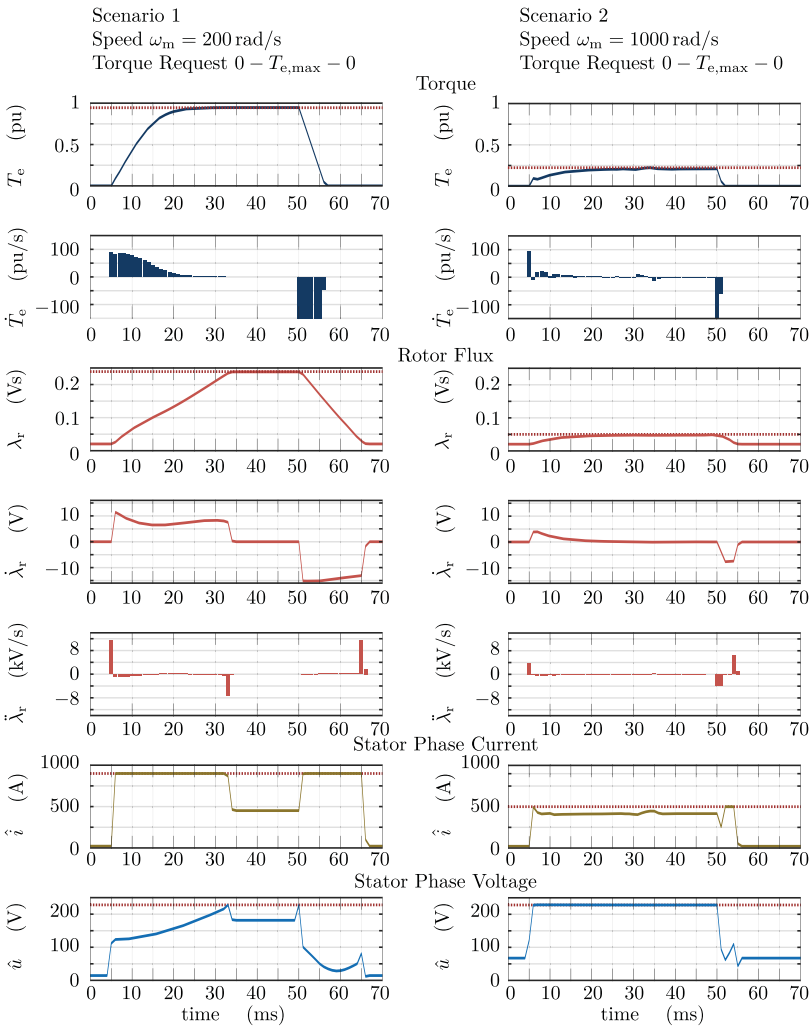

Figure 3.16: Direct multiple shooting optimization results.

In the case of the second scenario at a considerably higher speed, the torque is limited by Algorithm 1 to 20 % of the maximum value due to the maximum attainable voltage limit. The voltage remains at its maximum value for a great part of the transition. Only during the decrease of the torque and the rotor flux magnitude the peak value of the voltage reference is reduced. Both the optimal torque trajectory and the flux trajectory approximately follow an exponential profile. Compared to the first scenario the transition time of the torque trajectory increases to 25 ms for a positive step change despite the lower terminal value. A reason for this is the reduced current limit of 500 A. The flux trajectory reaches its low reference value of 0.05 Vs within 30 ms. The negative step change of the torque is completed in 2 ms and the rotor flux returns to its idling level in 5 ms. During the return of the rotor flux, the transition time is affected by the maximum current limit.

Summarizing the results, both scenarios show that for an increasing torque and flux magnitude the optimal division between the torque producing component i_{qs} and the flux producing component i_{ds}, which follow similar profiles as the torque and flux trajectory, is influenced by the current and voltage limit in a non-intuitive manner. While the voltage constraint essentially limits the flux and torque magnitude at high speeds, the current limit mainly has an influence on the transition time, and in particular on the optimal flux profile. This observation is confirmed by the results of all considered step scenarios. As long as the transition is not confined by a current limit, the optimal flux trajectory can be described by an exponential function. This is the case for the positive step change in the second scenario. However, a stricter bound of the current limit leads to an increase of the transition time with an optimal flux trajectory that is described by a linear function. This is observed in the first scenario as well as for the negative step change of the second scenario. Since loss processes support a decreasing torque and flux magnitude, a negative step change is demonstrated to be less demanding. In this case the voltage limit has a minor influence, whereas a current limit still affects the transition time.

Real-Time Reference Governor

Based on the findings which are derived from more than 5000 different step changes, the optimized transition trajectories are characterized by the representative function

$$T_{\mathrm{e}}(t) = T_{\mathrm{e}}|_{t_0} + \left(T_{\mathrm{e}}|_{t_{\mathrm{f}}} - T_{\mathrm{e}}|_{t_0}\right)\left(1 - \mathrm{e}^{-t/\tau_{\mathrm{Te}}}\right), \tag{3.66}$$

and by a representative function for the rotor flux

$$\lambda_{\mathrm{r}}(t) = \begin{cases} \lambda_{\mathrm{r}}|_{t_0} + \operatorname{sign}\left(\lambda_{\mathrm{r}}|_{t_{\mathrm{f}}} - \lambda_{\mathrm{r}}|_{t_0}\right)\lambda' t, & \omega_{\mathrm{m}} \leq \bar{\omega}_{\mathrm{m}} \\ \lambda_{\mathrm{r}}|_{t_0} + \left(\lambda_{\mathrm{r}}|_{t_{\mathrm{f}}} - \lambda_{\mathrm{r}}|_{t_0}\right)\left(1 - \mathrm{e}^{-t/\tau_{\lambda}}\right), & \omega_{\mathrm{m}} > \bar{\omega}_{\mathrm{m}} \end{cases}. \tag{3.67}$$

It is noted that (3.66) and the function with the exponential term in (3.67) are analogously defined to the approach presented in [214]. To be able to quantify the

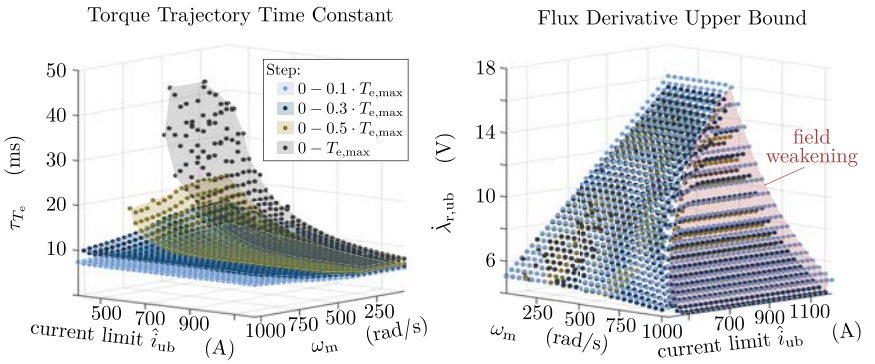

Figure 3.17: Characteristics of optimized flux and torque trajectories for different step changes.

influence of current and voltage constraints, the defining parameters of (3.66) and (3.67), for various step changes, are displayed in Figure 3.17 as a function of the specified current limit and the rotor speed. Four reference changes $T_e|_{t_0} - T_e|_{t_f}$ are considered and indicated in different colors. The left graph shows the results of the identified time constant $\tau_{Te} \in \mathbb{R}_+$. Compared to the optimal trajectory, (3.66) is conservative as its first derivative is below the optimal value. This in turn leads to a slight increase of the required transition time. At speeds below base speed, the time constant τ_{Te} and accordingly the transition time of the torque trajectory decrease exponentially with increasing current limit. With increasing speed, however, the effect of the current limit is reduced while the voltage limit gains more influence. Above base speed, the time constant is bound from below. This lower bound of τ_{Te} rises with increasing speed and with increasing torque magnitude $T_e|_{t_f}$.

For the majority of the transition time $t_f - t_0$, the phase current is influenced by the shape of the flux trajectory mainly due to the comparable slow transition time. Below the speed threshold $\bar{\omega}_m \in \mathbb{R}_+$, the shape is determined by an almost constant slope, which is parameterized by $\lambda' \in \mathbb{R}_+$. Above $\bar{\omega}_m$, the trajectory is better described by the second term of (3.67). The speed threshold $\bar{\omega}_m$ depends on the maximum attainable voltage range and is defined by the region of $\mathcal{X}_{IM} \backslash \mathcal{X}_{volt}$ indicated in Figure 3.7. Within this region, both flux and torque trajectories are hardly limited by the voltage constraint which is only active during the voltage peak that occurs as soon as a reference change is initiated. The maximum magnitude of the slope $\dot{\lambda}_{ub}$ that is observed during the flux transition is shown on the right of Figure 3.17. In this graph, the field weakening region $\mathcal{X}_{volt}$ is clearly visible. The characteristic of the

average slope, reveals that the optimized flux trajectory is proportional to the current limit. In the region of $\mathcal{X}_{\mathrm{volt}}$, however, the slope is bound from above. The parameter $\dot{\lambda}_{\mathrm{ub}}$ and λ' ar thus well suited to characterize (3.67), where the time constant $\tau_\lambda \in \mathbb{R}_+$ is defined by

$$\tau_\lambda = \frac{\left| \lambda_{\mathrm{r}}|_{t_f} - \lambda_{\mathrm{r}}|_{t_0} \right|}{\dot{\lambda}_{\mathrm{ub}}} \,. \tag{3.68}$$

In the case of step changes that start from $T_{\mathrm{e}} > 0$ as well as from an initial rotor flux that is above the idling level, the characteristics of τ_{Te} and $\dot{\lambda}_{\mathrm{ub}}$ change in that the transition time of the flux and torque trajectory decrease. This is expected, since for a higher flux level the transition benefits from the energy that is stored in the coupling field. Qualitatively, however, the characteristics are similar to those presented in Figure 3.17. Therefore, (3.66) and (3.67) may be considered as conservative, sub-optimal approximations of the DMS solution when parameterized by the values shown in Figure 3.17.

For a practical implementation, the advantages of both the FIR trajectory planner and the approximation of the DMS solution are combined. A FIR order one torque trajectory and order two flux trajectory are generated as illustrated in Figure 3.14 according to [16]. The reference input is governed by the representative functions (3.66) and (3.67). The defining parameters of the reference trajectory are stored in lookup tables as functions of the vehicle speed and current limit. Therefore, the characteristics with the highest value of τ_{Te} and the lowest value of λ', $\dot{\lambda}_{\mathrm{ub}}$ are chosen. As the transition is assumed to end in a steady state, the reference set-point of the rotor flux is computed as shown in Figure 3.13 by means of Algorithm 1. Even though the FIR filters are not required to comply with the physical limitations, an appropriate design of these can be used to account for additional constraints and driveability requirements. To stay within the desired transition time of the representative function, the time constants τ_{i} of the FIR filter used for the flux trajectory can be set to

$$\tau_1 = \tau_2 = \tau_3 = \frac{5\lambda_{ub}}{\max\{\dot{\lambda}_{\mathrm{ub}}\}} \,, \tag{3.69}$$

where the maximum value of the $\dot{\lambda}_{\mathrm{ub}}$ characteristic is chosen. In view of Figure 3.17, this value is given by $\max\{\dot{\lambda}_{\mathrm{ub}}\} = 16\,\mathrm{V}$. Due to requirements on the driving comfort, the time constants of the FIR torque trajectory planner is defined by the maximum jerk $\dot{T}_{\mathrm{e,ub}}$ which yields

$$\tau_1 = \tau_2 = \frac{T_{\mathrm{e,ub}}}{\dot{T}_{\mathrm{e,ub}}} \,. \tag{3.70}$$

3.5 Comparison of EDM Control Strategies

This section compares the EDM control strategies, which are introduced in the previous sections. These are the

- FOC with loss minimizing flux level (LMT strategy),
- flatness based 2DOF control with optimized references (NMPC strategy),
- flatness based 2DOF control with sub-optimal references and FIR trajectory planner (FIR strategy).

For evaluation purposes, all strategies are implemented in *Matlab Simulink v2018b* and tested against a *PLECS Blockset* v4.1.5 circuit model of the IM and VSI [179]. This circuit model uses a none-saturable squirrel cage IM which is powered by a three-phase two-level IGBT converter [4]. The gate inputs of the six ideal IGBTs with forward voltage and on-resistance are controlled by a symmetrical, regular sampled SVPWM with a carrier frequency of 10 kHz at a constant supply voltage of 395 V. Compared to the dq-model introduced in this study, the IM PLECS model also considers higher harmonics of the modulated phase voltage.

Based on the simplified plant models introduced in Section 3.1 and a simple dead time approximation, the control loops of current, flux and torque are designed as shown in Figure 3.6. A flux estimation is computed using the indirect method of the stator current model depicted in Figure 3.3. Algorithm 1 is implemented to compute the reference for the loss minimizing flux level as a function of the rotor speed and torque. The optimizd trajectories obtained by the NMPC scheme are computed offline.

Figure 3.18 presents the step responses of the control methods from zero to 150 N at a vehicle speed of 30 km/h. The torque reference is set back to zero after 100 ms. Two scenarios are considered for an upper phase current limit of 600 A and 1000 A. From the top to the bottom, the graphs display the torque, the rotor flux, the stator phase current peak value and the stator phase voltage peak value.

Following the designed trajectory, the optimized control strategies smoothly reach their desired torque reference. During the transition, these comply with all predefined limits on the jerk, flux derivatives and the phase voltage. The phase current trajectories of the NMPC strategy are confined within the imposed limits, yet slightly violate the constraints. These violations, which on average amount to approximately 6 %, mainly attribute to model uncertainties and in particular to the higher harmonic excitation of the VSI, which is considered for simulation but not within the optimization process. Due to the conservative selection of the bound on the rotor flux derivative, the FIR strategy stays within the current limits. In comparison, the LMT strategy leads to a

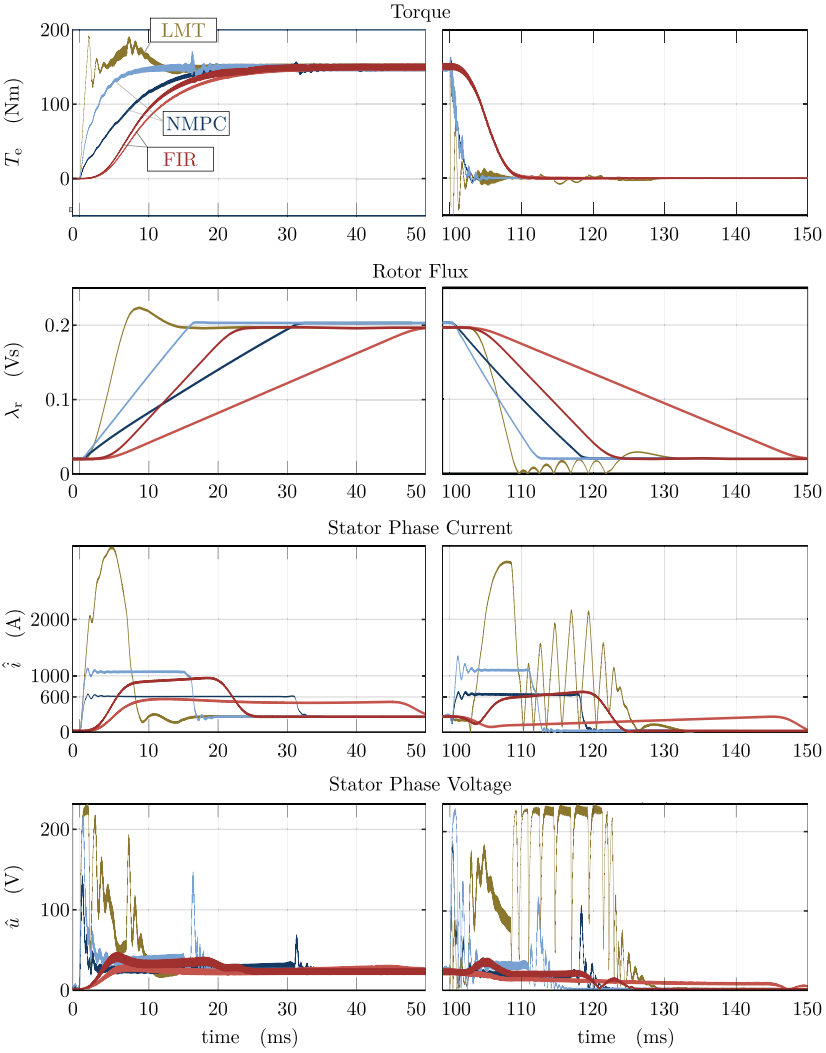

Figure 3.18: Electric drive module step response at a vehicle speed of 30 km/h.

temporary and high frequent oscillating behavior followed by a clear overshoot with a torque peak which is 25 % above the reference. This in turn, results in a phase current peak of approximately 3000 A. Returning to zero torque near 110 ms, the LMT control reaches the maximum voltage limit. The subsequent toggling behavior leads to a drop of the rotor flux below the minimum idling level and therefore to an increased power demand. The main reason for the oscillating behavior in this scenario of a very dynamic step change, is that the phase correct splitting strategy of a standard LMTs does not adequately handle voltage constraints . The optimized trajectories, however, smoothly approach their desired reference, all following the same profile.

Compared to the FIR strategy, the NMPC strategy reaches the desired torque and flux level and therefore a steady state in a much shorter duration. This increase in transition time is mainly due to the FIR filters. As the reference trajectory is filtered, it is delayed by approximately 3 ms. Furthermore, the FIR strategy does not fully exploit the voltage range of the VSI.

Figure 3.19 presents the time integral of the EDM energy loss (including VSI losses). The energy amount is normalized to the total energy that is dissipated by applying a conventional LMT control. It is noted, that for all optimized trajectories the dissipated energy is clearly reduced compared to the conventional LMT approach. Furthermore, a more efficient operation of the FIR trajectories compared to the NMPC generated trajectories is observed. With 1.14 kWs at a current limit of 1000 A and 0.78 kWs at a limit of 600 A, the FIR strategy requires 30 % less energy than the NMPC strategy with 1.6 kWs and 1.08 kWs respectively. However, this reduced energy amount comes at the cost of a transition time of the torque trajectory which is more than doubled compared to the NMPC approach. If the transition time of the NMPC is adjusted to the slower value, the computed solution results in a trajectory that requires less energy than the FIR approach.

3.6 Summary

The main contribution of this study is presented in Figure 3.12 which shows the differential flat IM model. Given a torque and speed trajectory of a driving cycle or motion control task, related phase currents and voltages can be computed, provided that the energy of the magnetic rotor field and its variation are known. In a steady state operation, this energy is determined by the magnitude of the rotor flux linkage, whereas in transient operations the variation of energy may be described in a canonical form by second order trajectory of $\lambda_{\mathrm{r}}(t) \in \mathcal{C}^2$. A FOC scheme allows for a direct and independent control of the rotor torque and rotor flux linkage. Consequently, the rotor flux represents a degree of freedom that can be exploited to find an optimal

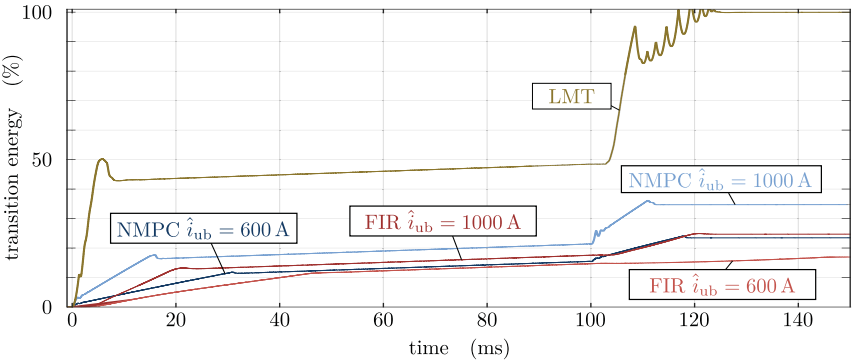

Figure 3.19: Electric drive module transition energy for a zero to 150 Nm step response at a vehicle speed of 30 km/h.

balance between different loss processes. An efficiency optimized control strategy, which computes the optimal flux level over the entire torque and speed range of the IM, is proposed by Algorithm 1. The algorithm solves a nonlinear, optimization problem in a computationally efficient manner and returns a flux level that either minimizes IM losses, the phase current, or the phase voltage. Validation analyses confirm that the electric drive of the experimental vehicle follows a LMT similar to the loss minimizing flux level of Algorithm 1. Along the solution process, the algorithm further computes the maximum and minimum torque ratings as a function of the vehicle speed, the current limit, and the DC terminal voltage. Comparing the different control strategies, which are referred to as LMT, MTPA, and MTPV, Figure 3.9 demonstrates that the rotor flux has a substantial impact on IM operation. For example, when compared to an LMT, an MTPA strategy may reduce the phase current by up to 20 %, whereas an MTPV strategy can cause losses that are more than ten times higher. The wide range of operating conditions that is achieved by adjusting the flux level offers great potential for an improvement of operational strategies. Particular examples are a higher regenerative braking potential or use cases for thermal management, in which a systematic increase of the phase current or power loss provides an additional degree of freedom for thermal control.

A major benefit of the inverse flat IM model, is its straight forward application in a feedforward control structure. Chapter 3 uses the flat state- and input parametrication to introduce a 2DOF control structure as well as an optimization based reference governor that is ideally suited for motion control. The general control structure illustrated in Figure 3.13 leads to the important finding, that in an optimal control

setup the rotor flux trajectory is governed by the motion of the vehicle. Consequently, flux dynamics are directly linked to the dynamics of the vehicle. The differential flat IM is thus considered as less dynamic than the equivalent dq-model.
A simulative study with a high fidelity PLECS model of the EDM demonstrates how a 2DOF controlled IM with optimized references outperforms a conventional FOC in terms of tracking performance and efficiency. On this detailed component level, however, it is difficult to evaluate the power saving potential for nominal operations where the governing longitudinal dynamics are by far less demanding than the contemplated example. Nevertheless, the improved dynamical performance, makes the 2DOF approach interesting for *Electronic Stability Control* (ESC) functions and in particular for *Antilock Braking* (ABS) and *Traction Control System* (ASR) [220]. Furthermore, given the possibility to limit the phase current, optimization potentials for the design of the electric powertrain are created. For example, demands on the power electronics can be reduced by lower current ratings and saturation of the IM can be avoided.

4 Energy Management Strategies for All-Wheel-Drive BEVs

Based on the differential flat representation of the electric motor, which is introduced in the previous chapter, as well as the average value model of the VSI and the chosen model structure of the drivetrain introduced in Chapter 2, it is possible to invert the causality and describe the EDMs energy conversion in the opposite direction. In doing so, EDM controls and BEV motion control strategies for economic driving can be integrated into the BEV system model in a straight-forward manner. The emerging model of the experimental vehicle is depicted in the block diagram of Figure 4.1 and is described in more detail in Section 4.1. The electric powertrain is equivalent to the model shown in Figure 2.1. The canonical form of the flat system structure is preferable mainly because load cycles as well as motion control tasks are intuitively represented through mechanical load profiles. Therefore, all electrical states of the BEV powertrain, including the electrical power through-put $P_{\mathrm{e,edm}}$, the magnetic field of the front and rear axle EDMs, and AC/DC currents and voltages, are computed, based on the input $\omega_{\mathrm{whl}}, T_{\mathrm{whl}}$, which is the wheel speed and overall wheel torque. Assuming an economic driving style, this input is determined by the longitudinal dynamics of the vehicle and an input of a speed, acceleration, and road grade profile.

Subject to the mechanical load, the central aim of energy management is to meet the driver's request considering all system boundaries and safety aspects. The secondary goal is to exploit the given degrees of freedom in order to optimize the dynamic driving behavior and the energy efficiency. Though both design requirements seem to follow contradictory goals from the perspective of the electric drive, energy efficiency and driving performance are strongly related. The maximum acceleration performance, an important performance quantifier, for example, is only reached for the most efficient operation of the powertrain and, therefore, can only be achieved with a suitable control strategy of the electric drive. A well suited strategy for IM drives is proposed in Section 3.4. However, the central motion control task that is investigated in this study is to improve the overall efficiency and, thus, ultimately the vehicle range. From previous discussions it becomes apparent that relevant loss processes for motion control can be divided into two major groups:

- electric drive losses and
- losses originating from the battery, mechanical friction, drag resistance, and rolling resistance.

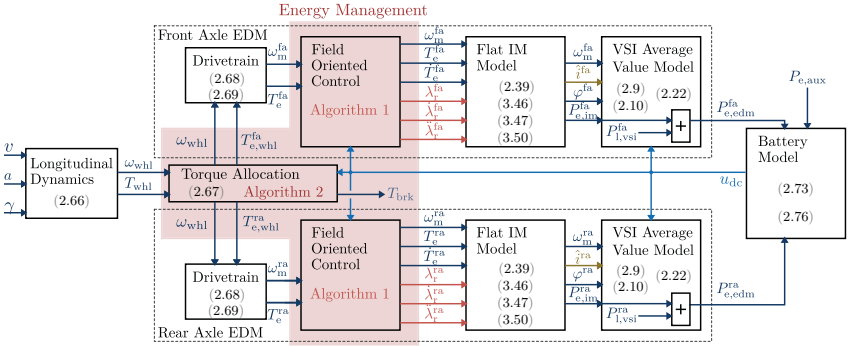

Figure 4.1: Differential flat system model of an all-wheel-drive battery electric vehicle.

Section 4.2 introduces a torque allocation strategy, as part of the AWD architecture, that influences the first group of losses. Similar to the LMT of the IM drive, this strategy is presented in an algorithmic form. This approach reaches its full potential with different solutions for drive designs. In the case of the experimental vehicle, two distinct IMs are used that are both designed for different speed ranges. The second group of losses can be influenced by ED strategies. A centralized optimization based approach that considers both the variable flux level and the torque allocation is proposed in Section 4.3. For a meaningful evaluation of these energy management strategies, it is essential that the flat system model provides accurate range related information. The model accuracy and performance is thus evaluated in the following Section 4.1.

4.1 Model-Based Range Analyses

One of the key questions of the model-based approach is whether the flat system model shown in Figure 4.1 is capable of providing accurate range-related information in a reasonable computation time. A main reason why sophisticated component models of the electric drive have not been considered for economic driving analyses are the long computation times, which are associated with the demanding time constant of the motors current dynamics. However, the flat system model can be considered as less dynamic, since all electrical states are determined by the flat output, i. e. the rotor speed, torque, and flux linkage. While the former two naturally describe a mechanical driving profile, the rotor flux is controlled via a loss minimizing FOC so that the mechanical load is converted in the most efficient manner. Consequently, the flux dynamics are governed by the speed and torque profile. This creates the prerequisite

for efficient formulations of optimal control problems.

To evaluate both the accuracy and computational effort, a field study was conducted covering a distance of 1.450 km on selected routes in the area around Stuttgart, Germany, in the period from August to November 2018 [151]. In total, five routes were driven at least twice by three different drivers yielding a total number of 32 test cycles. Along with the mixed and urban route, which are used for the experimental validation of Section 2.6, additional routes are considered that mainly run on freeways at an average speed of 80 km/h as well as on priority roads and federal highways in the suburban area with an average speed of 40 km/h. All routes exhibit a relatively large variation in elevation. Further information on the field study and key characteristics of the individual routes are listed in Appendix A.4.

The modeled BEV range is evaluated by looking at the total energy depletion from the battery

$$E_{\mathrm{bat}}|_{\mathrm{mea}} = \int_{t_0}^{t_\mathrm{f}} u_{\mathrm{dc,bat}}\, i_{\mathrm{dc,bat}}\, \mathrm{dt}\,, \tag{4.1}$$

where $u_{\mathrm{dc,bat}}$ and $i_{\mathrm{dc,bat}}$ are the measured battery terminal voltage and current. This is compared to the modeled results of

$$E_{\mathrm{bat}}|_{\mathrm{mod}} = \int_{t_0}^{t_\mathrm{f}} P_{\mathrm{e,edm}}^{\mathrm{fa}} + P_{\mathrm{e,edm}}^{\mathrm{ra}} + P_{\mathrm{e,aux}}\, \mathrm{dt}\ . \tag{4.2}$$

The input of the BEV system model is the measured vehicle speed and the road grade obtained from GPS data. The wheel torque and speed are computed according to the longitudinal dynamics of the vehicle. Subsequently, the torque allocation strategy that is implemented on the MCU of the experimental vehicle is used to compute the front and rear axle torque requests $T_{\mathrm{e}}^{\mathrm{fa}}$, $T_{\mathrm{e}}^{\mathrm{ra}}$. These are controlled in a decentralized manner by each individual low-level EDM control. Due to the dynamic capabilities of the electric motor and the comparably slow longitudinal dynamics of the BEV, it is assumed that the torque reference is ideally tracked. Consequently, all electrical variables downstream of the electric motor can be computed by means of the state and input parametrization of the equivalent flat system and the average value model of the VSI. Algorithm 1 computes the flux level λ_{r} as a function of the mechanical load $\omega_{\mathrm{m}}, T_{\mathrm{e}}$. Derivatives of the speed, torque and flux profile are computed using a differentiating Savitzky-Golay filter [198]. If the rotor flux profile is known, the analytical expressions of the drive train {(2.68),(2.69)}, the differential flat state- and input-parametrization of the IM {(3.46),(3.47),(3.50)}, the average value model of the

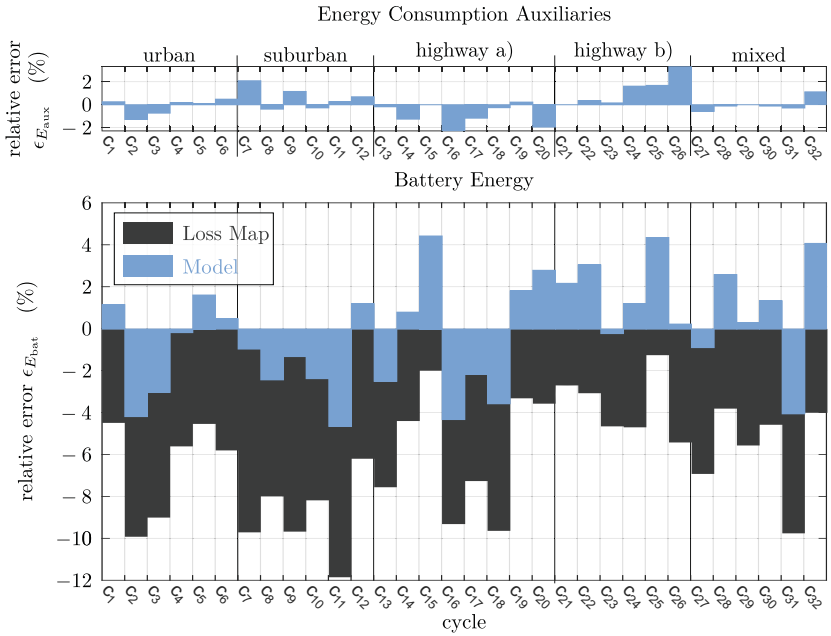

Figure 4.2: Relative error of the total energy depletion computed for the 32 test cycles of the field study (cf. [149, 151]).

VSI {(2.9),(2.10),(2.22)}, and finally the battery model {(2.76),(2.73)} are computed without any notable effort. When it is not known, the computation of the rotor flux by means of Algorithm 1 is the only demanding procedure. Since the defining problems of a loss minimizing FOC strategy are shown to be convex, in the case of driving, efficient algorithms can be used to implement Algorithm 1. Though the problem is not convex in the case of braking, positive convergence properties for same algorithms are observed. The EDM model and the algorithm are, thus, successfully implemented on an experimental build of the MCU software. When computed on a single thread of an *Intel Core* i7-5600U processor, the full BEV system model of Figure 4.1 requires less than 4 s on average to simulate a driving cycle with a duration of one hour.

Table 4.1: Percentage share of power loss sources observed during the field study.

route	recording time h	amb. temp. °C	avg. speed km/h	EDM losses %	auxiliaries %	battery %
urban	1.12	14	24	58	40	2
urban	2.07	4	26	34	64	2
suburban	5.70	3	41	32	65	3
highway	1.67	27	81	58	33	9
highway	5.00	20	80	59	32	9
highway	3.40	12	80	58	34	8
highway	1.64	6	82	48	45	7
mixed	3.93	29	54	53	41	6

The quality of the predicted range is evaluated by the relative error in energy consumption

$$\epsilon_{E_{\mathrm{bat}}} = \frac{E_{\mathrm{bat}}|_{\mathrm{mod}} - E_{\mathrm{bat}}|_{\mathrm{mea}}}{E_{\mathrm{bat}}|_{\mathrm{mea}}} \,. \tag{4.3}$$

This error is indicated in Figure 4.2 for all five routes and test cycles $\mathrm{c_i} \forall \mathrm{i} \in 1(1)32$ of the field study. For reference purposes, the error of the estimated auxiliary power consumption

$$\epsilon_{E_{\mathrm{aux}}} = \frac{E_{\mathrm{aux}}|_{\mathrm{mod}} - E_{\mathrm{aux}}|_{\mathrm{mea}}}{E_{\mathrm{bat}}|_{\mathrm{mea}}} \tag{4.4}$$

is shown in the top graph. This error takes on rather small values, indicating that the average auxiliary power is estimated well. The error of the modeled battery energy is below $|\epsilon_{E_{\mathrm{bat}}}| < 5\,\%$ with a standard deviation over all cycles of 2.7 %. If the same quantity is computed using the EDM loss map, the error increases with $\epsilon_{E_{\mathrm{bat}}} \in (-1, -12)\,\%$ and a standard deviation of 2.8 %. This behavior is expected, as seen in Figure 2.15, which shows that the loss map mostly underestimates losses. However, it is noted that the maps bias of a $-6\,\%$ error can be corrected in order to derive more accurate range information.

A similar analysis is conducted in [149] based on the same field study, however, using empirically determined loss models (cf. Figure 2.21; Input $\mathcal{U}_v$; mixed: R1, highway a): R2, highway b): R3, urban: R4, suburban: R5). Compared to a relative error of $\epsilon_{E_{\mathrm{bat}}} \in (-10, 4)\,\%$ that is achieved in the presented approach, the proposed model-based framework considerably improves the prediction accuracy, particularly on urban routes that are influenced by a multitude of transient stop and go maneuvers. In summary, on all routes of the field study the mean relative error of the the flat BEV system model is $-0.1\,\%$ with a standard deviation of 2.8 %, which demonstrates that realistic range-related information can be provided at a computational effort that

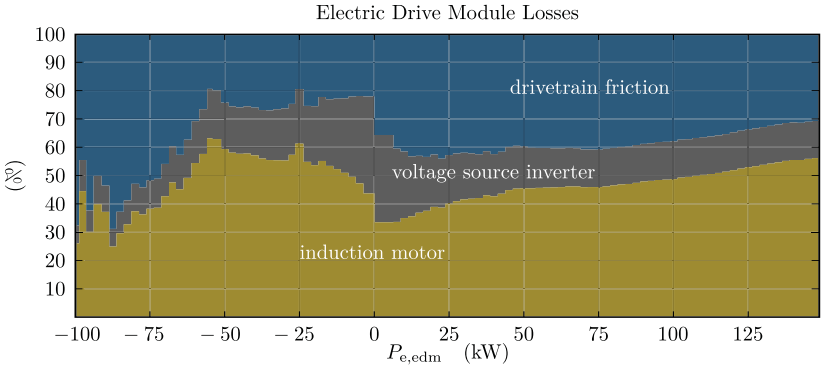

Figure 4.3: Distribution of EDM power loss sources observed during the PIC test series.

is comparable to characteristic loss maps.

To identify saving potentials of energy management strategies, it is useful to know the distribution of losses within the electrical powertrain. Table 4.1 shows how the power loss is separated into drive modules, auxiliaries, and the battery on different routes of the field study and how they depend on the ambient temperature. The indicated percentage share is computed by using the time average of the battery power, the EDM power, the mechanical power, and a model-based approximation of the internal battery loss, which is derived form the DC-link current measurement. For reference purposes, the overall recording time, the time average of the ambient temperature and the average vehicle speed are listed. The high share of EDM and auxiliary losses underlines the potential of improved operational strategies and entails the need for accurate loss models. Furthermore, by reducing the losses in the EDM and, consequently, the battery discharge, auxiliary losses will decrease due to lower cooling demands that are placed on the thermal management system.

The distribution of the EDM power losses among the individual EDM components, i. e. the IM, VSI and drivetrain, is shown in Figure 4.3 for one of the motors. The indicated values sum up to 100 % and represent the average value over all data points collected during the PIC test series. The highest proportion of losses are attributed to the IM during regenerative braking and a moderate power throughput of $P_{\mathrm{e,edm}} > -75\,\mathrm{kW}$. In this region, the VSI and IM make up over 70 % of all EDM losses. For driving operation, within the region of $P_{\mathrm{e,edm}} < 75\,\mathrm{kW}$, the loss distribution between the drivetrain and the IM is almost the same with approximately 40 % each. However,

the amount of IM losses climb with increasing power demand and current. Looking at the VSI, it is noted that the switching and conduction losses only make up a small amount of the EDM losses, except for the operating region of $|P_{\mathrm{e,edm}}| < 25\,\mathrm{kW}$ with a share of up to 34 %. In conclusion, this analysis shows that the main factor of EDM losses, that can be influenced by control strategies, is the IM phase current. One possibility to reduce the phase current is to reallocate the traction or brake energy to another motor in an AWD BEV.

4.2 Torque Allocation Strategies for All-Wheel-Drive BEVs

A variable torque allocation offers a high flexibility to improve both the driving performance and energy efficiency of a AWD BEV. In a BEV with both a front and rear axle motor, the driver's request can be achieved by an infinite number of torque distributions. This torque distribution is modeled by means of the coefficient $\theta_{\mathrm{spl}} \in [0, 1]$, which allocates

$$T_{\mathrm{e,whl}}^{\mathrm{fa}} = \theta_{\mathrm{spl}} T_{\mathrm{e,whl}} \tag{4.5}$$

to the front axle and

$$T_{\mathrm{e,whl}}^{\mathrm{ra}} = (1 - \theta_{\mathrm{spl}})\, T_{\mathrm{e,whl}} \tag{4.6}$$

to the rear axle, where $T_{\mathrm{e,whl}}$ is the electric wheel torque defined in (2.67). For simplicity and since the dynamic driving behavior is not the major focus in this study, the front and rear axle are assumed to have the same angular speed.

As a consequence of a high power demand, the DC voltage drops, which in turn influences the control and flux strategy of the EDMs as well as the torque allocation strategy. One of the most important performance quantifiers that is influenced by the voltage level is the minimum and maximum torque ratings $T_{\mathrm{e,whl,lb}}, T_{\mathrm{e,whl,ub}}$. These are both defined by the operational region of the BEV and the limitations of each individual EDM

$$\mathcal{O}_{\mathrm{ev}} = \left\{ \omega_{\mathrm{whl}}, T_{\mathrm{e,whl}} \in \mathbb{R}_+ \times \mathbb{R} |\ \omega_{\mathrm{m}}^{\mathrm{fa}}, T_{\mathrm{e}}^{\mathrm{fa}} \in \mathcal{O}_{\mathrm{edm}}^{\mathrm{fa}}\,,\ \omega_{\mathrm{m}}^{\mathrm{ra}}, T_{\mathrm{e}}^{\mathrm{ra}} \in \mathcal{O}_{\mathrm{edm}}^{\mathrm{ra}}\,. \right\} \tag{4.7}$$

It is necessary to know these boundaries in order to define the feasible region of the torque split coefficient $\theta_{\mathrm{spl}} \in [\theta_{\mathrm{spl,lb}}, \theta_{\mathrm{spl,ub}}]$ with

$$\theta_{\mathrm{spl,lb}} = \min\left\{\theta_{\mathrm{spl}}^{\mathrm{fa}}, \theta_{\mathrm{spl}}^{\mathrm{ra}}\right\}\,, \qquad \theta_{\mathrm{spl,ub}} = \max\left\{\theta_{\mathrm{spl}}^{\mathrm{fa}}, \theta_{\mathrm{spl}}^{\mathrm{ra}}\right\}\,, \tag{4.8a}$$

where

$$\theta_{\mathrm{spl}}^{\mathrm{fa}} = \begin{cases} \min\left\{\dfrac{T_{\mathrm{e,whl,ub}}^{\mathrm{fa}}}{T_{\mathrm{e,whl}}}, 1\right\}, & T_{\mathrm{e,whl}} \in \left(0, T_{\mathrm{e,whl,ub}}^{\mathrm{fa}} + T_{\mathrm{e,whl,ub}}^{\mathrm{ra}}\right] \\ \min\left\{\dfrac{T_{\mathrm{e,whl,lb}}^{\mathrm{fa}}}{T_{\mathrm{e,whl}}}, 1\right\}, & T_{\mathrm{e,whl}} \in \left[T_{\mathrm{e,whl,lb}}^{\mathrm{fa}} + T_{\mathrm{e,whl,lb}}^{\mathrm{ra}}, 0\right) \\ 1, & T_{\mathrm{e,whl}} = 0 \end{cases}, \tag{4.8b}$$

$$\theta_{\mathrm{spl}}^{\mathrm{ra}} = \begin{cases} \max\left\{1 - \dfrac{T_{\mathrm{e,whl,ub}}^{\mathrm{ra}}}{T_{\mathrm{e,whl}}}, 0\right\}, & T_{\mathrm{e,whl}} \in \left(0, T_{\mathrm{e,whl,ub}}^{\mathrm{fa}} + T_{\mathrm{e,whl,ub}}^{\mathrm{ra}}\right] \\ \max\left\{1 - \dfrac{T_{\mathrm{e,whl,lb}}^{\mathrm{ra}}}{T_{\mathrm{e,whl}}}, 0\right\}, & T_{\mathrm{e,whl}} \in \left[T_{\mathrm{e,whl,lb}}^{\mathrm{fa}} + T_{\mathrm{e,whl,lb}}^{\mathrm{ra}}, 0\right) \\ 0, & T_{\mathrm{e,whl}} = 0 \end{cases}. \tag{4.8c}$$

Along with the flux level, Algorithm 1 is capable of computing these boundaries for all possible operating conditions.

4.2.1 Energy-Efficient Torque Allocation

A re-allocation of traction or braking energy to the other motor reduces the power throughput in both motors and, consequently, the magnitude of associated DC and AC currents. As EDM losses increase at a higher than linear rate with the current magnitude, a re-allocation of energy can improve the overall performance at high power demands. At low power demands, however, the support of a second EDM may negatively effect the energy efficiency by introducing an additional source of losses, e. g. the switching and conduction losses of the second VSI. This section proposes a real-time capable analytical framework for an optimized energy management strategy, which maximizes the powertrain efficiency via the torque split coefficient θ_{spl}.

Assuming steady state operating conditions, the optimal torque allocation is computed based on the constrained one-dimensional optimization problem

$$\underset{\theta_{\mathrm{spl}}}{\text{minimize}} \quad P_{\mathrm{l,edm}}^{\mathrm{fa}}\left(\omega_{\mathrm{m}}^{\mathrm{fa}}, T_{\mathrm{e}}^{\mathrm{fa}}, u_{\mathrm{dc}}\right) + P_{\mathrm{l,edm}}^{\mathrm{ra}}\left(\omega_{\mathrm{m}}^{\mathrm{ra}}, T_{\mathrm{e}}^{\mathrm{ra}}, u_{\mathrm{dc}}\right) \tag{4.9a}$$

$$\text{subject to} \quad T_{\mathrm{e}}^{\mathrm{fa}} = \frac{\theta_{\mathrm{spl}}\, T_{\mathrm{e,whl}} + T_{\mathrm{dt}}^{\mathrm{fa}}\left(\omega_{\mathrm{whl}}, \theta_{\mathrm{spl}} T_{\mathrm{e,whl}}\right)}{\iota_{\mathrm{dt}}^{\mathrm{fa}}}, \tag{4.9b}$$

$$T_{\mathrm{e}}^{\mathrm{ra}} = \frac{\left(1 - \theta_{\mathrm{spl}}\right)\, T_{\mathrm{e,whl}} + T_{\mathrm{dt}}^{\mathrm{ra}}\left(\omega_{\mathrm{whl}}, \left(1 - \theta_{\mathrm{spl}}\right) T_{\mathrm{e,whl}}\right)}{\iota_{\mathrm{dt}}^{\mathrm{ra}}}, \tag{4.9c}$$

$$\omega_{\mathrm{m}}^{\mathrm{fa}} = \omega_{\mathrm{whl}}\, \iota_{\mathrm{dt}}^{\mathrm{fa}}, \tag{4.9d}$$

$$\omega_{\mathrm{m}}^{\mathrm{ra}} = \omega_{\mathrm{whl}}\, \iota_{\mathrm{dt}}^{\mathrm{ra}}, \tag{4.9e}$$

$$\theta_{\mathrm{spl,lb}} \leq \theta_{\mathrm{spl}} \leq \theta_{\mathrm{spl,ub}}\,, \tag{4.9f}$$

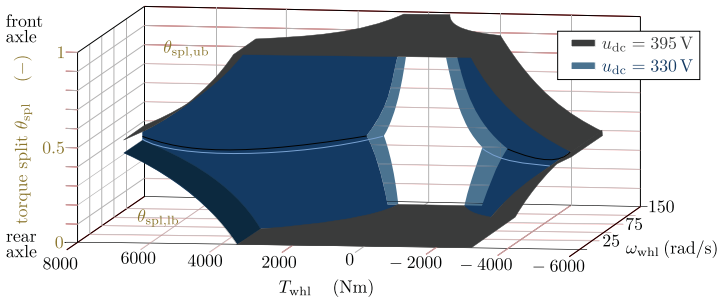

Figure 4.4: Lower and upper limits of the torque split coefficient at different voltage levels.

which yields a solution θ^*_{spl} for a specific operating point $(u_{\mathrm{dc}}, \omega_{\mathrm{whl}}, T_{\mathrm{e,whl}})$. The objective (4.9a) is to minimize front and rear axle EDM losses. As shown in Figure 4.1, these are computed using Algorithm 1, the differential flat IM model, and the average value model of the VSI. The torque request of each individual motor $T_{\mathrm{e}}^{\{\mathrm{fa,ra}\}}$ depends on the respective gear ratio $\iota_{\mathrm{dt}}^{\{\mathrm{fa,ra}\}}$ as well as the torque split coefficient, which also has an influence on the resulting drivetrain friction torque $T_{\mathrm{dt}}^{\{\mathrm{fa,ra}\}}$. The latter is computed as a function of the wheel speed and resulting electric wheel torque. By definition of the upper and lower bounds of the torque split coefficient according to (4.8) and by computing the maximum or minimum torque rating via Algorithm 1, the solution θ^*_{spl} is guaranteed to comply with the IM current and voltage limits. If the magnitude of the electric wheel torque is close to its maximum attainable value, the impact of the restriction on (4.9f) increases. For example, when $T_{\mathrm{e,whl}} \approx T^{\mathrm{fa}}_{\mathrm{e,ub}}\,\iota^{\mathrm{fa}}_{\mathrm{dt}} + T^{\mathrm{ra}}_{\mathrm{e,ub}}\,\iota^{\mathrm{ra}}_{\mathrm{dt}}$, the number of possible distributions $\theta_{\mathrm{spl}} \in [\theta_{\mathrm{spl,lb}}, \theta_{\mathrm{spl,ub}}]$ is reduced to a single feasible point. The feasible set $[\theta_{\mathrm{spl,lb}}, \theta_{\mathrm{spl,ub}}]$ for different voltage levels is depicted in Figure 4.4 as a function of the wheel speed and torque. Figure 4.4 only shows the limits, which are imposed by the operational boundaries of the IM. As the voltage level decreases, the upper and lower bounds become more strict, especially at high vehicle speeds. It is noted that the feasible set of the torque split coefficient may change in the case of a possible current limit as well as for different driving modes with the corresponding minimum regenerative brake torque shown in Figure 2.8.

With increasing complexity, algorithms are unlikely to be implemented on the MCU of the BEV. Therefore, there is a clear need for simple and computationally efficient control algorithms in vehicle applications. Problem (4.9) belongs to the class of nonlinear multi-level optimization problems, as the evaluation of the objective function needs to solve an underlying optimization problem defined within Algorithm 1. Though

this formulation seems complex, it is demonstrated in the previous section, that the LMT algorithm and the BEV system model are highly efficient and computed in real-time. In fact, by defining the boundaries of the torque split coefficient based on the maximum or minimum torque rating of Algorithm 1 and by inclusion of the equality constraints in the cost function, problem (4.9) is reformulated as a one-dimensional problem with a simple box constraint. In this case, the objective function $f_\mathrm{c} : [\theta_\mathrm{spl,lb}, \theta_\mathrm{spl,ub}] \to \mathbb{R}_+$ at a pre-defined wheel speed ω_whl and load torque $T_\mathrm{e,whl}$ is

$$\begin{aligned} f_\mathrm{c}\left(\theta_\mathrm{spl}\right) = & P_\mathrm{l,edm}^\mathrm{fa}\left(\omega_\mathrm{whl}\,\iota_\mathrm{dt}^\mathrm{fa},\ \frac{\theta_\mathrm{spl}\,T_\mathrm{e,whl} + T_\mathrm{dt}^\mathrm{fa}\left(\omega_\mathrm{whl}, \theta_\mathrm{spl} T_\mathrm{e,whl}\right)}{\iota_\mathrm{dt}^\mathrm{fa}},\ u_\mathrm{dc}\right) \ + \\ & P_\mathrm{l,edm}^\mathrm{ra}\left(\omega_\mathrm{whl}\,\iota_\mathrm{dt}^\mathrm{ra},\ \frac{\left(1-\theta_\mathrm{spl}\right)T_\mathrm{e,whl} + T_\mathrm{dt}^\mathrm{ra}\left(\omega_\mathrm{whl}, \left(1-\theta_\mathrm{spl}\right)\,T_\mathrm{e,whl}\right)}{\iota_\mathrm{dt}^\mathrm{ra}},\ u_\mathrm{dc}\right) . \end{aligned} \tag{4.10}$$

With help of the flat state and input parameterization as well as the analytically derived solution of the rotor flux, introduced in Section 3.2, it can be easily verified that the objective function is continuous. Since the box constraint (4.9f) implicitly considers the voltage and current limits of the EDM, no additional constraints are required.

A computationally efficient solution of the reformulated problem is the golden-section search [166]. By applying this search method, a practical torque allocation procedure is implemented in Algorithm 2. The procedure searches for an extremum of a function inside the interval $[\theta_\mathrm{spl,lb}, \theta_\mathrm{spl,ub}]$. With every iteration $\mathrm{i} \in \mathbb{N}$ of the while-loop, the diameter of the search interval

$$d^{[\mathrm{i}]} = {\theta_\mathrm{spl,ub}}^{[\mathrm{i}]} - {\theta_\mathrm{spl,lb}}^{[\mathrm{i}]} \tag{4.11}$$

is reduced until the extremum is located with a specified tolerance of $d^{[\mathrm{i}]} \leq \varepsilon \in \mathbb{R}_+$. By the definition of the golden ratio, each iteration only requires a single evaluation of the objective function (4.10) apart from basic mathematical and memory operations. The golden ratio

$$\alpha_\mathrm{gr} = \frac{\sqrt{5}-1}{2} \approx 0.618 \tag{4.12}$$

is equal to the contraction ratio of the interval. The number of iterations N, required to locate a minimum within the specified tolerance of ε, is given by [166]

$$\mathrm{N} = \left\lfloor \frac{\ln\left(\varepsilon\right) - \ln\left(\theta_\mathrm{spl,ub} - \theta_\mathrm{spl,lb}\right)}{\ln\left(\alpha_\mathrm{gr}\right)} \right\rfloor . \tag{4.13}$$

For example, in the worst case of $\theta \in [0, 1]$, the search interval is reduced to $d < 0.01$ within nine iterations. This narrows down the optimal torque allocation up to a 1 % tolerance of the traction or braking torque $T_\mathrm{e,whl}$.

By applying Algorithm 2, the torque split coefficient for the minimum power loss θ_spl^* and the coefficient for the maximum power loss θ_spl^{wc} are derived for a constant voltage

Algorithm 2 : Efficiency Optimized Torque Allocation

Require: tolerance ε, golden ratio α_{gr}, EDM system model and parameter.

procedure $\theta^{*}_{\mathrm{spl}}(u_{\mathrm{dc}}, \omega_{\mathrm{whl}}, T_{\mathrm{e,whl}})$
  for front and rear axle **do**
    if $T_{\mathrm{e,whl}} \geq 0$ **then** ▷ check if BEV is in driving or braking operation.
      $T^{\mathrm{axle}}_{\mathrm{e,ub}} \leftarrow$ (3.26a) ▷ solve (3.26a) for maximum torque rating.
      $T^{\mathrm{axle}}_{\mathrm{e,whl,ub}} \leftarrow$ (2.69b) ▷ account for friction losses.
    else
      $T^{\mathrm{axle}}_{\mathrm{e,lb}} \leftarrow$ (3.26b) ▷ solve (3.26a) for minimum torque rating.
      $T^{\mathrm{axle}}_{\mathrm{e,whl,lb}} \leftarrow$ (2.69b) ▷ account for friction losses.
    end if
  end for
  $\theta_{\mathrm{spl,lb}}, \theta_{\mathrm{spl,ub}} \leftarrow$ (4.8) ▷ initialize search interval.
  $d \leftarrow \theta_{\mathrm{spl,ub}} - \theta_{\mathrm{spl,lb}}$ ▷ initialize diameter of search interval.
  $cost_{\mathrm{lb}} \leftarrow f_{\mathrm{c}}|_{\theta_{\mathrm{spl,lb}}}$ ▷ compute EDM losses (4.10) for lower bound $\theta_{\mathrm{spl,lb}}$.
  $cost_{\mathrm{ub}} \leftarrow f_{\mathrm{c}}|_{\theta_{\mathrm{spl,ub}}}$ ▷ compute EDM losses (4.10) for upper bound $\theta_{\mathrm{spl,ub}}$.
  $\theta_{\mathrm{a}} \leftarrow \theta_{\mathrm{spl,lb}} + (1 - \alpha_{\mathrm{gr}})\, d$ ▷ first internal point $\theta_{\mathrm{a}} \in [\theta_{\mathrm{spl,lb}}, \theta_{\mathrm{spl,ub}}]$
  $\theta_{\mathrm{b}} \leftarrow \theta_{\mathrm{spl,lb}} + \alpha_{\mathrm{gr}} d$ ▷ second internal point $\theta_{\mathrm{b}} \in [\theta_{\mathrm{spl,lb}}, \theta_{\mathrm{spl,ub}}]\,,\ \theta_{\mathrm{b}} > \theta_{\mathrm{a}}$
  $cost_{\mathrm{a}} \leftarrow f_{\mathrm{c}}|_{\theta_{\mathrm{spl,a}}}$ ▷ compute EDM losses (4.10) for $\theta_{\mathrm{spl,a}}$.
  $cost_{\mathrm{b}} \leftarrow f_{\mathrm{c}}|_{\theta_{\mathrm{spl,b}}}$ ▷ compute EDM losses (4.10) for $\theta_{\mathrm{spl,b}}$.
  while $d > \varepsilon$ **do**
    if $cost_{\mathrm{a}} < cost_{\mathrm{b}}$ **then** ▷ compare cost values of internal points.
      $\theta_{\mathrm{spl,ub}} \leftarrow \theta_{\mathrm{b}}$ ▷ minimum must lie within $[\theta_{\mathrm{spl,lb}}, \theta_{\mathrm{b}}]$.
      $cost_{\mathrm{ub}} \leftarrow cost_{\mathrm{b}}$ ▷ update cost for upper bound.
      $\theta_{\mathrm{b}} \leftarrow \theta_{\mathrm{a}};\ \ cost_{\mathrm{b}} \leftarrow cost_{\mathrm{a}}$ ▷ replace second with first inter. point.
      $d \leftarrow \theta_{\mathrm{spl,ub}} - \theta_{\mathrm{spl,lb}}$ ▷ update diameter of search interval.
      $\theta_{\mathrm{a}} \leftarrow \theta_{\mathrm{spl,lb}} + (1 - \alpha_{\mathrm{gr}})\, d$ ▷ update first internal point.
      $cost_{\mathrm{a}} \leftarrow f_{\mathrm{c}}|_{\theta_{\mathrm{spl,a}}}$ ▷ update cost (4.10) for first internal point.
    else
      $\theta_{\mathrm{spl,lb}} \leftarrow \theta_{\mathrm{a}}$ ▷ minimum must lie within $[\theta_{\mathrm{spl,a}}, \theta_{\mathrm{ub}}]$.
      $cost_{\mathrm{lb}} \leftarrow cost_{\mathrm{a}}$ ▷ update cost for lower bound.
      $\theta_{\mathrm{a}} \leftarrow \theta_{\mathrm{b}};\ \ cost_{\mathrm{a}} \leftarrow cost_{\mathrm{b}}$ ▷ replace first with second inter. point.
      $d \leftarrow \theta_{\mathrm{spl,ub}} - \theta_{\mathrm{spl,lb}}$ ▷ update diameter of search interval.
      $\theta_{\mathrm{b}} \leftarrow \theta_{\mathrm{spl,lb}} + \alpha_{\mathrm{gr}} d$ ▷ update second internal point.
      $cost_{\mathrm{b}} \leftarrow f_{\mathrm{c}}|_{\theta_{\mathrm{spl,b}}}$ ▷ update cost (4.10) for second internal point.
    end if
  end while
  return: $\operatorname{argmin}\{cost_{\mathrm{lb}}, cost_{\mathrm{a}}, cost_{\mathrm{b}}, cost_{\mathrm{ub}}\}$ ▷ return the split coefficient with the lowest cost

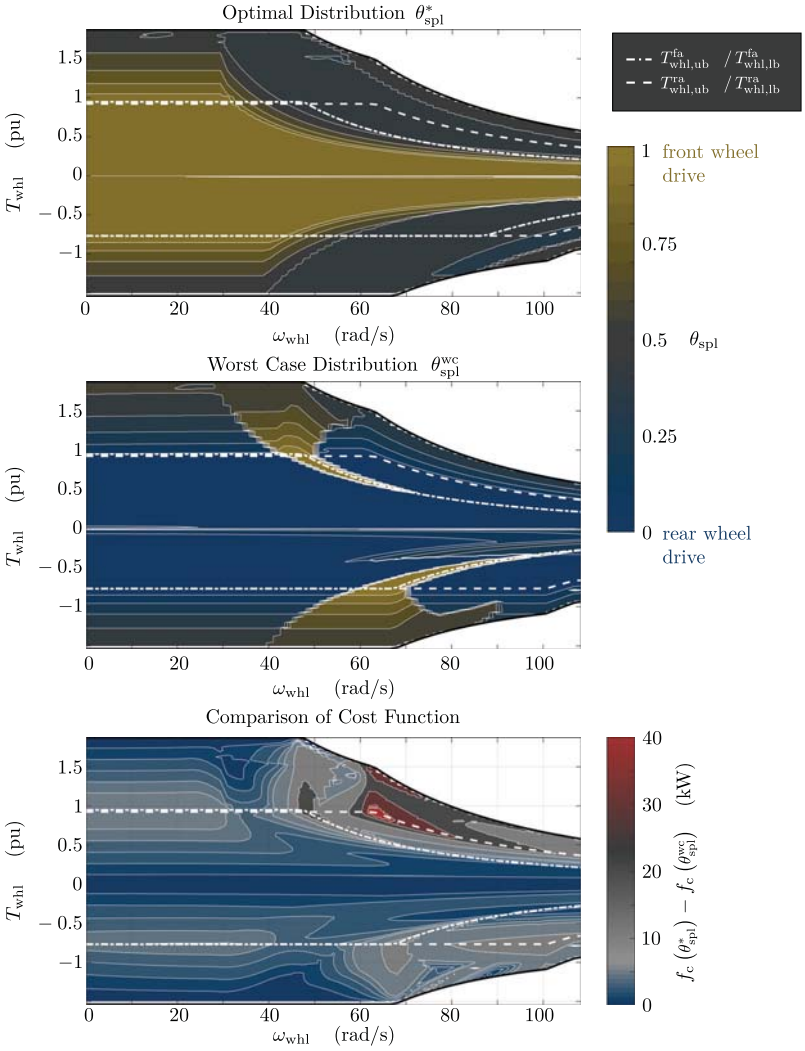

Figure 4.5: Comparison of optimal and worst case torque distributions computed by Algorithm 2.

level and for all feasible operating points $\omega_{\mathrm{whl}}, T_{\mathrm{whl}} \in \mathcal{O}_{\mathrm{ev}}$. Figure 4.5 summarizes the results and displays the solution $\theta^{*}_{\mathrm{spl}}$ with the highest efficiency in the upper graph. The characteristic of the worst case coefficient $\theta^{wc}_{\mathrm{spl}}$ is shown in the second graph. The bottom graph compares the resulting cost functions (4.10) and illustrates the cost difference of $f_{\mathrm{c}}\left(\theta^{wc}_{\mathrm{spl}}\right) - f_{\mathrm{c}}\left(\theta^{*}_{\mathrm{spl}}\right)$. Isolines, connecting points of equal value, are shown as white lines.

Looking at the optimal distribution, it is observed that the front axle EDM is more efficient at low speeds, whereas for an increasing speed, a higher amount of torque is allocated to the rear axle. Up to a speed of 30 rad/s during driving and a speed of 40 rad/s during braking, the wheel torque is fully allocated to the front axle as long as $T^{\mathrm{fa}}_{\mathrm{e}} \in \mathcal{O}^{\mathrm{fa}}_{\mathrm{edm}}$. Above these speed values, torque is also allocated to the rear axle before the front axle reaches its maximum rating. As soon as the requested torque exceeds the maximum or minimum torque rating the optimal distribution more and more resembles an AWD strategy with equal split.

In the worst case, the wheel torque is almost fully allocated to the rear axle within $T^{\mathrm{ra}}_{\mathrm{e}} \in \mathcal{O}^{\mathrm{ra}}_{\mathrm{edm}}$. However, in the region of (3.19b), where the wheel torque is limited by the maximum attainable phase voltage, and for a torque, which is close to the lower or upper bound of the front axle EDM $T_{\mathrm{e,whl}} \approx T^{\mathrm{fa}}_{\mathrm{e,whl},\{\mathrm{ub,lb}\}}$, the worst strategy would be to operate the BEV as a FWD.

The comparison of the optimal and worst-case strategy reveals a energy saving potential of up to 3 kW in the partial load area and a saving of up to 5 kW at high power demands and low speeds. However, the greatest advantage with savings of up to 40 kW, is achieved at speeds above 60 rad/s and high power demands, which exceed the operating regions of each individual EDM, $\mathcal{O}^{\mathrm{fa}}_{\mathrm{edm}}$ and $\mathcal{O}^{\mathrm{ra}}_{\mathrm{edm}}$. These analyses confirm that a re-allocation of traction or braking torque to a second EDM can improve the overall efficiency of a BEV.

4.2.2 Experimental Validation

The proposed allocation strategy is tested during the PIC test series, which is introduced in Section 2.6. Algorithm 2 is implemented on the MCU of the experimental vehicle and adapted to compute the optimal distribution based on the BEV system model as well as by using characteristic loss maps of the EDMs. The model-based approach is denoted by $\theta^{*}_{\mathrm{spl}}\big|_{mdl}$ and the map-based strategy is referred to as $\theta^{*}_{\mathrm{spl}}\big|_{map}$. Both are compared to a pure front and RWD mode, where

$$\theta^{\mathrm{fa}}_{\mathrm{spl}} = 1, \qquad \theta^{\mathrm{ra}}_{\mathrm{spl}} = 0\,, \tag{4.14}$$

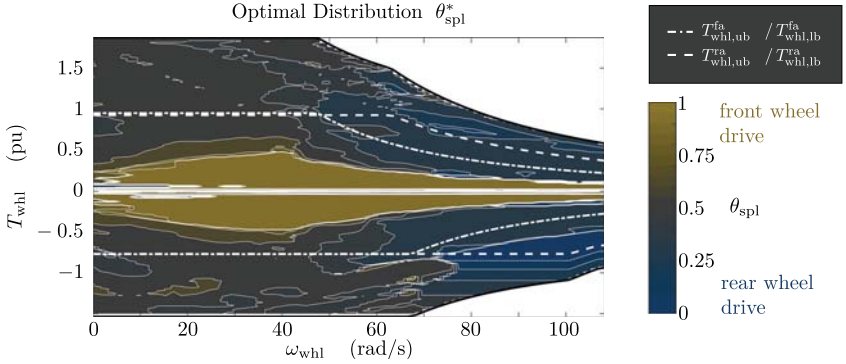

Figure 4.6: Optimal torque distribution computed via the characteristic loss map.

as well as to an even AWD distribution between front and rear axle with

$$\theta^{50/50}_{\mathrm{spl}} = 0.5\,. \tag{4.15}$$

For the PIC test series a different set of model parameters is used as in the case for the validation results of Section 2.6, since these are identified afterwards, based on the recorded data. The torque split strategy, which corresponds to the adapted parameter set closely resembles the strategy of the map-based approach. An exemplary characteristic of $\theta^*_{\mathrm{spl}}\big|_{map}$ for a constant terminal voltage is shown in Figure 4.6. This strategy is different when it is compared to the characteristics of Figure 4.5, where the full operational range of the front axle is not fully exploited for speeds below 40 rad/s. Moreover, above this speed value, traction and braking energy is already reallocated to the rear axle starting at lower torque requests.

For the evaluation and comparison of all strategies, the traction energy is obtained by

$$E_{\mathcal{T}} = \int_{t_0}^{t_{\mathrm{f}}} (u^{\mathrm{fa}}_{\mathrm{dc,edm}}\, i^{\mathrm{fa}}_{\mathrm{dc,edm}})\big|_{T_{\mathrm{whl}}>0} + (u^{\mathrm{ra}}_{\mathrm{dc,edm}}\, i^{\mathrm{ra}}_{\mathrm{dc,edm}})\big|_{T_{\mathrm{whl}}>0}\,\mathrm{dt}\,, \tag{4.16}$$

where $u_{\mathrm{dc,edm}}$ and $i_{\mathrm{dc,edm}}$ are the measurements of the respective EDM terminal voltage and current, which are only recorded during driving. Analogously, the braking energy is defined by

$$E_{\mathcal{B}} = \int_{t_0}^{t_{\mathrm{f}}} (u^{\mathrm{fa}}_{\mathrm{dc,edm}}\, i^{\mathrm{fa}}_{\mathrm{dc,edm}})\big|_{T_{\mathrm{whl}}<0} + (u^{\mathrm{ra}}_{\mathrm{dc,edm}}\, i^{\mathrm{ra}}_{\mathrm{dc,edm}})\big|_{T_{\mathrm{whl}}<0}\,\mathrm{dt}\,. \tag{4.17}$$

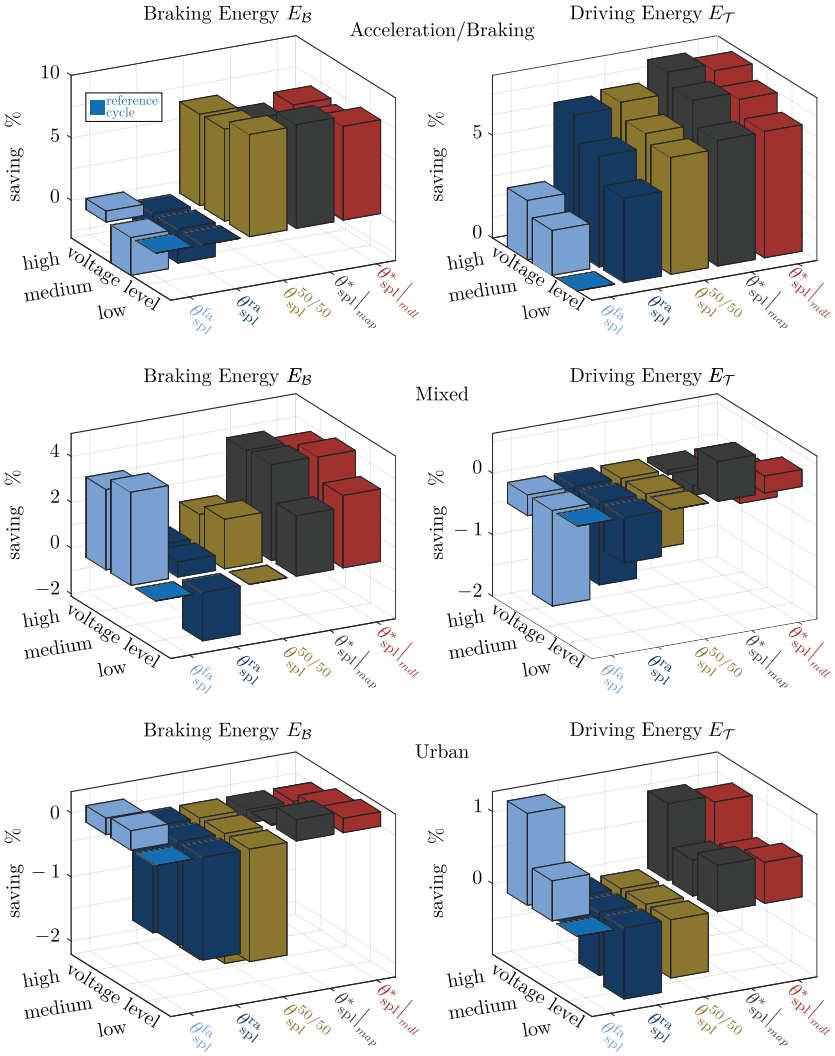

Figure 4.7: PIC experimental results: Energy saving potential for different torque allocation strategies.

Both traction and braking energy are computed for the acceleration and braking scenario, the mixed route, and the urban route. These three scenarios are repeated for a high, medium, and low initial voltage level of the battery as well as for the operational strategies of $\theta_{\mathrm{spl}}^{\mathrm{fa}}$, $\theta_{\mathrm{spl}}^{\mathrm{ra}}$, $\theta_{\mathrm{spl}}^{50/50}$, $\theta_{\mathrm{spl}}^{*}\big|_{map}$, and $\theta_{\mathrm{spl}}^{*}\big|_{mdl}$. The results of all fifteen cycles are shown in Figure 4.7. The graphs present the energy saving potential compared to the cycle with the lowest voltage level and FWD mode. All cycles are evaluated in relation to the FWD mode, since the front axle EDM is identified as the most efficient motor over a wide speed range. If different strategies are compared to each other, the difference in saving potential is always compared to the cycle with the same voltage level. A negative saving potential indicates that less energy is regenerated during braking and that more energy is consumed during traction. The reverse applies for a positive saving potential. The left column displays the braking energy, the right column the traction energy. Several important conclusions can be drawn from this analysis.

First, it is observed that the initial voltage level of the battery has a notable impact on the traction or braking energy. This is most evident for the acceleration and braking scenario, where for a high voltage level 3 % less traction energy is required than for a low voltage level. Therefore, it is important to account for the voltage dependency in any powertrain related operational strategy. The model-based approach is particularly suited to consider this influence.

Secondly, in nearly all cases the allocation strategy of Algorithm 2 achieves an improved efficiency compared to a FWD, RWD, or an even torque split. Though the map-based strategy generally performs better, similar positive results are also obtained for the model-based approach. Considering the inferior choice of the parameter set, which was used for the test series, as well as the improved accuracy observed in Figure 2.15 for the newly identified parameter set, it is expected that the performance of the model-based approach can be further improved. The highest saving potential of 9.5 % is attained during braking for the acceleration and braking cycle with a medium initial voltage. For the same cycle, 5 % less energy is required during traction. This is expected, as for the scenario under consideration, the BEV is predominantly operated in high speed and high torque regions. In the previous section, these are identified as the regions with the greatest advantage. It is noted that for this very dynamic and demanding cycle, the performance of an even torque split is similar to the optimized strategy.

Finally, in the case of the mixed and urban route, the vehicle is mainly operated in the partial load area. Nevertheless, looking at the mixed routes, Algorithm 2 achieves a saving potential of up to 3 % during braking and up to 1.4 % during traction. However, the advantage over the FWD is reduced, as less energy is regenerated for a medium

and high voltage level. This degradation becomes even more evident for the urban route, where a FWD outperforms the optimized torque allocation. Only at a low voltage level is there an advantage for Algorithm 2, due to the reduced maximum torque rating. This result suggests that the optimized characteristic in Figure 4.5, which is derived from the EDM model with the newly identified parameter set, is closer to the actual optimum than the map-based characteristic of Figure 4.6. The reason for this conclusion is, that the updated model-based approach and resulting allocation strategy uses the front axle EDM more extensively in the partial load area.

To summarize, the proposed allocation strategy consumes between 0.6 % and 2 % less battery energy on the mixed route compared to a FWD. This demonstrates that an AWD powertrain which adopts Algorithm 2 can improve the overall efficiency and extend the vehicle's range. However, to achieve a significant improvement within partial load areas, a precise representation of EDM losses is required. The model-based approach is capable of providing this information. Furthermore, in order to reach its full potential, control strategies need to be incorporated into the design process of the EDMs. If electric drive designs focus on economical aspects rather than on driving performance, smaller motors could be used which are designed to operate either at low or high speeds. A downsizing of motors will lead to an operation that is shifted from the partial load area towards the maximum power ratings. As demonstrated in the previous chapter, these regions particularly benefit from Algorithm 2.

4.3 Model Predictive Control Strategies for Economic Driving

In the final section all energy management strategies presented so far are joined to a centralized, predictive control strategy for ED. Due to the fast response behavior of the EDM, its control is designed independently of the torque allocation strategy. However, both are not necessarily decoupled. Furthermore, as the allocation strategy is only designed for stationary conditions, the question arises whether an optimization-based strategy for transient operation can improve the energy efficiency of the electric powertrain.

To thoroughly plan the allocation of traction and braking energy, but also of the energy that is stored in the magnetic field of an IM, it is desirable to include predictions on future power demands into the optimization process [219, 251]. The differential flat system model shown in Figure 4.1 is particularly well suited to derive meaningful forecasts from vehicle speed predictions. The main influencing factor and greatest source of uncertainties of speed predictions is the driver's behavior [241]. Assuming that the trip destination is known and communicated to a navigation system, further information including the slope, traffic condition and the road infrastructure (speed limits, road curvature, yield signs, roundabouts, traffic lights, etc.) are provided by

navigation services, for example by HERE technologies. Different prediction methods essentially differ in the length of the look-ahead horizon, which can be expressed in terms of time or distance. Long-horizon predictions over several km are anticipated for traffic management, routing problems or energy forecasts [150]. Short-horizon predictions, over the time scale of a view seconds, are required for autonomous driving functions [152] and for energy management [26]. The shorter the horizon and the denser the traffic, the stronger the driving behavior is influenced by the vehicle's environment and the traffic-dictated speed. In these cases, information is preferably derived from sensors, including cameras as well as radar and lidar sensors, and moreover, may be provided by vehicle-to-vehicle and vehicle-to-infrastructure communication technologies [231]. One widely discussed use case of these technologies is the possibility to gain information on traffic-light states in order to optimally guide the vehicle through "green windows" [5, 46]. A comprehensive survey on driving prediction techniques is found in [251]. Research on speed and power demand predictions have utilized artificial intelligence based methods [213, 246] as well as Marcov based methods [26, 211].

Given the large number of published studies on speed prediction and keeping the objective of ED in mind, the following section focuses on an optimization framework that is designed to follow a commanded speed reference and to incorporate any form of speed prediction with a reasonable prediction horizon. Even if no state-of-the-art prediction method can be used, a speed reference may be derived under the assumption that a driver will continue with the current maneuver within his or her perception-reaction time. As drivers have shown themselves capable of responding to road stimuli in less than 2.5 s [226], it is assumed that the commanded traction and brake torque and therefore the vehicles longitudinal acceleration does not change within one to two seconds.

4.3.1 Nonlinear Model Predictive Control

The objective of the proposed ED strategy is to minimize energy losses under consideration of the operational boundaries and dynamic capabilities of the EDMs while following a desired or predicted speed trajectory. In view of the differential flat system representation, the control variables, representing the degrees of freedom, are chosen to be the first time derivative of the overall electromagnetic rotor torque

$$\dot{T}_\mathrm{e} = \dot{T}_\mathrm{e}^\mathrm{fa} + \dot{T}_\mathrm{e}^\mathrm{ra}\,, \tag{4.18}$$

the derivative of the torque split coefficient $\dot{\theta}_\mathrm{spl}$, and the first derivatives of the front and rear axle rotor flux $\dot{\lambda}_\mathrm{r}^\mathrm{fa}, \dot{\lambda}_\mathrm{r}^\mathrm{ra}$. In vector notation, these are summarized as

$$\boldsymbol{u} = \left[\dot{T}_\mathrm{e}\ \dot{\theta}_\mathrm{spl}\ \dot{\lambda}_\mathrm{r}^\mathrm{fa}\ \dot{\lambda}_\mathrm{r}^\mathrm{ra}\right]^T \in \mathbb{R}^4\,. \tag{4.19}$$

In order to reduce the complexity, it is assumed that the flux trajectory is of order one $\mathcal{C}^1$ so that the second derivative $\ddot{\lambda}_\mathrm{r}$ can be neglected. The reason for this is that the influence of the second derivative only becomes relevant on a much shorter time scale. For example, this is demonstrated in the optimized step response in Figure 3.16, where it is seen that the optimal $\ddot{\lambda}_\mathrm{r}$ only initiates changes of motion and for most of the time is equal to zero. Furthermore it is assumed that the speed trajectory does not result in a regenerative brake torque outside the BEV's operating region $\mathcal{O}_\mathrm{ev}$. In the case of a dynamic driving scenario, where this assumption is violated, the problem can be easily extended by an additional control input of the mechanical brake torque T_brk. For the experimental vehicle, this assumption is verified, since due to the high power ratings of the EDMs nearly all braking scenarios can be accomplished through regeneration.

Using (4.19), the rotor torque derivatives of the individual axles are defined by

$$\dot{T}_\mathrm{e}^\mathrm{fa} = \dot{T}_\mathrm{e}\theta_\mathrm{spl} + T_\mathrm{e}\dot{\theta}_\mathrm{spl}\,, \tag{4.20}$$

$$\dot{T}_\mathrm{e}^\mathrm{ra} = \dot{T}_\mathrm{e}(1-\theta_\mathrm{spl}) - T_\mathrm{e}\dot{\theta}_\mathrm{spl}\,. \tag{4.21}$$

After integration of (4.20), the wheel torque is computed applying the inverse model of the drivetrain (2.69b). Subsequently the rotor speed is obtained via the simulation of the longitudinal dynamics model. The resulting power losses are modeled by the front and rear axle state and input parametrization of the IM as well as the average value model of the VSI. The system states are thus defined as

$$\boldsymbol{x} = \left[\omega_\mathrm{whl}\ T_\mathrm{e}\ \theta_\mathrm{spl}\ \lambda_\mathrm{r}^\mathrm{fa}\ \lambda_\mathrm{r}^\mathrm{ra}\right]^T \in \mathbb{R}^5\,. \tag{4.22}$$

All other electrical and mechanical states can be derived from the system states $\boldsymbol{x}$ and control inputs $\boldsymbol{u}$. Based on the BEV system model and the selected inputs and

states, the general constrained problem for ED is formulated as

$$\underset{\boldsymbol{u}}{\text{minimize}} \quad \int_{t_0}^{t_f} \mathrm{w}_e \left(P_{\mathrm{l,edm}}^{\mathrm{fa}}(\boldsymbol{x},\boldsymbol{u}) + P_{\mathrm{l,edm}}^{\mathrm{ra}}(\boldsymbol{x},\boldsymbol{u}) \right) + \left(\omega_{\mathrm{whl}}^* - \omega_{\mathrm{whl}}\right)^2 \mathrm{d}t + \vartheta_f\left(\boldsymbol{x}|_{t_f}\right) \tag{4.23a}$$

$$\text{subject to} \quad \dot{\boldsymbol{x}} = f(\boldsymbol{x},\boldsymbol{u},\gamma^*)\,, \tag{4.23b}$$

$$\boldsymbol{x}|_{t_0} = \boldsymbol{x}_0, \tag{4.23c}$$

$$a_{\mathrm{pwm}}\frac{2}{\pi}\left(\frac{u_{\mathrm{ocv}} + \sqrt{u_{\mathrm{ocv}}^2 - 4R_{\mathrm{bat}}P_{\mathrm{bat}}(\boldsymbol{x},\boldsymbol{u})}}{2}\right) - \hat{u}^{\mathrm{fa}}(\boldsymbol{x},\boldsymbol{u}) \geq 0\,,\ \forall t \in [t_0,t_f]\,, \tag{4.23d}$$

$$a_{\mathrm{pwm}}\frac{2}{\pi}\left(\frac{u_{\mathrm{ocv}} + \sqrt{u_{\mathrm{ocv}}^2 - 4R_{\mathrm{bat}}P_{\mathrm{bat}}(\boldsymbol{x},\boldsymbol{u})}}{2}\right) - \hat{u}^{\mathrm{ra}}(\boldsymbol{x},\boldsymbol{u}) \geq 0\,,\ \forall t \in [t_0,t_f]\,, \tag{4.23e}$$

$$\hat{i}_{\mathrm{ub}}^{\mathrm{fa}} - \hat{i}^{\mathrm{fa}}(\boldsymbol{x},\boldsymbol{u}) \geq 0\,, \qquad \forall t \in [t_0,t_f]\,, \tag{4.23f}$$

$$\hat{i}_{\mathrm{ub}}^{\mathrm{ra}} - \hat{i}^{\mathrm{ra}}(\boldsymbol{x},\boldsymbol{u}) \geq 0\,, \qquad \forall t \in [t_0,t_f]\,, \tag{4.23g}$$

$$\boldsymbol{x}_{\mathrm{lb}} \leq \boldsymbol{x} \leq \boldsymbol{x}_{\mathrm{ub}}\,, \qquad \forall t \in [t_0,t_f]\,, \tag{4.23h}$$

$$\boldsymbol{u}_{\mathrm{lb}} \leq \boldsymbol{u} \leq \boldsymbol{u}_{\mathrm{ub}}\,, \qquad \forall t \in [t_0,t_f]\,. \tag{4.23i}$$

The time integral in (4.23a) is equal to the energy that is dissipated via the front and rear axle EDM plus the l_2 norm that penalizes the difference between the controlled speed trajectory ω_{whl} and the speed reference ω_{whl}^*. A weighting factor w_e is introduced to balance between the two objectives of energy efficiency and tracking performance. If the emphasis is placed on the consumption rather than on the tracking performance, a deviation of the predicted trajectory can lead to additional energy savings. The remaining penalty on the terminal state is imposed by the distance function

$$\vartheta_f = \sum_{\mathrm{i}=1}^{5} \mathrm{w}_{x,\mathrm{i}} \left(x_{\mathrm{i}}^*|_{t_f} - x_{\mathrm{i}}|_{t_f} \right)^2 . \tag{4.24}$$

This penalty is viewed as an attractive potential that pulls the speed trajectory towards the desired terminal speed $x_1^*|_{t_f} = \omega_{\mathrm{whl}}^*|_{t_f}$ as well as the entire system to a steady state

$$\boldsymbol{x}_{2:4}^*|_{t_f} = \left[T_{\mathrm{e}}^* \ \theta_{\mathrm{spl}}^* \ \lambda_{\mathrm{r}}^{\mathrm{fa}*} \ \lambda_{\mathrm{r}}^{\mathrm{ra}*} \right]^T , \tag{4.25}$$

where T_{e}^* is the required torque that holds the terminal speed. Based on the final load conditions $(\omega_{\mathrm{whl}}^*, T_{\mathrm{e}}^*)|_{t_f}$, the torque split coefficient θ_{spl}^* is determined by Algorithm 2 and the optimal field strategy $\lambda_{\mathrm{r}}^{\mathrm{fa}*}, \lambda_{\mathrm{r}}^{\mathrm{ra}*}$ is computed by Algorithm 1. The weights $\mathrm{w}_x \in \mathbb{R}^5$ are additionally introduced to w_e as tuning parameters.

The constraint (4.23b) and (4.23c) restrict the solution to comply with the BEV state dynamics. Except for the longitudinal dynamics

$$\dot{\omega}_{\mathrm{whl}} = \frac{T_{\mathrm{e}}^{\mathrm{fa}} \iota_{\mathrm{dt}}^{\mathrm{fa}} - T_{\mathrm{dt}}^{\mathrm{fa}} + T_{\mathrm{e}}^{\mathrm{ra}} \iota_{\mathrm{dt}}^{\mathrm{ra}} - T_{\mathrm{dt}}^{\mathrm{ra}} - r_{\mathrm{whl}} F_{\mathrm{res}}(\omega_{\mathrm{whl}},\gamma^*)}{r_{\mathrm{whl}}^2 m + J} \tag{4.26}$$

these are expressed in a canonical form, which is represented by a simple integration of $\dot{\theta}_{\mathrm{spl}}$, $\dot{T}_{\mathrm{e}}$, $\dot{\lambda}_{\mathrm{r}}^{\mathrm{fa}}$ and $\dot{\lambda}_{\mathrm{r}}^{\mathrm{ra}}$. The average road grade over the prediction horizon is denoted by γ^*. Furthermore, constraints are imposed for the phase voltage and current of each IM in (4.23d)-(4.23g). The formulation of the maximum attainable voltage (4.23d) and (4.23e) considers the fact, that the battery voltage drops at high power demands. Within the considered time horizon, it can be assumed that the open circuit voltage of the battery u_{ocv} is constant. Both voltage and current constraints implicitly limit the maximum or minimum torque. Nevertheless, further limitations, for example, on the driving mode dependent minimum regenerative brake torque, can be defined via the box constraints. These also limit the vehicles jerk $\dot{T}_{\mathrm{e}}$ in order to account for driveablity requirements.

Similarly as done in Section 3.4.1, problem (4.23) is reformulated as a DMS problem and solved by applying a NMPC scheme. The DMS problem has the same general structure as (3.60). The only notable difference is due to the state discretization of the wheel speed ω_{whl}. The defining IVP associated with the corresponding continuity constraint, can not be solved analytically. Instead it is approximated numerically through a Runge-Kutta fourth order integration with variable step size. In order to improve the solution quality and convergence speed of the numerical solution method, a l_1 norm regularization is introduced for all inputs. By solving the DMS problem, EDM state and input trajectories are obtained, which are intended to govern the reference of EDM controls in a feedforward manner.

4.3.2 Simulative Evaluation

As an illustrative example, the NMPC scheme is tested against a simulation of the mixed route with a high initial voltage level. This cycle is part of the PIC test series, which is introduced in Section 2.6. The scenario is chosen, since the identified BEV system model shows a high level of accuracy on the mixed route and since the stationary allocation strategy only offers a relatively small saving potential (cf. Section 4.2.2). It is assumed that the load profile over the optimization horizon of two seconds is known. The DMS version of problem (4.23) with l_1 regularization is solved on a single thread of an *Intel Core* i7-5600U processor using the modeling language *JuMP* v0.20.0 for mathematical optimization [57]. Table 4.3.2 lists the considered time horizon $t_{\mathrm{f}} - t_0$, the time discretization t_{d}, the MPC update rate t_{mpc}, the problem weights $\mathrm{w}_e, \mathrm{w}_x, \mathrm{w}_u$, and the l_1 regularization factors of input (4.19). A detailed discussion of the numerical solution method for the DMS problem is found in Appendix A.3. On average, the DMS problem of a single MPC step converges within five seconds. The chosen numerical solution method is thus not suited to be implemented on an embedded system. Nevertheless, considering the number of states and inputs, as well as the time scale and modeling detail, the proposed method is

Table 4.2: Direct multiple shooting parameter of the BEV economic driving problem.

$t_\mathrm{f} - t_0$	t_d	t_mpc	w_e	w_x	ς_{T_e}	ς_θ	$\varsigma_\lambda^\mathrm{fa}$	$\varsigma_\lambda^\mathrm{ra}$
2 s	100 ms	1 s	$0.3 \cdot t_\mathrm{d}$	$(10\,, 0.1\,, 1\,, 0.1\,, 0.1)$	$1e{-}2$	$1e{-}2$	$1e{-}3$	$1e{-}3$

computationally more effective than a DP approach, which is typically used for hybrid powertrains and vehicle speed optimization [175]. What is more, further measures can be taken to improve the computational performance, which is why the proposed problem structure is well suited for ED analyses.

The altitude of the mixed route and the optimized speed trajectory are presented in the top graph of Figure 4.8. The speed reference and the optimized speed profile are indistinguishable but not identical. In terms of distance, the optimized route is 34 m longer, which corresponds to 0.1 % of the actual route. Typically, ED problems are expressed in terms of distance and not time so that the optimized and actual travel distance are consistent. Up to 1400 s the deviation of the optimized distance stays below 10 m and then rises steadily to 34 m. This minor deviations can be neglected as they doe not affect the simulation results. The bottom two graphs of Figure 4.8 show the time integral of the EDM energy loss for braking and traction

$$E_{l,\mathcal{B}} = \int_{t_0}^{t_\mathrm{f}} P_{\mathrm{l,edm}}^{\mathrm{fa}}\Big|_{T_\mathrm{e}<0} + P_{\mathrm{l,edm}}^{\mathrm{ra}}\Big|_{T_\mathrm{e}<0} \,\mathrm{dt}\,, \tag{4.27}$$

$$E_{l,\mathcal{T}} = \int_{t_0}^{t_\mathrm{f}} P_{\mathrm{l,edm}}^{\mathrm{fa}}\Big|_{T_\mathrm{e}\geq 0} + P_{\mathrm{l,edm}}^{\mathrm{ra}}\Big|_{T_\mathrm{e}\geq 0} \,\mathrm{dt}\,. \tag{4.28}$$

Three different strategies are compared:

- a FWD strategy,
- the NMPC strategy,
- the *Stationary Operational Strategy* (STOS), represented by Algorithm 1 and Algorithm 2.

During braking, all three approaches hardly show any difference. However, when driving, a FWD dissipates 1034 Wh due to EDM loss processes, whereas the losses of STOS amount to 1021 Wh and the NMPC losses are 963 Wh. This corresponds to a saving potential of 7 %, comparing NMPC with FWD, while a saving potential of 6 % is achieved when compared to STOS. Overall, the EDM efficiency has improved by 4.3 % over the STOS approach and by 4.9 % over a FWD. To be able to understand the causes of this improvement better, the following section closely analyses the simulation results of the NMPC and STOS approach on selected subsection of the mixed route.

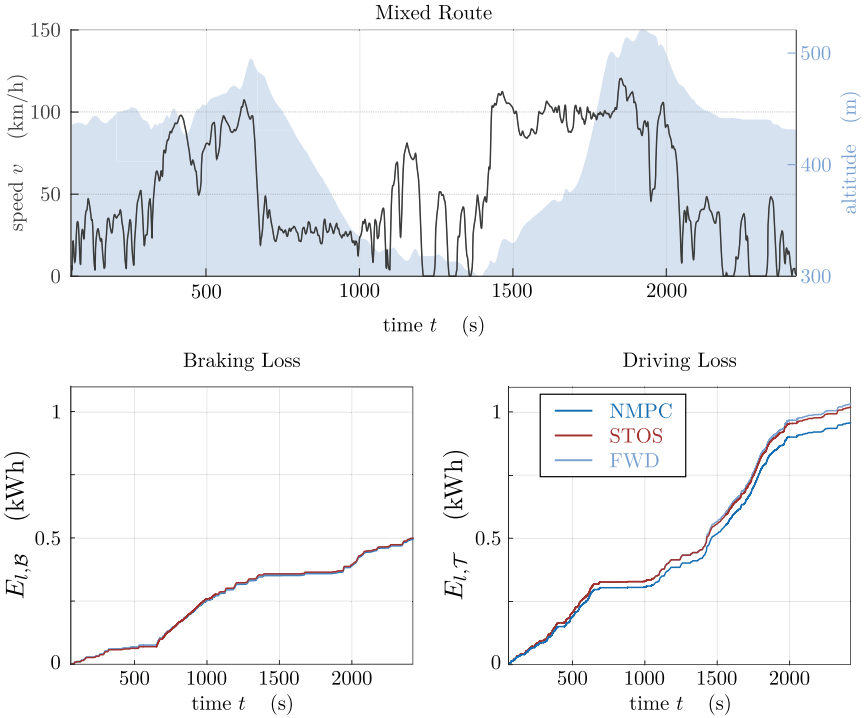

Figure 4.8: Optimization results of the mixed route.

The load cycle of the first subsection $t \in [1240, 1260]$ s is depicted in the left column of Figure 4.9. From top to bottom, the graphs show the vehicle speed, the corresponding acceleration and the road grade. Within twenty seconds the vehicle accelerates from zero speed to 50 km/h, first at a rapid acceleration of more than $3\,\mathrm{m/s^2}$ and after the first eight seconds with a moderate acceleration below $1\,\mathrm{m/s^2}$. As shown in the top graph, the NMPC solution closely tracks the speed reference, however limits the maximum acceleration to $2.5\,\mathrm{m/s^2}$.

The right column displays the combined front and rear axle rotor torque, the torque split coefficient, the front axle rotor flux and the sum of both EDM losses. As seen for the torque trajectory and the optimized split coefficient, the NMPC scheme shows a tendency of maintaining a steady system state. This behavior mainly attributes to the l_1 regularization, which forces the control inputs to stay close to zero. IM controls benefit from this behavior, since numerous transition phases with possible

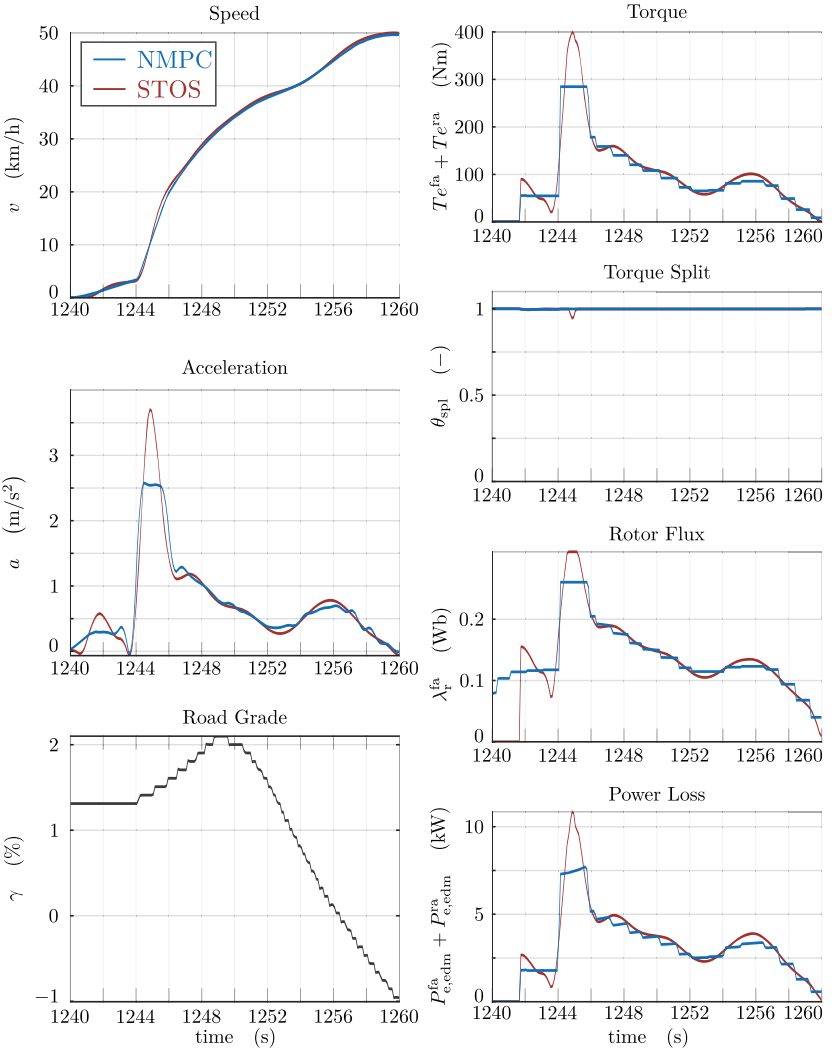

Figure 4.9: Comparison of stationary (STOS) and predictive control strategy (NMPC) for the first subsection of the mixed route.

high magnitudes of $\dot{\lambda}_\mathrm{r}$ are avoided. As discussed in Section 3.4.2, these transitions can lead to high current peaks and therefore to an increased power loss. Even though the torque trajectory complies with specified limitations on the jerk, the gradual change may be disadvantageous from a driveability perspective. However, jerky torque variations can be reduced by enforcing stricter limitations on $\dot{T}_\mathrm{e}$ or by a subsequent filtering approach. Based on the speed prediction, the NMPC control increases the front axle flux level before the peak demand at 1242 s. At 1245 s the STOS allocates 5 % of the traction torque to the rear axle because of the high torque demand, which is above the maximum torque rating of the front axle EDM. All of these measures lead to a reduction of the EDM power loss, which is evident when looking at the bottom graph. For the load cycle of Figure 4.9, 4.8 % less energy is dissipated via both EDMs for NMPC than is the case for STOS, which is nearly equivalent to a FWD.

The load cycle and optimization results of the second subsection $t \in [399, 419]$ s are displayed in Figure 4.10. The scenario is an acceleration at a high speed and a negative road grade. The vehicle is mostly operated in the partial load area with relatively low torque demands. Given the preview of the negative road grade, the NMPC solution demonstrates a behavior that is typical for ED. It exploits the prior knowledge of the road grade and predicted power demand in order to plan for an extensive coasting phase within $t \in [400, 411]$ s. After 415 s a power loss peak occurs for the SOST. Since the SOST does not relay on a prediction and just reacts to the current power demand, the rotor flux is almost reduced to zero just before the acceleration is raised. This leads to an inefficient operation over a very short time scale. Despite the low power demand of the Figure 4.11 load cycle, the smoothed optimized trajectories lead to a 7 % improvement of the EDM efficiency compared to the stationary strategy or the FWD.

The final subsection $t \in [1690, 1850]$ s in Figure 4.11 shows a speed profile of a vehicle on a highway with a preceding vehicle. Nearby to 1840 s, the speed limit changes from 100 km/h to 120 km/h. As expected in the case of ED, the maximum values of acceleration and deceleration are reduced. At this high speed and power demand, the vehicle is repeatedly operated at the maximum attainable voltage level of the front axle EDM. The NMPC scheme and the STOS find an optimized flux trajectory that complies with the voltage limitation. Due to this operational boundary, a sudden drop of the torque split coefficient is observed during high acceleration and power peaks, for example at 1698 s, 1739 s and 1844 s. The NMPC control dissipates 4.7 % less energy than the STOS in the Figure 4.11 load cycle.

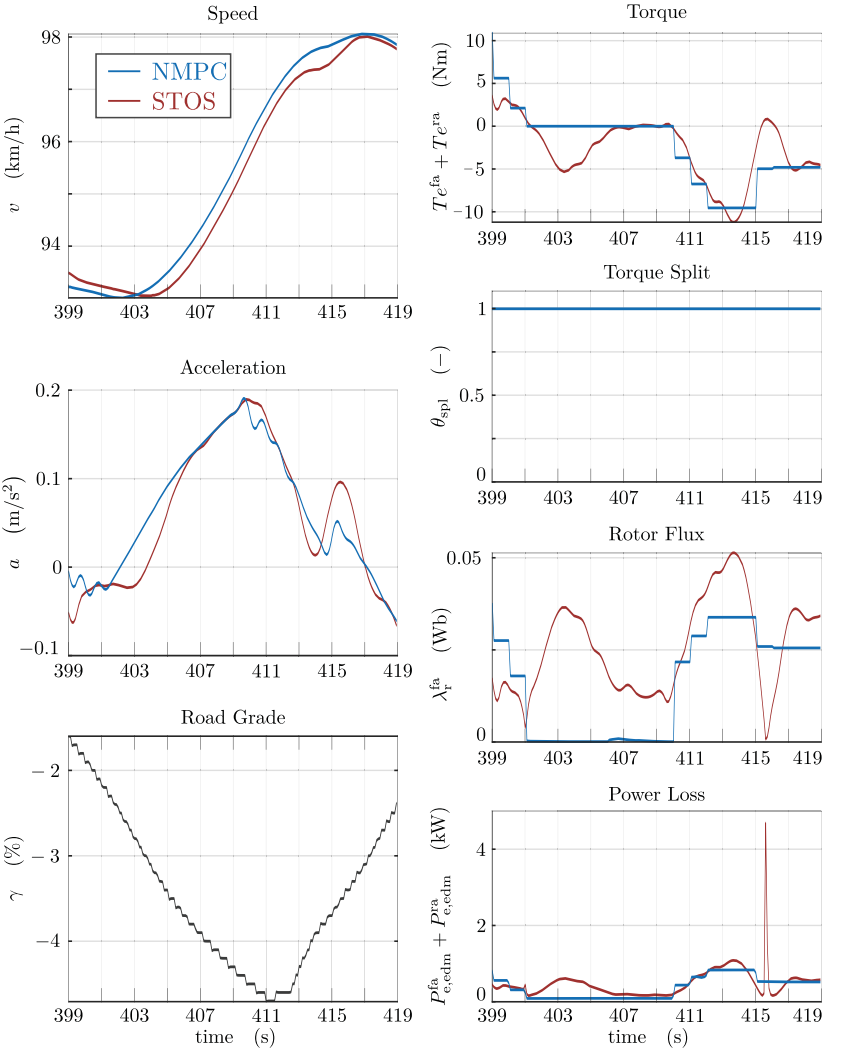

Figure 4.10: Comparison of stationary (STOS) and predictive control strategy (NMPC) for the second subsection of the mixed route.

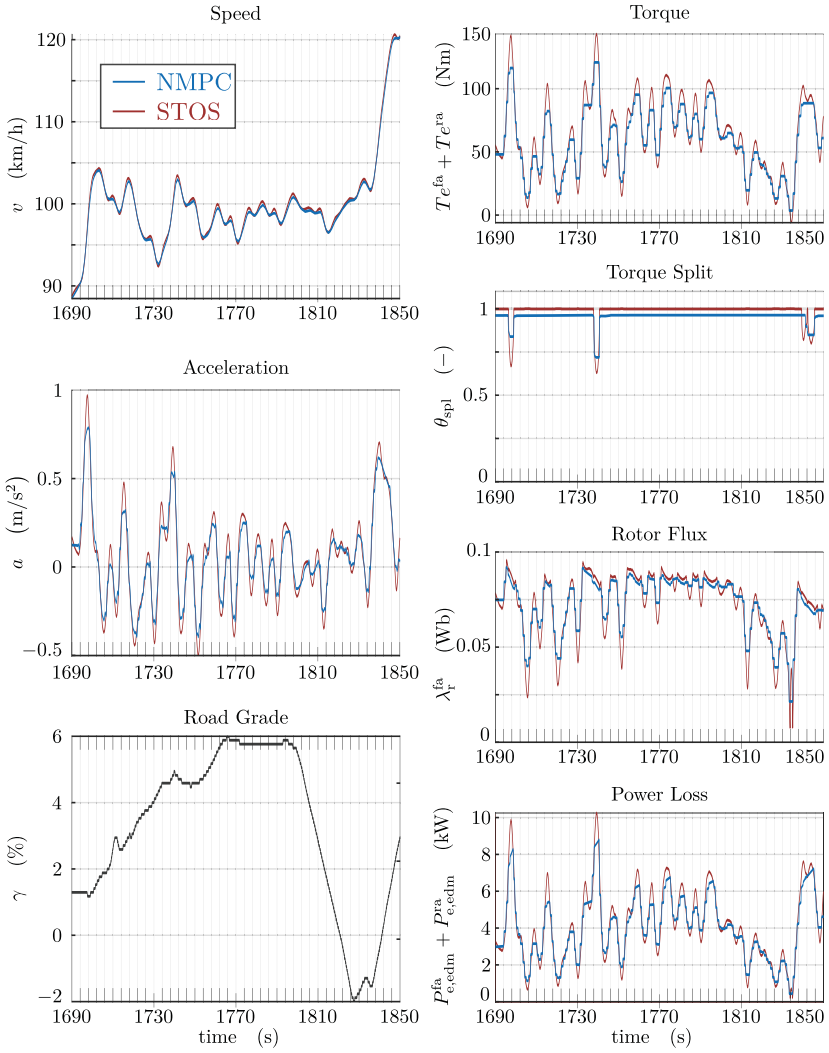

Figure 4.11: Comparison of stationary (STOS) and predictive control strategy (NMPC) for the third subsection of the mixed route.

4.4 Summary

This chapter shows how the IM and its control are integrated into a flat system model of the experimental vehicle, which computes EDM losses and electrical states of the powertrain as a function of a speed, acceleration, and road grade profile in real time. A model-based range analysis and field study demonstrate an estimation accuracy of $-0.1\,\%$ with a standard deviation of $2.8\,\%$ for thirty-two driving cycles. The high share of EDM losses, observed during the field study, underlines the potential of improved energy management strategies, of which a variable torque distribution between front and rear axle drives is identified as a promising solution. An efficiency optimized allocation strategy, which implicitly considers the voltage and current limits of the EDM, is implemented in Algorithm 2 and tested on the MCU of the experimental vehicle. On the PIC and the mixed route (see Appendix A.4) it is demonstrated that Algorithm 2 leads to a $0.6\,\% - 2\,\%$ efficiency improvement compared to a FWD. However, as indicated in an acceleration and braking scenario, the saving potential can increase up to $8\,\%$, when for example motors with lower power ratings are used.

Finally, flux and allocation strategies are combined into a centralized NMPC strategy that further exploits an economic adaptation of the vehicle's speed. Simulation results indicate that on selected subsections of the mixed route the predictive NMPC strategy achieves efficiency improvements of up to $7\,\%$ when compared to a decentralized and stationary optimization of the torque split and rotor flux. For the entire cycle, the potential is still more than $4\,\%$. When compared to a FWD, improvements of almost $5\,\%$ are observed. These positive results demonstrate that the EDM efficiency is clearly improved by a predictive control strategy. However, looking at the NMPC and the trajectories of the rotor flux and the torque split coefficient that are obtained by Algorithm 1 and Algorithm 2 in a decentralized approach, strong similarities are notable. This suggests a minor coupling between the individual control strategies, which is supported by the conclusion of Section 2.7, that both a stationary and dynamic model of an electric drive represent the losses of a dynamic driving cycle equally well. Consequently, both controls can be designed independently of each other.

Due to the similarity of a centralized and decentralized approach, and since most of the savings are obtained from utilizing the speed and acceleration profiles, it is expected that an efficiency improvement of $4\,\%$ can also be achieved with a decentralized torque allocation and flux strategy, in which control references are obtained from a separate optimization of the vehicle speed. Similar results with savings in the same order of magnitude, are achieved for the same experimental vehicle by a discrete DP and quadratic programming approach in [149], that solely utilizes the vehicle speed and acceleration. Contrary to the results of this chapter, the ED approach presented in [149] leads to a minor increase of the traveling time.

5 Conclusion

Energy management strategies and in particular ED strategies that are specifically designed for BEVs can significantly improve the overall efficiency of the electric powertrain without any structural or mechanical changes. The development of these strategies and their implementation in software solutions requires a clear understanding of how far the energy conversion processes, from the electrochemical energy stored in the battery to the potential and kinetic energy of the vehicle, can be influenced by appropriate control methods. If all dominant loss processes along the energy conversion chain are considered with sufficient accuracy, a model-based approach can provide a systematic and understanding framework for this purpose.

Chapter 2 forms the foundation for a suited model-based framework by using the example of the Mercedes-Benz EQC prototype. A dynamical model of the IM is introduced which is widely used for motor analysis and control design. However, this model is rarely used in automotive applications due to the wide spectrum of involved time constants, for example, comparing the current dynamics and the vehicle's longitudinal and drivetrain dynamics. Even more challenging are parasitic effects due to semi-conductor switchings of the VSI with switching frequencies in the range of 10 kHz. For these reasons, vehicle simulations mostly represent power electronics and electric motors as speed and torque dependent loss maps and thereby neglect dynamic effects and the resulting physical limitations. Above all, the operation of the electric motor is limited by the voltage range of the VSI, which in effect determines maximum torque ratings. In this study PWM methods are thus thoroughly investigated on the basis of which a new average value model of the VSI conduction and switching losses is proposed. This model is derived from a double Fourier integral analysis of the PWM switching signals, whose series expansion are subsequently used to compute the semi-conductor switched current in the frequency domain. Following this approach a general VSI model, that accounts for higher harmonic dissipative effects of carrier based PWM methods, is successfully integrated into vehicle simulations.
While the automotive sector prefers loss maps of the EDM to model-based approaches, mainly due to their lower complexity and inexplicable derivation of the model parameter, the experimental validation conducted in Section 2.6 demonstrates that the proposed model achieves a considerably higher level of accuracy than empirically determined loss maps or polynomial approximations and can also provide more realistic range related information. Moreover, it is possible to compute meaningful estimations of internal electrical EDM states, which are otherwise only made available

by empirical methods at unreasonable costs. In order to increase the acceptance of the model-based framework, parameter identification methods are presented in Section 2.2. Compared to procedures that identify a characteristic loss map, parameter estimation methods of the IM model have reached a maturity level with considerably lower costs and time expenditure. Since measurements of the phase voltage and stator current at the required sampling rate were not available, an in-vehicle identification method is proposed that only relies on states of the vehicle's internal communication bus system. In view of the positive validation results, the identification method has proven to effectively determine the model parameters.

However, the central contribution of this study, that further allows to integrate the IM in automotive applications, is the representation of the motor's current and flux dynamics as an equivalent differential flat system based on a new definition of a flat output. The substantial role of the magnetic field during the electromechanical energy conversion of an electric motor suggests that the magnetic field is also important from a system theoretical perspective, for example, in terms of observability and controllability. In fact, the rotor flux along with the electromechanical torque and rotor speed define a flat output of the IM. The state- and input-parametrization of the differential flat IM, which in other words are analytical expressions of the phase current and phase voltage, are thus derived in Chapter 3 in the context of FOC. These expressions allow for a remarkably efficient implementation of the IM model and control method into vehicle simulations and even in embedded systems, such as the MCU of the experimental vehicle. This real-time capability is not achieved with the typical equivalent IM model. What is more, the flat system representation is particularly well suited for the design of optimization-based control strategies for BEVs. Exploiting the structural properties of the flat system, an LMT for the IM is proposed by the field strategy of Algorithm 1. Any standard FOC method is readily extended by this strategy. Furthermore, a 2DOF control strategy is proposed that improves the dynamic performance and energy efficiency of the EDM during sudden torque transients. Taking advantage of the IM state- and input-parametrization, a nonlinear optimal control problem is formulated and solved in the receding horizon manner of MPC via a direct multiple shooting method. Analyzing the solution for various step changes, a real-time sub-optimal control method is proposed and implemented as a reference governor within the 2DOF control structure. A unique feature of this control approach is the possibility to limit the IM phase current during transients. A detail PLECS simulation of the EDM and a step change from zero to 50 % of the maximum rated torque demonstrates an energy saving potential of more than 60 % compared to an FOC with loss minimizing field strategy while approximately maintaining the same dynamic performance. However, it is noted that typical driving conditions are by far less demanding than the considered simulation scenario. Therefore, the overall efficiency of the BEV is expected to improve only slightly. Nevertheless, the control method is extremely interesting when potentially used in ESC, ABS, and ASR

functions, which could lead to less frequent engagements of the friction brakes. The arising possibilities represent the most significant differences and advantages compared to HEVs and conventional ICE vehicles.

The full differential flat BEV system model of the experimental vehicle is presented in Chapter 4. Based on this model, optimization-based energy management is proposed for AWD vehicles with two distinct IMs in longitudinal alignment on the front and rear axle. A torque allocation strategy is introduced by Algorithm 2 and implemented on the MCU of the experimental vehicle. The results of an extensive experimental test series, conducted on a powertrain test rig, demonstrate an energy saving potential of up to 2 % in real world driving conditions when compared to a FWD. Given the powertrain configuration of the experimental vehicle, an allocation that is predominantly operated on the front axle EDM has shown to be the most energy efficient strategy for an urban driving cycle and a mixed cycle, with urban, suburban and highway sections. However, in a generic scenario of several accelerations and decelerations, in which the vehicle is operated close to its maximum power ratings, an even torque split becomes more appropriate. As in this case savings of 8 % are observed, it is expected that BEVs with lower power ratings could benefit more from an efficiency optimized torque allocation strategy. To be able to reach the full saving's potential, operational and control strategies need to be considered and analyzed during the design process of the EDMs. The model-based framework in its differential flat form is particularly well suited for this purpose, due to the exceptional computational efficiency. Finally, once more the advantages of the flat system representation are demonstrated in a simulative study of a predictive NMPC strategy, which indicates energy savings of 5 % compared to a FWD without any notable increase in the traveling time for a real world driving cycle. This is achieved in a centralized approach that for the first time exploits all operational degrees of freedom, which are the vehicle speed profile, the front and rear axle magnetic flux and the variable torque allocation.

A Appendix

A.1 Reference Frame Transformation

A.1.1 dq0 Formulation

The reference frame transformation of a three-phase variable

$$\boldsymbol{x}_{\mathrm{abc}} = [x_{\mathrm{a}}\ x_{\mathrm{b}}\ x_{\mathrm{c}}]^T \tag{A.1}$$

into a real valued dq0 (direct-quadrature-zero) vector

$$\boldsymbol{x}_{\mathrm{dq0}} = [x_{\mathrm{d}}\ x_{\mathrm{q}}\ x_0]^T \tag{A.2}$$

is defined as

$$\boldsymbol{x}_{\mathrm{dq0}} = \boldsymbol{K}_\alpha \boldsymbol{x}_{\mathrm{abc}} \tag{A.3}$$

with orientation α and transformation matrix

$$\boldsymbol{K}_\alpha = \frac{2}{3}\begin{bmatrix} \cos(\alpha) & \cos\left(\alpha - \frac{2\pi}{3}\right) & \cos\left(\alpha + \frac{2\pi}{3}\right) \\ -\sin(\alpha) & -\sin\left(\alpha - \frac{2\pi}{3}\right) & -\sin\left(\alpha + \frac{2\pi}{3}\right) \\ \frac{1}{2} & \frac{1}{2} & \frac{1}{2} \end{bmatrix}. \tag{A.4}$$

The inverse transoformation is given by

$$\boldsymbol{K}_\alpha^{-1} = \begin{bmatrix} \cos(\alpha) & -\sin(\alpha) & 1 \\ \cos\left(\alpha - \frac{2\pi}{3}\right) & -\sin\left(\alpha - \frac{2\pi}{3}\right) & 1 \\ \cos\left(\alpha + \frac{2\pi}{3}\right) & -\sin\left(\alpha + \frac{2\pi}{3}\right) & 1 \end{bmatrix}. \tag{A.5}$$

For a balanced set of variables

$$\boldsymbol{x}_{\mathrm{abc}} = \hat{x}\begin{bmatrix} \cos(\beta) \\ \cos\left(\beta - \frac{2\pi}{3}\right) \\ \cos\left(\beta + \frac{2\pi}{3}\right) \end{bmatrix}, \tag{A.6}$$

it holds that x_0 is equal to zero, so that the transformation is simplified to

$$\boldsymbol{x}_{\mathrm{dq}} = \begin{bmatrix} x_{\mathrm{d}} \\ x_{\mathrm{q}} \end{bmatrix} = \frac{2}{3}\begin{bmatrix} \cos(\alpha) & \cos\left(\alpha - \frac{2\pi}{3}\right) & \cos\left(\alpha + \frac{2\pi}{3}\right) \\ -\sin(\alpha) & -\sin\left(\alpha - \frac{2\pi}{3}\right) & -\sin\left(\alpha + \frac{2\pi}{3}\right) \end{bmatrix} \boldsymbol{x}_{\mathrm{abc}} \tag{A.7}$$

and

$$\boldsymbol{x}_{\mathrm{abc}} = \begin{bmatrix} \cos(\alpha) & -\sin(\alpha) \\ \cos\left(\alpha - \frac{2\pi}{3}\right) & -\sin\left(\alpha - \frac{2\pi}{3}\right) \\ \cos\left(\alpha + \frac{2\pi}{3}\right) & -\sin\left(\alpha + \frac{2\pi}{3}\right) \end{bmatrix} \boldsymbol{x}_{\mathrm{dq}} \,. \tag{A.8}$$

Since for a balanced set of variables $x_{\mathrm{c}} = -x_{\mathrm{a}} - x_{\mathrm{b}}$, equation (A.7) can be further simplified to

$$\boldsymbol{x}_{\mathrm{dq}} = \frac{2}{\sqrt{3}} \begin{bmatrix} \cos\left(\alpha - \frac{\pi}{6}\right) & \sin(\alpha) \\ -\sin\left(\alpha - \frac{\pi}{6}\right) & \cos(\alpha) \end{bmatrix} \begin{bmatrix} x_{\mathrm{a}} \\ x_{\mathrm{b}} \end{bmatrix} \,. \tag{A.9}$$

A.1.2 Space Vector Formulation

Analog to the dq0 formulation, the reference frame transformation of a balanced three-phase variable $\boldsymbol{x}_{\mathrm{abc}} \in \mathbb{R}^3$ into a complex valued space vector is defined as

$$\underline{x}_{\mathrm{dq}} = \frac{2}{3} \left(x_{\mathrm{a}} + x_{\mathrm{b}}\, \mathrm{e}^{\mathrm{j}2\pi/3} + x_{\mathrm{c}}\, \mathrm{e}^{-\mathrm{j}2\pi/3} \right) \mathrm{e}^{-\mathrm{j}\alpha} \,, \tag{A.10}$$

$$= x_{\mathrm{d}} + \mathrm{j} x_{\mathrm{q}} \,. \tag{A.11}$$

The inverse transformation is

$$\boldsymbol{x}_{\mathrm{abc}} = \Re \left\{ \begin{bmatrix} 1 & \mathrm{e}^{-\mathrm{j}2\pi/3} & \mathrm{e}^{\mathrm{j}2\pi/3} \end{bmatrix}^T \underline{x}_{\mathrm{dq}}\, \mathrm{e}^{\mathrm{j}\alpha} \right\} \,. \tag{A.12}$$

A.1.3 Induction Motor Reference Frames

Reference frames commonly used in the analysis of electric machines are listed in Table A.1.3. The orientation used to define the dq0 or space vector transformation is

Table A.1: Commonly used Reference Frames.

Reference Frame	Speed	Transformation Stator Variables	Transformation Rotor Variables
stationary	0	$\alpha = 0$	$\alpha = -\theta_{\mathrm{e}}$
rotor	ω_{e}	$\alpha = \theta_{\mathrm{e}}$	$\alpha = 0$
synchronous	ω_0	$\alpha = \int \omega_0$	$\alpha = \int \omega_0 - \theta_{\mathrm{e}}$

listed for stator and rotor variables.
The real axis of the stationary reference frame is fixed to the phase *a*-axis of the

stator. Balanced stator variables are transformed into the stationary reference frame by Clarke's transformation

$$\boldsymbol{x}_{\alpha\beta,s} = \begin{bmatrix} x_{\alpha s} \\ x_{\beta s} \end{bmatrix} = \begin{bmatrix} 1 & 0 \\ \frac{1}{\sqrt{3}} & \frac{2}{\sqrt{3}} \end{bmatrix} \begin{bmatrix} x_{\mathrm{as}} \\ x_{\mathrm{bs}} \end{bmatrix}, \tag{A.13}$$

$$\underline{x}_{\alpha\beta,s} = \frac{2}{3}\left(x_{\mathrm{as}} + x_{\mathrm{bs}}\,\mathrm{e}^{\mathrm{j}2\pi/3} + x_{\mathrm{cs}}\,\mathrm{e}^{-\mathrm{j}2\pi/3}\right). \tag{A.14}$$

Instead of the dq-notation, variables in the stationary reference frame are typically denoted by a $\alpha\beta$-notation.
The real axis of the rotor reference frame is fixed to the a-axis of the rotor circuit and rotates with the electrical angular speed ω_{e} of the rotor. The corresponding transformation is commonly known as Park's transformation. The synchronous reference frame rotates at the fundamental electrical angular frequency corresponding to the fundamental frequency of the variables associated with the stator.

A.2 Pulse Width Modulation

In the triangle intersection method shown in Figure 2.3, the modulation signals are compared with the triangle carrier wave. The resulting intersection points define the switching instants of the PWM method. The zero-sequence system of a modulator significantly influences the switching frequency characteristics. However, it does not affect the per-carrier cycle average value of the VSI line-to-line voltage. The zero-sequence signal u_{zss} for different PWM methods are listed in Table A.2 and Table A.3. Furthermore, the tables list the maximum linear voltage range a_{pwm}. For more detailed information, the interested reader is referred to [84, 92].

Table A.2: Zero-sequence systems and maximum voltage range of continuous PWM methods.

Modulation Method	Zero-Sequence System u_{zss}	Voltage Range a_{pwm}
sinusoidal	0	$\pi/4 = 0.785$
third harmonic injection 1/4	$-\frac{M_{\mathrm{i}}}{4}\cos(3\omega_0 t)$	0.882
third harmonic injection 1/6	$-\frac{M_{\mathrm{i}}}{6}\cos(3\omega_0 t)$	0.907
space vector	$0.5\min\{\lvert u_{\mathrm{as,n}}\rvert, \lvert u_{\mathrm{bs,n}}\rvert, \lvert u_{\mathrm{cs,n}}\rvert\}$	0.907

Table A.3: Zero-sequence systems and maximum voltage range of discontinous PWM methods.

Modulation Method	Zero-Sequence System u_{zss}	Voltage Range a_{pwm}
intermediate	$\begin{cases} 0.5\,\mathrm{sign}\left(u_{\mathrm{as,n}}\right) - u_{\mathrm{as,n}}, & \lvert u_{\{b,c\}s,\mathrm{n}}\rvert \leq \lvert u_{\mathrm{as,n}}\rvert \leq \lvert u_{\{b,c\}s,\mathrm{n}}\rvert \\ 0.5\,\mathrm{sign}\left(u_{\mathrm{bs,n}}\right) - u_{\mathrm{bs,n}}, & \lvert u_{\{a,c\}s,\mathrm{n}}\rvert \leq \lvert u_{\mathrm{bs,n}}\rvert \leq \lvert u_{\{a,c\}s,\mathrm{n}}\rvert \\ 0.5\,\mathrm{sign}\left(u_{\mathrm{cs,n}}\right) - u_{\mathrm{cs,n}}, & \lvert u_{\{a,b\}s,\mathrm{n}}\rvert \leq \lvert u_{\mathrm{as,n}}\rvert \leq \lvert u_{\{a,b\}s,\mathrm{n}}\rvert \end{cases}$	0.907
max	$0.5 - \max\left\{u_{\mathrm{as,n}}, u_{\mathrm{bs,n}}, u_{\mathrm{cs,n}}\right\}$	0.907
min	$0.5 - \min\left\{u_{\mathrm{as,n}}, u_{\mathrm{bs,n}}, u_{\mathrm{cs,n}}\right\}$	0.907

A.3 Algorithmic Development for Direct Multiple Shooting

The following section provides a basic overview of the numerical method which is used to solve the DMS problem in the way of NMPC [51]. The discussion emphasizes on aspects, that are specific to the flat problem formulation and that to some extent are already used in the algorithmic development. These aspects offer even further potential to improve the computation performance of the proposed method. While viable numerical methods for large-scale nonlinear programming, are the *Augmented Lagrangian* method [39, 94] and SQP [122], this chapter focuses on the IP method [239, 250].

A specific structural property of the DMS problem is its separability [112], which roughly means that there either is no coupling or merely a linear coupling between two decision variables $\tilde{\boldsymbol{x}}^{[\mathrm{i}]}, \boldsymbol{u}_{\mathrm{fl}}{}^{[\mathrm{i}]}$ and $\tilde{\boldsymbol{x}}^{[\mathrm{j}]}, \boldsymbol{u}_{\mathrm{fl}}{}^{[\mathrm{j}]}$ on different nodes $\mathrm{i,j} \in 1(1)\mathrm{N}+1,\ \mathrm{i} \neq \mathrm{j}$ of the shooting grid. The only linear couplings that exist, are due to the final control variables (3.60d) and the continuity constraint (3.60b). Algorithms applied to DMS problems, exploit this separable structure to efficiently compute first and second order derivatives as well as the arising linear and quadratic subproblems. To elaborate this in more detail, the Lagrangian of the problem (3.60) is defined by

$$L = \begin{pmatrix} \sum\limits_{\mathrm{k}=1}^{\mathrm{N}} P_{\mathrm{l}}{}^{[\mathrm{k}]} + \vartheta_f + \left(\boldsymbol{u}_{\mathrm{fl}}{}^{[\mathrm{N}]} - \boldsymbol{u}_{\mathrm{fl}}{}^{[\mathrm{N}+1]}\right)^T \boldsymbol{\mu}_{\mathrm{u}} + \left(\boldsymbol{x}_0 - \boldsymbol{x}_{\mathrm{fl}}{}^{[1]}\right)^T \boldsymbol{\mu}_{\mathrm{x}}{}^{[1]} + \\ \sum\limits_{\mathrm{k}=1}^{\mathrm{N}} \left(\boldsymbol{x}_{\mathrm{kfl}}\big|_{t_{\mathrm{k}+1}} - \boldsymbol{x}_{\mathrm{fl}}{}^{[\mathrm{k}+1]}\right)^T \boldsymbol{\mu}_{\mathrm{x}}{}^{[\mathrm{k}+1]} - \sum\limits_{\mathrm{k}=1}^{\mathrm{N}+1} \left(\boldsymbol{C}_{\mathrm{g}}^{T[\mathrm{k}]} \boldsymbol{\mu}_{\mathrm{g}}{}^{[\mathrm{k}]} + \boldsymbol{C}_{\mathrm{b}}^{T[\mathrm{k}]} \boldsymbol{\mu}_{\mathrm{b}}{}^{[\mathrm{k}]}\right) \end{pmatrix}. \tag{A.15a}$$

Variables $\boldsymbol{\mu}_{\mathrm{x}} \in \mathbb{R}^{\mathrm{n}_x}$ are the Lagrange multipliers of the continuity constraints (3.60b), $\boldsymbol{\mu}_{\mathrm{u}} \in \mathbb{R}^{\mathrm{n}_u}$ of the terminal input constraint (3.60d), $\boldsymbol{\mu}_{\mathrm{g}} \in \mathbb{R}_{+}^{\mathrm{n}_c}$ of the general inequality constraints (3.60e), and finally $\boldsymbol{\mu}_{\mathrm{b}} \in \mathbb{R}_{+}^{2(\mathrm{n}_x+\mathrm{n}_u)}$ are the Lagrange multipliers of the box constraints where $\boldsymbol{C}_{\mathrm{g}} : \mathbb{R}^{\mathrm{n}_x} \times \mathbb{R}^{\mathrm{n}_u} \to \mathbb{R}^{\mathrm{n}_c}$ and $\boldsymbol{C}_{\mathrm{b}} : \mathbb{R}^{\mathrm{n}_x} \times \mathbb{R}^{\mathrm{n}_u} \to \mathbb{R}^{2(\mathrm{n}_x+\mathrm{n}_u)}$ are given in

vector notation

$$\boldsymbol{C}_{\mathrm{g}}{}^{[\mathrm{k}]} = \begin{bmatrix} c_1{}^{[\mathrm{k}]} \\ \vdots \\ c_{\mathrm{n}_c}{}^{[\mathrm{k}]} \end{bmatrix}, \quad \boldsymbol{C}_{\mathrm{b}}{}^{[\mathrm{k}]} = \begin{bmatrix} \boldsymbol{x}_{\mathrm{fl}}{}^{[\mathrm{k}]} - \boldsymbol{x}_{\mathrm{lb}} \\ \boldsymbol{x}_{\mathrm{ub}} - \boldsymbol{x}_{\mathrm{fl}}{}^{[\mathrm{k}]} \\ \boldsymbol{u}_{\mathrm{fl}}{}^{[\mathrm{k}]} - \boldsymbol{u}_{\mathrm{lb}} \\ \boldsymbol{u}_{\mathrm{ub}} - \boldsymbol{u}_{\mathrm{fl}}{}^{[\mathrm{k}]} \end{bmatrix}, \tag{A.15b}$$

with $c_{\mathrm{i}}{}^{[\mathrm{k}]} = c_{\mathrm{i}}\left(\boldsymbol{x}_{\mathrm{fl}}{}^{[\mathrm{k}]}, \boldsymbol{u}_{\mathrm{fl}}{}^{[\mathrm{k}]}\right)\ \forall \mathrm{i} \in 1(1)\mathrm{n}_c$. It is convenient to split the gradient of the Lagrangian into $\mathrm{N}+1$ systems

$$\nabla_{\boldsymbol{x}_{\mathrm{fl}}{}^{[\mathrm{N}+1]}} L = \nabla_{\boldsymbol{x}_{\mathrm{fl}}{}^{[\mathrm{N}+1]}} \vartheta_f - \boldsymbol{\mu}_{\mathrm{x}}{}^{[\mathrm{N}+1]} - \frac{\partial \boldsymbol{C}_{\mathrm{g}}^{T\,[\mathrm{N}+1]}}{\partial \boldsymbol{x}_{\mathrm{fl}}{}^{[\mathrm{N}+1]}} \boldsymbol{\mu}_{\mathrm{g}}{}^{[\mathrm{N}+1]} - \boldsymbol{J}_{\mathrm{x}}^T \boldsymbol{\mu}_{\mathrm{b}}{}^{[\mathrm{N}+1]}, \tag{A.16a}$$

$$\nabla_{\boldsymbol{u}_{\mathrm{fl}}{}^{[\mathrm{N}+1]}} L = -\boldsymbol{\mu}_{\mathrm{u}} - \frac{\partial \boldsymbol{C}_{\mathrm{g}}^{T\,[\mathrm{N}+1]}}{\partial \boldsymbol{u}_{\mathrm{fl}}{}^{[\mathrm{N}+1]}} \boldsymbol{\mu}_{\mathrm{g}}{}^{[\mathrm{N}+1]} - \boldsymbol{J}_{\mathrm{u}}^T \boldsymbol{\mu}_{\mathrm{b}}{}^{[\mathrm{N}+1]}, \tag{A.16b}$$

$$\nabla_{\boldsymbol{x}_{\mathrm{fl}}{}^{[\mathrm{N}]}} L = \nabla_{\boldsymbol{x}_{\mathrm{fl}}{}^{[\mathrm{N}]}} P_{\mathrm{l}}{}^{[\mathrm{N}]} + \frac{\partial \boldsymbol{x}_{\mathrm{nfl}}}{\partial \boldsymbol{x}_{\mathrm{fl}}{}^{[\mathrm{N}]}}\bigg|_{t_{\mathrm{N}+1}}^{T} \boldsymbol{\mu}_{\mathrm{x}}{}^{[\mathrm{N}+1]} - \boldsymbol{\mu}_{\mathrm{x}}{}^{[\mathrm{N}]} - \frac{\partial \boldsymbol{C}_{\mathrm{g}}^{T\,[\mathrm{N}]}}{\partial \boldsymbol{x}_{\mathrm{fl}}{}^{[\mathrm{N}]}} \boldsymbol{\mu}_{\mathrm{g}}{}^{[\mathrm{N}]} - \boldsymbol{J}_{\mathrm{x}}^T \boldsymbol{\mu}_{\mathrm{b}}{}^{[\mathrm{N}]}, \tag{A.16c}$$

$$\nabla_{\boldsymbol{u}_{\mathrm{fl}}{}^{[\mathrm{N}]}} L = \nabla_{\boldsymbol{u}_{\mathrm{fl}}{}^{[\mathrm{N}]}} P_{\mathrm{l}}{}^{[\mathrm{N}]} + \frac{\partial \boldsymbol{x}_{\mathrm{nfl}}}{\partial \boldsymbol{u}_{\mathrm{fl}}{}^{[\mathrm{N}]}}\bigg|_{t_{\mathrm{N}+1}}^{T} \boldsymbol{\mu}_{\mathrm{x}}{}^{[\mathrm{N}+1]} + \boldsymbol{\mu}_{\mathrm{u}} - \frac{\partial \boldsymbol{C}_{\mathrm{g}}^{T\,[\mathrm{N}]}}{\partial \boldsymbol{u}_{\mathrm{fl}}{}^{[\mathrm{N}]}} \boldsymbol{\mu}_{\mathrm{g}}{}^{[\mathrm{N}]} - \boldsymbol{J}_{\mathrm{u}}^T \boldsymbol{\mu}_{\mathrm{b}}{}^{[\mathrm{N}]}, \tag{A.16d}$$

$$\vdots$$

$$\nabla_{\boldsymbol{x}_{\mathrm{fl}}{}^{[\mathrm{k}]}} L = \nabla_{\boldsymbol{x}_{\mathrm{fl}}{}^{[\mathrm{k}]}} P_{\mathrm{l}}{}^{[\mathrm{k}]} + \frac{\partial \boldsymbol{x}_{\mathrm{kfl}}}{\partial \boldsymbol{x}_{\mathrm{fl}}{}^{[\mathrm{k}]}}\bigg|_{t_{\mathrm{k}+1}}^{T} \boldsymbol{\mu}_{\mathrm{x}}{}^{[\mathrm{k}+1]} - \boldsymbol{\mu}_{\mathrm{x}}{}^{[\mathrm{k}]} - \frac{\partial \boldsymbol{C}_{\mathrm{g}}^{T\,[\mathrm{k}]}}{\partial \boldsymbol{x}_{\mathrm{fl}}{}^{[\mathrm{k}]}} \boldsymbol{\mu}_{\mathrm{g}}{}^{[\mathrm{k}]} - \boldsymbol{J}_{\mathrm{x}}^T \boldsymbol{\mu}_{\mathrm{b}}{}^{[\mathrm{k}]}, \tag{A.16e}$$

$$\nabla_{\boldsymbol{u}_{\mathrm{fl}}{}^{[\mathrm{k}]}} L = \nabla_{\boldsymbol{u}_{\mathrm{fl}}{}^{[\mathrm{k}]}} P_{\mathrm{l}}{}^{[\mathrm{k}]} + \frac{\partial \boldsymbol{x}_{\mathrm{kfl}}}{\partial \boldsymbol{u}_{\mathrm{fl}}{}^{[\mathrm{k}]}}\bigg|_{t_{\mathrm{k}+1}}^{T} \boldsymbol{\mu}_{\mathrm{x}}{}^{[\mathrm{k}+1]} - \frac{\partial \boldsymbol{C}_{\mathrm{g}}^{T\,[\mathrm{k}]}}{\partial \boldsymbol{u}_{\mathrm{fl}}{}^{[\mathrm{k}]}} \boldsymbol{\mu}_{\mathrm{g}}{}^{[\mathrm{k}]} - \boldsymbol{J}_{\mathrm{u}}^T \boldsymbol{\mu}_{\mathrm{b}}{}^{[\mathrm{k}]}, \tag{A.16f}$$

$$\vdots$$

$$\nabla_{\boldsymbol{x}_{\mathrm{fl}}{}^{[1]}} L = \nabla_{\boldsymbol{x}_{\mathrm{fl}}{}^{[1]}} P_{\mathrm{l}}{}^{[1]} + \frac{\partial \boldsymbol{x}_{1\mathrm{fl}}}{\partial \boldsymbol{x}_{\mathrm{fl}}{}^{[1]}}\bigg|_{t_2}^{T} \boldsymbol{\mu}_{\mathrm{x}}{}^{[2]} - \boldsymbol{\mu}_{\mathrm{x}}{}^{[1]} - \frac{\partial \boldsymbol{C}_{\mathrm{g}}^{T\,[1]}}{\partial \boldsymbol{x}_{\mathrm{fl}}{}^{[1]}} \boldsymbol{\mu}_{\mathrm{g}}{}^{[1]} - \boldsymbol{J}_{\mathrm{x}}^T \boldsymbol{\mu}_{\mathrm{b}}{}^{[1]}, \tag{A.16g}$$

$$\nabla_{\boldsymbol{u}_{\mathrm{fl}}{}^{[1]}} L = \nabla_{\boldsymbol{u}_{\mathrm{fl}}{}^{[1]}} P_{\mathrm{l}}{}^{[1]} + \frac{\partial \boldsymbol{x}_{1\mathrm{fl}}}{\partial \boldsymbol{u}_{\mathrm{fl}}{}^{[1]}}\bigg|_{t_2}^{T} \boldsymbol{\mu}_{\mathrm{x}}{}^{[2]} - \frac{\partial \boldsymbol{C}_{\mathrm{g}}^{T\,[1]}}{\partial \boldsymbol{u}_{\mathrm{fl}}{}^{[1]}} \boldsymbol{\mu}_{\mathrm{g}}{}^{[1]} - \boldsymbol{J}_{\mathrm{u}}^T \boldsymbol{\mu}_{\mathrm{b}}{}^{[1]}, \tag{A.16h}$$

with

$$\boldsymbol{J}_{\mathrm{x}} = \begin{bmatrix} \boldsymbol{I}_{\mathrm{n}_x \times \mathrm{n}_x} & -\boldsymbol{I}_{\mathrm{n}_x \times \mathrm{n}_x} & \boldsymbol{0}_{\mathrm{n}_x \times 2\mathrm{n}_u} \end{bmatrix}^T, \quad \boldsymbol{J}_{\mathrm{u}} = \begin{bmatrix} \boldsymbol{0}_{\mathrm{n}_u \times 2\mathrm{n}_x} & \boldsymbol{I}_{\mathrm{n}_u \times \mathrm{n}_u} & -\boldsymbol{I}_{\mathrm{n}_u \times \mathrm{n}_u} \end{bmatrix}^T. \tag{A.16i}$$

Matrices $\boldsymbol{I}$ and $\boldsymbol{0}$ are respectively the identity matrix and the zero matrix and their subscripts indicate the dimension. It is noted, that each of the above $\mathrm{N}+1$ systems only depend on the decision variables and the Lagrange multipliers at the individual time instance of the shooting grid $\{t_{\mathrm{k}}\}$ as well as on $\boldsymbol{\mu}_{\mathrm{x}}$ of the subsequent shooting interval. The exception in (A.16a)-(A.16d) is due to the terminal input constraint and $\boldsymbol{\mu}_{\mathrm{u}}$. Applying a Newton's method to a linear model of the KKT necessary conditions, built from (A.16) along with the continuity constraints (3.60b)-(3.60d) and active inequality constraints (3.60e)-(3.60g), is equivalent for solving a sequence of constrained quadratic

subproblems as it is done for SQP. These subroblems are formulated using a local quadratic model of the Lagrangian (A.15a), which is minimized on a linearization of the feasible set (cv. [158] chapter 18).

A.3.1 Interiour Point Method

Alternatively, IP methods redefine the KKT conditions to a system known as the primal-dual system (cv. [158] chapter 19). Therefore inequality constraints (A.15) are transformed into equality constraints by subtractions of the positive slack variables $s_\mathrm{g} \in \mathbb{R}_+^{\mathrm{n}_c}$ and $s_\mathrm{b} \in \mathbb{R}_+^{2(\mathrm{n}_x+\mathrm{n}_u)}$

$$\boldsymbol{C}_{\mathrm{gs}}{}^{[\mathrm{k}]} = \boldsymbol{C}_{\mathrm{g}}{}^{[\mathrm{k}]} - s_{\mathrm{g}}{}^{[\mathrm{k}]}\,, \quad \boldsymbol{C}_{\mathrm{bs}}{}^{[\mathrm{k}]} = \boldsymbol{C}_{\mathrm{b}}{}^{[\mathrm{k}]} - s_{\mathrm{b}}{}^{[\mathrm{k}]}\,. \tag{A.17}$$

Starting from an initial guess for the decision variables, the Lagrange multipliers and the slack variables:

$$\tilde{\boldsymbol{v}}^{[\mathrm{k}]} = \begin{bmatrix} \boldsymbol{x}_{\mathrm{fl}}^{T[\mathrm{k}]} & \boldsymbol{u}_{\mathrm{fl}}^{T[\mathrm{k}]} & s_{\mathrm{g}}^{T[\mathrm{k}]} & s_{\mathrm{b}}^{T[\mathrm{k}]} & \boldsymbol{\mu}_{\mathrm{x}}^{T[\mathrm{k}]} & -\boldsymbol{\mu}_{\mathrm{g}}^{T[\mathrm{k}]} & -\boldsymbol{\mu}_{\mathrm{b}}^{T[\mathrm{k}]} \end{bmatrix}^T\,, \quad \forall \mathrm{k} \in 1(1)\mathrm{N}{+}1\,, \tag{A.18}$$

as well as for $\boldsymbol{\mu}_\mathrm{u}$, IP methods solve a sequence of linear equations, which are variants of the symmetrical primal-dual system:

$$\begin{bmatrix} \boldsymbol{0} & \boldsymbol{J}_{\mu u} & -\boldsymbol{J}_{\mu u} & & & & & & & \\ \boldsymbol{J}_{\mu u}^T & \boldsymbol{B}^{[\mathrm{N}+1]} & \boldsymbol{S}_0^{T[\mathrm{N}]} & & & & & & & \\ -\boldsymbol{J}_{\mu u}^T & \boldsymbol{S}_0{}^{[\mathrm{N}]} & \boldsymbol{B}^{[\mathrm{N}]} & \boldsymbol{S}_0^{T[\mathrm{N}\text{-}1]} & & & & & & \\ & & \ddots & & & & & & & \\ & & \boldsymbol{S}_0{}^{[\mathrm{k}+1]} & \boldsymbol{B}^{[\mathrm{k}+1]} & \boldsymbol{S}_0^{T[\mathrm{k}]} & & & & & \\ & & & \boldsymbol{S}_0{}^{[\mathrm{k}]} & \boldsymbol{B}^{[\mathrm{k}]} & \boldsymbol{S}_0^{T[\mathrm{k}\text{-}1]} & & & & \\ & & & & & \ddots & & & & \\ & & & & & \boldsymbol{S}_0{}^{[2]} & \boldsymbol{B}^{[2]} & \boldsymbol{S}_0^{T[1]} & \\ & & & & & & \boldsymbol{S}_0{}^{[1]} & \boldsymbol{B}^{[1]} & \end{bmatrix} \begin{bmatrix} \delta\boldsymbol{\mu}_\mathrm{u} \\ \delta\tilde{\boldsymbol{v}}^{[\mathrm{N}+1]} \\ \delta\tilde{\boldsymbol{v}}^{[\mathrm{N}]} \\ \vdots \\ \delta\tilde{\boldsymbol{v}}^{[\mathrm{k}+1]} \\ \delta\tilde{\boldsymbol{v}}^{[\mathrm{k}]} \\ \vdots \\ \delta\tilde{\boldsymbol{v}}^{[2]} \\ \delta\tilde{\boldsymbol{v}}^{[1]} \end{bmatrix} = - \begin{bmatrix} \boldsymbol{u}_{\mathrm{fl}}{}^{[\mathrm{N}]} - \boldsymbol{u}_{\mathrm{fl}}{}^{[\mathrm{N}+1]} \\ \boldsymbol{b}^{[\mathrm{N}+1]} \\ \boldsymbol{b}^{[\mathrm{N}]} \\ \vdots \\ \boldsymbol{b}^{[\mathrm{k}+1]} \\ \boldsymbol{b}^{[\mathrm{k}]} \\ \vdots \\ \boldsymbol{b}^{[2]} \\ \boldsymbol{b}^{[1]} \end{bmatrix}. \tag{A.19}$$

For the ease of notation, the matrices defined at the most recent iterate of $\tilde{\boldsymbol{v}}^{[\mathrm{k}]}$, are given by

$$\boldsymbol{B}^{[\mathrm{k}]} = \begin{bmatrix} H^{[\mathrm{k}]} & \boldsymbol{0}_{\mathrm{n}_{xu}\times\mathrm{n}_{cc}} & \boldsymbol{J}_{\mu x}^T & \boldsymbol{J}_{\mathrm{C}}^{T[\mathrm{k}]} \\ \boldsymbol{0}_{\mathrm{n}_{cc}\times\mathrm{n}_{xu}} & \mathrm{diag}\left(\boldsymbol{s}_{\mathrm{g}}{}^{[\mathrm{k}]}, \boldsymbol{s}_{\mathrm{b}}{}^{[\mathrm{k}]}\right)^{-1}\mathrm{diag}\left(\boldsymbol{\mu}_{\mathrm{g}}{}^{[\mathrm{k}]}, \boldsymbol{\mu}_{\mathrm{b}}{}^{[\mathrm{k}]}\right) & \boldsymbol{0}_{\mathrm{n}_{cc}\times\mathrm{n}_x} & -\boldsymbol{I}_{\mathrm{n}_{cc}\times\mathrm{n}_{cc}} \\ \boldsymbol{J}_{\mu x} & \boldsymbol{0}_{\mathrm{n}_x\times\mathrm{n}_{cc}} & \boldsymbol{0}_{\mathrm{n}_x\times\mathrm{n}_x} & \boldsymbol{0}_{\mathrm{n}_x\times\mathrm{n}_{cc}} \\ \boldsymbol{J}_{\mathrm{C}}{}^{[\mathrm{k}]} & -\boldsymbol{I}_{\mathrm{n}_{cc}\times\mathrm{n}_{cc}} & \boldsymbol{0}_{\mathrm{n}_{cc}\times\mathrm{n}_x} & \boldsymbol{0}_{\mathrm{n}_{cc}\times\mathrm{n}_{cc}} \end{bmatrix}, \quad \forall \mathrm{k} \in 1(1)\mathrm{N}{+}1\,, \tag{A.20a}$$

$$\boldsymbol{S}_0{}^{[\mathrm{k}]} = \begin{bmatrix} \boldsymbol{0}_{\mathrm{n}_{xu}\times\mathrm{n}_{xu}+\mathrm{n}_{cc}} & \boldsymbol{S}^{T[\mathrm{k}]} & \boldsymbol{0}_{\mathrm{n}_{xu}\times\mathrm{n}_{cc}} \\ \boldsymbol{0}_{2\mathrm{n}_{cc}+\mathrm{n}_x\times\mathrm{n}_{xu}+\mathrm{n}_{cc}} & \boldsymbol{0}_{2\mathrm{n}_{cc}+\mathrm{n}_x\times\mathrm{n}_x} & \boldsymbol{0}_{2\mathrm{n}_{cc}+\mathrm{n}_x\times\mathrm{n}_{cc}} \end{bmatrix}, \quad \forall \mathrm{k} \in 1(1)\mathrm{N}\,, \tag{A.20b}$$

$$\boldsymbol{b}^{[\mathrm{k}]} = \begin{bmatrix} \nabla L^{[\mathrm{k}]} \\ \Lambda^{[\mathrm{k}]} \\ \boldsymbol{x}_{\mathrm{kfl}}|_{t_{\mathrm{k}+1}} - \boldsymbol{x}_{\mathrm{fl}}{}^{[\mathrm{k}+1]} \\ \boldsymbol{C}^{[\mathrm{k}]} \end{bmatrix}, \quad \forall \mathrm{k} \in 2(1)\mathrm{N}{+}1\,, \quad \boldsymbol{b}^{[1]} = \begin{bmatrix} \nabla L^{[1]} \\ \Lambda^{[1]} \\ \boldsymbol{x}_{\mathrm{fl}}{}^{[1]} - \boldsymbol{x}_0 \\ \boldsymbol{C}^{[1]} \end{bmatrix}, \tag{A.20c}$$

with $\mathrm{n}_{xu} = \mathrm{n}_x + \mathrm{n}_u$, $\mathrm{n}_{cc} = \mathrm{n}_c + 2\mathrm{n}_{xu}$, and

$$\nabla \boldsymbol{L}^{[\mathrm{k}]} = \begin{bmatrix} \nabla_{\boldsymbol{x}_{\mathrm{fi}}{}^{[\mathrm{k}]}} L \\ \nabla_{\boldsymbol{u}_{\mathrm{fi}}{}^{[\mathrm{k}]}} L \end{bmatrix}, \quad \boldsymbol{H}^{[\mathrm{k}]} = \begin{bmatrix} \nabla^2_{\boldsymbol{x}_{\mathrm{fi}}{}^{[\mathrm{k}]}\boldsymbol{x}_{\mathrm{fi}}{}^{[\mathrm{k}]}} L & \nabla^2_{\boldsymbol{x}_{\mathrm{fi}}{}^{[\mathrm{k}]}\boldsymbol{u}_{\mathrm{fi}}{}^{[\mathrm{k}]}} L \\ \nabla^2_{\boldsymbol{u}_{\mathrm{fi}}{}^{[\mathrm{k}]}\boldsymbol{x}_{\mathrm{fi}}{}^{[\mathrm{k}]}} L & \nabla^2_{\boldsymbol{u}_{\mathrm{fi}}{}^{[\mathrm{k}]}\boldsymbol{u}_{\mathrm{fi}}{}^{[\mathrm{k}]}} L \end{bmatrix}, \quad \boldsymbol{S}^{[\mathrm{k}]} = \begin{bmatrix} \frac{\partial \boldsymbol{x}_{\mathrm{fi}}}{\partial \boldsymbol{x}_{\mathrm{fi}}{}^{[\mathrm{k}]}}\Big|_{t_{\mathrm{k}+1}} & \frac{\partial \boldsymbol{x}_{\mathrm{fi}}}{\partial \boldsymbol{u}_{\mathrm{fi}}{}^{[\mathrm{k}]}}\Big|_{t_{\mathrm{k}+1}} \end{bmatrix}, \tag{A.20d}$$

$$\boldsymbol{C}^{[\mathrm{k}]} = \begin{bmatrix} \boldsymbol{C}_{\mathrm{gs}}{}^{[\mathrm{k}]} \\ \boldsymbol{C}_{\mathrm{bs}}{}^{[\mathrm{k}]} \end{bmatrix}, \quad \boldsymbol{J}_{\mathrm{C}}{}^{[\mathrm{k}]} = \begin{bmatrix} \frac{\partial \boldsymbol{C}_{\mathrm{g}}{}^{[\mathrm{k}]}}{\partial \boldsymbol{x}_{\mathrm{fi}}{}^{[\mathrm{k}]}} & \frac{\partial \boldsymbol{C}_{\mathrm{g}}{}^{[\mathrm{k}]}}{\partial \boldsymbol{u}_{\mathrm{fi}}{}^{[\mathrm{k}]}} \\ \boldsymbol{J}_{\mathrm{x}} & \boldsymbol{J}_{\mathrm{u}} \end{bmatrix}, \quad \Lambda^{[\mathrm{k}]} = \begin{bmatrix} \boldsymbol{\mu}_{\mathrm{g}}{}^{[\mathrm{k}]} - \kappa \operatorname{diag}\left(\boldsymbol{s}_{\mathrm{g}}{}^{[\mathrm{k}]}\right)^{-1} \mathbb{1} \\ \boldsymbol{\mu}_{\mathrm{b}}{}^{[\mathrm{k}]} - \kappa \operatorname{diag}\left(\boldsymbol{s}_{\mathrm{b}}{}^{[\mathrm{k}]}\right)^{-1} \mathbb{1} \end{bmatrix}, \tag{A.20e}$$

$$\boldsymbol{J}_{\mu x} = \begin{bmatrix} -\boldsymbol{I}_{\mathrm{n}_x \times \mathrm{n}_x} & \boldsymbol{0}_{\mathrm{n}_x \times \mathrm{n}_u} \end{bmatrix}, \quad \boldsymbol{J}_{\mu u} = \begin{bmatrix} \boldsymbol{0}_{\mathrm{n}_u \times \mathrm{n}_x} & -\boldsymbol{I}_{\mathrm{n}_u \times \mathrm{n}_u} & \boldsymbol{0}_{\mathrm{n}_u \times 2\mathrm{n}_{cc}+\mathrm{n}_x} \end{bmatrix}. \tag{A.20f}$$

The operator $\operatorname{diag} : \mathbb{R}^{n1} \times \mathbb{R}^{n2} \times \ldots \to \mathbb{R}^{n1+n2+\ldots \times n1+n2+\ldots}$ takes the elements of one or more vectors and returns a diagonal matrix whose main diagonal contains the elements of these vectors. The parameter $\kappa \in \mathbb{R}_+$ used in (A.20e) is known as the barrier parameter and $\mathbb{1}$ is a vector with all entries equal to one. After (A.19) is solved, the next iterate of the IP method is obtained by

$$\boldsymbol{\mu}_{\mathrm{u}}^{+} = \boldsymbol{\mu}_{\mathrm{u}} + \alpha_\mu \delta \boldsymbol{\mu}_{\mathrm{u}}, \quad \tilde{\boldsymbol{v}}^{+[\mathrm{k}]} = \tilde{\boldsymbol{v}}^{[\mathrm{k}]} + \operatorname{diag}\left(\boldsymbol{\alpha}_v\right) \delta \tilde{\boldsymbol{v}}^{[\mathrm{k}]}, \quad \forall \mathrm{k} \in 1(1)\mathrm{N}{+}1, \tag{A.21}$$

where $\boldsymbol{\alpha}_v \in \mathbb{R}^{\mathrm{n}_{xu}+2\mathrm{n}_{cc}+\mathrm{n}_x}$ and $\alpha_\mu \in \mathbb{R}$ represent an appropriate step size, for example determined by a backtracking line search, trust-region method or filter method [12, 240]. As the iterations proceed, the sequence of barrier parameters $\{\kappa\}$ must converge to zero, so that the solution of the original problem (3.60) is recovered in the limit. Different barrier reduction strategies are analyzed in [157]. The state-of-the-art IP solver used in this study is IPOPT [239]. Very recently an extension of the commercial IP solver *FORCES PRO* [55] was introduced by [250]. This extension is tailored to the sparse block structure of the DMS primal-dual system (A.19) and therefore promises a significant speedup of selected examples in comparison to IPOPT.

A.3.2 Integration and Differentiation

As mentioned by [51] and [250], computationally expensive steps associated with the DMS primal-dual system (A.19) or comparable subproblems of SQP methods, belong to the generation of the derivative information required in (A.20d) as well as the integration of a possibly stiff IVP. The latter is required for the residual of the continuity constraint, for example, used in case of the IVP defined by the vehicle longitudinal dynamics. Depending on the properties of the dynamical system, the residual can be efficiently computed by means of explicit or implicit integration methods [89, 184]. More demanding, is the sensitivity generation for the general nonlinear IVP on the shooting grid $\{t_{\mathrm{k}}\}$

$$\dot{\boldsymbol{x}}_{\mathrm{k}} = f\left(\boldsymbol{x}_{\mathrm{k}}, \boldsymbol{u}^{[\mathrm{k}]}\right), \tag{A.22a}$$

$$\boldsymbol{x}_{\mathrm{k}}\big|_{t_{\mathrm{k}}} = \boldsymbol{x}^{[\mathrm{k}]}, \tag{A.22b}$$

with a constant input $\boldsymbol{u}^{[\mathrm{k}]} \in \mathbb{R}^{\mathrm{n}_u}$ and continuous state $\boldsymbol{x}_\mathrm{k} \in \mathbb{R}^{\mathrm{n}_x}$. The sensitivities $\frac{\partial \boldsymbol{x}_\mathrm{k}}{\partial \boldsymbol{x}^{[\mathrm{k}]}} \in \mathbb{R}^{\mathrm{n}_x \times \mathrm{n}_x}$ and $\frac{\partial \boldsymbol{x}_\mathrm{k}}{\partial \boldsymbol{u}^{[\mathrm{k}]}} \in \mathbb{R}^{\mathrm{n}_x \times \mathrm{n}_u}$ are defined by the variational differential equation

$$\frac{\mathrm{d}}{\mathrm{d}t}\frac{\partial \boldsymbol{x}_\mathrm{k}}{\partial \boldsymbol{x}^{[\mathrm{k}]}} = \frac{\partial f}{\partial \boldsymbol{x}_\mathrm{k}}\frac{\partial \boldsymbol{x}_\mathrm{k}}{\partial \boldsymbol{x}^{[\mathrm{k}]}}\,, \qquad \left.\frac{\partial \boldsymbol{x}_\mathrm{k}}{\partial \boldsymbol{x}^{[\mathrm{k}]}}\right|_{t_\mathrm{k}} = \boldsymbol{I}_{\mathrm{n}_x \times \mathrm{n}_x}\,, \tag{A.23a}$$

$$\frac{\mathrm{d}}{\mathrm{d}t}\frac{\partial \boldsymbol{x}_\mathrm{k}}{\partial \boldsymbol{u}^{[\mathrm{k}]}} = \frac{\partial f}{\partial \boldsymbol{x}_\mathrm{k}}\frac{\partial \boldsymbol{x}_\mathrm{k}}{\partial \boldsymbol{u}^{[\mathrm{k}]}} + \frac{\partial f}{\partial \boldsymbol{u}^{[\mathrm{k}]}}\,, \qquad \left.\frac{\partial \boldsymbol{x}_\mathrm{k}}{\partial \boldsymbol{u}^{[\mathrm{k}]}}\right|_{t_\mathrm{k}} = \boldsymbol{0}_{\mathrm{n}_x \times \mathrm{n}_u}\,, \tag{A.23b}$$

which can be solved simultaneously with (A.22). Apart from this first order derivative information, it is desirable to compute second order sensitivities, i. e. the adjoint sensitivity of $\boldsymbol{\mu}_\mathrm{x}^T \frac{\partial \boldsymbol{x}_\mathrm{k}}{\partial \boldsymbol{x}^{[\mathrm{k}]}}$ and $\boldsymbol{\mu}_\mathrm{x}^T \frac{\partial \boldsymbol{x}_\mathrm{k}}{\partial \boldsymbol{u}^{[\mathrm{k}]}}$, in order to obtain the exact Hessian $\boldsymbol{H}^{[\mathrm{k}]}$ used in (A.20d). An overview of sensitivity generation methods based on the forward and reverse mode of *Automatic Differentiation* (AD), also referred to as *Algorithmic Differentiation*, is found in [2] and the textbook [77].

Due to the canonical form of the flat system (3.56), however, the solution of the IVP (3.58) and therefore the sensitivities are computed explicitly as a function of the discrete time interval t_d of the shooting grid (3.54). For the integrator chain of a single flat output $\boldsymbol{x}_\mathrm{z} = (z\ \dot{z}\ \ddot{z}\ \dots\ z^{(\mathrm{r}-1)}) \in \mathbb{R}^\mathrm{r}$ with differential order r, the sensitivities at the end of a shooting interval $t_{\mathrm{k}+1}$ are

$$\left.\frac{\partial \boldsymbol{x}_\mathrm{kz}}{\partial \boldsymbol{x}_\mathrm{z}^{[\mathrm{k}]}}\right|_{t_{\mathrm{k}+1}} = \begin{bmatrix} 1 & t_\mathrm{d} & \frac{t_\mathrm{d}}{2} & & \dots & & \frac{t_\mathrm{d}^{\mathrm{r}-1}}{(\mathrm{r}-1)!} \\ 0 & 1 & t_\mathrm{d} & \frac{t_\mathrm{d}}{2} & \dots & & \frac{t_\mathrm{d}^{\mathrm{r}-2}}{(\mathrm{r}-2)!} \\ & & \ddots & & & & \\ \vdots & & & \ddots & & & \vdots \\ & & & & \ddots & & \\ & & & & & 1 & t_\mathrm{d} \\ 0 & & \dots & & & 0 & 1 \end{bmatrix}, \qquad \left.\frac{\partial \boldsymbol{x}_\mathrm{kz}}{\partial z^{(\mathrm{r})^{[\mathrm{k}]}}}\right|_{t_{\mathrm{k}+1}} = \begin{bmatrix} \frac{t_\mathrm{d}^\mathrm{r}}{\mathrm{r}!} \\ \frac{t_\mathrm{d}^{\mathrm{r}-1}}{(\mathrm{r}-1)!} \\ \vdots \\ \\ t_\mathrm{d} \end{bmatrix}. \tag{A.24}$$

Applying (A.24) to the example of the IM with the reduced flat output $\boldsymbol{z} = (T_\mathrm{e}, \lambda_\mathrm{r})$ of differential order one and two and system state $\boldsymbol{x}_\mathrm{fl} = (T_\mathrm{e}\ \lambda_\mathrm{r}\ \dot{\lambda}_\mathrm{r})$ yields

$$\left.\frac{\partial \boldsymbol{x}_\mathrm{kfl}}{\partial \boldsymbol{x}_\mathrm{fl}^{[\mathrm{k}]}}\right|_{t_{\mathrm{k}+1}} = \begin{bmatrix} 1 & 0 & 0 \\ 0 & 1 & t_\mathrm{d} \\ 0 & 0 & 1 \end{bmatrix}, \qquad \left.\frac{\partial \boldsymbol{x}_\mathrm{kfl}}{\partial \boldsymbol{u}_\mathrm{fl}^{[\mathrm{k}]}}\right|_{t_{\mathrm{k}+1}} = \begin{bmatrix} t_\mathrm{d} & 0 \\ 0 & \frac{t_\mathrm{d}^2}{2} \\ 0 & t_\mathrm{d} \end{bmatrix}. \tag{A.25}$$

Accordingly, (A.24) is easily generalized for systems with multiple flat outputs. Since the sensitivities of a flat system are independent of the initial state and input, their second order or adjoint sensitivities vanish. Consequently, the block diagonal elements

of the exact Hessian of the Lagrangian (A.15a) are given by

$$\boldsymbol{H}^{[\mathrm{k}]} = \begin{bmatrix} \nabla^2_{x_{\mathrm{fl}} x_{\mathrm{fl}}} P_{\mathrm{l}}{}^{[\mathrm{k}]} + \sum_{\mathrm{i}=1}^{\mathrm{n_c}} \mu_{\mathrm{g,i}}{}^{[\mathrm{k}]} \nabla^2_{x_{\mathrm{fl}} x_{\mathrm{fl}}} c_{\mathrm{i}}{}^{[\mathrm{k}]} & \nabla^2_{x_{\mathrm{fl}} u_{\mathrm{fl}}} P_{\mathrm{l}}{}^{[\mathrm{k}]} + \sum_{\mathrm{i}=1}^{\mathrm{n_c}} \mu_{\mathrm{g,i}}{}^{[\mathrm{k}]} \nabla^2_{x_{\mathrm{fl}} u_{\mathrm{fl}}} c_{\mathrm{i}}{}^{[\mathrm{k}]} \\ * & \nabla^2_{u_{\mathrm{fl}} u_{\mathrm{fl}}} P_{\mathrm{l}}{}^{[\mathrm{k}]} + \sum_{\mathrm{i}=1}^{\mathrm{n_c}} \mu_{\mathrm{g,i}}{}^{[\mathrm{k}]} \nabla^2_{u_{\mathrm{fl}} u_{\mathrm{fl}}} c_{\mathrm{i}}{}^{[\mathrm{k}]} \end{bmatrix}, \quad \forall \mathrm{k} \in 1(1)\mathrm{N} \tag{A.26}$$

$$\boldsymbol{H}^{[\mathrm{N+1}]} = \begin{bmatrix} \nabla^2_{x_{\mathrm{fl}} x_{\mathrm{fl}}} \vartheta_f + \sum_{\mathrm{i}=1}^{\mathrm{n_c}} \mu_{\mathrm{g,i}}{}^{[\mathrm{N+1}]} \nabla^2_{x_{\mathrm{fl}} x_{\mathrm{fl}}} c_{\mathrm{i}}{}^{[\mathrm{N+1}]} & \nabla^2_{x_{\mathrm{fl}} u_{\mathrm{fl}}} \vartheta_f + \sum_{\mathrm{i}=1}^{\mathrm{n_c}} \mu_{\mathrm{g,i}}{}^{[\mathrm{N+1}]} \nabla^2_{x_{\mathrm{fl}} u_{\mathrm{fl}}} c_{\mathrm{i}}{}^{[\mathrm{N+1}]} \\ * & \nabla^2_{u_{\mathrm{fl}} u_{\mathrm{fl}}} \vartheta_f + \sum_{\mathrm{i}=1}^{\mathrm{n_c}} \mu_{\mathrm{g,i}}{}^{[\mathrm{N+1}]} \nabla^2_{u_{\mathrm{fl}} u_{\mathrm{fl}}} c_{\mathrm{i}}{}^{[\mathrm{N+1}]} \end{bmatrix}. \tag{A.27}$$

The loss function P_{l}, the terminal cost ϑ_f and the general inequality constraints c_{i} considered in this work are factorable functions (see Definition 2.2. in [2]), which roughly means that they can be evaluated and represented in a computational graph that is build from elementary functions. Therefore, the gradients and Hessians can be computed by means of AD, which in the context of this thesis is done, using the *ForwardDiff.jl* package [190].

A.4 Experimental Study

A.4.1 Field Study

The field study is introduced in Section 4.1. Table A.4.1 summarizes the key characteristics of the considered routes, including the length, the percentage share of road classes (HERE maps classification), the overall height increment as well as the mean value of the speed limit and the base speed. The base speed represents the average speed derived from historical data. Table A.4.1 lists the main characteristics of all thirty two test cycles, i. e. the duration, the average vehicle speed $\bar{v}$, the maximum and minimum acceleration, and the ambient temperature. Maps of each route and selected speed profiles are presented in Figure A.1 - Figure A.4.

A.4.2 Powertrain Integration Center Test Series

The PIC experimental series is introduced in Section 2.6. The speed, acceleration, and road grade profiles are shown in Figure A.5 - Figure A.7. A robotic setup was installed that actuated the speed and brake pedal. By means of a dedicated feedback loop, this setup is able to follow the commanded speed profile.

Table A.4: Key characteristics of field study routes.

	Urban	Suburban	Highway a)	Highway b)	Mixed
length (km)	13.3	37.7	67.4	67.7	35.2
hight increment (m)	0	0	-196	196	0
average base speed (km/h)	39	54	93	104	60
average speed limit (km/h)	49	63	105	118	72
class 1 share % (freeway)	0	0	81	80	40
class 2 share % (hihgway)	0	28	7	8	28
class 3 share % (priority/main roads)	75	70	10	10	28
class 4 share % (low priority, urban)	25	3	2	2	4

Table A.5: Key characteristics of field study cycles.

Cycle		Duration (min)	$\bar{v}$ (km/h)	max (a) (m/s^2)	min (a) (m/s^2)	Ambient Temp. (°C)
c_1	urban	34	24	2.7	-3.2	14
c_2		29	28	2.8	-3.9	3
c_3		34	23	2.6	-4.0	14
c_4		36	22	3.4	-3.1	3
c_5		31	26	3.3	-4.3	6
c_6		30	26	3.2	-4.9	4
c_7	suburban	75	30	4.4	-4.2	3
c_8		46	49	2.9	-3.4	4
c_9		77	29	3.2	-4.4	2
c_{10}		48	47	2.8	-3.6	3
c_{11}		48	47	3.7	-4.9	4
c_{12}		48	47	3.1	-4.0	4
c_{13}	highway a)	55	72	3.1	-3.9	21
c_{14}		48	84	3.2	-3.9	23
c_{15}		48	84	3.2	-3.5	13
c_{16}		50	80	2.9	-3.0	18
c_{17}		47	85	2.8	-3.1	17
c_{18}		58	69	2.5	-4.8	11
c_{19}		45	88	4.7	-4.7	26
c_{20}		49	82	2.4	-4.5	6
c_{21}	highway b)	50	81	5.0	-4.5	23
c_{22}		50	80	2.5	-3.9	13
c_{23}		51	80	3.4	-3.8	19
c_{24}		46	88	3.3	-3.0	12
c_{25}		55	73	2.5	-4.5	27
c_{26}		49	82	6.4	-3.8	5
c_{27}	mixed	36	58	2.7	-3.2	28
c_{28}		39	53	3.8	-3.9	30
c_{29}		35	60	3.2	-3.8	28
c_{30}		45	47	3.7	-3.5	30
c_{31}		37	57	6.0	-3.7	29
c_{32}		44	48	4.2	-4.9	30

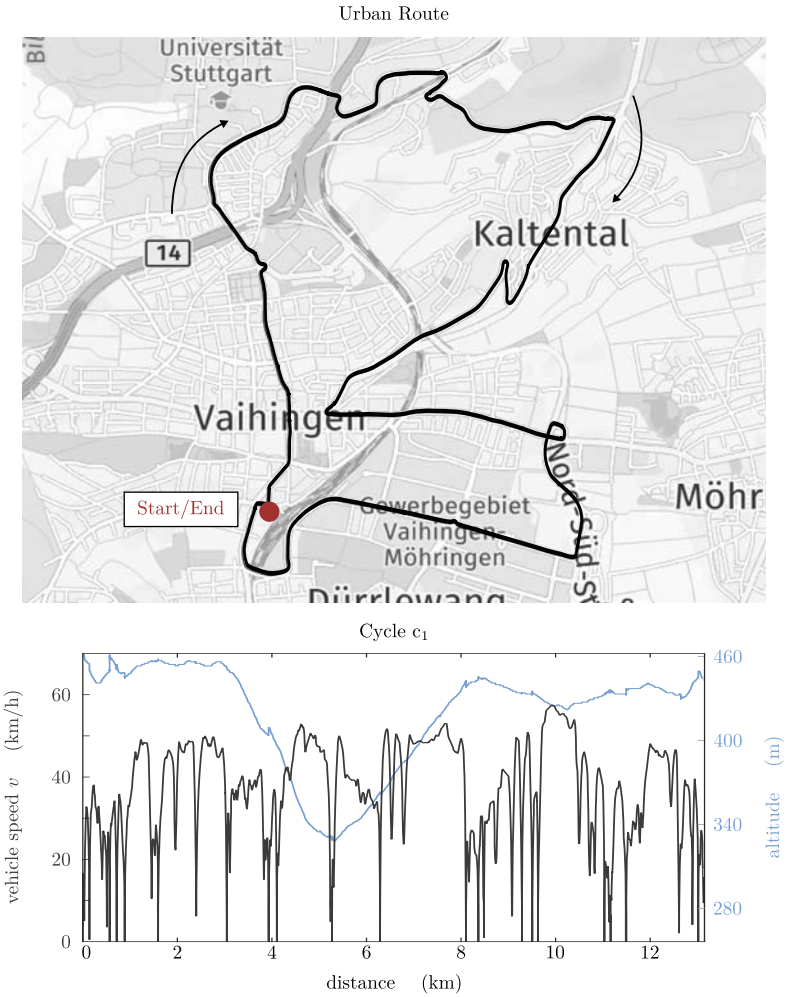

Figure A.1: Map and altitude of the urban route; speed profile of cycle c_1.

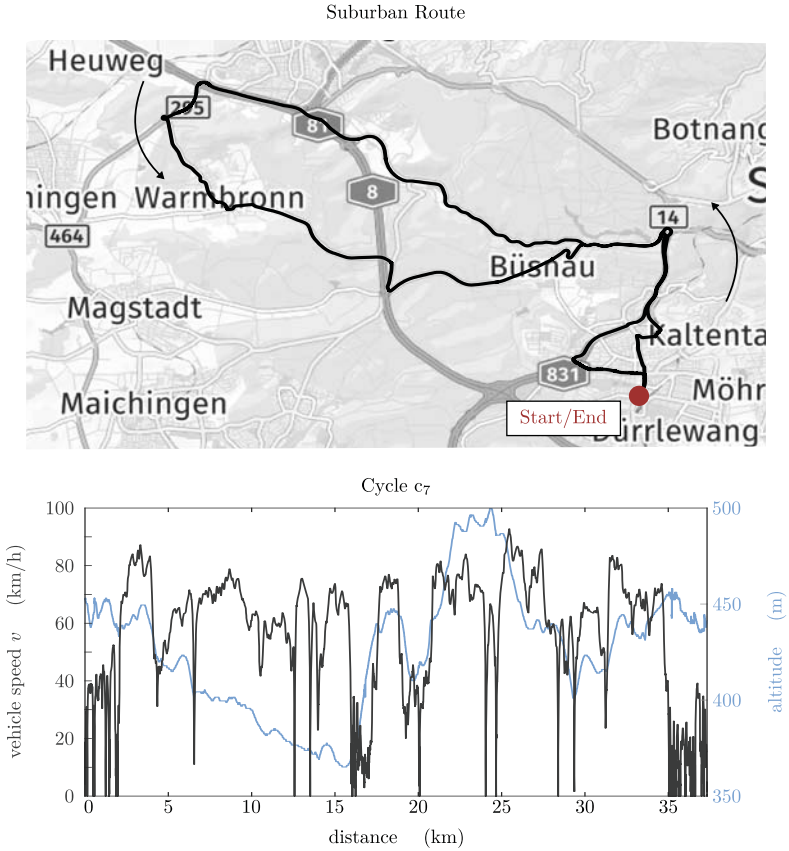

Figure A.2: Map and altitude of the suburban route; speed profile of cycle c_7.

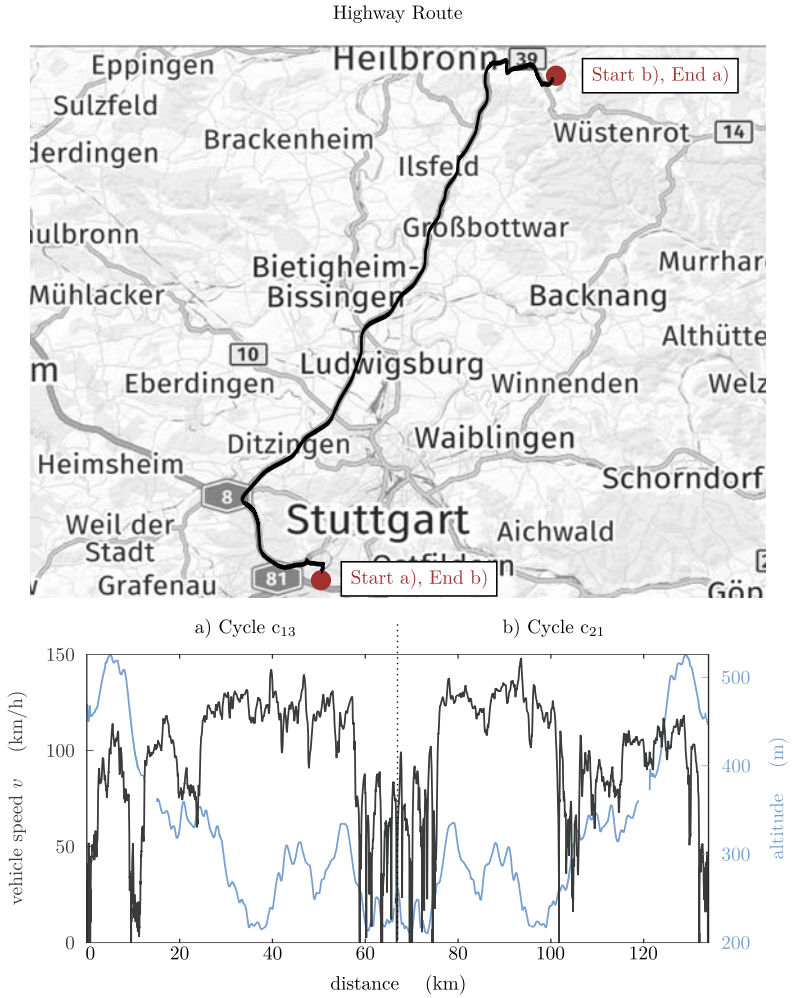

Figure A.3: Map and altitude of the highway route; speed profile of cycle c_{13} and c_{21}.

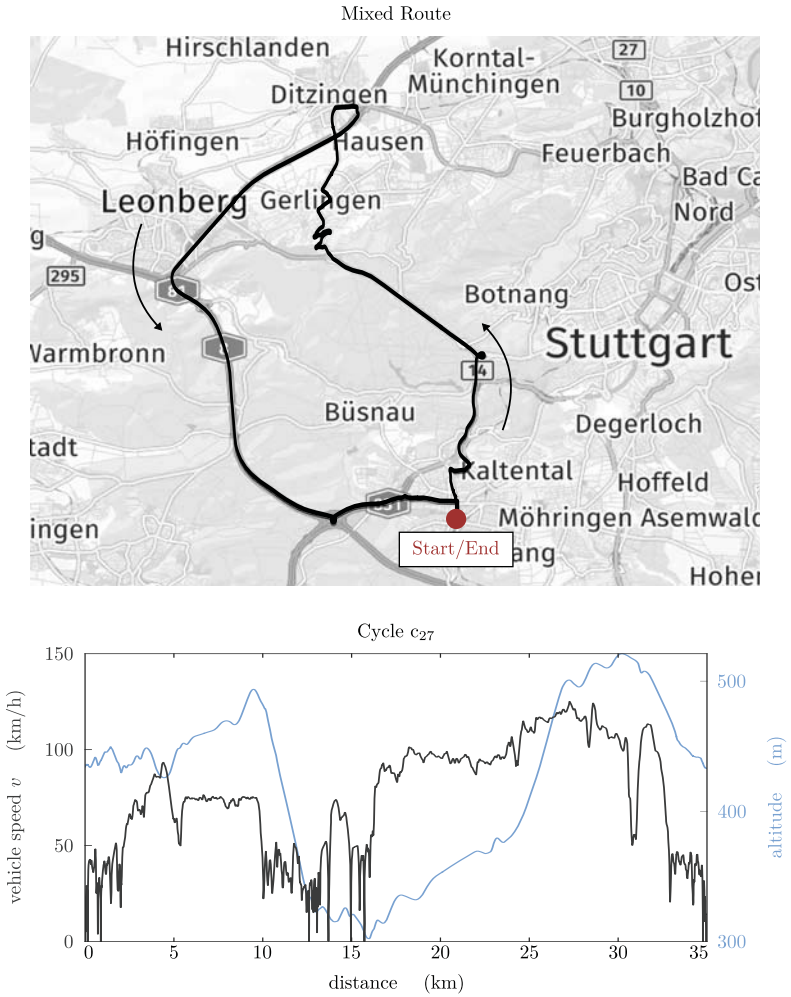

Figure A.4: Map and altitude of the mixed route; speed profile of cycle c_{27}.

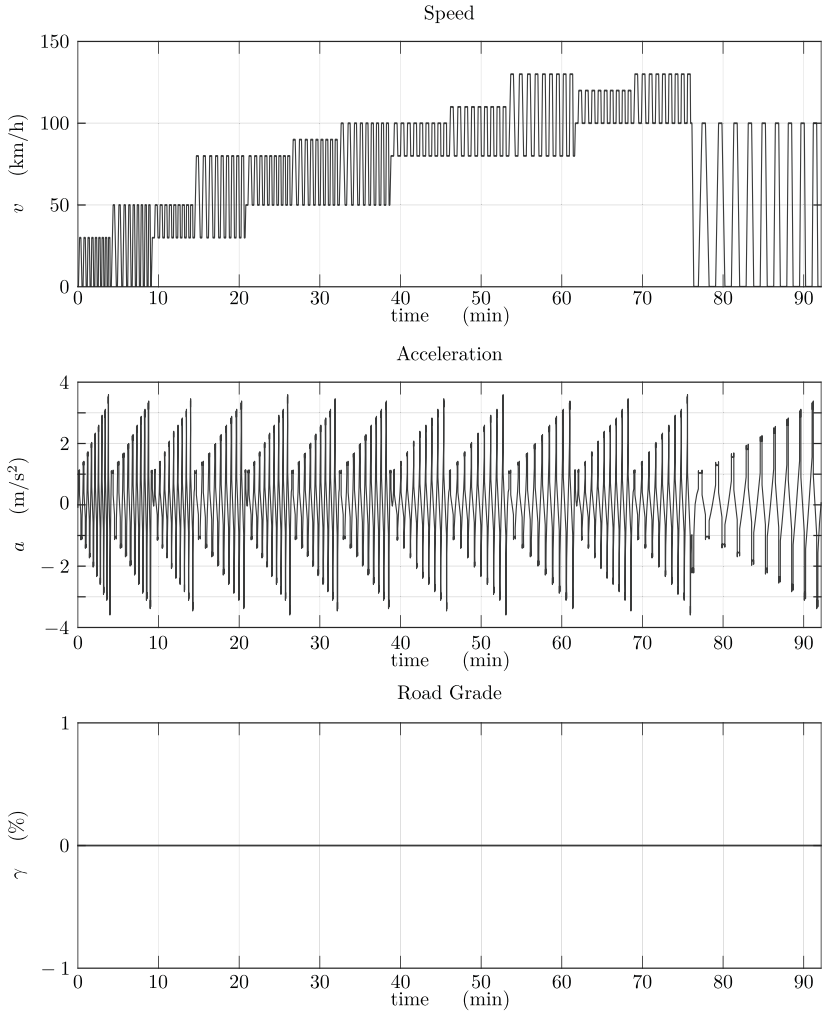

Figure A.5: PIC test series: acceleration and braking cycle.

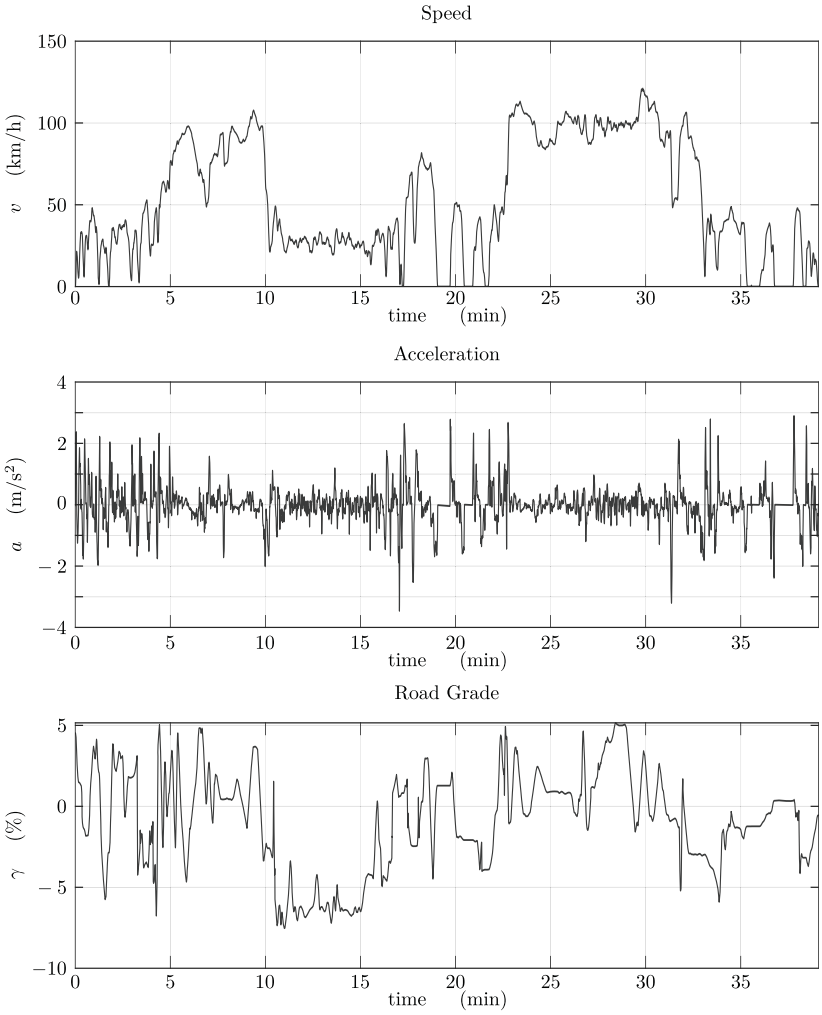

Figure A.6: PIC test series: mixed cycle.

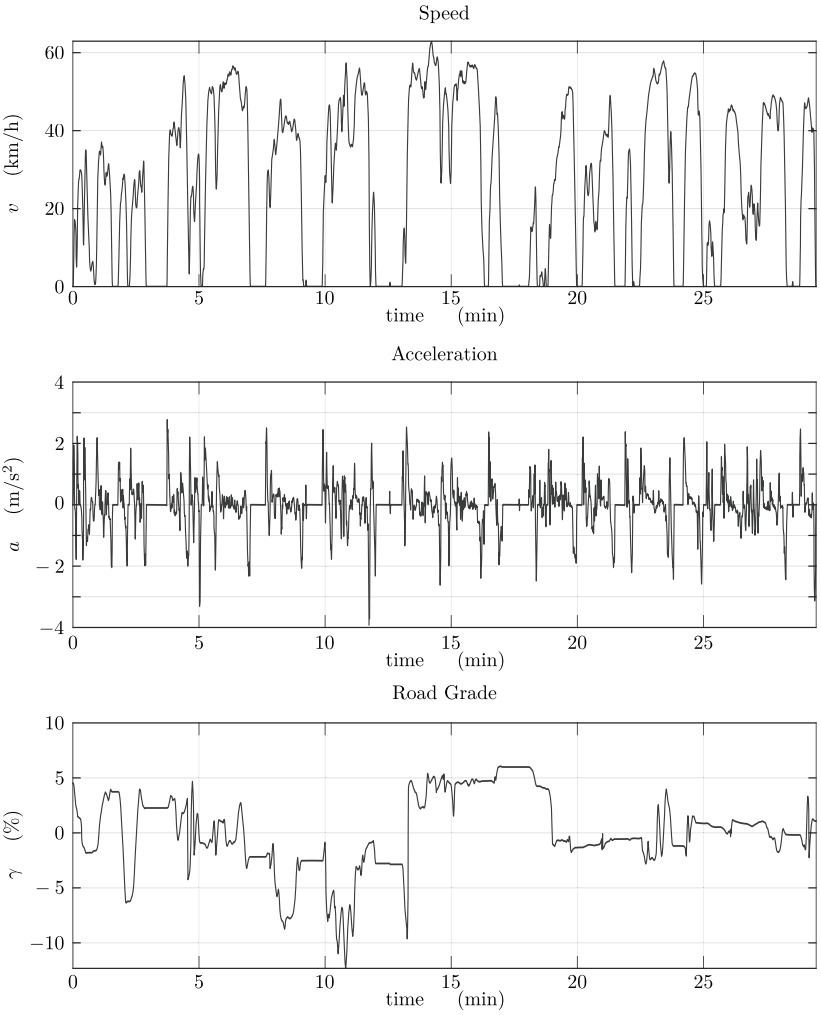

Figure A.7: PIC test series: urban cycle.

Acronyms

2DOF *Two Degree of Freedom.*

ABS *Antilock Braking*, German Antiblockiersystem.

AC *Alternating Current.*

AD *Automatic Differentiation.*

ASR *Traction Control System*, German Antriebsschlupfregelung.

AWD *All-Wheel-Drive.*

BEV *Battery Electric Vehicle.*

CAN *Controller Area Network.*

CNN *Convolutional Neural Network.*

CO_2 *Carbon Dioxide.*

DC *Direct Current.*

DMS *Direct Multiple Shooting.*

DP *Dynamic Programming.*

DTC *Direct Torque Control.*

ED *Economic Driving.*

EDM *Electric Drive Module.*

EKF *Extended Kalman Filter.*

ESC *Electronic Stability Control.*

EV *Electric Vehicle.*

FCEV *Fuel Cell Electric Vehicle.*

FEA *Finite Element Analysis.*

FIR *Finite Impulse Response.*

FOC *Field Oriented Control.*

FWD *Front Wheel Drive.*

GHGE *Greenhouse Gas Emission.*

GPS *Global Positioning System.*

HDF *Harmonic Distortion Function.*

HEV *Hybrid Electric Vehicle.*

ICE *Internal Combustion Engine.*

IGBT *Insulated-Gate Bipolar Transistor.*

IM *Induction Motor.*

IP *Interior Point.*

IPOPT *Interior Point Optimizer.*

IVP *Initial Value Problem.*

KKT *Karush-Kuhn-Tucker.*

LICQ *Linear Independent Constraint Qualification.*

LMT *Loss Minimizing Technique.*

MCU *Motor Control Unit.*

MEC *Magnetic Equivalent Circuit.*

MMF *Magneto-Motive-Force.*

MPC *Model Predictive Control.*

MRAS *Model Reference Adaptive System.*

MTPA *Maximum Torque Per Ampere.*

MTPV *Maximum Torque Per Volt.*

NMPC *Nonlinear Model Predictive Control.*

ODE *Ordinary Differential Equation.*

PHEV *Plug-In Hybrid Electric Vehicle.*

PIC *Powertrain Integration Center.*

PMP *Pontryagin's Maximum Principle.*

PMSM *Permanent Magnet Synchronous Motor.*

PTC *Positive Temperature Coefficient.*

PWM *Pulse Width Modulation.*

REST *Representational State Transfer.*

RMS *Root Mean Square.*

RWD *Rear Wheel Drive.*

SLF *Switching Loss Function.*

SOC *State of Charge.*

SQP *Sequential Quadratic Programming.*

STOS *Stationary Operational Strategy.*

SUV *Sport Utility Vehicle.*

SVPWM *Space Vector PWM.*

VSI *Voltage Source Inverter.*

WFT *Winding Function Theory.*

Notation

The following glossary lists the notation of frequently used sets, operators, functions sub- and superscripts as well as the main model parameters and variables. Sets, variables and parameters that are only used occasionally are omitted. However, all are explained at their first occurrence.

Sets

$\mathbb{C}$	Complex numbers
$\mathbb{R}$	Real numbers
$\mathbb{R}^{\mathrm{n}}$	n-dimensional Vectors
$\mathbb{R}^{\mathrm{n}\times\mathrm{m}}$	Matrices with n rows and m columns
$\mathbb{R}_{-}$	Negative real numbers
$\mathbb{R}_{+}$	Nonnegative real numbers
$\mathbb{Z}$	Integer
$\mathbb{N}$	Natural numbers
i(n)j	Evenly spaced n $\in \mathbb{Z}$ integer topology starting at i $\in \mathbb{Z}$ and ending at j $\in \mathbb{Z}$
$\mathcal{B}$	BEV braking
$\mathcal{C}$	BEV coasting
$\mathcal{C}^n$	Trajectoreis of order n
$\mathcal{O}_{\mathrm{edm}}$	EDM speed and torque operating region
$\mathcal{O}_{\mathrm{ev}}$	BEV speed and torque operating region
$\mathcal{T}$	BEV traction
$\mathcal{X}_{\mathrm{cur}}$	Operating points of the IM that are limited by the maximum phase current
$\mathcal{X}_{\mathrm{im}}$	IM speed and torque operating region
$\mathcal{X}_{\mathrm{pl}}$	Operating points of the IM in the partial load area
$\mathcal{X}_{\mathrm{sat}}$	Operating points of the IM that are limited by saturation
$\mathcal{X}_{\mathrm{volt}}$	Operating points of the IM that are limited by the maximum phase voltage

Functions and Operators

$\mathrm{d}\,\cdot/\mathrm{dt},\ \dot{(\cdot)}$	First time derivative
$\mathrm{d}^2\,\cdot/\mathrm{dt}^2,\ \ddot{(\cdot)}$	Second time derivative
$\mathrm{d}^\mathrm{n}\,\cdot/\mathrm{dt}^\mathrm{n},\ (\cdot)^{(\mathrm{n})}$	Time derivative of order n
$\partial\,\cdot/\partial x$	Partial derivative with respect to x
$L_f\,\cdot$	Lie derivative along the vector field f
$\nabla\,\cdot$	Gradient
$\boldsymbol{H}$	Hessian
$\lvert\cdot\rvert$	Absolute value or modulus
$\bar{\cdot}$	Average value
$\lfloor\cdot\rfloor$	Floor function
$(\cdot)^{[\mathrm{k}]}$	Discrete variable at time t_k
$x\big\rvert_y$	Evaluate variable x at condition y (e.g. time or temperature)
$g \circ f$	Composition of functions g and f $(g \circ f)(x) = g(f(x))$
$\mathrm{diag}\,(\cdot)$	Takes the elements of one or more vectors and returns a diagonal matrix whose main diagonal contains the elements of these vectors
$\mathrm{sign}\,(\cdot)$	Signum function
$\Im\{\cdot\}$	Imaginary part of complex number
$\Re\{\cdot\}$	Real part of complex number
$\delta\,(\cdot)$	Dirac delta function
ϵ_x	Relative difference or error of variable x
Ψ_u	Flat input parametrization
Ψ_x	Flat state parametrization
$\vartheta\,(\cdot)$	Penalty term and distance function
$\vartheta_f\,(\cdot)$	Terminal cost
$C(s)$	Control transfer function
e_x	Absolute error of variable x
$G_\mathrm{yu}(s)$	Transfer function from input u to output y
$\mathrm{J_n}\,(\cdot)$	Bessel function of the first kind and order n
$P(s)$	Plant transfer function

Indices, Sub- and Superscripts

$\hat{\cdot}$	Estimated value or current/voltage peak value
$(\cdot)'$	Variation rate or slope
$(\cdot)^*$	Optimal value, control reference or prediction

$(\cdot)_{\{x,y,z\}}$	Set of diefferent variables
$(.)_{\mathrm{aux}}$	Auxilliary
$(.)_{\mathrm{bat}}$	Battery
$(.)_{\mathrm{dt}}$	Drivetrain
$(.)_{\mathrm{edm}}$	Electric drive module
$(.)_{\mathrm{fl}}$	Flat coordinates
$(.)_{\mathrm{im}}$	Induction motor
$(.)_{\mathrm{lb}}$	Lower bound
$(.)_{\mathrm{nom}}$	Nominal value
$(.)_{\cdot\mathrm{r}}$	Rotor
$(.)_{\cdot\mathrm{s}}$	Stator
$(.)_{\mathrm{sat}}$	Saturation
$(.)_{\mathrm{ub}}$	Upper bound
$(.)^{\mathrm{fa}}$	EDM front axle
$(.)^{\mathrm{lmt}}$	Optimum for unconstrained loss minimizing technique
$(.)^{\mathrm{mpta}}$	Optimum for unconstrained maximum torque per ampere strategy
$(.)^{\mathrm{mptv}}$	Optimum for unconstrained maximum torque per volt strategy
$(.)^{\mathrm{ra}}$	EDM rear axle
$(.)^{\mathrm{st}}$	Assuming steady state conditions
$(.)^{\mathrm{tr}}$	Assuming transient conditions

Space Vectors, Vectors and MatricesMVParameter and Variables

$\underline{x}$	Complex valued space vector
$(\underline{.})^{\alpha}$	Space vector reference frame orientation ($\alpha = 0$ stationary frame; $\alpha = \omega_{\mathrm{e}}$ rotor frame; α omitted for the reference frame in field orientation)
$(\cdot)_{\alpha}$	Real component of space vector in stationary reference frame fixed to the stator (phase a)
$(\cdot)_{\beta}$	Imaginary component of space vector in reference frame fixed to the stator (phase a)
$(\cdot)_{\mathrm{d}}$	Direct (real) component of space vector in field orientation
$(\cdot)_{\mathrm{q}}$	Quadrature (imaginary) component of space vector in field orientation
$\mathbf{0}_{\mathrm{n}\times\mathrm{m}}$	Zero matrix with n rows and m columns

$\boldsymbol{I}_{\mathrm{n}\times\mathrm{m}}$	Identitiy matrix with n rows and m columns
$\boldsymbol{M}$	Matrices are represented by bold variables and capital letters
$\boldsymbol{x}$	Column vectors are represented by bold variables
x_{i}	Element $\mathrm{i} \in \mathbb{N}$ of vector $\boldsymbol{x}$
$\boldsymbol{x}_{\mathrm{i:j}}$	Subvector composed of elemets $\mathrm{i} \in \mathbb{N}$ to $\mathrm{j} \in \mathbb{N}$ of vector $\boldsymbol{x}$

Parameter and Variables

α	IM refernce frame angle	rad
$\dot{\alpha}$	IM refernce frame angular frequency	rad/s
α_{gr}	Golden ratio	-
α_{R}	Temperautre coefficient	1/K
ϵ_x	Relative error or difference of variable x	
η	Efficiency	-
γ	Road grade	rad
ι_{dt}	Drivetrain paramter: gear ratio	-
$\boldsymbol{\lambda}_{\mathrm{abc,\{s,r\}}}$	IM stator and rotor flux linking coils a, b, and c, balanced set $\boldsymbol{\lambda}_{\mathrm{abc,\{s,r\}}} = \left(\lambda_{a\{\mathrm{s,r}\}}, \lambda_{b\{\mathrm{s,r}\}}, \lambda_{c\{\mathrm{s,r}\}}\right)^T$	Wb
λ'	Slope of optimized torque trajectory	V
λ_{r}	IM rotor flux linkage	Wb
$\lambda_{\mathrm{r,cur}}$	IM rotor flux level of maximum phase current	Wb
λ_{lb}	IM lower bound of rotor flux linkage	Wb
λ^{lmt}	IM loss minimizing rotor flux level	Wb
λ^{mtpa}	IM phase current minimizing rotor flux level	Wb
λ^{mtpv}	IM phase voltage minimizing rotor flux level	Wb
λ_{ub}	IM upper bound of rotor flux linkage	Wb
$\lambda_{\mathrm{r,volt}}$	IM rotor flux level of maximum phase voltage	Wb
$\mu_{\cdot}$	Lagrange multiplier	-
ω_0	IM fundamental elctrical angular frequency	rad/s
ω_{e}	IM elctric rotor angular frequency	rad/s
ω_{m}	IM rotor angular frequency	rad/s
ω_{nom}	Nominal angular frequency	rad/s
ω_{sl}	IM slip angular frequency	rad/s
ω_{whl}	Drivetrain wheel angular frequency	rad/s
φ	IM power factor angle	rad
ρ	Air density	$\mathrm{kg/m^3}$

σ	IM paramter: leakage coefficient	-
τ_c	IM paramter: current time constant	s
τ_d	VIS parmeter: computational delay of regular sampled PWM method	s
τ_λ	Time constant of optimized rotor flux trajectory	s
τ_r	IM parmeter: rotor time constant	s
τ_Te	Time constant of optimized torque trajectory	s
θ_e	IM electrical rotor angle	rad
θ_m	IM rotor angle	rad
θ_spl	Torque split coefficient between front and rear axle	-
ς	l_1 norm regularization factor used in optimization problems as tuning parameter	-
ϑ_0	Reference temperature	°C
ϑ_amb	Ambient temperature	°C
ϑ_bat	Battery temperature	°C
ϑ_s	IM stator temperature	°C
a	Vehicle acceleration	$\mathrm{m/s^2}$
a_pwm	VSI paramter: maximum attainable voltage range of the PWM method	-
A_f	BEV paramter: projectred vehicle frontal area	$\mathrm{m^2}$
$A_\mathrm{mn}, B_\mathrm{mn}$	VSI coefficients of the double Fourier series expansion of the PWM switching signal	-
c_d	BEV paramter: drag coefficient	-
c_r	BEV paramter: rolling resistance coefficient	-
d_d	IM disturbance in the direct component of voltage control	V
d_q	IM disturbance in the quadrature component of voltage control	V
E	Energy	J
E_aux	Auxiliary energy consumption	J
$E_\mathcal{B}$	Braking energy	J
E_bat	Battery energy	J
E'_rec	VSI paramter: average variation rate of the diode reverse recovery energy $\partial E_\mathrm{rec}/\partial i_\mathrm{D}$	Vs
E_l	Dissipated energy	J
$E_{\mathrm{l},\mathcal{B}}$	Dissipated energy of powertrain losses during braking	J
$E_{\mathrm{l},\mathcal{T}}$	Dissipated energy of powertrain losses during traction	J
$E_\mathrm{on,off}$	VSI transistor switching energy	J

E_{rec}	VSI diode reverse recovery energy	J
e_x	Absolute error of variable x	
$E_{\mathcal{T}}$	Traction energy	J
$E'_{\mathrm{on,off}}$	VSI paramter: average variation rate of the turn-off and turn-on transistor switching energy $\partial E_{\mathrm{on,off}}/\partial i_{\mathrm{Tr}}$	Vs
f_{c}	VSI parameter: PWM carrier frequency	Hz
F_{res}	Sum of aerodynamic resistance, rolling firction force and the force induced by gravity	N
g	Acceleration due to gravity	$\mathrm{m/s^2}$
h_{pwm}	VSI harmonic factor of the PWM method	-
$\boldsymbol{i}_{\mathrm{abc,s}}$	IM balanced set of stator phase currents $\boldsymbol{i}_{\mathrm{abc,s}} = (i_{\mathrm{as}}, i_{\mathrm{bs}}, i_{\mathrm{cs}})^T$	A
$i_{\alpha\mathrm{s}}$	IM stator phase current real component of space vector in the stationary reference frame	A
$i_{\beta\mathrm{s}}$	IM stator phase current imaginary component of space vector in the stationary reference frame	A
i_{D}	VSI diode current	A
$\overline{i}_{\mathrm{D},\{u,l\}}$	VSI per fundamental average diode current of the upper and lower switch	A
i_{dc}	DC-link or terminal current	A
i_{ds}	IM stator phase current direct component of space vector	A
$\hat{i}$	IM stator phase current peak value	A
$\hat{i}_{\mathrm{ub}}$	IM upper bound of phase current peak value	A
i_{qs}	IM stator phase current quadrature component of space vector	A
i_{rms}	IM stator phase current RMS value	A
i_{s}	IM stator phase current	A
i_{Tr}	VSI transistor current	A
$\overline{i}_{\mathrm{Tr},\{u,l\}}$	VSI per fundamental average transistor current of the upper and lower switch	A
J	Drivetrain paramter: inertia of all rotating components	$\mathrm{kg\,m^2}$
L'_{lr}	IM paramter: rotor leakage self-inductance related to the stator coils	H
$L_{\mathrm{l\{s,r\}}}$	IM paramter: stator and rotor leakage self-inductance	H
L_{m}	IM paramter: mutual inductance, is equal to three halves of the stator self-inductance	H

$L_{\mathrm{m\{s,r\}}}$	IM paramter: stator and rotor self-inductance	H
L_{r}	IM paramter: rotor inductance	H
L_{s}	IM paramter: stator inductance	H
$L_{\mathrm{s,r}}$	IM paramter: mutual stator and rotor inductance	H
m	BEV paramter: vehicle mass	kg
M_{i}	VSI modulation index	-
$N_{\{s,r\}}$	IM paramter: turns of stator and rotor coils	-
p	PWM carrier ratio	-
$p_{\{0,1,2\}dt,\{\mathcal{T},\mathcal{B}\}}$	Drivetrain parameter: emperically determined quasitationary model of the parasitic friction torqe	N
$p_{\{0,1\}dt}$	Drivetrain parameter: emperically determined quasitationary model of the parasitic friction torqe	N
P_{bat}	Battery power demand	W
P_{e}	Electric power	W
$P_{\mathrm{e,aux}}$	Auxiliary power demand	W
$P_{\mathrm{e,edm}}$	EDM input power	W
$P_{\mathrm{e,im}}$	IM electrical input power	W
P_{EV}	Overall electric power demand	W
P_{l}	Power loss	W
$P_{\mathrm{l,core}}$	IM core losses	W
$P_{\mathrm{l,edm}}$	EDM power loss	W
$P_{\mathrm{l,im}}$	IM cundoction, leakage and core losses	W
$P_{\mathrm{l,vsi}}$	VSI conduction and switching losses	W
P_{m}	Mechanical power	W
Q_{nom}	Battery paramter: nominal capacity	C
R_{bat}	Battery paramter: internal resistance	Ω
R_{D}	VSI paramter: conduction resistance diode	Ω
R_{fe}	IM paramter: core loss resistance	Ω
R_{r}	IM paramter: rotor resistance	Ω
R'_{r}	IM paramter: rotor resistance related to the stator coils	Ω
R_{s}	IM paramter: stator resistance	Ω
R_{Tr}	VSI paramter: conduction resistance transistor	Ω
r_{whl}	Drivetrain paramter: wheel radius	m
s	Laplace variable	
$s_{\{\mathrm{a,b,c}\}}$	PWM switching or gating signal of the upper phase switches	-

$\bar{s}_{\{\mathrm{a,b,c}\}}$	PWM switching or gating signal of the lower phase switches	-
s_n	Slack variable for negative values	
SOC	Battery state of charge	-
s_p	Slack variable for postive values	
s_{sl}	IM slip factor	-
t	Time	s
t_0	Initial time	s
t_{d}	Discrete time interval of shooting/dsicretization grid	s
t_{f}	Time at the end of a scenario/transition	s
t_{k}	Discrete time	s
t_{mpc}	MPC update rate	s
T_{brk}	Drivetrain friciton brake torque	Nm
T_{dt}	Drivetrain parasitic friction torque	Nm
T_{e}	IM electromagnetic rotor torque	Nm
$T_{\mathrm{e},\{\mathrm{lb,ub}\}}$	IM upper and lower bound of electromagnetic rotor torque	Nm
$T_{\mathrm{e,whl}}$	Drivetrain electrical wheel torque	Nm
T_{fric}	Drivetrain friction brake offset	Nm
T_{nom}	Nominal torque	Nm
T_{whl}	Drivetrain wheel torque	Nm
$T_{\mathrm{whl},\{\mathrm{lb,ub}\}}$	Drivetrain upper and lower bound of wheel torque	Nm
$\boldsymbol{u}_{\mathrm{abc,s}}$	IM balanced set of stator lin-to-neutral voltages $\boldsymbol{u}_{\mathrm{abc,s}} = (u_{\mathrm{as}}, u_{\mathrm{bs}}, u_{\mathrm{cs}})^T$	V
$u_{\alpha\mathrm{s}}$	IM stator phase voltage real component of space vector in the stationary reference frame	V
$u_{\mathrm{as,n}}$	PWM reference voltage of phase a	V
$u_{\beta\mathrm{s}}$	IM stator phase voltage imaginary component of space vector in the stationary reference frame	V
u_{D}	VSI diode voltage	V
$\bar{u}_{\mathrm{Tr},\{u,l\}}$	VSI per fundamental average transistor voltage of the upper and lower switch	V
u_{dc}	DC-link or terminal voltage	V
U_{D}	VSI paramter: diode forward voltage	V
u_{ds}	IM stator phase voltage direct component of space vector	V
$\boldsymbol{u}_{\mathrm{fl}}$	Input of flat system	
u_{ocv}	Battery open cirquit voltage	V

$\hat{u}$	IM stator phase voltage peak value	V
u_{qs}	IM stator phase voltage quadrature component of space vector	V
u_{s}	IM stator phase voltage	V
u_{Tr}	VSI transistor voltage	V
$\bar{u}_{\mathrm{D},\{u,l\}}$	VSI per fundamental average diode voltage of the upper and lower switch	V
U_{Tr}	VSI paramter: transistor forward voltage	V
u_{ub}	IM upper bound of stator phase voltage	V
v	Vehicle speed	m/s
w.	Weighting factor used in optimization problems as tuning parameter	-
$\boldsymbol{x}$	System state	
$\boldsymbol{x}_{\mathrm{fl}}$	State of flat system	
x	PWM time variable of the modulation carrier wave	rad
y	PWM time variable of the reference wave	rad
$\boldsymbol{z}$	Flat output	
Z_{IM}	IM input inpedance	Ω
Z_{p}	IM paramter: number of pole pairs	-

List of Figures

List of Tables

Bibliography

[1] J. Ackermann. *Sampled-Data Control Systems: analysis and synthesis, robust system design*. Springer-Verlag, Berlin, Heidelberg, 1985.

[2] J. Albersmeyer. "Adjoint-Based Algorithms and Numerical Methods for Sensitivity Generation and Optimization of Large Scale Dynamic Systems". PhD thesis. Naturwissenschaflich-Mathematische Gesamtfakultät der Ruprecht-Karls-Universität Heidelberg, 2010.

[3] A. Ali, R. Shivapurkar, and D. Söffker. "Optimal Situation-Based Power Management and Application to State Predictive Models for Multi-Source Electric Vehicles". *IEEE Transactions on Vehicular Technology* 68 (2019), pp. 11473–11482.

[4] J. H. Alimeling and W. P. Hammer. "PLECS-Piece-Wise Linear Electrical Circuit Simulation for Simulink". *Proceedings of the IEEE International Conference on Power Electronics and Drive Systems*. 1999, pp. 355–360.

[5] B. Asadi and A. Vahidi. "Predictive Cruise Control: Utilizing Upcoming Traffic Signal Information for Improving Fuel Economy and Reducing Trip Time". *IEEE Transactions on Control Systems Technology* 19 (2011), pp. 707–714.

[6] K. J. Åström and T. Hägglund. *Advanced PID Control*. International Society of Automation, Durham, NC, 2006.

[7] D. Atkinson, P. Acarnley, and J. Finch. "Observers for Induction Motor State and Parameter Estimation". *IEEE Transactions on Industry Applications* 27 (1991), pp. 1119–1127.

[8] A. Basler. "Eine Modulare Funktionsarchitektur zur Umsetzung einer Gesamtheitlichen Betriebsstrategie für Elektrofahrzeuge". PhD thesis. Karlsruher Schriftenreihe Fahrzeugsystemtechnik, Institut für Fahrzeugsystemtechnik, 2015.

[9] M. Bayer. *Online Identification of Induction Machine Parameters for Battery Electric Vehicles*. Master Thesis, University of Stuttgart, Institute for System Dynamics. 2017.

[10] A. Bazzi and P. Krein. “Comparative Evaluation of Machines for Electric and Hybrid Vehicles Based on Dynamic Operation and Loss Minimization”. *Proceedings of the IEEE Energy Conversion Congress and Exposition*. 2010, pp. 3345–3351.

[11] A. Bazzi and P. Krein. “Review of Methods for Real-Time Loss Minimization in Induction Machines”. *IEEE Transactions on Industry Applications* 46 (2010), pp. 2319–2328.

[12] H. Benson, R. Vanderbei, and D. Shanno. “Interior-Point Methods for Nonconvex Nonlinear Programming: Filter Methods and Merit Functions”. *Computational Optimization and Applications* 23 (2002), pp. 257–272.

[13] D. Bertsekas. *Dynamic Programming and Optimal Control*. Athena Scientific, Belmont, MA, 1995.

[14] G. Besançon, A. Besançon-Voda, and G. Bornard. “A Note on Identifiability of Induction Motors”. *Proceedings of the European Control Conference*. 2001, pp. 3576–3579.

[15] J. Betts. *Practical Methods for Optimal Control and Estimation Using Nonlinear Programming*. Vol. 2. Society for Industrial and Applied Mathematics, Philadelphia, PA, 2010.

[16] L. Biagiotti and C. Melchiorri. “FIR Filters for Online Trajectory Planning with Time- and Frequency-Domain Specifications”. *Control Engineering Practice* 20 (2012), pp. 1385–1399.

[17] A. Biswas and A. Emadi. “Energy Management Systems for Electrified Powertrains: State-of-the-Art Review and Future Trends”. *IEEE Transactions on Vehicular Technology* 68 (2019), pp. 6453–6467.

[18] F. Blaschke. “Das Verfahren der Feldorientierung zur Regelung der Drehfeldmaschine”. PhD thesis. Technische Universität Braunschweig, 1973.

[19] H. Bock and K. Plitt. “A Multiple Shooting Algorithm for Direct Solution of Optimal Control Problems*”. *IFAC Proceedings Volumes* 17 (1984), pp. 1603–1608.

[20] A. Boglietti, A. Cavagnino, L. Ferraris, and M. Lazzari. “Skin Effect Experimental Validations of Induction Motor Squirrel Cage Parameters”. *Proceedings of the International Conference on Electrical Machines*. 2008, pp. 1–4.

[21] B. K. Bose. *Power Electronics and Variable Frequency Drives: Technology and Applications*. Wiley-IEEE Press, Piscataway, NJ, 1997.

[22] G. Bossio, C. De Angelo, J. Solsona, G. Garcia, and M. Valla. "A 2-D Model of the Induction Machine: An Extension of the Modified Winding Function Approach". *IEEE Transactions on Energy Conversion* 19 (2004), pp. 144–150.

[23] A. Bryson and Y.-C. Ho. *Applied Optimal Control: Optimization, Estimation and Control. Optimization, Estimation, and Control*. 14th ed. Hemisphere Publ. Corp., NY, 1988.

[24] S. Buller, M. Thele, R. De Doncker, and E. Karden. "Impedance-Based Simulation Models of Supercapacitors and Li-Ion Batteries for Power Electronic Applications". *IEEE Transactions on Industry Applications* 41 (2005), pp. 742–747.

[25] V. Buyukdegirmenci, A. Bazzi, and P. Krein. "Evaluation of Induction and Permanent-Magnet Synchronous Machines Using Drive-Cycle Energy and Loss Minimization in Traction Applications". *IEEE Transactions on Industry Applications* 50 (2014), pp. 395–403.

[26] S. D. Cairano, D. Bernardini, A. Bemporad, and I. V. Kolmanovsky. "Stochastic MPC With Learning for Driver-Predictive Vehicle Control and its Application to HEV Energy Management". *IEEE Transactions on Control Systems Technology* 22 (2014), pp. 1018–1031.

[27] C. Canudas de Wit and J. Ramirez. "Optimal Torque Control for Current-Fed Induction Motors". *IEEE Transactions on Automatic Control* 44 (1999), pp. 1084–1089.

[28] D. Casadei, F. Profumo, G. Serra, and A. Tani. "FOC and DTC: Two Viable Schemes for Induction Motors Torque Control". *IEEE Transactions on Power Electronics* 17 (2002), pp. 779–787.

[29] B. Cassimere, S. Sudhoff, D. Aliprantis, and M. Swinney. "IGBT and PN Junction Diode Loss Modeling for System Simulations". *Proceedings of the IEEE International Conference on Electric Machines and Drives*. 2005, pp. 941–949.

[30] P. Castaldi and A. Tilli. "Parameter Estimation of Induction Motor at Standstill with Magnetic Flux Monitoring". *IEEE Transactions on Control Systems Technology* 13 (2005), pp. 386–400.

[31] B. Chalmers and R. Dodgson. "Waveshapes Of Flux Density In Polyphase Induction Motors Under Saturated Conditions". *IEEE Transactions on Power Apparatus and Systems* PAS-90 (1971), pp. 564–569.

[32] D. Chang and E. Morlok. "Vehicle Speed Profiles to Minimize Work and Fuel Consumption". *Journal of Transportation Engineering* 131 (2005), pp. 173–182.

[33] J. Chiasson. “Dynamic Feedback Linearization of the Induction Motor”. *IEEE Transactions on Automatic Control* 38 (1993), pp. 1588–1594.

[34] E. Clarke. *Circuit Analysis of A-C Power Systems: Symmetrical and Related Components*. 4th ed. Vol. 1. Wiley, NY, 1950.

[35] T. I. C. on Clean Transportation. *Light-Duty Vehicle Greenhouse Gas and Fuel Economy Standards - 2017 Global Update*. 2017.

[36] T. I. C. on Clean Transportation. *A Global Snapshot of the Air Pollution-Related Health Impacts of Transportation Sector Emissions in 2010 and 2015*. 2019.

[37] T. I. C. on Clean Transportation. *Overview of Global Zero-Emission Vehicle Mandate Programs*. 2019.

[38] T. I. C. on Clean Transportation. *European Electric Vehicle Factbook 2019/2020*. 2020.

[39] A. Conn, N. Glould, and P. Toint. *LANCELOT: a Fortran Package for Large-Scale Nonlinear Optimization*. Springer, Berlin, Heidelberg, 1992.

[40] F. Conte. “Battery and Battery Management for Hybrid Electric Vehicles: A Review”. *Elektrotechnik und Informationstechnik* 123 (2006), pp. 424–431.

[41] Daimler AG. *Mercedes-Benz EQC*. `https://www.mercedes-benz.com/en/eq/eqc/`. [Online; accessed 18-July-2020]. 2020.

[42] J. Dannehl and F. Fuchs. “Flatness-Based Control of an Induction Machine Fed via Voltage Source Inverter - Concept, Control Design and Performance Analysis”. *Proceedings of the IEEE Conference on Industrial Electronics*. 2006, pp. 5125–5130.

[43] R. W. De Doncker. “Parameter Sensitivity of Indirect Universal Field-Oriented Controllers”. *IEEE Transactions on Power Electronics* 9 (1994), pp. 367–376.

[44] R. De Doncker and D. Novotny. “The Universal Field Oriented Controller”. *IEEE Transactions on Industry Applications* 30 (1994), pp. 92–100.

[45] A. De Keyser, M. Vandeputte, and G. Crevecoeur. “Convex Mapping Formulations Enabling Optimal Power Split and Design of the Electric Drivetrain in All-Electric Vehicles”. *IEEE Transactions on Vehicular Technology* 66 (2017), pp. 9702–9711.

[46] G. De Nunzio, C. Canudas de Wit, P. Moulin, and D. Di Domenico. “Eco-Driving in Urban Traffic Networks Using Traffic Signal Information”. *Int. J. Robust. Nonlinear Control* 26 (2016), pp. 1307–1324.

[47] E. Delaleau, J. Louis, and R. Ortega. "Modeling and Control of Induction Motors". *International Journal of Applied Mathematics and Computer Science* 11 (2001), pp. 105–129.

[48] M. Depenbrock. "Direct Self-Control (DSC) of Inverter-Fed Induction Machine". *IEEE Transactions on Power Electronics* 3 (1988), pp. 420–429.

[49] W. Dib, A. Chasse, P. Moulin, A. Sciarretta, and G. Corde. "Optimal Energy Management for an Electric Vehicle in ECO-Driving Applications". *Control Engineering Practice* 29 (2014), pp. 299–307.

[50] M. Diehl, H. Bock, H. Diedam, and P.-B. Wieber. "Fast Direct Multiple Shooting Algorithms for Optimal Robot Control". In: *Fast Motions in Biomechanics and Robotics: Optimization and Feedback Control*. Ed. by M. Diehl and K. Mombaur. Springer, Berlin, Heidelberg, 2006, pp. 65–93.

[51] M. Diehl, H. Ferreau, and N. Haverbeke. "Efficient Numerical Methods for Nonlinear MPC and Moving Horizon Estimation". In: *Nonlinear Model Predictive Control*. Ed. by L. Magni, D. Raimondo, and F. Allgöwer. Springer, Berlin, Heidelberg, 2009, pp. 391–417.

[52] M. Diehl, R. Findeisen, and F. Allgöwer. "A Stabilizing Real-Time Implementation of Nonlinear Model Predictive Control". In: *Real-Time PDE-Constrained Optimization*. Ed. by L. Biegler, D. Keyes, O. G. B. van Bloemen Waanders, and M. Heinkenschloss. Society for Industrial and Applied Mathematics, Philadelphia, 2007, pp. 25–52.

[53] A. M. Dizqah, B. Lenzo, A. Sorniotti, P. Gruber, S. Fallah, and J. De Smet. "A Fast and Parametric Torque Distribution Strategy for Four-Wheel-Drive Energy-Efficient Electric Vehicles". *IEEE Transactions on Industrial Electronics* 63 (2016), pp. 4367–4376.

[54] J. Doerr, N. Ardey, G. Mendl, G. Fröhlich, R. Straßer, and T. Laudenbach. "The New Full Electric Drivetrain of the Audi E-Tron". In: *Der Antrieb von morgen 2019*. Ed. by J. Liebl. Springer Vieweg, Wiesbaden, 2019, pp. 13–37.

[55] A. Domahidi and J. Jerez. *FORCES Professional*. `https://embotech.com/FORCES-Pro`. [Online; accessed 18-July-2020]. 2019.

[56] E. dos Santos and E. da Silva. *Advanced Power Electronics Converters: PWM Converters Processing AC Voltages*. Wiley, Hoboken, 2015.

[57] I. Dunning, J. Huchette, and M. Lubin. "JuMP: A Modeling Language for Mathematical Optimization". *SIAM Review* 59 (2017), pp. 295–320.

[58] T. Englert and K. Graichen. “Nonlinear Model Predictive Torque Control of PMSMs for High Performance Applications”. *Control Engineering Practice* 81 (2018), pp. 43–54.

[59] T. Englert and K. Graichen. “Optimal Setpoint Computation for Constrained Torque Control of PMSMs”. *Proceedings of the European Control Conference*. 2018, pp. 2671–2677.

[60] T. Englert and K. Graichen. “Nonlinear Model Predictive Torque Control and Setpoint Computation of Induction Machines for High Performance Applications”. *Control Engineering Practice* 99 (2020), p. 104415.

[61] European Environment Agency. *Electric Vehicles From Life Cycle and Circular Economy Perspectives*. 2018.

[62] European Environment Agency. *Monitoring CO_2 Emissions from New Passenger Cars and Vans in 2017*. 2019.

[63] European Environment Agency. *Transport: Increasing Oil Consumption and Greenhouse Gas Emissions Hamper EU Progress Towards Environment and Climate Objectives*. 2020.

[64] M. Felden, P. Bütterling, P. Jeck, L. Eckstein, and K. Hameyer. “Electric Vehicle Drivetrains: From the Specification Sheet to the Drive-Train Concept”. *Proceedings of the International Power Electronics and Motion Control Conference*. 2010, S11-9 - S11–16.

[65] T. Finken, M. Felden, and K. Hameyer. “Comparison and Design of Different Electrical Machine Types Tegarding their Applicability in Hybrid Electrical Vehicles”. *Proceedings of the International Conference on Electrical Machines*. 2008, pp. 1–5.

[66] M. Fliess, J. Levine, P. Martin, F. Ollivier, and P. Rouchon. “Flatness and Dynamic Feedback Linearizability: Two Approaches”. *Proceedings of the European Control Conference*. 1995, pp. 649–654.

[67] M. Fliess, J. Levine, P. Martin, and P. Rouchon. “A Lie-Backlund Approach to Equivalence and Flatness of Nonlinear Systems”. *IEEE Transactions on Automatic Control* 44 (1999), pp. 922–937.

[68] O. Föllinger, U. Konigorski, B. Lohmann, G. Roppenecker, and A. Trächtler. *Regelungstechnik: Einführung in die Methoden und ihre Anwendung*. VDE Verlag, Berlin, Offenbach, 2016.

[69] A. Fotouhi, D. J. Auger, K. Propp, S. Longo, and M. Wild. “A Review on Electric Vehicle Battery Modelling: From Lithium-Ion toward Lithium–Sulphur”. *Renewable and Sustainable Energy Reviews* 56 (2016), pp. 1008–1021.

[70] A. Freuer. *Ein Assistenzsystem für die Energetisch Optimierte Längsführung eines Elektrofahrzeugs*. Springer Vieweg, Wiesbaden, 2016.

[71] A. Freuer and H.-C. Reuss. "Consumption Optimization in Battery Electric Vehicles by Autonomous Cruise Control using Predictive Route Data and a Radar System". *SAE International Journal of Alternative Powertrains* 2 (2013), pp. 304–313.

[72] B. Frieden. *Physics from Fischer Information*. Cambridge University Press, Cambridge, 1998.

[73] R. Gabriel, W. Leonhard, and C. Nordby. "Field-Oriented Control of a Standard AC Motor Using Microprocessors". *IEEE Transactions on Industry Applications* IA-16 (1980), pp. 186–192.

[74] E. Garone, S. Di Cairano, and I. Kolmanovsky. "Reference and Command Governors for Systems with Constraints: A Survey on Theory and Applications". *Automatica* 75 (2017), pp. 306–328.

[75] A. Gasparetto, P. Boscariol, A. Lanzutti, and R. Vidoni. "Trajectory Planning in Robotics". *Mathematics in Computer Science* 6 (2012), pp. 269–279.

[76] T. Geyer. "Computationally Efficient Model Predictive Direct Torque Control". *IEEE Transactions on Power Electronics* 26 (2011), pp. 2804–2816.

[77] A. Griewank and A. Walther. *Evaluating Derivatives: Principles and Techniques of Algorithmic Differentiation*. 2nd ed. SIAM, Philadelphia, 2008.

[78] L. Guzzella and A. Sciarretta. *Vehicle Propulsion Systems: Introduction to Modeling and Optimization. Introduction to Modeling and Optimiztion*. Vol. 3. Springer, Berlin, Heidelberg, 2013.

[79] A. Haddoun, M. Benbouzid, D. Diallo, R. Abdessemed, J. Ghouili, and K. Srairi. "A Loss-Minimization DTC Scheme for EV Induction Motors". *IEEE Transactions on Vehicular Technology* 56 (2007), pp. 81–88.

[80] J. Han, A. Vahidi, and A. Sciarretta. "Fundamentals of Energy Efficient Driving for Combustion Engine and Electric Vehicles: An Optimal Control Perspective". *Automatica* 103 (2019), pp. 558–572.

[81] M. Hannan, M. Lipu, A. Hussain, and A. Mohamed. "A Review of Lithium-Ion Battery State of Charge Estimation and Management System in Electric Vehicle Applications: Challenges and Recommendations". *Renewable and Sustainable Energy Reviews* 78 (2017), pp. 834–854.

[82] K. Hasse. "Zur Dynamik Drehzahlgeregelter Antriebe mit Stromrichtergespeisten Asynchron-Kurzschlussläufermaschinen". PhD thesis. TH Darmstadt, 1969.

[83] A. Hava, R. J. Kerkman, and T. Lipo. “Carrier-based PWM-VSI Overmodulation Strategies: Analysis, Comparison, and Design”. *IEEE Transactions on Power Electronics* 13 (1998), pp. 674–689.

[84] A. Hava, R. Kerkman, and T. Lipo. “Simple Analytical and Graphical Methods for Carrier-Based PWM-VSI Drives”. *IEEE Transactions on Power Electronics* 14 (1999), pp. 49–61.

[85] E. Hellström, M. Ivarsson, J. Åslund, and L. Nielsen. “Look-Ahead Control for Heavy Trucks to Minimize Trip Time and Fuel Consumption”. *Control Engineering Practice* 17 (2009), pp. 245–254.

[86] G. Heppeler, M. Sonntag, and O. Sawodny. “Fuel Efficiency Analysis for Simultaneous Optimization of the Velocity Trajectory and the Energy Management in Hybrid Electric Vehicles”. *IFAC Proceedings Volumes* 47 (2014), pp. 6612–6617.

[87] G. Heppeler, M. Sonntag, U. Wohlhaupter, and O. Sawodny. “Predictive Planning of Optimal Velocity and State of Charge Trajectories for Hybrid Electric Vehicles”. *Control Engineering Practice* 61 (2017), pp. 229–243.

[88] M. Heppeler. “Prädiktive Fahr- und Betriebsstrategie für Elektrische Hybrid-PKW”. PhD thesis. Institute for System Dynamics, University of Stuttgart, 2019.

[89] A. Hindmarsh, P. Brown, K. Grant, S. Lee, R. Serban, D. Shumaker, and C. Woodward. “SUNDIALS: Suite of Nonlinear and Differential/Algebraic Equation Solvers”. *ACM Trans. Math. Softw.* 31 (2005), pp. 363–396.

[90] D. Holmes. “A General Analytical Method for Determining the Theoretical Harmonic Components of Carrier Based PWM Strategies”. *Proceedings of the IEEE Industry Applications Conference*. 1998, pp. 1207–1214.

[91] D. Holmes and T. Lipo. *Pulse Width Modulation For Power Converters: Principles and Practice*. Vol. 18. John Wiley , Hoboken, NJ, 2003.

[92] J. Holtz. “Pulsewidth Modulation for Electronic Power Conversion”. *Proceedings of the IEEE* 82 (1994), pp. 1194–1214.

[93] C. Hou, M. Ouyang, L. Xu, and H. Wang. “Approximate Pontryagin’s Minimum Principle Applied to the Energy Management of Plug-In Hybrid Electric Vehicles”. *Applied Energy* 115 (2014), pp. 174–189.

[94] B. Houska, J. Frasch, and M. Diehl. “An Augmented Lagrangian Based Algorithm for Distributed NonConvex Optimization”. *SIAM Journal on Optimization* 26 (2016), pp. 1101–1127.

[95] X. Hu, Y. Li, C. Lv, and Y. Liu. "Optimal Energy Management and Sizing of a Dual Motor-Driven Electric Powertrain". *IEEE Transactions on Power Electronics* 34 (2019), pp. 7489–7501.

[96] "IEEE Standard Test Code for Resistance Measurement". *IEEE Std 118-1978* (1978), pp. 1–20.

[97] "IEEE Standard Test Procedure for Polyphase Induction Motors and Generators". *IEEE Std 112-2017 (Revision of IEEE Std 112-2004)* (2018), pp. 1–115.

[98] International Energy Agency. *CO_2 Emissions from Fuel Combustion: Overview*. 2019.

[99] International Energy Agency. *World Energy Balances 2019*. 2019.

[100] International Energy Agency. *Global EV Outlook 2020*. 2020.

[101] S. Jahdi, O. Alatise, C. Fisher, L. Ran, and P. Mawby. "An Evaluation of Silicon Carbide Unipolar Technologies for Electric Vehicle Drive-Trains". *IEEE Journal of Emerging and Selected Topics in Power Electronics* 2 (2014), pp. 517–528.

[102] P. Jansen and R. Lorenz. "A Physically Insightful Approach to the Design and Accuracy Assessment of Flux Observers for Field Oriented Induction Machine Drives". *IEEE Transactions on Industry Applications* 30 (1994), pp. 101–110.

[103] J. N. Juang and M. Phan. "Deadbeat Predictive Controllers". *NASA Technical Report NASA-TM-112862* (1997), pp. 1–37.

[104] J. Kelly, Q. Dai, and M. Wang. "Globally Regional Life Cycle Analysis of Automotive Lithium-Ion Nickel Manganese Cobalt Batteries". *Mitigation and Adaptation Strategies for Global Change* 25 (2020), pp. 371–396.

[105] R. Kerkman. "Twenty Years of PWM AC Drives: When Secondary Issues Become Primary Concerns". *Proceedings of the IEEE International Conference on Industrial Electronics, Control, and Instrumentation*. 1996, pp. LVII–LXIII.

[106] A. Khambadkone and J. Holtz. "Vector-Controlled Induction Motor Drive with a Self-Commissioning Scheme". *IEEE Transactions on Industrial Electronics* 38 (1991), pp. 322–327.

[107] H. G. Kim, S. K. Sul, and M. H. Park. "Optimal Efficiency Drive of a Current Source Inverter Fed Induction Motor by Flux Control". *IEEE Transactions on Industry Applications* IA-20 (1984), pp. 1453–1459.

[108] N. Kim, S. Cha, and H. Peng. "Optimal Control of Hybrid Electric Vehicles Based on Pontryagin's Minimum Principle". *IEEE Transactions on Control Systems Technology* 19 (2011), pp. 1279–1287.

[109] S.-J. Kim, K. Koh, S. Boyd, and D. Gorinevsky. "l_1 Trend Filtering". *SIAM Review* 51 (2009), pp. 339–360.

[110] T. S. Kim, C. Manzie, and R. Sharma. "Two-Stage Optimal Control of a Parallel Hybrid Vehicle with Traffic Preview". *IFAC Proceedings Volumes* 44 (2011). 18th IFAC World Congress, pp. 2115–2120.

[111] I. Kioskeridis and N. Margaris. "Loss Minimization in Induction Motor Adjustable-Speed Drives". *IEEE Transactions on Industrial Electronics* 43 (1996), pp. 226–231.

[112] C. Kirches. *Fast Numerical Methods for Mixed-Integer Nonlinear Model-Predictive Control*. Vieweg+Teubner, Wiesbaden, 2011.

[113] D. S. Kirschen, D. W. Novotny, and W. Suwanwisoot. "Minimizing Induction Motor Losses by Excitation Control in Variable Frequency Drives". *IEEE Transactions on Industry Applications* (1984), pp. 1244–1250.

[114] K. Knierim and O. Sawodny. "Real-Time Trajectory Generation for Three-Times Continuous Trajectories". *Proceedings of the IEEE Conference on Industrial Electronics and Applications*. 2012, pp. 1462–1467.

[115] S. Koehler, A. Viehl, O. Bringmann, and W. Rosenstiel. "Energy-Efficient torque Distribution for Axle-Individually Propelled Electric Vehicles". *Proceedings of the IEEE Intelligent Vehicles Symposium*. 2014, pp. 1109–1114.

[116] J. W. Kolar, H. Ertl, and F. C. Zach. "Influence of the Modulation Method on the Conduction and Switching Losses of a PWM Converter System". *IEEE Transactions on Industry Applications* 27 (1991), pp. 1063–1075.

[117] J. Kolar, F. Zach, and F. Casanellas. "Losses in PWM Inverters using IGBTs". *IEE Proceedings - Electric Power Applications* 142 (1995), pp. 285–288.

[118] K. P. Kovacs and I. Racz. *Transiente Vorgänge in Wechselstrommaschinen Band 1 & 2*. Budapest: Verlag der Ungarischen Akademie der Wissenschaften, Budapest, 1959.

[119] P. C. Krause and C. H. Thomas. "Simulation of Symmetrical Induction Machinery". *IEEE Transactions on Power Apparatus and Systems* 84 (1965), pp. 1038–1053.

[120] P. C. Krause, O. Wasynczuk, S. Sudhoff, and S. Pekarek. *Analysis of Electric Machinery and Drive Systems*. Wiley, Hoboken, New Jersy; Piscataway, NJ, 2013.

[121] C. Kwon and S. D. Sudhoff. "Genetic Algorithm-Based Induction Machine Characterization Procedure with Application to Maximum Torque per Amp Control". *IEEE Transactions on Energy Conversion* 21 (2006), pp. 405–415.

[122] D. Leineweber, I. Bauer, H. Bock, and J. Schlöder. "An Efficient Multiple Shooting Based Reduced SQP Strategy for Large-Scale Dynamic Process Optimization. (Part I and II)". *Computers and Chemical Engineering* 27 (2003), pp. 157–174.

[123] B. Lenzo, G. De Filippis, A. Dizqah, A. Sorniotti, P. Gruber, S. Fallah, and W. De Nijs. "Torque Distribution Strategies for Energy-Efficient Electric Vehicles With Multiple Drivetrains". *Journal of Dynamic Systems, Measurement, and Control* 139 (2017), pp. 121004-1 - 121004–13.

[124] W. Leonhard. "Microcomputer Control of High Dynamic Performance AC-Drives - A survey". *Automatica* 22 (1986), pp. 1–19.

[125] W. Leonhard. "30 Years Space Vectors, 20 Years Field Orientation, 10 Years Digital Signal Processing with Controlled AC-Drives, a Review (Part 1 and 2)". *EPE Journal* 1 (1991), pp. 13–19.

[126] W. Leonhard. *Control of Electrical Drives*. Springer, Berlin, Heidelberg, 2001.

[127] E. Levi, M. Sokola, A. Boglietti, and M. Pastorelli. "Iron Loss in Rotor-Flux-Oriented Induction Machines: Identification, Assessment of Detuning, and Compensation". *IEEE Transactions on Power Electronics* 11 (1996), pp. 698–709.

[128] J. Levine. *Analysis and Control of Nonlinear Systems - A Flatness-based Approach*. Springer, Berlin, Heidelber, 2009.

[129] S. Li, K. Li, R. Rajamani, and J. Wang. "Model Predictive Multi-Objective Vehicular Adaptive Cruise Control". *IEEE Transactions on Control Systems Technology* 19 (2011), pp. 556–566.

[130] S. E. Li, K. Deng, Y. Zheng, and H. Peng. "Effect of Pulse-and-Glide Strategy on Traffic Flow for a Platoon of Mixed Automated and Manually Driven Vehicles". *Computer-Aided Civil and Infrastructure Engineering* 30 (2015), pp. 892–905.

[131] S. Lim and K. Nam. "Loss-Minimising Control Scheme for Induction Motors". *IEE Proceedings - Electric Power Applications* 151 (2004), pp. 385–397.

[132] A. Linder, R. Kanchan, P. Stolze, and R. Kennel. *Model-Based Predictive Control of Electric Drives*. Cuvillier, Göttingen, 2010.

[133] H. O. List and P. Schoeggl. "Objective Evaluation of Vehicle Driveability". *SAE Technical Paper*. 1998, pp. 1–9.

[134] J. Liu and H. Peng. "Modeling and Control of a Power-Split Hybrid Vehicle". *IEEE Transactions on Control Systems Technology* 16 (2008), pp. 1242–1251.

[135] K. Liu, J. Wang, T. Yamamoto, and T. Morikawa. "Exploring the Interactive Effects of Ambient Temperature and Vehicle Auxiliary Loads on Electric Vehicle Energy Consumption". *Applied Energy* 227 (2018), pp. 324–331.

[136] M. M. Liwschitz-Garik. "Computation of Skin Effect in Bars of Squirrel-Cage Rotors". *Transactions of the American Institute of Electrical Engineers. Part III: Power Apparatus and Systems* 74 (1955), pp. 768–771.

[137] R. Lorenz and S.-. Yang. "Efficiency-Optimized Flux Trajectories for Closed-Cycle Operation of Field-Orientation Induction Machine Drives". *IEEE Transactions on Industry Applications* 28 (1992), pp. 574–580.

[138] X. Luo, Y. Liao, H. Toliyat, A. El-Antably, and T. A. Lipo. "Multiple Coupled Circuit Modeling of Induction Machines". *Proceedings of the IEEE Industry Applications Conference*. 1993, pp. 203–210.

[139] E. Lwithwaite. "Magnetic Equivalent Circuits for Electrical Machines". *Proceedings of the Institution of Electrical Engineers* 114 (1967), pp. 1805–1809.

[140] P. Martin and P. Rouchon. "Flatness and Sampling Control of Induction Motors". *IFAC Proceedings Volumes* 29 (1996), pp. 2786–2791.

[141] P. Martin and P. Rouchon. "Two Remarks on Induction Motors". *Proceedings of the CESA'96 IMACS Multiconference*. 1996, pp. 76–9.

[142] A. Massarini, U. Reggiani, and M. Kazimierczuk. "Analysis of Networks with Ideal Switches by State Equations". *IEEE Transactions on Circuits and Systems I: Fundamental Theory and Applications* 44 (1997), pp. 692–697.

[143] B. McGrath and D. Holmes. "A General Analytical Method for Calculating Inverter DC-Link Current Harmonics". *IEEE Transactions on Industry Applications* 45 (2009), pp. 1851–1859.

[144] R. C. McIlroy, N. A. Stanton, and L. Godwin. "Good Vibrations: Using a Haptic Accelerator Pedal to Encourage ECO-Driving". *Transportation Research Part F: Traffic Psychology and Behaviour* 46 (2017), pp. 34–46.

[145] F. Mensing, E. Bideaux, R. Trigui, and H. Tattegrain. "Trajectory Optimization for ECO-Driving Taking Into Account Traffic Constraints". *Transportation Research Part D: Transport and Environment* 18 (2013), pp. 55–61.

[146] H.-T. Moon, H.-S. Kim, and M.-J. Youn. "A Discrete-Time Predictive Current Control for PMSM". *IEEE Transactions on Power Electronics* 18 (2003), pp. 464–472.

[147] J. Moreira and T. Lipo. "Modeling of Saturated AC Machines Including Air Gap Flux Harmonic Components". *IEEE Transactions on Industry Applications* 28 (1992), pp. 343–349.

[148] S. Morimoto, Y. Tong, Y. Takeda, and T. Hirasa. "Loss Minimization Control of Permanent Magnet Synchronous Motor Drives". *IEEE Transactions on Industrial Electronics* 41 (1994), pp. 511–517.

[149] F. Morlock. "Personalisierter Reichweitenassistent für Batterieelektrische Fahrzeuge". PhD thesis. Institute for System Dynamics, University of Stuttgart, 2020.

[150] F. Morlock, B. Rolle, M. Bauer, and O. Sawodny. "Time Optimal Routing of Electric Vehicles Under Consideration of Available Charging Infrastructure and a Detailed Consumption Model". *IEEE Transactions on Intelligent Transportation Systems* (2019), pp. 1–13.

[151] F. Morlock, B. Rolle, M. Bauer, and O. Sawodny. "Forecasts of Electric Vehicle Power Consumption Based on Characteristic Speed Profiles and Real-Time Traffic Data". *IEEE Transactions on Vehicular Technology* (2020).

[152] F. Morlock and O. Sawodny. "An Economic Model Predictive Cruise Controller for Electric Vehicles using Gaussian Process Prediction". *IFAC-PapersOnLine* 51 (2018), pp. 876–881.

[153] Motor CAD Ltd. *Motor CAD*. `https://www.motor-design.com/motor-cad-software/`. [Online; accessed 18-July-2020]. 2020.

[154] J. N. Nash. "Direct Torque Control, Induction Motor Vector Control Without an Encoder". *IEEE Transactions on Industry Applications* 33 (1997), pp. 333–341.

[155] G. Naus, R. van den Bleek, J. Ploeg, B. Scheepers, R. van de Molengraft, and M. Steinbuch. "Explicit MPC Design and Performance Evaluation of an ACC Stop-&-Go". *Proceedings of the American Control Conference*. 2008, pp. 224–229.

[156] H. Neudorfer, A. Binder, and N. Wicker. "Analyse von Unterschiedlichen Fahrzyklen für den Einsatz von Elektrofahrzeugen". *Elektrotechnik und Informationstechnik* 123 (2006), pp. 352–360.

[157] J. Nocedal, A. Wächter, and R. Waltz. "Adaptive Barrier Update Strategies for Nonlinear Interior Methods". *SIAM Journal on Optimization* 19 (2009), pp. 1674–1693.

[158] J. Nocedal and S. Wright. *Numerical Optimization*. 2nd ed. Springer, New York, NY, 2006.

[159] D. Novotny and T. Lipo. *Vector Control and Dynamics of AC Drives*. Calarendon Press, Oxford, 1996.

[160] N. Al-Nuaim and H. Toliyat. “A Novel Method for Modeling Dynamic Air-Gap Eccentricity in Synchronous Machines Based on Modified Winding Function Theory”. *IEEE Transactions on Energy Conversion* 13 (1998), pp. 156–162.

[161] H. Ohlsson, F. Gustafsson, L. Ljung, and S. Boyd. “Trajectory Generation Using Sum-of-Norms Regularization”. *Proceedings of the IEEE Conference on Decision and Control*. 2010, pp. 540–545.

[162] S. Onori, L. Serrao, and G. Rizzoni. *Hybrid Electric Vehicles: Energy Management Strategies*. Springer-Verlag, London, 2016.

[163] E. Ozatay, U. Ozguner, and D. Filev. “Velocity Profile Optimization of On Road Vhicles: Pontryagin’s Maximum Principle Based Approach”. *Control Engineering Practice* 61 (2017), pp. 244–254.

[164] PA Consulting. *CO_2 Emissions Are Increasing - Car Makers Must Act*. `https://www.paconsulting.com/insights/2019/co2-emissions-are-increasing/`.
[Online; accessed 18-July-2020]. 2020.

[165] G. Paganelli, S. Delprat, T. Guerra, J. Rimaux, and J. Santin. “Equivalent Consumption Minimization Strategy for Parallel Hybrid Powertrains”. *Proceedings of the IEEE Vehicular Technology Conference*. 2002, pp. 2076–2081.

[166] M. Papageorgiou, M. Leibold, and M. Buss. *Optimierung: Statische, Dynamische, Stochastische Verfahren für die Anwendung. Statische, dynamische, stochastische Verfahren für die Anwendung*. Springer Vieweg, Berlin, Heidelberg, 2012.

[167] R. Park. “Two-Reaction Theory of Synchronous Machines-Generalized Method of Analysis-Part I”. *AlEE Transactions* 48 (1929), pp. 716–727.

[168] T. E. Parliament and T. C. of the European Union. *Regulation (EC) No 443/2019*. 2019.

[169] G. Pellegrino, A. Vagati, B. Boazzo, and P. Guglielmi. “Comparison of Induction and PM Synchronous Motor Drives for EV Application Including Design Examples”. *IEEE Transactions on Industry Applications* 48 (2012), pp. 2322–2332.

[170] J. Peng, H. He, and R. Xiong. “Rule Based Energy Management Strategy for a Series–Parallel Plug-In Hybrid Electric Bus Optimized by Dynamic Programming”. *Applied Energy* 185 (2017). Clean, Efficient and Affordable Energy for a Sustainable Future, pp. 1633–1643.

[171] A. Pennycott, L. D. Novellis, P. Gruber, and A. Sorniotti. “Sources of Power Loss During Torque-Vectoring for Fully Electric Vehicles”. *International Journal of Vehicle Design* 67 (2015), pp. 157–177.

[172] A. Pennycott, L. D. Novellis, P. Gruber, A. Sorniotti, and T. Goggia. "Enhancing the Energy Efficiency of Fully Electric Vehicles via the Minimization of Motor Power Losses". *Proceedings of the IEEE International Conference on Systems, Man, and Cybernetics*. 2013, pp. 4167–4172.

[173] A. Pennycott, L. D. Novellis, A. Sorniotti, P. Gruber, and A. Sorniotti. "Reducing the Motor Power Losses of a Four-Wheel Drive, Fully Electric Vehicle via Wheel Torque Allocation". *Proceedings of the Institution of Mechanical Engineers, Part D: Journal of Automobile Engineering* 228 (2014), pp. 830–839.

[174] L. V. Perez, G. R. Bossio, D. Moitre, and G. O. Garcia. "Optimization of Power Management in an Hybrid Electric Vehicle using Dynamic Programming". *Mathematics and Computers in Simulation* 73 (2006), pp. 244–254.

[175] W. Perez, A. Ruhela, and P. Tulpule. "Benchmarking Computational Time of Dynamic Programming for Autonomous Vehicle Powertrain Control". *Proceedings of the WCX SAE World Congress Experience*. 2020.

[176] N. Petit and A. Sciarretta. "Optimal Drive of Electric Vehicles using an Inversion-Based Trajectory Generation Approach". *IFAC Proceedings Volumes* 44 (2011), pp. 14519–14526.

[177] P. Pisu and G. Rizzoni. "A Comparative Study Of Supervisory Control Strategies for Hybrid Electric Vehicles". *IEEE Transactions on Control Systems Technology* 15 (2007), pp. 506–518.

[178] S. J. Plathottam and H. Salehfar. "Transient Energy Efficiency Analysis of Field Oriented Induction Machines". *IEEE Access* 5 (2017), pp. 20545–20556.

[179] PLECS. *PLECS Blockset*.
`https://plexim.com/products/plecs_blockset`.
[Online; accessed 18-July-2020]. 2020.

[180] G. Plett. "Extended Kalman Filtering for Battery Management Systems of LiPB-Based HEV Battery Packs: Part 1-3., Part 1: Background, Part 2: Modeling and Identification, Part 3: State and Parameter Estimation". *Journal of Power Sources* (2004).

[181] M. Preindl and S. Bolognani. "Model Predictive Direct Torque Control With Finite Control Set for PMSM Drive Systems, Part 1: Maximum Torque Per Ampere Operation". *IEEE Transactions on Industrial Informatics* 9 (2013), pp. 1912–1921.

[182] A. B. Proca and A. Keyhani. "Sliding-Mode Flux Observer With Online Rotor Parameter Estimation for Induction Motors". *IEEE Transactions on Industrial Electronics* 54 (2007), pp. 716–723.

[183] N. P. Quang and J. A. Dittrich. *Vector Control of Three-Phase AC Machines*. Springer, Berlin, Heidelberg, 2015.

[184] C. Rackauckas and Q. Nie. "DifferentialEquations.jl – A Performant and Feature-Rich Ecosystem for Solving Differential Equations in Julia". *Journal of Open Research Software* (2017), pp. 1–10.

[185] T. Radke. *Energieoptimale Längsführung von Kraftfahrzeugen durch Einsatz Vorausschauender Fahrstrategien*. Vol. 19. Springer Vieweg, Wiesbaden, 2013.

[186] K. Rajashekara. "Present Status and Future Trends in Electric Vehicle Propulsion Technologies". *IEEE Journal of Emerging and Selected Topics in Power Electronics* 1 (2013), pp. 3–10.

[187] J. Randles. "Kinetics of Rapid Electrode Reactions". *Discuss. Faraday Soc.* 1 (1947), pp. 11–19.

[188] S. Rechkemmer. "Lifetime Modeling and Model-Based Lifetime Optimization of Li-Ion Batteries for use in Electric Two-Wheelers". PhD thesis. Institut for System Dynamics, University of Stuttgart, 2020.

[189] H.-C. Reuss, A. Freuer, and M. Grimm. "Automatic Cruise Control for Electric Vehicles - Statistical Consumption and Driver Acceptance Analysis in a Representative Test Person Study on Public Roads". *Proceedings of the Internationales Stuttgarter Symposium*. Wiesbaden, 2014, pp. 1565–1585.

[190] J. Revels, M. Lubin, and T. Papamarkou. "Forward-Mode Automatic Differentiation in Julia". *arXiv:1607.07892 [cs.MS]* (2016), pp. 1–4.

[191] B. Rolle and O. Sawodny. "Analytical Voltage-Source Inverter Current and Conduction Loss Models for EV Power Train Simulations". *IFAC-PapersOnLine* 51 (2018), pp. 479–484.

[192] B. Rolle and O. Sawodny. "Flatness Based Optimal Control for Induction Machine Drives". *IFAC-PapersOnLine* 52 (2019), pp. 591–596.

[193] B. Rolle and O. Sawodny. "In-Vehicle System Identification of a Differential Flat Induction Motor". *Proceedings of the IFAC World Congress*. 2020.

[194] M. Ruff, A. Bunte, and H. Grotstollen. "A New Self-Commissioning Scheme for an Asynchronous Motor Drive System". *Proceedings of the IEEE Industry Applications Society Annual Meeting*. 1994, pp. 616–623.

[195] R. Russell and L. Shampine. "A Collocation Method for Boundary Value Üroblems". *Numerische Mathematik* 19 (1972), pp. 1–28.

[196] C. Sagert. “Strom und Spannungsoberwellen im Hochvolt-Bordnetz von Elektrofahrzeugen”. PhD thesis. University of Stuttgart, Institute for System Dynamics, 2015.

[197] C. Sagert, B. Rolle, M. Walter, and O. Sawodny. “Current and Voltage Harmonics in the Powertrain of Electric Vehicles”. *IEEE Transactions on Vehicular Technology* (2020), pp. 1–14.

[198] A. Savitzky and M. Golay. “Smoothing and Differentiation of Data by Simplified Least Squares Procedures.” *Analytical Chemistry* 36 (1964), pp. 1627–1639.

[199] L. H. Saw, Y. Ye, and A. A. Tay. “Integration Issues of Lithium-Ion Battery Into Electric Vehicles Battery Pack”. *Journal of Cleaner Production* 113 (2016), pp. 1032–1045.

[200] S. Schaut and O. Sawodny. “Thermal Management for the Cabin of a Battery Electric Vehicle Considering Passengers’ Comfort”. *IEEE Transactions on Control Systems Technology* (2019), pp. 1–17.

[201] Q. Schiermeier. *The Science Behind the Volkswagen Emissions Scandal*. `https://www.nature.com/news/the-science-behind-the-volkswagen-emissions-scandal-1.18426`.
Nature News, [Online; accessed 18-July-2020]. 2015.

[202] A. Schönung and H. Stemmler. “Static Frequency Changers with Subharmonic Control in Conjunction with Reversible Variable-Speed AC Drives”. *Brown Boveri Review* 51 (1964), pp. 555–577.

[203] D. Schröder. *Elektrische Antriebe - Regelung von Antriebssystemen*. Vol. 10. Springer, Berlin, Heidelberg, 2009.

[204] D. Schröder. *Elektrische Antriebe - Grundlagen*. Vol. 6. Springer Vieweg, Berlin, Heidelberg, 2017.

[205] A. Sciarretta, G. De Nunzio, and L. L. Ojeda. “Optimal Ecodriving Control: Energy-Efficient Driving of Road Vehicles as an Optimal Control Problem”. *IEEE Control Systems Magazine* 35 (2015), pp. 71–90.

[206] A. Sciarretta and A. Vahidi. *Energy-Efficient Driving of Road Vehicles: Toward Cooperative, Connected, and Automated Mobility*. Springer, Cham, Switzerland, 2020.

[207] P. Seewald, J. Josten, A. Zlocki, and L. Eckstein. “User Acceptance Evaluation Approach of Energy Efficient Driver Assistance Systems”. *Proceedings of the ITS European Congress*. 2013.

[208] L. Serrao, S. Onori, and G. Rizzoni. “ECMS as a Realization of Pontryagin’s Minimum Principle for HEV Control”. *Proceedings of the American Control Conference*. 2009, pp. 3964–3969.

[209] A. Sforza, B. Lenzo, and F. Timpone. “A State-Of-The-Art Review on Torque Distribution Strategies Aimed at Enhancing Energy Efficiency for Fully Electric Vehicles with Independently Actuated Drivetrains”. *International Journal of Mechanics and Control* 20 (2019), pp. 3–15.

[210] S. R. Shaw and S. B. Leeb. “Identification of Induction Motor Parameters from Transient Stator Current Measurements”. *IEEE Transactions on Industrial Electronics* 46 (1999), pp. 139–149.

[211] J. Shin and M. Sunwoo. “Vehicle Speed Prediction Using a Markov Chain With Speed Constraints”. *IEEE Transactions on Intelligent Transportation Systems* 20 (2019), pp. 3201–3211.

[212] I. Skinner, H. van Essen, R. Smokers, and N. Hill. “Towards the Decarbonisation of EU’s Transport Sector by 2050”. *Komisja Europejska, Bruksela* (2010), pp. 1–84.

[213] P. Somers. *Short Horizon Learning-Based Speed Prediction for Electric Vehicles*. Master Thesis, Institute for System Dynamics, University of Stuttgart. 2020.

[214] J. Stumper, A. Dötlinger, and R. Kennel. “Loss Minimization of Induction Machines in Dynamic Operation”. *IEEE Transactions on Energy Conversion* 28 (2013), pp. 726–735.

[215] J. Stumper, V. Hagenmeyer, S. Kuehl, and R. Kennel. “Flatness-Based Deadbeat Control Revisited: Robust and High-Performance Design for Electrical Drives”. *Proceedings of the IEEE American Control Conference*. 2013, pp. 1822–1827.

[216] J. F. Stumper. “Flatness-based predictive and optimal control for electrical drives”. PhD thesis. Lehrstuhl für elektrische Antriebssysteme und Leistungselektronik der Technischen Universität München, 2012.

[217] S. D. Sudhoff, B. T. Kuhn, K. A. Corzine, and B. T. Branecky. “Magnetic Equivalent Circuit Modeling of Induction Motors”. *IEEE Transactions on Energy Conversion* 22 (2007), pp. 259–270.

[218] S. Sudhoff. “Magnetic Core Loss”. In: *Power Magnetic Devices: A Multi-Objective Design Approach*. Ed. by S. Sudhoff. IEEE Press, Piscataway, NJ, 2014, pp. 178–204.

[219] C. Sun, X. Hu, S. J. Moura, and F. Sun. “Velocity Predictors for Predictive Energy Management in Hybrid Electric Vehicles”. *IEEE Transactions on Control Systems Technology* 23 (2015), pp. 1197–1204.

[220] D. Tavernini, M. Metzler, P. Gruber, and A. Sorniotti. "Explicit Nonlinear Model Predictive Control for Electric Vehicle Traction Control". *IEEE Transactions on Control Systems Technology* 27 (2019), pp. 1438–1451.

[221] R. Tibshirani. "Regression Shrinkage and Selection Via the Lasso". *Journal of the Royal Statistical Society: Series B (Methodological)* 58 (1996), pp. 267–288.

[222] F. Tinazzi, S. Bolognani, S. Calligaro, P. Kumar, R. Petrella, and M. Zigliotto. "Classification and Review of MTPA Algorithms for Synchronous Reluctance and Interior Permanent Magnet Motor Drives". *Proceedings of the European Conference on Power Electronics and Applications*. 2019, pp. 1–10.

[223] H. Toliyat, E. Levi, and M. Raina. "A Review of RFO Induction Motor Parameter Estimation Techniques". *IEEE Transactions on Energy Conversion* 18 (2003), pp. 271–283.

[224] H. Toliyat, T. Lipo, and J. White. "Analysis of a Concentrated Winding Induction Machine for Adjustable Speed Drive Applications." *IEEE Transactions on Energy Conversion* 6 (1991), pp. 679–683.

[225] Transport & Environment. *Electric Surge: Carmaker's Electric Car Plans Across Europe 2019-2025*. 2019.

[226] T. J. Triggs, W. G. Harris, H. F. Group, T. J. Triggs, and W. G. Harris. *Reaction Time of Drivers to Road Stimuli*. Tech. rep. 1982.

[227] T. H. Tsang, D. M. Himmelblau, and T. F. Edgar. "Optimal Control via Collocation and Non-Linear Programming". *International Journal of Control* 21 (1975), pp. 763–768.

[228] M. N. Uddin and S. W. Nam. "New Online Loss-Minimization-Based Control of an Induction Motor Drive". *IEEE Transactions on Power Electronics* 23 (2008), pp. 926–933.

[229] S. Vaez-Zadeh and E. Jalali. "Combined Vector Control and Direct Torque Control Method for High Performance Induction Motor Drives". *Energy Conversion and Management* 48 (2007), pp. 3095–3101.

[230] A. Vahidi and A. Eskandarian. "Research Advances in Intelligent Collision Avoidance and Adaptive Cruise Control". *IEEE Transactions on Intelligent Transportation Systems* 4 (2003), pp. 143–153.

[231] A. Vahidi and A. Sciarretta. "Energy Saving Potentials of Connected and Automated Vehicles". *Transportation Research Part C: Emerging Technologies* 95 (2018), pp. 822–843.

[232] K. van Berkel, B. de Jager, T. Hofman, and M. Steinbuch. "Implementation of Dynamic Programming for Optimal Control Problems With Continuous States". *IEEE Transactions on Control Systems Technology* 23 (2015), pp. 1172–1179.

[233] A. van der Schaft and D. Jeltsema. "Port-Hamiltonian Systems Theroy: An Introductory Overview". *Foundations and Trends in Systems and Control* 1 (2014), pp. 173–378.

[234] T. van Keulen, D. van Mullem, B. de Jager, J. Kessels, and M. Steinbuch. "Design, Implementation, and Experimental Validation of Optimal Power Split Control for Hybrid Electric Trucks". *Control Engineering Practice* 20 (2012), pp. 547–558.

[235] M. J. Van Nieuwstadt and R. M. Murray. "Real-Time Trajectory Generation for Differentially Flat Systems". *International Journal of Robust and Nonlinear Control* 8 (1998), pp. 995–1020.

[236] P. Vas. "Generalized Analysis of Saturated AC Machines". *Archiv für Elektrotechnik* 64 (1981), pp. 57–62.

[237] P. Vas, K. E. Hallenius, and J. E. Brown. "Cross-Saturation in Smooth-Air-Gap Electrical Machines". *IEEE Transactions on Energy Conversion* EC-1 (1986), pp. 103–112.

[238] G. C. Verghese and S. R. Sanders. "Observers for Flux Estimation in Induction Machines". *IEEE Transactions on Industrial Electronics* 35 (1988), pp. 85–94.

[239] A. Wächter and L. T. Biegler. "On the Implementation of an Interior-Point Filter Line-Search Algorithm for Large-Scale Nonlinear Programming". *Mathematical Programming* 106 (2006), pp. 25–57.

[240] R. Waltz, J. Morales, J. Nocedal, and D. Orban. "An Interior Algorithm for Nonlinear Optimization that Combines Line Search and Trust Region Steps". *Mathematical Programming* 107 (2006), pp. 391–408.

[241] R. Wang and S. M. Lukic. "Review of Driving Conditions Prediction and Driving Style Recognition Based Control Algorithms for Hybrid Electric Vehicles". *Proceedings of the IEEE Vehicle Power and Propulsion Conference*. 2011, pp. 1–7.

[242] T. Windisch and W. Hofmann. "Loss Minimizing and Saturation Dependent Control of Induction Machines in Vehicle Applications". *Proceedings of the Annual Conference of the IEEE Industrial Electronics Society*. 2015, pp. 001530–001535.

[243] S. G. Wirasingha and A. Emadi. "Classification and Review of Control Strategies for Plug-In Hybrid Electric Vehicles". *IEEE Transactions on Vehicular Technology* 60 (2011), pp. 111–122.

[244] S. Xie, X. Hu, Z. Xin, and J. Brighton. "Pontryagin's Minimum Principle Based Model Predictive Control of Energy Management for a Plug-In Hybrid Electric Bus". *Applied Energy* 236 (2019), pp. 893–905.

[245] S. Yang, D. Ding, X. Li, Z. Xie, X. Zhang, and L. Chang. "A Novel Online Parameter Estimation Method for Indirect Field Oriented Induction Motor Drives". *IEEE Transactions on Energy Conversion* 32 (2017), pp. 1562–1573.

[246] F. Ye, P. Hao, X. Qi, G. Wu, K. Boriboonsomsin, and M. J. Barth. "Prediction-Based Eco-Approach and Departure at Signalized Intersections With Speed Forecasting on Preceding Vehicles". *IEEE Transactions on Intelligent Transportation Systems* 20 (2019), pp. 1378–1389.

[247] M. Yilmaz. "Limitations/Capabilities of Electric Machine Technologies and Modeling Approaches for Electric Motor Design and Analysis in Plug-In Electric Vehicle Applications". *Renewable and Sustainable Energy Reviews* 52 (2015), pp. 80–99.

[248] M. Yilmaz and P. Krein. "Capabilities of Finite element Analysis and Magnetic Equivalent Circuits for Electrical Machine Analysis and Design". *Proceedings of the IEEE Power Electronics Specialists Conference*. 2008, pp. 4027–4033.

[249] L. Zai, C. DeMarco, and T. Lipo. "An Extended Kalman Filter Approach to Rotor Time Constant Measurement in PWM Induction Motor Drives". *IEEE Transactions on Industry Applications* (1992), pp. 96–104.

[250] A. Zanelli, A. Domahidi, J. Jerez, and M. Morari. "FORCES NLP: An Efficient Implementation of Interior-Point Methods for Multistage Nonlinear Nonconvex Programs". *International Journal of Control* 93 (2020), pp. 13–29.

[251] Y. Zhou, A. Ravey, and M.-C. Pera. "A Survey on Driving Prediction Techniques for Predictive Energy Management of Plug-In Hybrid Electric Vehicles". *Journal of Power Sources* 412 (2019), pp. 480–495.

[252] Z. Q. Zhu and D. Howe. "Electrical Machines and Drives for Electric, Hybrid, and Fuel Cell Vehicles". *Proceedings of the IEEE* 95 (2007), pp. 746–765.